Fabrication of Engineered Ceramic Components by the Slurry-Based Three Dimensional Printing Process

by

Jason E. Grau

B.S., M.S. Materials Science and Engineering
Iowa State University, 1994

Submitted to the Department of Materials Science and Engineering in Partial Fulfillment of the Requirements for the Degree of

DOCTOR OF PHILOSOPHY
in Ceramics

at the
MASSACHUSETTS INSTITUTE OF TECHNOLOGY

June 1998

© 1998 Massachusetts Institute of Technology.
All rights reserved.

Signature of Author:_____
Department of Materials Science and Engineering
May 1, 1998

Certified by:_____
Professor Michael J. Cima
Sumitomo Electric Industries Professor of Materials Science Engineering
Thesis Supervisor

Accepted by:_____
Professor Linn W. Hobbs
John F. Elliott Professor of Materials
Chairman, Committee for Graduate Students

ARCHIVES
MASSACHUSETTS INSTITUTE OF TECHNOLOGY
OCT 06 1998
LIBRARIES

Fabrication of Engineered Ceramic Components by the Slurry-Based Three Dimensional Printing Process

by

Jason E. Grau

Submitted to the Department of Materials Science and Engineering
on May 1, 1998 in Partial Fulfillment of the
Requirements for the Degree of Doctor of Philosophy in
Ceramics

ABSTRACT

The slurry-based 3DP process is a novel process that has been developed for fabricating engineered ceramic components. The process is a solid freeform fabrication (SFF) technique that builds components directly from a computer CAD file on a layer-by-layer basis. Solid-liquid interactions play a primary role in the process physics of each stage of the process. The formation of the powder bed is the first critical step in the slurry-based 3DP process. Powder bed microstructure is controlled by slurry stability and the slip casting rate. Capillary pressure must be controlled to produce crack-free powder beds. A critical saturation thickness (CST) was identified above which powder beds would crack. The CST increased with variables that reduced the capillary pressure. Conditions to fabricate crack-free powder beds using a multi-layer slurry deposition process were outlined. Solid-liquid interactions also affected the rate of infiltration of liquid into the powder bed. The rate of liquid infiltration affected the binder infiltration into the powder bed and the slip casting rate of the slurry. Slip casting rates of the slurry differed for regions of the powder bed printed with binder. The differential casting kinetics lead to two phenomena: density variation and slurry migration. The packing density of powder beds was higher in regions printed with binder, indicating that the density was higher in regions with lower casting rates. Slurry migration occurred due to the difference in liquid flux over the binder-printed region compared to the unprinted region of the powder bed. A model of the slip casting process was developed to identify variables to minimize the differential casting kinetics. The contact angle of the solvent and volume fraction of binder printed into the part affect the casting rate. The relative magnitude of the contact angles was calculated for a given volume fraction of binder to match the casting kinetics. This fundamental understanding of the solid-liquid interactions indicates routes to fabricate engineered ceramic components from numerous materials systems. Alumina components with green densities greater than 60% theoretical and sintered densities greater than 99% were fabricated. The general process has also been applied to silicon nitride.

Thesis Supervisor: Michael Cima
Title: Sumitomo Electric Industries Professor of Materials Science Engineering

ACKNOWLEDGEMENTS

First of all, I would like to thank my wife, Amber, for her love and constant support throughout my studies at M.I.T. She has been an endless source of inspiration and encouragement. I would also like to thank my family for their tremendous support.

The list of people to thank at M.I.T. is too long to list everyone by name. I would like to thank my thesis advisor, Professor Michael Cima, for guidance and instilling in me a sense of scientific curiosity. I also want to thank Professor Ely Sachs for his valuable suggestions throughout my research. Both of you have helped foster the dynamic environment of the 3DP group that has enabled me to grow both personally and professionally.

The 3DP project is a team project in every sense. I learned more during brainstorming sessions with the 3DP group than in any class. I would especially like to thank members of the 3DP materials group: Ben, Satbir, Jae, Daniel, Bugra, Mike, Bob, Scott, Dai, and Richard. Special thanks go to Jooho Moon. We worked very well together and were able to get some great results. The 3DP staff has also been tremendous. Jim Serdy and Dave Brancazio have always been willing to put in the time to help out and answer questions.

The group of people at the CPRL (you know who you are) has helped smooth the ride. Lenny, Barbara, and John are the glue that holds the CPRL together. I value the friendships I have made with all of my co-workers.

TABLE OF CONTENTS

TITLE PAGE **1**
ABSTRACT **2**
ACKNOWLEDGEMENTS **3**
TABLE OF CONTENTS **4**
LIST OF FIGURES **8**
LIST OF TABLES **12**
EXECUTIVE SUMMARY **13**

1. INTRODUCTION **21**
1.1. Three Dimensional Printing (3DP) 21
1.2. Requirements for Fabricating Engineered Ceramic Components 25
1.2.1. Powder Size Requirements 26
1.2.2. Uniformity of the Microstructure 26
1.2.3. Effect of Packing Density of the Green Body 27
1.3. Traditional Ceramics Processing Techniques 29
1.3.1. Dry Pressing 29
1.3.2. Injection Molding 29
1.3.3. Tape Casting 29
1.3.4. Slip Casting 30
1.4. Previous Attempts at Fabricating Structural Ceramics Using 3DP 31
1.4.1. Press Rolling Approach 31
1.4.2. Spray Dried Granules 32
1.5. Slurry-Based 3DP Process 32
1.6. Introduction to Solid-Liquid Interactions 33
1.7. Scope of this Thesis 37
1.8. Organization of the Thesis 39

2. OPTIMIZING SLURRY COMPOSITION FOR STABILITY AND REDISPERSION BEHAVIOR **40**

2.1. Introduction 40
2.2. Attractive Forces in Colloidal Systems 42
2.2.1. van der Waals Forces Between Molecules 42
2.2.2. Attractive Forces Between Macroscopic Bodies 42
2.3. Repulsive Forces Between Particles 45
2.3.1. How particles acquire charge 45
2.3.2. The Electrical Double Layer 47
2.3.3. Repulsive Potential Due to the Electrical Double Layer 50
2.4. DLVO Theory – Total Potential Between Particles 52
2.4.1. Implications of Total Potential Curves 52
2.4.2. Shulze-Hardy Rule – Effect of Indifferent Ions 54
2.4.3. Kinetics of Coagulation 55
2.5. Polymeric Stabilization 56
2.5.1. Poly(methacrylic acid) - Darvan 57
2.5.2. Poly(acrylic acid) 58
2.5.3. Dispersion in Organic Media 59
2.6. Measuring Colloidal Stability 59
2.6.1. Electrokinetic phenomena 59
2.6.2. Indirect Measurements 60
2.7. Optimization of Alumina Slurry Stability for Slurry-Based 3DP 60
2.7.1. Slurry Preparation 61
2.7.2. Zeta potential measurements 62
2.7.3. Green density of slip cast samples 65
2.7.4. Effect of Acid Concentration on Alumina Slurry Stability 65
2.7.5. Stabilization with Darvan 821A 67
2.8. Redispersion Behavior of Slip Cast Alumina Powder Beds 69
2.8.1. Effect of Powder Type 73
2.8.2. Effect of Adding Polyethylene Glycol to the Slurry 75
2.8.3. Effect of the Redispersion Solvent 79
2.9. Discussion 82

2.10 Conclusions 85

3. POWDER BED FORMATION AND MICROSTRUCTURE 87

3.1. Introduction 87

3.2. Spray Deposition 87

3.3. Slurry Jetting 91

3.3.1. Effect of Slurry Jetting Conditions on Powder Bed Microstructure 93

3.3.2. Defects in Slurry-Jetted Powder Beds 96

3.3.3. Sintered Powder Beds 102

3.3.4. Sintered microstructures 106

3.4. Tape Casting 109

3.5. Conclusions 112

4. CONTROLLING CRACKING IN MULTI-LAYER CERAMIC BODIES 114

4.1. Introduction 114

4.2. Literature Review 114

4.3. Experimental Procedure 117

4.4. Experimental Observations 118

4.4.1. Impact of Powder Size 122

4.4.2. Impact of Liquid Surface Tension 122

4.4.3. Impact of Liquid Distribution 127

4.4.4. Effect of Saturation Thickness on Microstructure 127

4.5. Determining Slurry Jetting Conditions 130

4.6. Discussion 133

4.7. Conclusions 135

5. IMPACT OF THE BINDER ON THE PROCESS 137

5.1. Introduction 137

5.2. Evaluation of Binder Systems 137

5.2.1. Emulsion Binders 138

5.2.2. Polyacrylic Acid (PAA) 138

5.2.3. Furfuryl Resin 140
5.2.4. Joncryl™ Binder 145
5.3. Binder-Powder Bed Interactions 145
5.3.1. Width of Binder Primitives 146
5.3.2. Binder Infiltration Kinetics 150
5.4. Impact of Binder on Slurry Casting Kinetics 157
5.4.1. Observations of Single Lines of Slurry 158
5.4.2. Direct Observation of Differential Casting Rates 161
5.4.3. Measuring the Slurry Casting Time 163
5.4.4. Profilometry of Test Bars 171
5.4.5. Microstructure of the powder bed 173
5.4.6. Modeling the Slurry Casting - Colloidal Filtration 175
5.5. Discussion 192
5.6. Conclusions 194

6. ALUMINA PARTS PRINTED WITH JONCRYL BINDER 196
6.1. Introduction 196
6.2. Printing Procedure 196
6.3. Binder Saturation Experiments 197
6.3.1. Surface Finish of Printed Parts 201
6.3.2. Mercury Porosimetry of Printed Parts 205
6.4. Complex-Shaped Parts 209
6.4.1. Rotors Printed on the Alpha Machine 209
6.4.2. Parts Printed while Shaving the Powder Bed 213
6.5. Conclusions 216

7. CONCLUSIONS 218
APPENDIX A 222
APPENDIX B 225
REFERENCES 227

6. ALUMINA PARTS PRINTED WITH JONCRYL BINDER 196
6.1. Introduction 196
6.2. Printing Procedure 196
6.3. Binder Saturation Experiments 197
6.3.1. Surface Finish of Printed Parts 201
6.3.2. Mercury Porosimetry of Printed Parts 205
6.4. Complex-Shaped Parts 209
6.4.1. Rotors Printed on the Alpha Machine 209
6.4.2. Parts Printed while Shaving the Powder Bed 213
6.5. Conclusions 216

7. CONCLUSIONS 218
APPENDIX A 222
APPENDIX B 225
REFERENCES 227

LIST OF FIGURES

Figure 1.1. Schematic of the standard 3DP process 22
Figure 1.2. Schematic of continuous jet 3DP print head 23
Figure 1.3. Configuration of the axes on the 3DP machine 24
Figure 1.4. Sintering trajectories for alumina 28
Figure 1.5. Schematic of the slurry-based 3DP process 34
Figure 1.6. Relationship between contact angle and interfacial energies 36
Figure 1.7. Capillary pressure as a function of saturation 38

Figure 2.1. Potential energy of attraction between two bodies 44
Figure 2.2. Schematic representation of the diffuse double layer 48
Figure 2.3. Electrostatic potential versus distance 51
Figure 2.4. Total potential curves for colloidal systems 53

Figure 2.5. Effect of valence on the CCC 55
Figure 2.6. Polymer unit of sodium - PMAA (Darvan 7) 57
Figure 2.7. Time-dependence of the zeta potential for Ceralox powders 64
Figure 2.8. Zeta potential versus density for Ceralox powders 66
Figure 2.9. Viscosity data for 40 volume percent alumina slurries 68
Figure 2.10. Zeta potential measurements for slurries with Darvan 821A 70
Figure 2.11. Schematic representation of part retrieval process 71
Figure 2.12. Schematic of the apparatus for measuring redispersion 72
Figure 2.13. Effect of powder type on redispersion behavior 74
Figure 2.14. Effect of PEG additions on the redispersion behavior 76
Figure 2.15. Effect of heating the samples on redispersion behavior 78
Figure 2.16. Redispersion behavior of powder beds with Darvan 821A 80
Figure 2.17. Effect of the solvent on the redispersion behavior 81
Figure 2.18. Solubility of $Al(OH)_3$ as a function of pH 83

Figure 3.1. Schematic of the raster pattern used to deposit slurry 88
Figure 3.2. Mercury porosimetry data of powder beds 90
Figure 3.3. Schematic of the slurry feed system 92
Figure 3.4. Mercury porosimetry data of slurry-jetted powder beds 95
Figure 3.5. Effect of print variables on the number of large pores 97
Figure 3.6. SEM X-section of slurry-jetted powder beds 98
Figure 3.7. Cross-section of a slurry line as it slip casts 100
Figure 3.8. Surface profilometry of slurry-jetted line pairs 101
Figure 3.9. Staggered raster pattern used for slurry-jetted beds 103
Figure 3.10. Effect of sintering temperature on density 104
Figure 3.11. Microstructures of jetted powder beds sintered at 1650°C 107
Figure 3.12. Slip cast samples sintered at 1650°C 108
Figure 3.13. Schematic representation of the tape casting process 110
Figure 3.14. Optical micrographs of sintered powder beds 111

Figure 4.1. Stress versus saturation 116

Figure 4.2. Schematic representation of the saturation thickness 120
Figure 4.3. Effect of saturation thickness on cracking behavior 121
Figure 4.4. Total layer thickness versus saturation thickness for 1.0 μm powder 123
Figure 4.5. Cracking behavior of powder beds with 4:1 water to methanol 124
Figure 4.6. Surface tension of methanol/water solutions at 20°C 125
Figure 4.7. Cracking behavior of powder beds with 0.1% Triton X-100 126
Figure 4.8. Cracking behavior of powder beds with two slurry jetting sequences 128
Figure 4.9. SEM micrographs of 0.5 μm powder bed cross-sections 129
Figure 4.10. Layer and saturation thickness calculations for jetted powder beds 131
Figure 4.11. Maximum layer thickness that can be formed 132
Figure 4.12. Schematic representation of liquid infiltration 134

Figure 5.1. Particle size of emulsion phase binders 139
Figure 5.2. Molecular structure of PAA 138
Figure 5.3. Molecular structure of furfuryl resin 140
Figure 5.4. Surface finish of parts printed with furfuryl resin binder 142
Figure 5.5. Mercury porosimetry of parts printed with furfuryl resin binder 143
Figure 5.6. Cross section of bar printed with furfuryl resin binder 144
Figure 5.7. Molecular structure of Joncryl binder 145
Figure 5.8. Line widths of solution phase binders 148
Figure 5.9. Joncryl binder line on the surface of the powder bed 151
Figure 5.10. Schematic representation of binder infiltration 152
Figure 5.11. Binder infiltration times into 1.0 μm powder bed 154
Figure 5.12. Effect of powder size on the infiltration time 155
Figure 5.13. Schematic of the bump at the interface 157
Figure 5.14. Photo of rectangular test bar 159
Figure 5.15. Singles lines of slurry jetted across the interface 160
Figure 5.16. Profiles of single lines of silicon nitride slurry 161
Figure 5.17. Photographs showing slurry casting at the interface 162
Figure 5.18. Schematic representation of the formation of the bump 164
Figure 5.19. Powder bed configuration for measuring casting times 165

Figure 5.20. Casting times of slurries 168
Figure 5.21. Effect of binder molecular weight on slurry casting time 169
Figure 5.22. Effect of the volume fraction of binder on slurry casting time 170
Figure 5.23. Photos showing the interface of the binder-printed region 172
Figure 5.24. Cumulative and differential intrusion volume data 174
Figure 5.25. Schematic representation of the filtration system 176
Figure 5.26. Hydraulic pressure profile across the mold and cast layer 178
Figure 5.27. Permeabilities calculated from (5.14) 180
Figure 5.28. Calculated casting times for 30 volume percent slurry 183
Figure 5.29. Critical cos θ ratio to match casting rates 185
Figure 5.30. Model of fluid flow resulting from differential casting kinetics 187
Figure 5.31. Volume of slurry transported, *V*, by differential casting 188
Figure 5.32. Disturbance length scale calculated from (5.21) 190

Figure 6.1. Effect of volume percent binder on the microstructure 200
Figure 6.2. Top surface finish of part # 12 202
Figure 6.3. Bottom surface finish of parts 203
Figure 6.4. Effect of layer height on the surface finish 204
Figure 6.5. Surface finish of part printed on the Alpha machine 206
Figure 6.6. Mercury porosimetry of printed parts 207
Figure 6.7. Sintered microstructure of printed part 208
Figure 6.8. Parts printed on the hood machine 211
Figure 6.9. Alumina rotors printed on the Alpha machine 212
Figure 6.10. Schematic of the shaving process to level the powder bed 214
Figure 6.11. Reconstructed alumina stator parts 215

LIST OF TABLES

Table 2.1. Examples of colloidal dispersions 40
Table 2.2. Hamaker constants for selected materials in water 45
Table 2.3. Isoelectric points for selected ceramic materials 47
Table 2.4. Zeta potential of the slurry and green density of slip cast samples 65
Table 2.5. Effect of nitric acid concentration on slurry properties 67
Table 2.6. PEG 400 content in HPA-1.0 samples after heating 77
Table 2.7. % Redispersed after 15 minutes 82

Table 3.1. Slurry jetting conditions used to generate powder beds 94
Table 3.2. Summary of mercury porosimetry data 96
Table 3.3. Densities of sintered powder beds 105
Table 3.4. Densities of powder beds sintered at 1650°C 106

Table 4.1. Selected jetting conditions and observations for powder beds 119

Table 5.1. Line widths of 10 weight percent PAA in different powder beds 149
Table 5.2. Surface tension and viscosity of binder solutions 153
Table 5.3. Binder infiltration times 157
Table 5.4. Binder regions used for slurry casting experiments 166
Table 5.5. Slurry compositions 166
Table 5.6. Casting times for single lines of slurry 167
Table 5.7. Binder printing conditions for 8-layer test bars 171
Table 5.8. Profilometry measurements 173
Table 5.9. Bulk densities of powder beds 175
Table 5.10. Contact angle and viscosity of solvents used in the slurry 182
Table 5.11. Ratio of cos θ's for slurry solvents 184

Table 6.1. Printing conditions for studying binder saturation 199
Table 6.2. Densities of parts printed with Joncryl 52 209
Table 6.3. Printing conditions for alumina stator part 213

EXECUTIVE SUMMARY

The Three Dimensional Printing (3DP) process has been modified to fabricate engineered ceramic components. The properties of engineered ceramic components are dependent upon the grain size, density, and microstructure uniformity. These requirements impose several constraints on the fabrication method. Components must be fabricated from fine powder (typically less than 1 μm in diameter) with high (>50%) and uniform packing density.

Previous attempts at fabricating structural ceramic components by 3DP were unsuccessful at producing uniform, high density powder beds. Van der Waal's forces become significant below about 10 μm, and inhibit the spreading of dry powder. The limitations of previous attempts indicated that wet processing techniques were necessary to form powder beds with high green density.

The slurry-based 3DP process has been developed to fabricate components using submicron powder sizes. The process flow chart is shown in Figure 1. The powder bed is formed by depositing a uniform layer of dispersed slurry onto a porous substrate. The powder bed is dried, and binder is printed into the powder bed. The piston is lowered, and the process is repeated until the part is completed. Powder beds prepared by the slurry-based 3DP process are cohesive. Printed parts are retrieved from the powder bed by *redispersing* the unprinted region of the powder bed. The powder bed and part are placed in water. The unprinted powder bed redisperses, while the binder-printed region remains intact.

Several critical criteria must be met for the slurry-based 3DP process. The microstructure of the parts will determine the ultimate effectiveness of components. The impact of each stage of the process on the microstructure was carefully investigated to develop the process. The critical criteria can be broadly classified as: powder bed formation, binder selection, and part retrieval. The powder bed must be crack-free with uniform porosity and high density. The binder must also be carefully selected to ensure that the binder infiltrates into the powder bed. The pore size of slurry-based 3DP powder beds is more than an order of magnitude smaller than powder beds in the standard 3DP process. Emulsion binders do not penetrate slurry-based 3DP powder beds, and solution

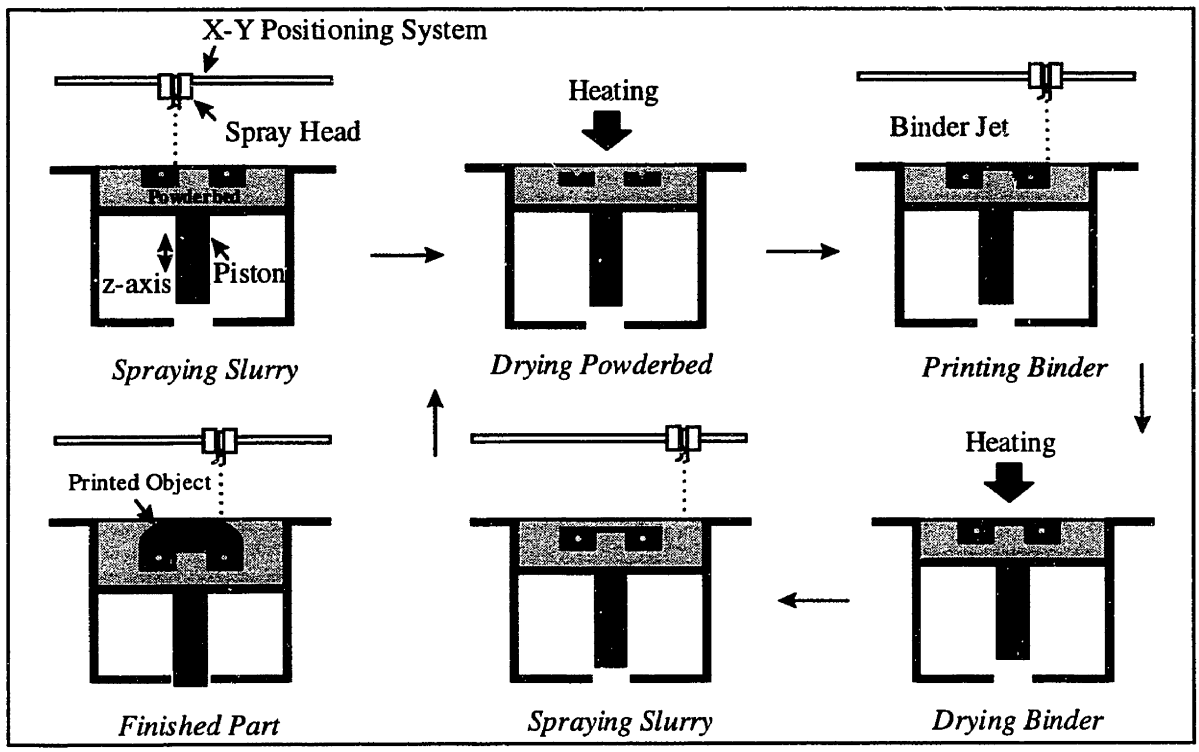

Printing Sequence

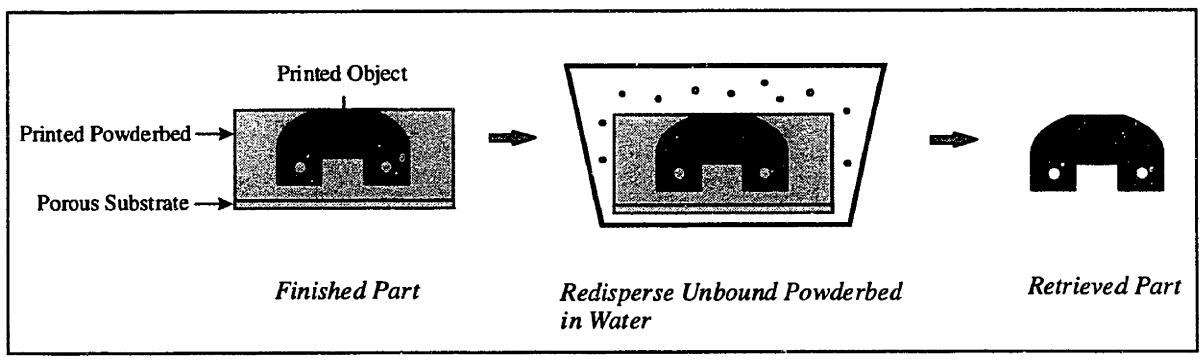

Part Retrieval

Figure 1. Schematic of the slurry-based 3DP process

phase binders must be used. The binder must also be insoluble after printing to enable part retrieval. Part retrieval is dependent upon the strength of the binder as well as the redispersion behavior of the powder bed.

The first step in achieving high and uniform packing density in the powder bed was optimizing the slurry stability. All materials are subjected to attractive van der Waal's forces. The attractive potential calculated by Hamaker for two spherical particles is:

$$V_A = -\frac{Aa}{12h}, \tag{1}$$

where A is the Hamaker constant, a the particle radius, and h the separation distance. The attractive potential must be offset by a repulsive potential for stable slurries. Repulsive potentials can be established between particles using electrostatic stabilization or polymeric stabilization. The surface potential of particles in slurries can be controlled by the concentration of *potential-determining ions*. In many ceramics, H^+ and OH^- are potential-determining ions, and the slurry stability can be controlled by varying the pH. The magnitude of the surface potential for alumina slurries was measured directly using zeta potential measurements. The maximum zeta potential for alumina was around pH 4. Slurries prepared at this pH had low viscosity and formed high density powder beds.

Powder bed redispersion is closely related to the slurry composition. Powder bed redispersion is controlled by two factors: the number of particle-particle contacts and the strength of the contacts. The number of particle-particle contacts is controlled by the particle size and packing density of the powder bed. The number of contacts varies inversely with the particle diameter cubed. Redispersion behavior improved substantially as the number of particle contacts decreased. However, sintering kinetics are adversely affected as particle diameter increases and packing density decreases. Reducing the strength of particle-particle contacts was, therefore, identified as the key to improving redispersion. Low molecular weight polyethylene glycol (PEG) significantly improved the redispersion of powder beds. PEG is believed to form soluble bridges between particles. The PEG may prevent soluble species from reprecipitating at the particle necks and forming hard agglomerates when the powder bed dries.

Several powder bed formation techniques were examined. The effect of the powder bed formation technique on the microstructure was studied in detail. Large pores within the powder beds act as performance-limiting defects. The number of large pores present in the powder bed was largest for powder beds formed by spray deposition. For slurry-jetted powder beds, the number of large pores increased with increasing line spacing. Defects are generated when the slurry interacts with the powder bed in isolated areas. Each time the slurry interacts with the powder bed, there is a probability that the slurry will not completely fill the underlying roughness. The number of defects was, therefore, largest for the spray deposition process where millions of slurry droplets are deposited per layer. Defects were substantially reduced for the slurry-jetting process. The number of slurry-powder bed interactions is reduced by orders of magnitude as the powder bed is formed by hundreds of slurry lines. Early experiments indicate that tape casting may further reduce the number of defects.

Cracking due to capillary stress can be a major problem during powder bed formation. The cracking behavior can be controlled by monitoring the saturation thickness, t_{sat}:

$$t_{sat} = t_{slurry}\left(\frac{\text{Liquid fraction of the slurry}}{\text{Pore fraction of the powder bed}}\right), \qquad (2)$$

where t_{slurry} is the thickness of the layer of slurry deposited. The saturation thickness essentially indicates the thickness of the powder bed that would be 100% saturated by a given volume of liquid. Powder beds displayed a critical saturation thickness (CST) above which powder beds would spontaneously crack. Plots of saturation thickness versus layer height identified the CST for different slurry compositions. The CST increased with factors that reduced the capillary stress. The CST was increased by increasing the pore size of the powder bed or reducing the surface tension of the solvent. Figure 2 shows a plot of saturation thickness versus layer height for 0.5 μm alumina powder. The CST for this system is about 65 μm, and crack-free powder beds were prepared by keeping the saturation thickness below 65 μm.

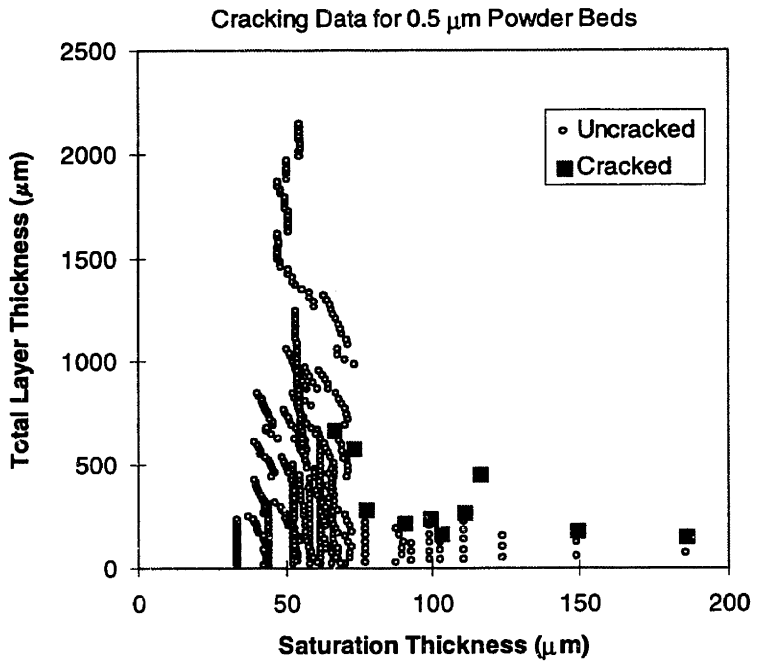

Figure 2. Effect of saturation thickness on the cracking behavior of 0.5 μm powder beds. Critical saturation thickness is about 65 μm.

The presence of binder had a significant impact upon the interactions between the slurry and the powder bed. The formation of the powder bed is a slip casting process. The solvent is withdrawn from the slurry by capillary forces, and the particles in the slurry build up a solid *cast* layer. The slip casting kinetics are dependent upon the capillary pressure, permeability, and pore fraction of the powder bed. The slip casting kinetics differ over the binder-printed region and the unprinted region of the powder bed. The differential casting kinetics has two effects: density variations and slurry migration. The packing density of the powder bed is dependent upon the casting rate. The packing density was higher for the binder-printed region where the casting kinetics are low. Slurry migration also resulted from the differential casting kinetics. Slip casting rates were higher over the unprinted region. The difference in casting rates leads to a net flux of slurry from the binder-printed region to the unprinted region. The slurry migration leads to the formation of a bump at the interface of the binder-printed region.

The slip casting kinetics were modeled to identify approaches to minimize the differential casting effects. Differences in the wetting behavior and the permeability

control the difference in casting rates for the binder-printed and unprinted regions. The casting rates are controlled by the contact angles of the slurry solvent on the binder-printed and unprinted regions in addition to the volume fraction of binder in the printed part. The ratio $\frac{\cos(\theta_{unprinted})}{\cos(\theta_{binder})}$ can be calculated for a given volume fraction of binder to match the slip casting kinetics. The plot of the critical cos θ ratio as a function of volume fraction binder is shown in Figure 3. The solvent must wet the binder-printed region better than the unprinted region to compensate for the reduced permeability. The slip casting rates deviate more moving away from the curve. The cos θ ratio for Water/IPA=1 is 0.97 and lies closest to the critical cos θ curve. Slurries prepared with Water/IPA=1 as the solvent significantly reduced the differential casting effect.

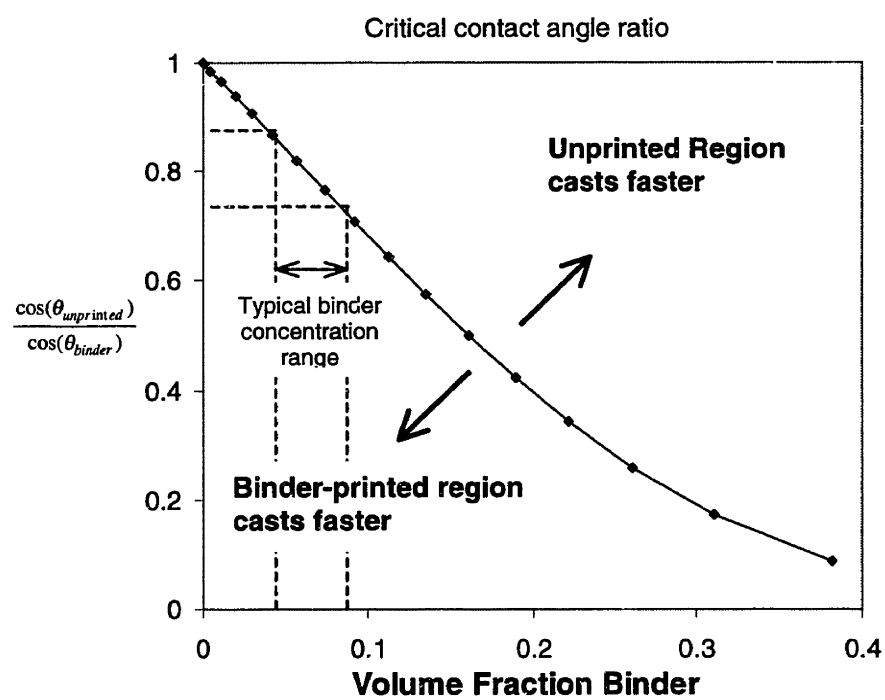

Figure 3. Critical cos θ ratio to match casting rates of binder-printed and unprinted regions. (Pore fraction = 0.60)

Parts were successfully printed using the slurry-based 3DP process. The surface finish was excellent. Surface roughness measured by surface profilometry was only ~ 2 μm. Uniform microstructures were achieved by controlling the binder concentration and powder bed formation variables. Moreover, the process has proven to be sufficiently generic to fabricate components from different materials systems. Figure 4 shows alumina and silicon nitride components fabricated by the slurry-based 3DP process.

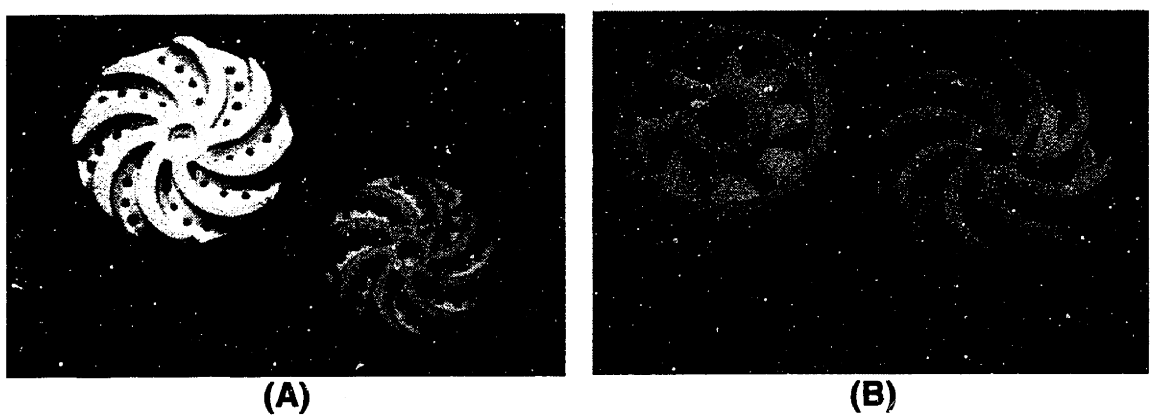

Figure 4. Alumina (A) and silicon nitride (B) components fabricated by the slurry-based 3DP process

Controlling and optimizing the process is possible by understanding the fundamental solid-liquid interactions that underlie each step of the process. Capillary-driven liquid transport affects several areas of the process. The driving force for capillary transport is the capillary pressure:

$$\Delta P = \frac{2\gamma_{LV}\cos\theta}{r_{pore}}. \qquad (3)$$

Capillary pressure leads to cracking during powder bed formation if the slurry deposition conditions are not carefully controlled. The capillary pressure is also the driving for slip casting and binder infiltration into the powder bed.

Solid-liquid interactions affect the rate of binder infiltration into the powder bed as well as the width of single line primitives. Low viscosity, low surface tension binders spread over a large area. The resolution and surface finish of parts are strongly affected by these properties.

The liquid infiltration kinetics are particularly important for interactions between the slurry and the powder bed. The packing density of slip cast powder beds depends on the slip casting rate. Slurry migration is also due to differential casting kinetics. A fundamental understanding of the solid-liquid interactions gives insight into approaches to optimize the process.

CHAPTER 1
INTRODUCTION

1.1. Three Dimensional Printing (3DP)

Computer-aided design (CAD) has become an integral component in the design and manufacturing process of numerous industries. CAD significantly improves the design process by reducing the cycle time for reiterations. A new class of manufacturing and prototyping techniques called solid freeform fabrication (SFF) has been developed in recent years to take advantage of CAD techniques. SFF techniques are tool-less fabrication methods in which components are fabricated directly from a CAD model of the component. The emergence of SFF techniques has been driven by the demand for flexible manufacturing techniques and reduced cycle times for the product development cycle. SFF technologies are capable of fabricating components with complex geometries that can not be manufactured by traditional techniques. For example, components fabricated by numerical control machining are limited by the selection of tools and the tool paths that can be followed. SFF techniques also offer significant cost advantages for prototypes and small production runs. Traditional manufacturing techniques are generally designed for high volume production runs to take advantage of economies of scale.

3-Dimensional Printing (3DP™) is an SFF technique that has been developed at M.I.T. Solid objects are created by *printing* a sequence of two-dimensional layers. The process has been used to fabricate numerous metal, ceramic, and polymeric components for a wide array of applications.[1,2,3,4,5] The standard process is pictured in Figure 1.1. Each layer of the part is created by spreading a thin layer of powdered material and selectively joining the powder by ink-jet printing a binder material. This sequence is repeated until the component is completed.

The binder material is selectively deposited using an ink-jet print head. A schematic of a continuous jet print head is shown in Figure 1.2. A piezoelectric transducer breaks the liquid up into uniform droplets. The droplets are selectively charged. The binder droplets pass through a deflection cell. Charged droplets are deflected into a catcher, while the uncharged droplets are deposited onto the powder bed. The nozzle is rastered across the powder bed as shown in Figure 1.3. The "fast axis" and

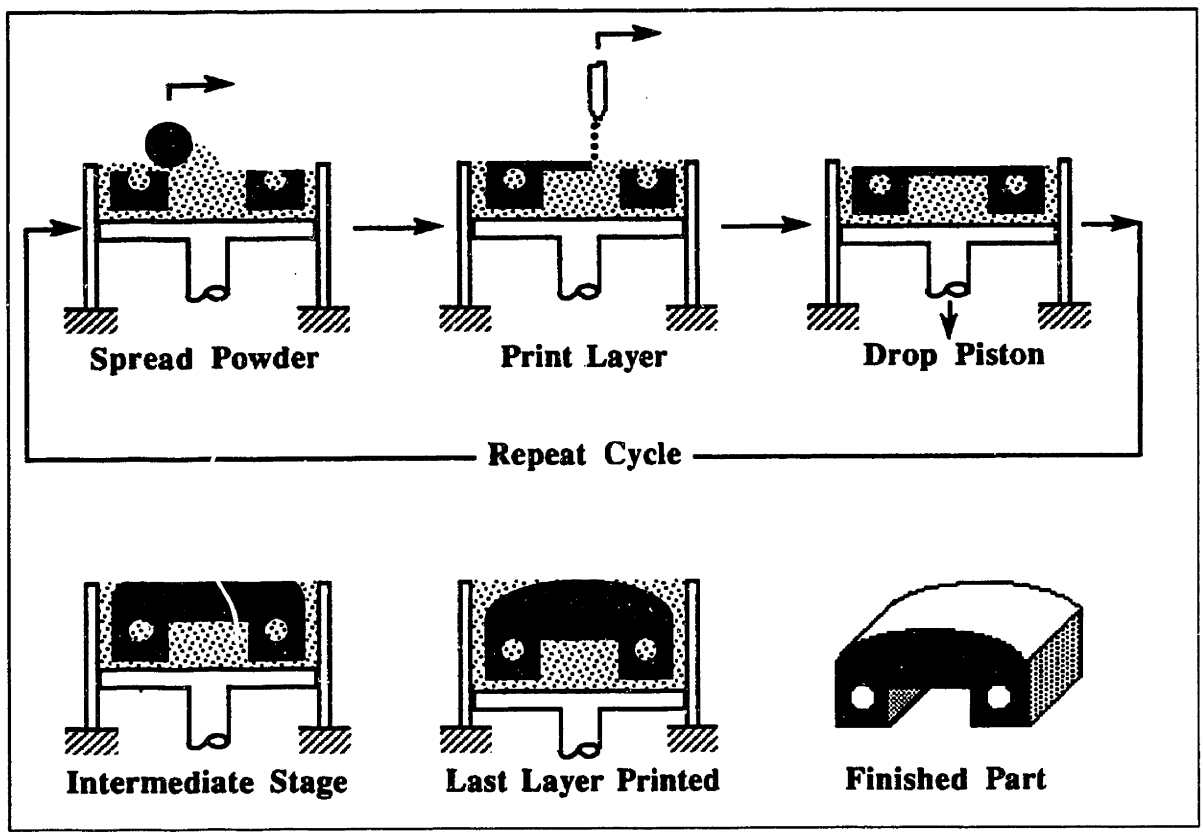

Figure 1.1. Schematic of the standard 3DP process.

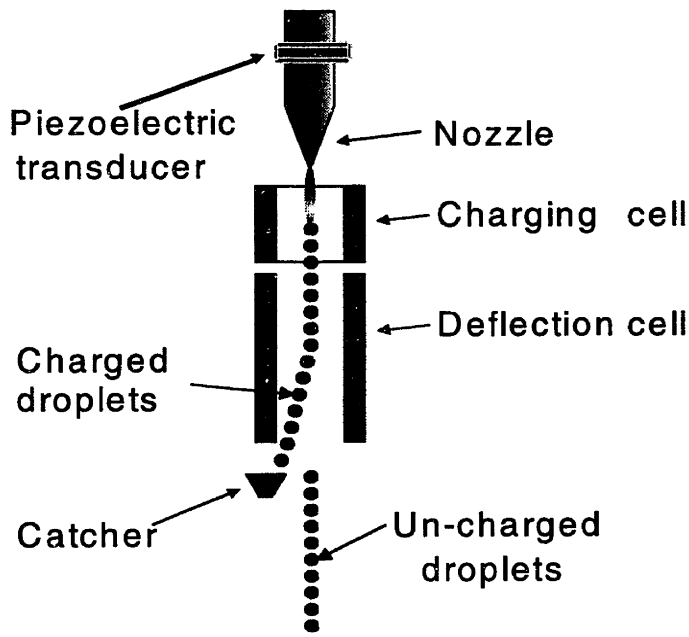

Figure 1.2. Schematic of continuous jet 3DP print head

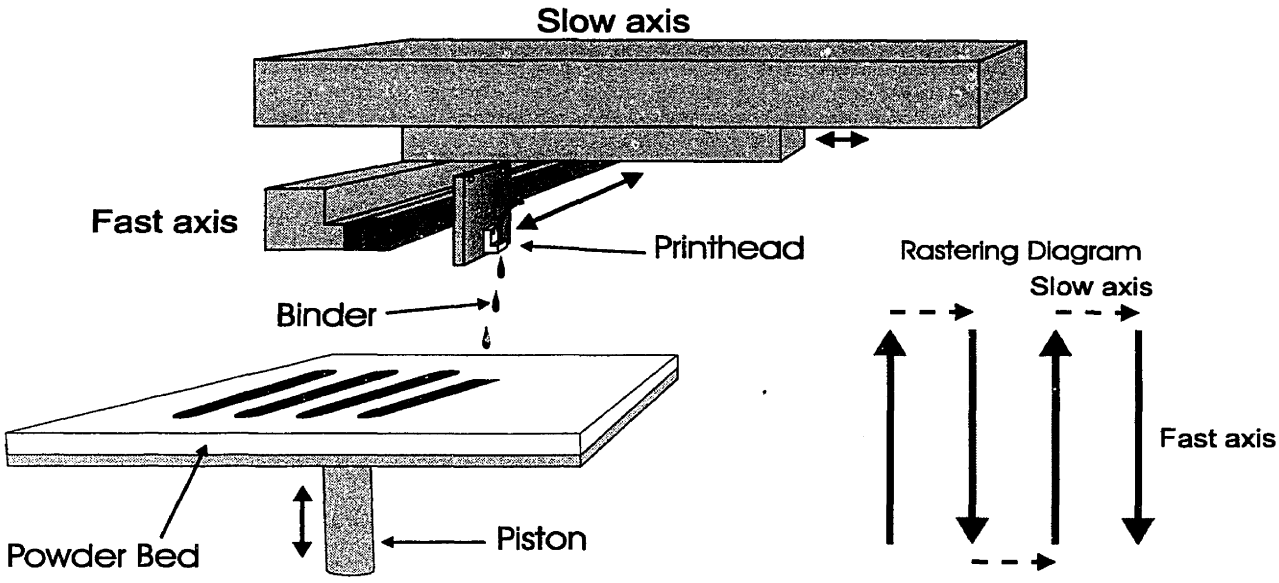

Figure 1.3. Configuration of the axes on the 3DP machine (courtesy B. Wu)

"slow axis" control the motion of the print head in an X-Y plane. Binder droplets are deposited as the print head traverses across the powder bed in the direction of the fast axis. At the end of each pass, the print head steps forward a specified distance along the slow axis. The size of the step in the slow axis direction is called the binder line spacing. The amount of binder material deposited into the powder bed is controlled by the flow rate of the binder through the print head, the fast axis speed, and the line spacing. The piston controls the height of the powder bed in the "Z direction".

The interaction of the binder with the powder bed forms a cohesive unit called a primitive. Primitives are the fundamental building units in the 3DP process. The geometry of primitives is dependent upon the characteristics of the binder and powder bed material. Primitive formation in 3DP is discussed in detail by Bredt[6] and Fan[7]. Primitive *stitching* is the joining of adjacent primitives. Stitching betweeen binder lines and stitching between layers are critical to forming parts with sufficient strength.

The standard 3DP process places limitations on the range of powder sizes that can be used. The powder material must be flowable and spread easily by the powder roller. Fine powders present problems because van der Waals attractive forces become significant. Powders less than about 10 μm in diameter tend to form clumps and stick to the powder roller. The packing density of the powder bed is also low since the particles are not free to rearrange and pack efficiently.

1.2. Requirements for Fabricating Engineered Ceramic Components

The goal of the 3DP ceramics effort is to fabricate fully dense, defect-free ceramic components. The green component produced by 3DP should be able to be sintered to full density without intermediate processing steps. Khanuja[8], Yoo[9], and Giritlioglu[10] investigated 3DP for fabricating structural ceramic components. The limitations and requirements for fabricating structural ceramic components were described in detail in these references and will be reviewed again in the following sections.

Engineered ceramics, such as high temperature structural components and electro-ceramic devices, generally require fine-grained microstructure for optimum performance. The strength and toughness of most structural ceramic components are improved with

smaller grain size. The necessary processing conditions for preparing engineered ceramic components will be discussed.

1.2.1. Powder Size Requirements

Dense ceramic components are fabricated by consolidating powder by various techniques and firing. The consolidated component generally consists of the ceramic powder mixture, a binder material to hold the component together, and sometimes a large volume fraction of open porosity. The component is referred to as being in the *green* state after the powder is consolidated. The green component is then densified by firing at high temperature.

Sintering is the process by which the pores in the green component are removed accompanied by the shrinkage of the component. Densifying mechanisms occur by the transport of matter from the grain boundaries between particles to the necks. Atomic transport mechanisms occur by diffusional processes in which the driving force is minimization of surface energy. Small particles lead to higher driving forces. The path length required for atomic species to migrate is also reduced, and sintering rates are greatly enhanced as particle size decreases.

Herring's scaling laws[11] can be used to understand the effect of powder size on the sintering behavior. The laws can be written in the general form

$$\left(\frac{\Delta t_2}{\Delta t_1}\right) = \left(\frac{R_2}{R_1}\right)^m, \tag{1.1}$$

where Δt is the time to produce a microstructural change, R is the particle radius, and m is an exponent that is dependent upon the sintering mechanism. The value of m is 3 for lattice diffusion and 4 for grain boundary diffusion.

1.2.2. Uniformity of the Microstructure

The densification of ceramics during sintering is also accompanied by grain growth, or coarsening, in which the average size of the grains and pores increases. Grain growth is considered *normal* if the grain sizes and shapes remain within a narrow distribution. *Abnormal* grain growth is characterized by the rapid growth of large grains that consume smaller grains within the body, and the distribution of grain sizes is not

within a narrow range. Abnormal grain growth traps pores within the sintered body which act as defects.

The green microstructure should be uniform to minimize abnormal grain growth. Powders with a broad distribution of particle sizes and agglomerates within the component can lead to abnormal grain growth. Dopants can be used to reduce abnormal grain growth and ensure dense, uniform microstructures. Small amounts of MgO added to alumina improve the sintering behavior and reduce abnormal grain growth.[12,13,14]

1.2.3. Effect of Packing Density of the Green Body

The driving force for sintering is dependent upon the number of particle-particle contacts. High packing density will result in higher sintering rates at lower temperatures. The effect of packing density on sintering rates and microstructure has been clearly explained by Bruch.[15] Sintering trajectories for alumina are shown in Figure 1.4. Powder compacts with low packing density exhibit significant grain growth. Sintered densities greater than 98% theoretical with fine grain size are not possible when the green density is low. Sintering behavior improves substantially with increasing packing density. The minimum packing density is approximately 50% in order to sinter alumina to high density, and packing densities greater than this are desired.

The green packing density also effects the amount of shrinkage that occurs during sintering. The strain that occurs during densification can be calculated:

$$\text{Strain} = 1 - \left(\frac{\rho_o}{\rho_f}\right)^{1/3}, \qquad (1.2)$$

where ρ_o and ρ_f are the initial and final densities, respectively. This equation implies that the linear strain to sinter to full density is 20.6% for an initial packing density of 50%. The linear strains for 60% and 70% green density would be 15.7% and 11.2%, respectively. Small strains are desirable to minimize distortion during firing. Density gradients also lead to differential strain and distortion.

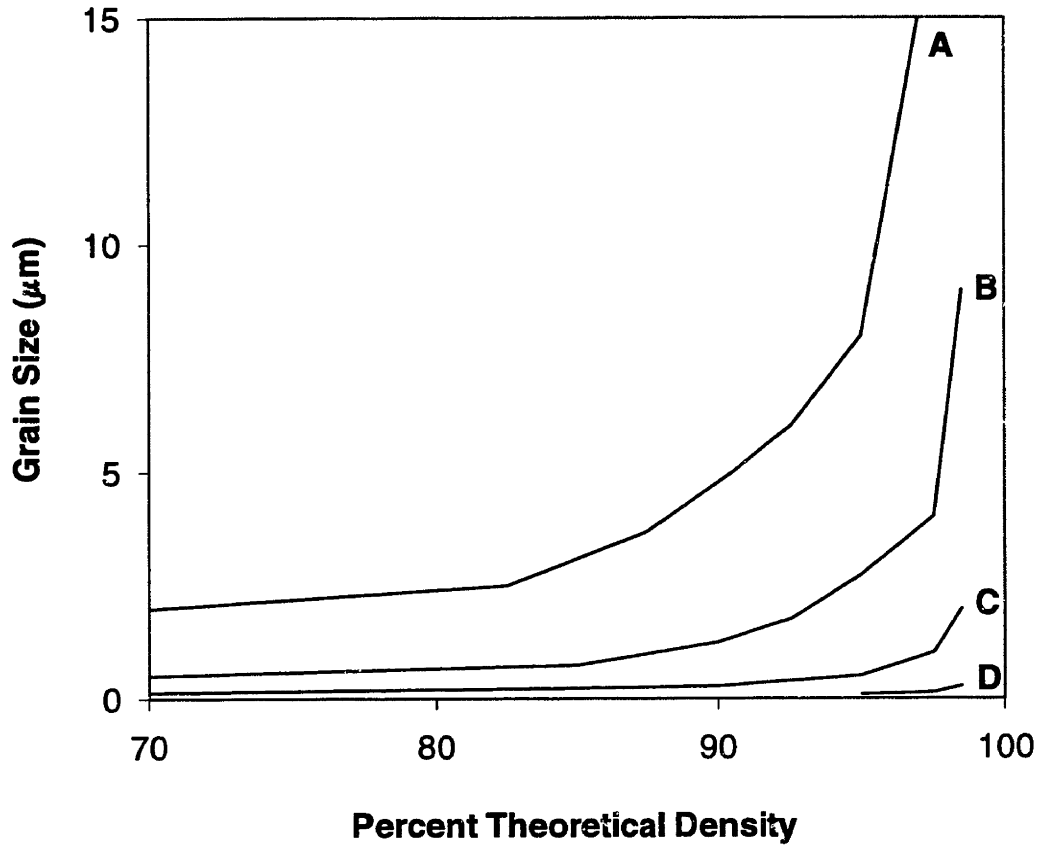

Figure 1.4. Sintering trajectories for alumina illustrating the effect of packing density on sintering behavior. Green density: **(A)** 30% **(B)** 40% **(C)** 50% **(D)** 60% (From Bruch)

1.3. Traditional Ceramics Processing Techniques

Numerous forming techniques exist to consolidate ceramic particles into functional shapes. These processes are described in detail in several texts and review papers.[16,17,18]

1.3.1. Dry Pressing

Dry pressing is a common forming process in which the component is fabricated by consolidating powder within a die cavity under pressure. Dry pressing is capable of very high production rates. Spark plugs, chip carriers, and tableware can be produced at rates as high as several hundred per minute. Dry pressing can produce only limited geometries. Die wall friction also leads to density gradients that result in distortion after firing. Density gradients in excess of 10% can be present across specimens prepared by dry pressing[19]

1.3.2. Injection Molding

Injection molding of ceramic components is a process in which ceramic powders are dispersed in an organic binder material. The mix is heated above the T_g (glass transition temperature) of the binder, forced into a mold cavity, and cooled to resolidify the mix in the shape of the desired part. Ceramic injection molding is capable of producing complex-shaped parts. The process is limited by several complexities. The binder-dispersant-ceramic mixture needs to be specifically tailored for various ceramic materials. Dimensional stability, reproducibility and tooling costs are major problems. Parts fabricated by injection molding are as high as 50 volume percent organic material. Problems during binder burn-out are well documented.[20] Thermal cycles may be as long as weeks to remove the binder, and distortion often occurs during this step.

1.3.3. Tape Casting

The tape casting process has been used for nearly 50 years for manufacturing ceramic sheets.[21,22] Tape casting utilizes a ceramic slurry prepared by dispersing ceramic powder in a solvent, usually an organic solvent. The slurry also contains significant

amounts of binder to give the tape strength and flexibility. The slurry is spread onto a carrier film using a doctor blade. The solvent is evaporated to yield the ceramic tape.

Multi-layer ceramic capacitors (MLC) and multi-layer ceramic packages (MLCP) are two devices in which ceramic tapes are stacked and laminated to form the component.[23] These devices form the basis of a multi-billion dollar industry. Laminated ceramics formed from tape cast sheets have also been studied for structural ceramic applications.[24,25] Unique mechanical properties may be achieved in layered ceramics by controlling the microstructure and composition accordingly.[26]

Tape cast layers have also been incorporated into SFF techniques. Computer-aided manufacturing of laminated engineering materials (CAM-LEM)[27] and laminated object manufacturing (LOM)[28,29] are two processes that utilize the stacking and lamination of green ceramic tapes. One advantage of these processes is that the feedstock material is readily available for numerous compositions. However, the lamination process must be carefully controlled to prevent interlayer defects.

1.3.4. Slip Casting

Slip casting is another wet processing technique in which components are formed using dispersions of ceramic powders in a liquid vehicle. Slip casting has long been used for producing large volumes of ceramic ware, and is an attractive forming method due to its ability to form complex-shaped components reliably and inexpensively. Slurry is poured into a porous mold. The capillary pressure from the mold withdraws solvent from the slurry and builds up a cast layer at the mold interface. The thickness of the cast layer increases approximately as the square root of time.

The formation of the powder bed using the slurry-based 3DP process is similar to a slip casting process. The powder bed is formed by depositing slurry onto a porous substrate that withdraws the solvent from the slurry. The slurry rapidly *slip casts* to produce the new layer of material. Models used to describe slip casting will be used to analyze the formation of the powder bed. Terminology such as *casting rate* will also be used to describe the process of solvent being withdrawn from the slurry.

The advantages of wet, or colloidal, processing techniques have been reviewed in detail by numerous authors.[30,31,32,33,34] Slip casting, tape casting, and centrifugal casting

processes are capable of producing components with high packing densities and minimal density gradients. Agglomerates and defects can be minimized by carefully controlling the slurry stability and processing conditions. Wet processing techniques are generally the method of choice for fabricating high-quality ceramics with minimal defects and complex shape.

1.4. Previous Attempts at Fabricating Structural Ceramics Using 3DP

The earliest attempts at fabricating structural ceramic components with 3DP were carried out by Khanuja and Yoo with submicron alumina powder. The high surface area and van der Waals forces between particles caused extensive agglomeration, and spreading uniform layers was very difficult. The packing densities of powder beds prepared with submicron powder spread with a roller were less than 30%. This value is far below the packing density required for sintering to near theoretical density. Khanuja, Yoo, and Giritlioglu examined modifications to the standard 3DP process to meet the needs of structural ceramic components, namely: fine powder, high and uniform green density, and elimination of defects.

1.4.1. Press Rolling Approach

The press rolling method was the first approach at increasing the packing density of the powder bed with submicron powder. The spreading sequence followed a two step approach. The piston was dropped and powder was spread with the roller using a counter-rotating motion. The powder bed was then raised and the roller was traversed across the powder with a forward rotating motion. The second pass of the roller acted to press the powder bed and increased the packing density.

Ballistic impact of the binder with the powder bed was eliminated since the powder bed was relatively cohesive. However, the packing density of the powder bed was increased to only ~40% using this method. Printed components were compressed under isostatic pressure to increase the green density prior to sintering. The density at each stage of the process was: ~40% as printed, ~60% after isostatic pressing, and up to 99% after sintering.

The press rolling process introduced voids between layers that aligned with the direction of the rolling.[9] These directional voids led to distortion during isostatic pressing. The layers sheared relative to one another as the voids collapsed. Distortion was also observed during isopressing due to density gradients in the powder bed. The voids produced by this process act as critical flaws in the final component, and distortion during post-processing steps makes dimensional control impossible.

1.4.2. Spray Dried Granules

Spray dried powders are agglomerates of submicron particles held together with an organic binder. Spray dried powders are commonly used in dry pressing processes because they are highly flowable and readily fill dies. Spray dried powders were incorporated into the 3DP process to overcome the poor spreading behavior of submicron powders. Layers of powder formed with spray dried powder were uniform.

Extensive distortion was observed with spray dried powders during the printing stage. Khanuja identified two factors responsible for distortion during printing: dissolution of the spray dried granules in the printed binder and interlayer liquid migration due to the fine pores of spray dried granules. Distortion due to these mechanisms was reduced by burning out the binder that is present in the spray dried granules and drying the powder bed after each layer.

The packing density of parts fabricated with spray dried powder was very low (~30%). Isopressing was required to increase the green density above 50% prior to sintering. Giritlioglu successfully demonstrated this approach to fabricate silicon nitride components with sintered densities >95% theoretical. However, isopressing introduces an additional step into the process. Isostatic pressing is also not feasible for complex structures. Slight distortion was still present with spray dried powder, even under optimized conditions. A new process was needed that eliminated the need for additional post-processing steps after the part is printed.

1.5. Slurry-Based 3DP Process

The limitations and failures of early attempts of fabricating structural ceramic components via 3DP indicated that a major modification to the process was necessary.

Forming the powder bed by spreading dry powder proved to be inadequate for forming a powder bed free of defects with high and uniform packing density. The requirements of the powder bed necessitated the use of a wet processing technique. Wet processing techniques are capable of producing ceramic components from submicron powder with green densities above 65% theoretical.

The powder bed in the slurry-based 3DP process is formed by depositing slurry in uniform layers, rather than spreading dry powder. The slurry layer is then dried and binder is printed into the powder bed as is done for the standard 3DP process. Powder beds prepared with submicron powder are very cohesive. Part retrieval is complicated because of this. The unprinted region of the powder bed can not be simply brushed away to retrieve the part. Instead, the unprinted region of the powder bed is *redispersed* by placing the powder bed in a liquid solvent. The process flow chart for the slurry-based 3DP process is shown in Figure 1.5.

The entire slurry-based 3DP process encompasses a series of phenomena that control the efficacy of the process. The slurry processing and chemistry must yield powder beds that are both redispersable and high density. The mechanism by which the powder bed is formed affects microstructure. Interactions between the slurry and the powder bed must also be understood to optimize the process.

1.6. Introduction to Solid-Liquid Interactions

Interactions between solids and liquids play a role in several aspects of the slurry-based 3DP process.

1. The interaction of the solvent in the slurry with underlying layers of the powder bed is critical to the microstructure of the powder bed. The slurry essentially *slips casts* against the previous layers to form the powder bed.
2. Capillary stress leads to cracking in the powder bed if deposition conditions are not controlled.
3. Interaction and spreading of the binder in the powder bed are controlled by solid liquid interactions.
4. Differences in wetting behavior for binder-printed regions and unprinted regions lead to differential rates of liquid infiltration.

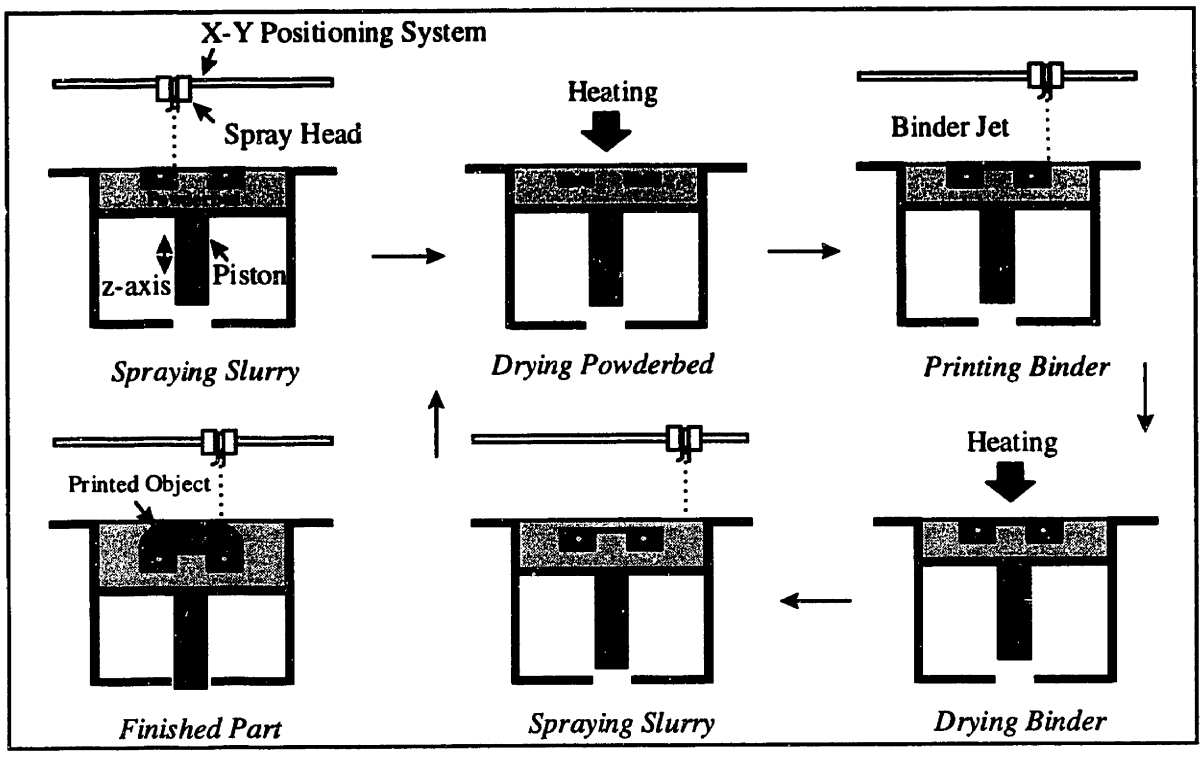

Printing Sequence

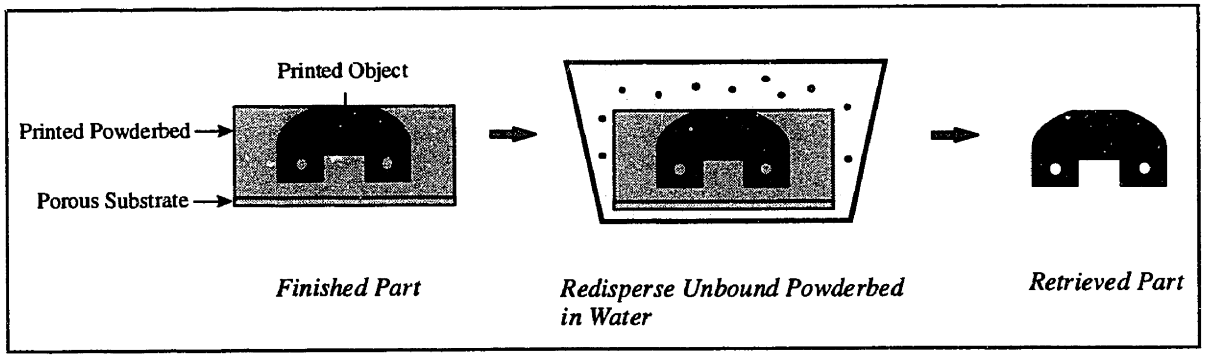

Part Retrieval

Figure 1.5. Schematic of the slurry-based 3DP process

Interactions between solids and liquids will be reviewed briefly with respect to relevant phenomena in the slurry-based 3DP process.

The interactions of liquids with solids play a key role in the formation of primitives and the development of microstructure of parts fabricated by 3DP. Bredt[6] presented an exhaustive review of capillary migration in porous materials relevant to the 3DP process.

The slurry-based 3DP process is fundamentally different than the standard 3DP process. Several key differences exist between the standard process and the slurry-based process with respect to solid/liquid interactions. First of all, the powder bed is deposited in a slurry form and the interaction of the carrier liquid must be understood. The powder bed is also composed of powder with a diameter typically less than 1 μm compared to powders with diameters on the order of tens of microns for the standard process. The powder bed is also cohesive and is tolerant to the ballistic impact of liquid droplets.

The thermodynamic interactions between solids and liquids are reviewed in detail by Adamson.[35] The fundamental equation of capillarity was introduced by Young and Laplace to describe the pressure difference across a bubble:

$$\Delta P = \gamma_{LV}\left(\frac{1}{R_1} + \frac{1}{R_2}\right), \tag{1.3}$$

where γ_{LV} is the surface tension of the liquid in equilibrium with its vapor and R_1 and R_2 are the radii of curvature of the surface of the bubble. The equation of Young and Laplace is easily modified to account for wetting of a capillary tube as shown in Figure 1.6. The equation accounts for the pressure difference for a liquid that wets the solid at a contact angle of θ:

$$\Delta P = \frac{2\gamma_{LV}\cos\theta}{r_c}, \tag{1.4}$$

where r_c is the radius of the capillary. This equation will be used to define the capillary pressure of liquids in a porous body by substituting the pore radius of the powder bed, r_p, for r_c. Capillary pressure acts as the driving force for liquid migration in porous bodies.

The flow of liquid in porous materials has been studied extensively in the soil mechanics field. Both capillary pressure and permeability are dependent upon the relative saturation of the powder bed. Capillary pressure displays hysteresis. The

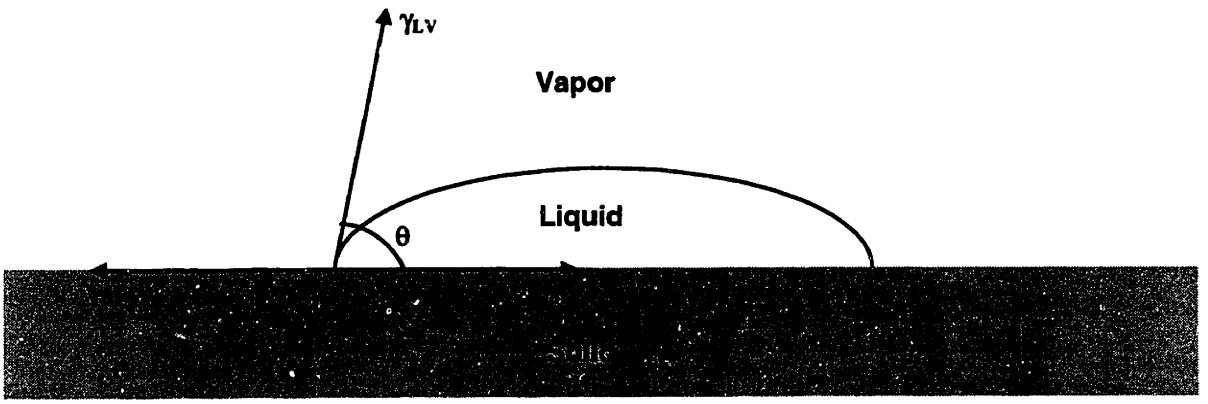

Figure 1.6. Relationship between contact angle and interfacial energies.

capillary pressure is plotted as a function of saturation in Figure 1.7.[36] The capillary pressure is lower at a given saturation as the liquid infiltrates the bed (imbibition) than during drainage. The capillary pressure decreases as the saturation of the bed increases.

The kinetics of flow in porous bodies is governed by Washburn's equation. Washburn's equation is reported in many different forms. The kinetics of liquid flow in a capillary is given by:

$$\frac{dl}{dt} = \frac{r_c \gamma_{LV} \cos\theta}{4\eta l}, \tag{1.5}$$

where l is the length of the capillary and η is the viscosity of the liquid. Levine and Neale[37] report Washburn's equation for flow in a porous powder bed as:

$$\frac{dl}{dt} = \frac{kP_c}{\varepsilon\eta l}, \tag{1.6}$$

where k is the permeability of the powder bed, P_c is the capillary pressure, ε is the void fraction of the powder bed, and η is the liquid viscosity. The rate of liquid infiltration plays a critical role in the interaction of the binder with the powder bed as well as the casting rate of the slurry on the powder bed. Understanding the solid-liquid interactions and the role of processing variables is paramount for optimizing the slurry-based 3DP process.

1.7. Scope of this Thesis

This dissertation will address the issues involved in fabricating engineered ceramics components using the slurry-based 3DP process. The process has been developed using alumina as a model ceramic system, although the process development was undertaken with the goal of developing a generic process applicable for numerous materials systems. Other researchers are currently exploring fabrication of components with silicon nitride and lead zirconate titanate materials based on the process that has been developed. The flexibility of the process and the procedure for developing new materials systems is illuminated with this work.

Solid-liquid interactions play a central role in understanding various phenomena associated with the process. The infiltration of binder into the powder bed has been

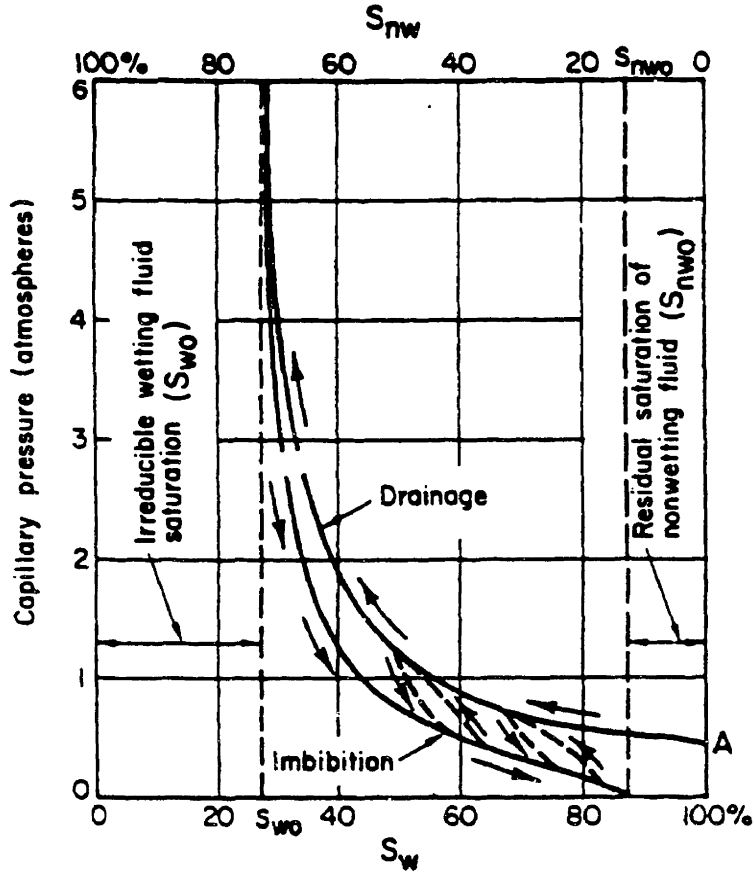

Figure 1.7. Capillary pressure as a function of saturation (From Bear)

studied by Arthur[38] and Knezevic.[39] This subject will be addressed only briefly in this dissertation.

The interaction of the slurry will be examined in greater detail. Slurry stability and deposition methods control the microstructure of the printed component. The capillary stress that develops due to the liquid in the slurry must be controlled. The amount of liquid that is deposited with the slurry must be below a critical value to prevent the powder bed from cracking. Differential wetting phenomena over binder-printed regions and unprinted regions leads to differential casting rates and slurry migration. Approaches to optimize the slurry-based 3DP process are brought to light by examining problems in terms of the fundamental solid-liquid interactions that govern the process.

1.8. Organization of the Thesis

The thesis is organized in such a way as to present the slurry-based 3DP process as a series of phenomena. Process development is very much an iterative process. As such, successful results require looking at the process as a whole and understanding the interactions between each of the components of the process.

Chapter 2 addresses slurry formulation for both optimum stability and redispersion behavior. Chapters 3 and 4 will discuss powder bed formation and controlling cracking in the powder bed, respectively. The impact of the binder on the process will be discussed in Chapter 5. This chapter will discuss various binders that were investigated. The infiltration behavior of the binder in the powder bed will be discussed briefly. The interaction of the slurry with binder-printed and unprinted regions will be discussed at depth. Chapter 6 will discuss the properties of alumina parts printed with Joncryl binder and propose techniques for optimizing the process. Chapter 7 will give conclusions drawn from this work and provide a framework for adapting new materials systems to the process.

CHAPTER 2
OPTIMIZING SLURRY COMPOSITION FOR STABILITY AND REDISPERSION BEHAVIOR

2.1. Introduction

The necessity of using a slurry-based process was outlined in Chapter 1. The functionality of ceramic components depends on the microstructure. Heterogeneities that arise during the processing stages affect the engineering reliability of components. Lange[30,31,32] has thoroughly reviewed the processing science for improved reliability of ceramics and cited the advantages of colloidal processing. Aksay and co-workers[33,34] have also extensively studied ceramic forming processes utilizing colloidal suspensions. Careful control of the colloidal stability is necessary to fabricate components with high green density and uniform microstructure so that full density can be achieved after sintering.[40]

The term colloidal dispersion describes materials systems in which the units of material which are dispersed are much larger than the solvent molecules in which they are dispersed, unlike solutions where the solvent and solute molecules are of comparable size. The phases of the dispersed phase and the dispersion medium can be solid, liquid, or gas. Examples of different colloidal dispersions are listed in Table 2.1.

Table 2.1. Examples of colloidal dispersions[41]

Disperse Phase	Dispersion Medium	Technical Name	Examples
Solid	Gas	Aerosol	Smoke
Liquid	Gas	Aerosol	Mist, fog
Solid	Liquid	Sol or dispersion	Ink, paint
Liquid	Liquid	Emulsion	Milk, mayonnaise
Gas	Liquid	Foam	Fire extinguisher foam
Solid	Solid	Solid dispersion	Ruby glass
Liquid	Solid	Solid emulsion	Ice cream
Gas	Solid	Solid foam	Insulating foam

This chapter will specifically address solids dispersed in a liquid. Solids can be classified as either lyophilic (liquid-loving) or lyophobic (liquid-hating). The terms hydrophilic and hydrophobic are used when the liquid is water. Lyophilic solids

inherently form stable colloidal dispersions. Ceramic powders are generally lyophobic, and the chemistry must be controlled to form stable dispersions. The fundamentals of forming stable dispersions will be reviewed with particular reference to ceramic materials in aqueous systems.

Knowledge of colloid and surface chemistry is fundamental to wet processing techniques used in ceramic processing. The stability and rheology of slurries is dependent upon the forces acting between particles. Horn[42] has reviewed surface forces in ceramic materials and their roles in powder processing, sintering, and fracture mechanics. Rahaman[43] also provides an excellent basic review of the science of colloidal processing for ceramic materials. Hunter[41,44] and Shaw[45] provide detailed references for the interested reader, and their work will be summarized briefly in following sections. Israelichvili[46] has also studied surface forces extensively and is a good source for additional detail.

The basis of forming stable dispersions is outlined in the DLVO theory. The theory has developed out of the work of Derjaguin and Landau[47] in Russia and Verwey and Overbeek[48] in The Netherlands. The theory examines colloidal stability in terms of the attractive and repulsive potentials that exist between colloidal particles. All particles experience attractive forces between one another due to van der Waals forces. For stable dispersions, repulsive potentials between particles need to be utilized to overcome these attractive potentials.

Two types of stabilization are generally used to offset the attractive potential:

1. Electrostatic stabilization
2. Polymeric stabilization

Electrostatic stabilization utilizes surface charges on the particles to yield repulsive forces between particles. Polymeric stabilization can utilize several different mechanisms to stabilize the colloidal system. Steric stabilization occurs when the polymer adsorbs to the surface of the particles. The thickness of the polymer coating is sufficient to keep the particles separated at a distance where the attractive forces are weak. Work is also required to bring the particles together and compress the polymer chains. Polymers may also impart electrosteric stabilization if the polymer has charged end groups. Depletion stabilization can also be used if the polymer does not adsorb to the particle. These

mechanisms are explained in greater detail in books by Sato and Ruch[49] and also by Napper.[50]

2.2. Attractive Forces in Colloidal Systems

2.2.1. van der Waals Forces Between Molecules

Attractive forces exist between all colloidal particles due to van der Waals forces. Three different interactions are responsible for van der Waals forces:

1. Permanent dipole – permanent dipole (Keesom forces)
2. Permanent dipole – induced dipole (Debye forces)
3. Induced dipole – induced dipole (London forces)

Keesom forces result between two polar molecules. The dipoles align themselves and are mutually attracted. Debye forces result when a permanent dipole induces a dipole in a polarizable molecule. London forces occur between nonpolar molecules. Perturbations of the electron cloud lead to instantaneous dipole moments within molecules. The instantaneous dipole moment induces dipoles in adjacent molecules, resulting in the London force. The direction of the induced dipole is always aligned such that the molecules attract one another.

The potential energy of attraction between molecules for these interactions, V_A, is proportional to x^{-6}, where x is the separation distance. These forces are therefore significant at short separation distances. Keesom and Debye forces require permanent dipoles to be present. London forces are present in all materials, regardless of the presence of permanent dipoles. The London forces are generally the largest of the van der Waals forces except in highly polar materials such as water. The London force is the primary van der Waals mechanism present in colloidal ceramic materials since ceramic powders are generally nonpolar.

2.2.2. Attractive Forces Between Macroscopic Bodies

The attraction of macroscopic bodies due to these forces can be easily understood by assuming that the atomic interactions are additive. Hamaker[51] calculated the force between macroscopic bodies by assuming that the interaction between one molecule and a macroscopic body is the sum of the interactions with all of the molecules in the body.

This approach assumes simple additivity and ignores how the intervening molecules affect the induced fields. Hamaker calculated the attractive potential between macroscopic bodies with different geometries. The attractive potential energy for three geometries is shown in Figure 2.1.

The potential energy of attraction between two spherical particles based on Hamaker's calculations is:

$$V_A = -\frac{Aa}{12h}, \ (h<<a) \tag{2.1}$$

where A is the Hamaker constant, a the particle radius, and h the separation distance. The Hamaker constant describes the van der Waals attraction between macroscopic bodies and is equal to $C\pi^2\rho_1\rho_2$, where C is a constant and ρ_1 and ρ_2 are the number of molecules per unit volume in the two bodies. The van der Waals attraction between macroscopic bodies is longer ranged compared to individual molecules. The attractive potential per unit area varies inversely with h^2 for two semi-infinite plates and varies inversely with h for two spherical particles.

The calculations by Hamaker assume the bodies are separated by vacuum. These calculations suffer from two restrictions: the assumption of pairwise additivity of London interactions and the neglect of retardation effects due to the dispersion medium. Modern colloidal theory developed by Lifshitz[52] treats the interactions between bodies in terms of the dielectric properties of the materials. The Lifshitz theory has an advantage over the classical approach in that the uncertainty in the additivity of atomic and molecular forces is automatically avoided. The Lifshitz theory also predicts the effect of temperature dependence of van der Waals forces. The theory shows that the Hamaker constant is reduced by the intervening medium:

$$A \propto \left(\frac{\varepsilon_s - \varepsilon_l}{\varepsilon_s + \varepsilon_l}\right)^2, \tag{2.2}$$

where ε_s and ε_l are the dielectric constants of the solid and liquid, respectively.

Hamaker constants for common materials dispersed in water are listed in Table 2.2. The polarizability of materials directly affects the van der Waals forces between particles. Not surprisingly, the Hamaker constants are significantly larger for metals than

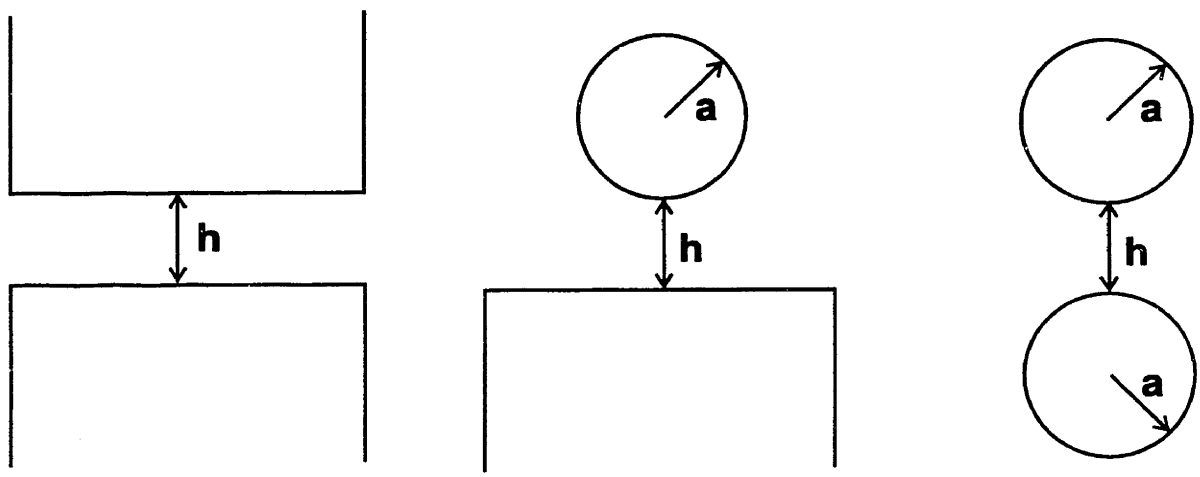

$$V_A = -\frac{A}{12\pi h^2} \qquad V_A = -\frac{Aa}{6h} \qquad V_A = -\frac{Aa}{12h}$$

Figure 2.1. The potential energy of attraction between two bodies by Hamaker's method. (A) Two semi-infinite plates, (B) A sphere and a semi-infinite plate, (C) Two spheres

for most ceramics and polymers. This fact, together with the relatively high density of metals, makes it difficult to form stable metal dispersions.

Table 2.2. Hamaker constants for selected materials in water (from Israelichvili)

Material	A (10^{-20} J)
Al_2O_3	4.2
Fused SiO_2	0.63
Mica	2.0
ZrO_2	13
TiO_2	26
Ag, Au, Cu	30-40
PTFE	0.29

2.3. Repulsive Forces Between Particles

2.3.1. How particles acquire charge

Repulsion between particles due to electrostatic charges on the particles enables electrostatic stabilization of colloids. Most materials acquire a surface electric charge when dispersed in a polar liquid. Possible charging mechanisms include preferential adsorption of ions, dissociation of surface groups, isomorphic substitution, adsorption of polyelectrolytes, and accumulation of electrolytes. Preferential adsorption of ions from solution is the most common process for ceramic materials.

The surface charge that is present on colloidal particles is often illustrated with the classic example of silver iodide. When AgI is placed in water a small amount of the solid dissolves to establish equilibrium according to the solubility product:

$$K_{sp}=[Ag^+][I^-]\cong 10^{-16}, \text{ at } 25°C. \tag{2.3}$$

A small shift in the concentration of Ag^+ or I^- ions has a dramatic impact on the surface charge of the AgI crystals. When equal concentrations of Ag^+ and I^- ions are present on the surface of the crystal, the surface of the particle will be uncharged. This is called the point of zero charge, PZC. Iodide ions have a higher affinity for the surface of the crystals, and the PZC for AgI occurs when $[Ag^+] \approx 10^{-5.5}$ and $[I^-] \approx 10^{-10.5}$. The surface charge becomes positive when the concentration of Ag^+ ions is greater than $10^{-5.5}$. Conversely, the surface becomes negative when the concentration of I^- ions is greater than $10^{-10.5}$. The surface charge can be changed from positive to negative by the addition of small amounts of silver ions (e.g. using $AgNO_3$) or iodide ions (e.g. using KI). Silver

and iodide ions are referred to as potential-determining ions since they control the surface charge of the crystal. Potassium ions (K^+) and nitrate ions (NO_3^-) are referred to as indifferent ions since their concentrations do not affect the surface potential.

The surface chemistry of oxides has been studied in detail.[53,54,55] Most metal oxide surfaces are hydrated, with M-OH groups present on the surface of the particle. Oxide surfaces become charged by the interaction of surface groups with hydrogen and hydroxyl ions:

$$\text{M-OH} + \text{OH}^- \rightarrow \text{M-O}^- + \text{H}_2\text{O} \tag{2.4}$$

$$\text{M-OH} + \text{H}^+ \rightarrow \text{MOH}_2^+. \tag{2.5}$$

The particles have a negative surface charge in basic solutions due to the adsorption of OH^- ions, while the surface charge is positive in acidic solutions due to the adsorption of H^+ ions. H^+ and OH^- are, therefore, the potential-determining ions for oxides. The PZC ranges from very acidic for quartz (pH~2) to very basic for magnesia (pH~12).

Electrokinetic phenomena are often used to characterize the surface potential of particles. The measurements characterize the electrostatic potential a short distance from the surface of the particles instead of measuring the surface potential directly. The ζ (zeta) potential measures the potential at the Stern layer, a short distance from the surface. The isoelectric point (IEP) is defined as the pH where the ζ potential is zero, while the PZC is the pH where the particle surface charge is zero. IEP's for several ceramic materials are listed in Table 2.3. The IEP can vary significantly for the same nominal material depending on the preparation technique, thermal history, storage environment, and impurities that may be present. For this reason, the electrokinetic behavior of different sources of material should be characterized to optimize the colloidal behavior.

Table 2.3. Isoelectric points for selected ceramic materials (from Rahaman)

Material	IEP
Al_2O_3	8-9
SiO_2	2
ZrO_2	4-6
TiO_2	4-6
Fe_2O_3	8-9
Cr_2O_3	6-7
ZnO	9
MgO	12

2.3.2. The Electrical Double Layer

The surface charge present on the particles influences the distribution of nearby ions in the medium. Counter-ions of charge opposite the surface are attracted to the surface of the particle. The counter-ions would adsorb onto the surface and neutralize it in the absence of thermal motion. However, thermal motion causes the counter-ions to spread out and form a diffuse double layer of electric charge. The electrical double layer is, therefore, viewed as consisting of two regions: an inner region which may include adsorbed ions, and a diffuse region in which ions are distributed according to the influence of electrical forces and random thermal motion.

The electrical double layer is shown schematically in Figure 2.2. The dispersion medium is filled with ions that interact with the particle surface. Ions of opposite charge to the surface, counter-ions, are attracted to the surface of the particle. Co-ions will be repulsed from the particle surface, and their concentration is depleted near the particle. The concentration of both types of ions will approach the bulk concentration moving away from the particle surface.

The variation of potential with distance from a charged surface of arbitrary shape is a classical electrostatic problem. The general problem is described by the Poisson equation:

$$\nabla^2\psi = -\frac{4\pi\rho}{\varepsilon}, \tag{2.6}$$

where ψ is the local electrostatic potential, ρ is the charge density, and ε is the dielectric constant of the medium. The electrostatic potential decreases from ψ_o at the surface to

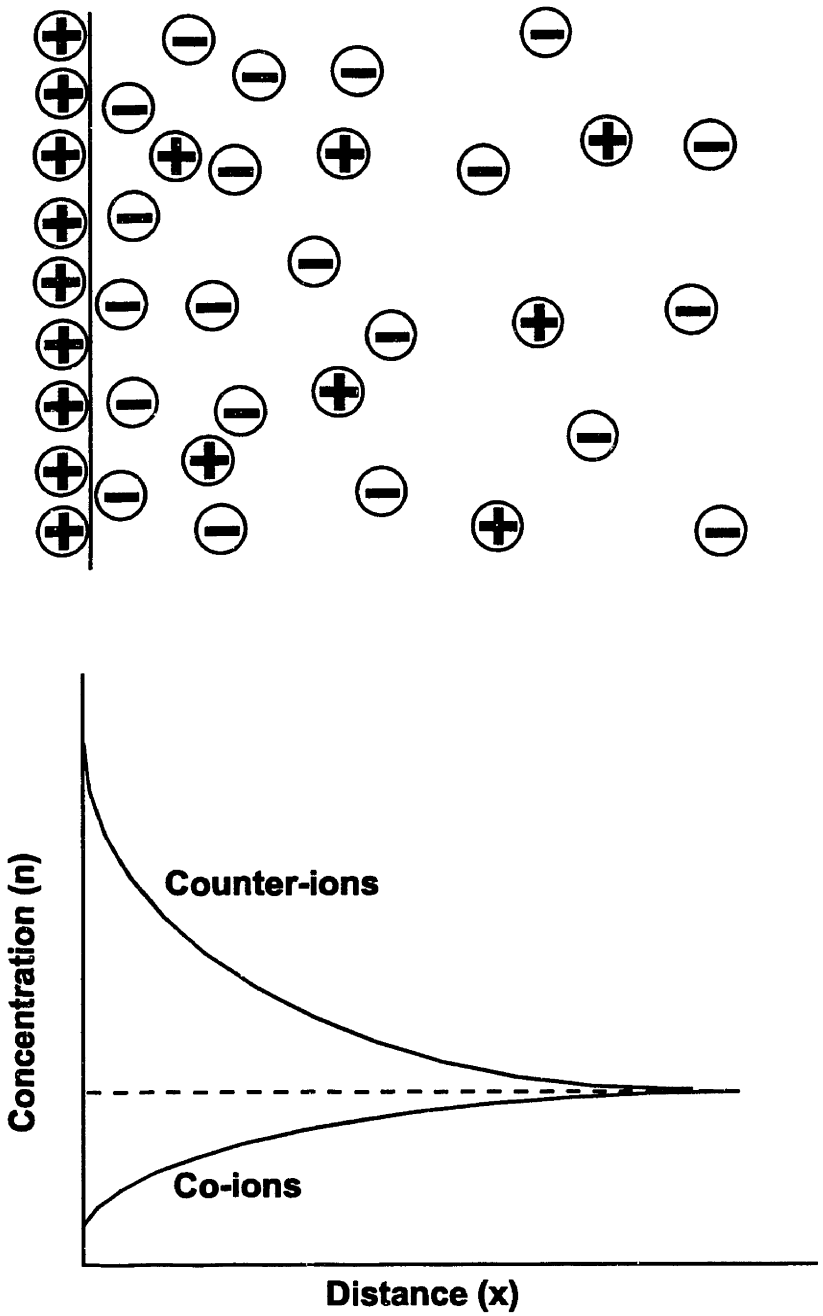

Figure 2.2. Schematic representation of the diffuse double layer and the concentration of ions.

zero as the distance from the surface increases to infinity. The concentration of ions in terms of the potential are determined using a Boltzmann factor:

$$\frac{n_i}{n_{io}} = \exp\left(\frac{-z_i e\psi}{kT}\right), \tag{2.7}$$

where n_i is the number of ions of type *i* per unit volume near the surface, n_{io} is the concentration in the bulk, z_i is the valence of the ion, and *e* is the elementary charge. The charge density can then be calculated:

$$\rho = \sum_i z_i e n_i = \sum_i z_i e n_{io} \exp\left(\frac{-z_i e\psi}{kT}\right). \tag{2.8}$$

Combining equations (2.6) and (2.8) forms the Poisson-Boltzmann equation:

$$\frac{d^2\psi}{dx^2} = -\frac{4\pi e}{\varepsilon}\sum_i z_i n_{io} \exp\left(\frac{-z_i e\psi}{kT}\right). \tag{2.9}$$

The Debye-Huckel approximation assumes $z_i e\psi < kT$ and (2.9) can be simplified:

$$\frac{d^2\psi}{dx^2} = \frac{4\pi e^2\psi}{\varepsilon kT}\sum_i z_i^2 n_{io}\ . \tag{2.10}$$

The relationship is often written:

$$\frac{d^2\psi}{dx^2} = \kappa^2 x, \tag{2.11}$$

where

$$\kappa^2 = \frac{4\pi e^2 \sum_i z_i^2 n_{io}}{\varepsilon kT}. \tag{2.12}$$

The solution to equation (2.11) with boundary conditions $\psi = \psi_o$ when $x = 0$, and $\psi = 0$, $d\psi/dx = 0$ when $x = \infty$, is:

$$\psi = \psi_o \exp(-\kappa x). \tag{2.13}$$

The quantity $(-\kappa x)$ is dimensionless and implies that κ^{-1} has units of length. The parameter κ^{-1} is called the Debye length and is one of the most important quantities to emerge from the Debye-Huckel approximation. The quantity expresses the effective length over which the double layer repulsion between particles acts. Equation (2.12) shows that the Debye length is dependent upon the valence and concentration of ions in

solution. The equation can be modified to express the value in terms of molar concentration of ions, M_i:

$$\kappa = \left(\frac{4\pi e^2 N_A}{1000\varepsilon kT} \sum_i z_i^2 M_i \right)^{1/2} = \left(\frac{8\pi e^2 N_A I}{1000\varepsilon kT} \right)^{1/2}, \tag{2.14}$$

where N_A is Avogadro's number and I is the ionic strength of the solution defined as:

$$I = \tfrac{1}{2} \sum_i z_i^2 M_i \,. \tag{2.15}$$

Equation (2.14) indicates that the Debye length varies inversely with the valence of the ions, z_i, and varies inversely with $M^{1/2}$. The Debye length decreases as the ionic strength increases, a process referred to as compression of the double layer. Figure 2.3 shows how the potential varies with distance for solutions with varying ionic strength.[44]

The Debye-Huckel approximation was derived for small potentials. Theoretical inconsistencies and small errors arise as the potential increases. The Guoy-Chapman model of the electrical double layer overcomes these limitations at larger potentials. The Guoy-Chapman model of the electrical double layer assumes that the electrical charge on the particle surface influences the distribution of ions in the electrolyte, so that an excess of ions of opposite sign is established in the layers of solution near the surface. The Guoy-Chapman model can be expressed:

$$\gamma = \gamma_o \exp(-\kappa x), \tag{2.16}$$

where $\gamma = \gamma_o$ at $x = 0$, and γ is defined:

$$\gamma = \frac{\exp\left(\frac{ze\psi}{2kT}\right) - 1}{\exp\left(\frac{ze\psi}{2kT}\right) + 1}. \tag{2.17}$$

The general effects of the concentration and valence of ions on the Debye length are the same as for the Debye-Huckel model. The variation between the two models is often small under most experimental conditions since $ze\psi_o/kT$ is often close to unity.

2.3.3. Repulsive Potential Due to the Electrical Double Layer

The electrical double layer surrounding particles leads to a repulsive potential between the particles as they approach each other. The interparticle repulsion is

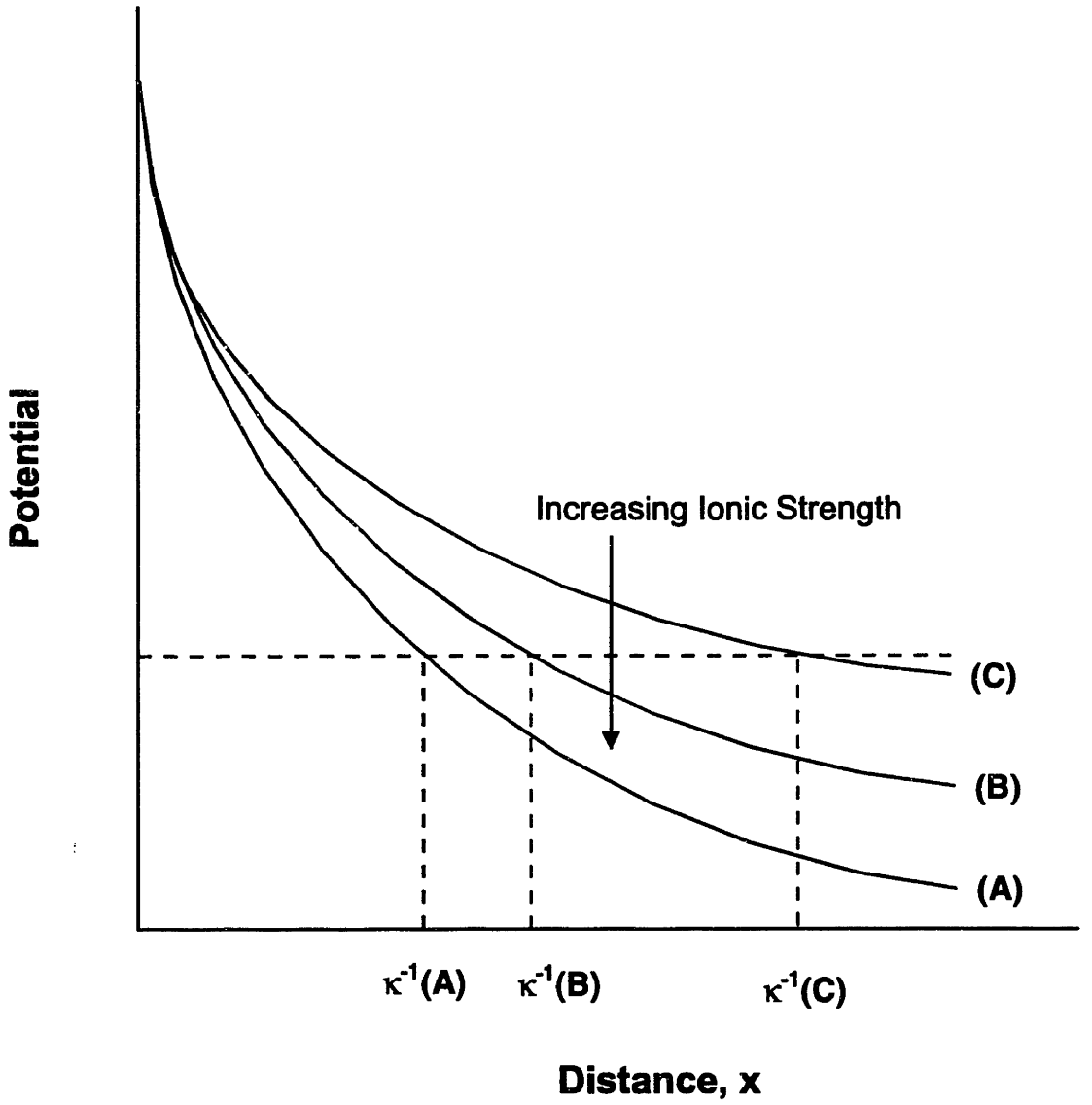

Figure 2.3. Electrostatic potential versus distance from the particle surface.

discussed in detail in Verwey and Overbeek's book. For two spherical particles, the potential energy of repulsion due to the overlap of their electrical double layers is:

$$V_R = 2\pi\varepsilon a\psi_o^2 \ln[1+\exp(-\kappa h)] \text{ (for } \kappa h > 10). \tag{2.18}$$

The energy of repulsion decreases as the Debye length, κ^{-1}, decreases. Increasing κ^{-1}, therefore, enhances colloidal stability for electrostatically-stabilized slurries.

2.4. DLVO Theory – Total Potential Between Particles

2.4.1. Implications of Total Potential Curves

The heart of DLVO theory is calculating the total potential between particles and understanding how the variation of total potential with separation distance affects the behavior of the colloidal system. The total potential between two particles can be calculated by adding the attractive potential due to van der Waals forces, V_A, and the repulsive potential due to double layer repulsion, V_R:

$$V_T = V_A + V_R. \tag{2.19}$$

The behavior of colloidal systems can be understood by examining total potential curves versus distance as shown in Figure 2.4. The total interaction energy is always attractive at very small and very large distances. Unstable colloidal systems are attractive over all distances. The interaction energy may be repulsive over a wide range of distances, producing a stable system.

Curve *c* in Figure 2.4 shows an unstable system that is attractive over all distances. The repulsive potential for this system, $(V_R)_c$, is small and is unable to overcome the attractive potential, V_A. Curve *a* shows a system with a large repulsive potential, and the repulsive energy is dominant at intermediate distances. Three distinct regions can be identified in system *a*. At short distances, there is a deep well where the potential energy is strongly attractive. This region is called the primary minimum. There is also a shallow attractive well at longer distances called the secondary minimum. The depth of this well is often sufficiently shallow that thermal energy is capable of overcoming it. There is also a peak at intermediate distances where repulsive forces dominate. The height of the peak is important since particles must overcome this repulsive potential to reach the primary minimum.

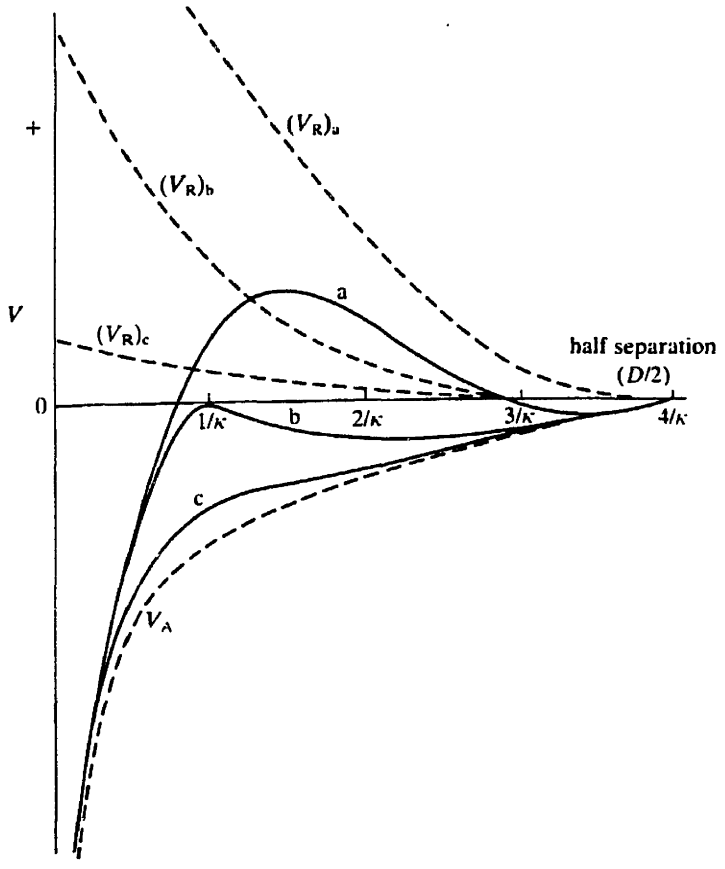

Figure 2.4. Total potential curves for colloidal systems with varying repulsive potential (from Hunter)

The DLVO theory can be summarized by the following statements:

1. The higher the potential at the surface of a particle – and therefore throughout the double layer – the larger the repulsion between the particles will be.
2. The lower the concentration of indifferent electrolyte, the longer is the distance from the surface before the repulsion drops significantly.
3. The larger the Hamaker constant, the larger is the attraction between molecules and, by extension, between macroscopic bodies.

The stability of a given system is optimized by maximizing the surface potential and minimizing the ionic strength of the system. Surface potential is controlled by the concentration of potential determining ions, e.g. by controlling pH in oxides. The attractive potential will be governed by the solid material and the dispersion medium that is used.

2.4.2. Shulze-Hardy Rule – Effect of Indifferent Ions

The ionic strength is a critical variable controlling the colloidal stability. The electrical double layer is compressed as the ionic strength increases. The electrostatic repulsion drops off accordingly, and the peak of the total potential curve will eventually drop to zero. The concentration at which this occurs is called the critical coagulation concentration, CCC. This condition is shown in curve *b* of Figure 2.4. The Shulze-Hardy rule states that the valence of the counter-ion has the principal effect on the stability of the colloid. The CCC value for a particular electrolyte is essentially determined by the valence of the counter-ion regardless of the nature of the ion with the same charge as the surface. The CCC corresponds to the point at which the maximum in the total potential energy curve becomes zero. Both V_T and dV_T/dD are zero at this point. Solving these equations for the ion concentration yields:

$$CCC = \frac{(1536\pi)^2 \varepsilon^3 k^5 T^5 Z^4 \exp(-4)}{2z^6 e^6 A^2}, \tag{2.20}$$

where $Z = \tanh(ze\psi/4kT)$. The CCC is therefore inversely proportional to the sixth power of the valence of the counterion. This result is illustrated in Figure 2.5 and highlights the importance of minimizing the concentration of multi-valent ions to maintain colloidal stability. The lines in Figure 2.5 show the CCC for z=1, 2, and 3. The

system is stable above the line where ψ is high. Below the line, the system is unstable and will flocculate spontaneously.

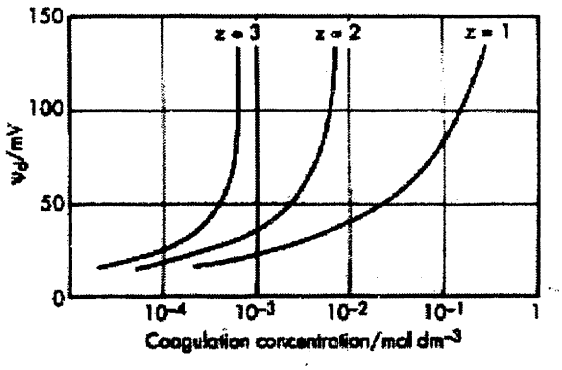

Figure 2.5. Effect of valence on the CCC (from Shaw)

Overbeek measured the CCC for several colloidal materials.[56] He measured a CCC of 5.2 x 10^{-2} M for monovalent counterions in alumina suspensions. The CCC decreased to 6.3 x 10^{-4} M and 8 x 10^{-5} M for di- and tri-valent counterions, respectively. The relative magnitudes of these values is close to the difference predicted by the Schulze-Hardy rule. The CCC will vary for different powder sources, but the values measured by Overbeek give order-of-magnitude estimates of the CCC for different counterions in alumina suspensions.

2.4.3. Kinetics of Coagulation

The Schulze-Hardy rule identifies conditions in which the slurry will spontaneously coagulate. However, slurries will flocculate over time even in the presence of repulsive forces. Hiemenz[57], Hunter, and Shaw all provide thorough reviews of the kinetics of coagulation. The rate of coagulation is analogous to ordinary chemical reactions in which the initial and final states are separated by an energy barrier. The peak in the total potential barrier, $V_{T(max)}$, corresponds to the activation energy for the flocculation reaction. The Schulze-Hardy rule identifies conditions in which there is no barrier to the reaction.

The kinetics of coagulation were first examined by Smoluchowski. Smolochowski applied the theory of diffusion to the rate of contact of particles. He assumed that each collision between particles resulted in the formation of a doublet. These are the conditions for what is considered rapid flocculation. The rate of doublet formation calculated by this method is:

$$Rate_{rapid} = -k_r N_o^2, \tag{2.21}$$

where k_r is a second order rate constant and N_o is the concentration of particles. The rate constant is dependent upon the particle radius and the diffusion coefficient of particles in the slurry. The number of collisions between particles increases with the square of the solids loading of the slurry.

Slow flocculation occurs when there is an energy barrier to flocculation and only a fraction of the collisions result in the formation of a doublet. The rate of slow flocculation is:

$$Rate_{slow} = (Rate_{rapid})/W, \tag{2.22}$$

where W is the stability ratio. W is the ratio of the number of collisions between particles to the number of collisions that result in coagulation. Values of W greater than 10^5 are easily obtained and values greater than 10^{10} are possible. The value of W is exponentially dependent upon the potential barrier. Overbeek reported an approximation for W:

$$W \cong \frac{1}{2\kappa a} \exp(V_{T(max)} / kT). \tag{2.23}$$

Flocculation therefore decreases as the repulsive potential between particles increases and the solids loading decreases.

2.5. Polymeric Stabilization

Polymeric dispersants are commonly used in the ceramics industry. In most aqueous systems, the polymers employed are block copolymers that have ionizable end groups. These dispersants are called polyelectrolytes and impart electrosteric stabilization. There are numerous polyelectrolytes that are commonly used: ammonium and sodium salts of polyacrylates, polyphosphates, poly(stryrene/maleate), poly(acrylic

acid), and poly(methacrylic acid). The functional groups of poly(methacrylic acid) (PMAA) and poly(acrylic acid) (PAA), are carboxylic groups (COOH) that can dissociate to form COO^-. The efficacy of polyelectrolyte dispersants is dependent upon the adsorption of the polymer on the solid surface and the conformation of the polymer chain.

The dispersants enable high solids loading in the slurries while maintaining relatively low viscosities. Polyelectrolytes are especially effective for stabilizing multi-component slurries. For example, silica and magnesia have isoelectric points around 2 and 12 respectively. For the pH range 2 to 12, the silica will have a negative surface charge and magnesia will have a positive surface charge. The particles will be spontaneously attracted to one another leading to heterocoagulation.

2.5.1. Poly(methacrylic acid) - Darvan

Cesarano et. al.[58] studied alumina slurries prepared with sodium salts of PMAA (Figure 2.6). PMAA dispersants are also called by the trade name Darvan™ (R.T. Vanderbilt, Norwalk, CT) and are frequently used for dispersing ceramic materials in aqueous suspensions. The dissociation of carboxylic groups on PMAA leads to a negative charge on the polyelectrolyte. The degree of dissociation increases as the pH and ionic strength of the solution increase, and the polymer will go from neutral to highly negative. The surface of alumina is positive for pH values below its isoelectric point (~9). The negatively charged PMAA will be strongly attracted to the alumina particles at pH below the isoelectric point. Cesarano et. al. showed that the amount of PMAA adsorbed onto the alumina increased with pH for values between 4 and 10.

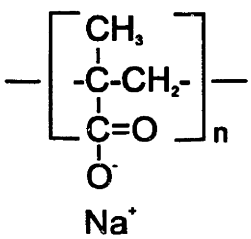

Figure 2.6. Polymer unit of sodium - PMAA (Darvan 7)

The conformation of the polymer adsorbed on the surface of the powder varies substantially. At high pH, the polyelectrolyte is nearly fully dissociated and the negative sites repel each other. The polyelectrolyte adsorbs in a flat conformation, and each chain covers a large area. At low pH, the polyelectrolyte chains form loops and occupy a smaller area on the particle surface.

Cesarano et. al. mapped the regions of stability for alumina slurries dispersed with PMAA. At pH below about 3.3, the slurry is stable. The polymer is essentially neutral at this range, and the stabilization is believed to be primarily electrostatic. Electrosteric stabilization occurs above pH 3.3 when sufficient polymer is present. The amount of polymer necessary to stabilize the slurry decreases as pH increases. The amount of polymer necessary for stabilization is also dependent upon the surface area of the powder since the polyelectrolyte adsorbs to the surface of the powder.

2.5.2. Poly(acrylic acid)

The effect of PAA on the stability of ceramic slurries has been thoroughly reviewed by Leong et. al.[59,60] Adsorbed PAA, like PMAA, imparts a negative charge on the particles due to dissociation of carboxylic groups. Leong reports that low molecular weight (less than ~5000) PAA acts primarily as a steric stabilizer for ceramic slurries. Biggs and Healy[61] reported that the conformation of adsorbed PAA changes dramatically with pH. The polymer forms compact coils at low pH, and the conformation changes to extended chains as the solution pH increases.

The yield stress and viscosity of zirconia slurries decreased substantially with increasing additions of low molecular weight PAA. The pH range over which the slurries were stable also increased with additions of PAA. High molecular weight PAA has the opposite effect and leads to flocculation. High molecular weight polymer additives are commonly used as flocculating agents to remove suspended particles during waste water treatment. Bridging flocculation occurs when the long-chained polymer joins two or more particles.

High molecular weight PAA is also commonly used as a binder. A key to the slurry-based 3DP process is redispersion of the unprinted powder bed. Any additives that

increase the strength of the powder bed will therefore have a negative impact upon the redispersion behavior.

2.5.3. Dispersion in Organic Media

Stable dispersions of ceramic powders can also be prepared in organic liquids. Parish et. al.[62], Fowkes[63], and Parfitt and Peacock[64] reviewed a wide array of organic systems for preparing stable ceramic dispersions. It is advantageous to process some non-oxide ceramic systems in nonaqueous media to prevent hydrolysis of the powder surface. Organic media also allow for broad ranges in the values of the surface tension, viscosity, and vapor pressure. Dispersants in organic media generally adsorb on the surface by Lewis acid-base reactions. Materials with acidic surfaces, such as silica, require dispersants that are basic, and vice versa.

The dielectric constant of the liquid plays a central role in the dispersion stability. Dielectric constants of organic liquids vary over a range of nearly 2 orders of magnitude from about 2 for ketones to 180 for some amides. Equation (2.18) indicates that the repulsive potential is directly proportional to the dielectric constant. The ionization of surface groups will vary for each solid/liquid system.

2.6. Measuring Colloidal Stability

2.6.1. Electrokinetic phenomena

Electrokinetic phenomena relate the combined effects of motion and electrical phenomena. The electrokinetic phenomena develop due to the displacement or distortion of the electrical double layer relative to the particle. The electrokinetic behavior can be used to determine the relative stability of a colloidal system. In an electrokinetic experiment, a portion of the double layer is sheared off at a plane in the solution, which is called the slipping plane or plane of shear. The potential at this plane is termed the zeta potential. The potential at the beginning of the diffuse part of the double layer can be approximated by measuring the zeta potential, ζ. Zeta potential can be measured by a number of processes.

Electrokinetic sonic amplitude, or ESA, effect is one method to measure the zeta potential. An alternating electric field is applied to the solution causing the particles to

move back and forth. If there is a density difference between the solid and liquid, the motion will produce an acoustic wave. The resulting sound wave is measured to determine the zeta potential. The advantage of this technique is that measurements can be taken in concentrated, opaque solutions.

Colloidal stability is best optimized by using zeta potential measurements. The zeta potential is measured as a function of the concentration of potential determining ions, or pH in most cases. Slurry stability will be highest where the zeta potential is large. The measurements can be repeated for numerous ionic strengths to characterize the effect of indifferent ions. The measurements can also be used to optimize the stability of slurries prepared with polyelectrolyte dispersants. The dispersant concentration and optimum pH is determined by titrating colloidal dispersions over a wide pH range.

2.6.2. Indirect Measurements

There are also a number of simple experimental techniques to evaluate the slurry stability. Viscosity measurements give an indirect observation of the slurry stability and are performed rapidly. Stable slurries will be nearly Newtonian. Flocculated slurries will generally exhibit a yield stress and high viscosity. Sedimentation techniques can give a clear indication of colloidal stability, but may take weeks to complete. A sample of the slurry is placed in a glass test tube or graduated cylinder. The rate at which the particles settle can be measured. Stokes' law can then be used to calculate an effective particle size. Unstable slurries will form flocs that rapidly settle out, while stable slurries will remain dispersed for extended lengths of time. The height of the layer of settled particles will also indicate the level of stability. Stable slurries will have repulsive forces between particles, allowing the particles to slide past one another to pack to an efficient state. Unstable slurries do not have sufficient repulsive forces between particles. The particles will stick together upon impact, and will not be free to rearrange to a high packing density as the particles settle.

2.7. Optimization of Alumina Slurry Stability for Slurry-Based 3DP

The alumina slurry stability must be optimized to maximize the packing density of the powder bed and ensure sinterability of the component. The slurry-based 3DP

process also places additional constraints on the slurry system. The method by which the powder bed is formed limits the maximum viscosity. The powder bed formation techniques will be described in detail in Chapter 3. The viscosity should be less than about 20 cP for slurry jetting or spray deposition techniques. Powder bed redispersion also places severe limitations on the slurry chemistry. Therefore, the slurry chemistry needs to be optimized with these constraints in mind.

2.7.1. Slurry Preparation

Alumina slurry was prepared in polyethylene bottles with ~3/8 inch alumina milling media. The order of operations is the most critical aspect of slurry preparation. The mixing procedure is as follows:

1. Add solvent.
2. Add dispersant. This is the acid or base for electrostatically-stabilized slurries.
3. Add PEG (if necessary). This is used to improve redispersion of the powder bed.
4. Add powder slowly. Adding all of the powder at once for high solids loading slurries will lead to pour mixing.
5. Add surfactant (if necessary) after the slurry has milled and is well-dispersed.

Solvent composition was variable. Pure water, water/methanol, and water/isopropyl alcohol (IPA) mixtures were investigated as the slurry solvent. The water content of the solvent was at least 50% in all slurries. Nitric acid was used to electrostatically stabilize alumina slurries. Darvan 821A (ammonium-PMAA, R.T. Vanderbilt Co., Norwalk, CT.) was also investigated as polyelectrolyte dispersant.

Milling media was filled to between 1/3 and 1/2 of the volume of the polyethylene mixing bottle. The acid or dispersant was mixed thoroughly with the solvent prior to adding powder. Acid concentrations for the slurry were studied to determine optimum slurry chemistry. The acid concentration will be reported in units of molarity (moles of acid/Liter of slurry). It is important to note that molarity is calculated using the <u>total</u> volume of the slurry, not the volume of only the solvent.

Powder was poured slowly into the solvent. The slurry would be very viscous and nonuniform if large amounts of powder were added without stirring. One half of the powder was typically added, and the mixture was ball-milled for approximately fifteen minutes. An additional one fourth of the total powder was then added and milled again for fifteen minutes. The remainder of the powder was then added, and the slurry was milled for several hours prior to use. This mixing procedure was varied slightly for slurries prepared with different solids loadings. The number of mixing steps was reduced for slurries prepared with solids loadings less than 30 volume percent (v/o) alumina and increased for slurries with solids loadings above 40 v/o.

Polyethylene glycol (Union Carbide, Danbury, CT.) was added to slurries to improve the redispersion behavior of the powder bed. This will be discussed in detail in following sections. The amount of PEG added was determined relative to the mass of alumina powder. The weight percent PEG is:

$$\textit{weight \%}\ \text{PEG} = 100\frac{\text{mass PEG}}{\textit{mass}\ \text{alumina}}. \tag{2.24}$$

Solids loading of the alumina varied from 25 to 45 volume percent. The slurries were ball-milled for 24 hours and de-aired prior to all experiments.

Surfactants, or surface active agents, were used to reduce the surface tension of the slurry. Surfactants may reduce the stability of the slurry, depending on the type of surfactant. The surfactants were added after the slurry had milled for several hours and stabilized to minimize the impact of the surfactant on slurry stability.

2.7.2. Zeta potential measurements

Zeta potential measurements were performed using electrokinetic sonic amplitude measurements (ESA-8000, Matec Applied Sciences, Hopkinton, MA.). The zeta potential was measured for each sample from pH 3 to pH 12 at increments of approximately 0.1. A series of experiments was performed using thirty-five v/o slurries prepared with 0.10 M nitric acid concentrations. The slurries were ball-milled for a specified period of time. The samples were then diluted to 10 v/o with 0.10 M nitric acid. Zeta potential measurements were performed on the 10 v/o slurries.

Zeta potential measurements were performed on three different grades of Ceralox™(Condea Vista, Tucson, AZ) alumina powder. The powders are designated APA-0.5, HPA-1.0, and APA-3.0. The APA-0.5 and HPA-1.0 powders contained 0.3% MgO as a sintering aid. Zeta potential measurements were performed at 24, 48, 72, and 96 hours for the three Ceralox powders. Graphs of zeta potential versus pH are shown in Figure 2.7. The isoelectric point (IEP) varies slightly between each of the powders. The isoelectric points are 10.0, 10.5 and 10.7 for APA-0.5, HPA-1.0, and APA-3.0. These values agree with reported values for alumina and indicate that the alumina surface is basic. The isoelectric points are constant with time for each of the powders. The maximum zeta potential is measured in acidic regions since alumina is basic. The maximum zeta potential is observed near pH~4.3 for all three powders. This is the pH at which repulsive forces will be the largest according to equation (2.18). The zeta potential is high from pH 3 to 6. The zeta potential quickly decreases as the pH increases above 6. The magnitude of the repulsive potential decreases until it reaches zero at the IEP. The zeta potential is negative for pH greater than the IEP. The repulsive potential begins to increase slightly as pH increases from the IEP, however the magnitude of the repulsive potential is small.

Alumina slurries are stable from pH 3 to 6. The pH of slurries prepared with 0.10 M nitric acid was approximately 4.3 after milling for 48 hours. This is near the maximum in the zeta potential curve and ensures a high degree of stability.

The magnitude of the zeta potential differs between the three Ceralox powders. The magnitude of the zeta potential is largest for the APA-3.0 powder. The APA-3.0 does not contain MgO, and this may affect the zeta potential. The zeta potential is calculated using the particle size and specific surface area of the powder. The calculations assume spherical particles. Therefore, morphology differences between the different powders will lead to variation in the zeta potential that is calculated. This must be kept in mind when comparing the zeta potential of different powders, and it may be necessary to classify powders to obtain well-controlled particle size distributions to compare powders directly.

The zeta potential also displays time-dependent behavior. The zeta potential for samples measured at 24 hour intervals is lowest for each sample after 24 hours. The

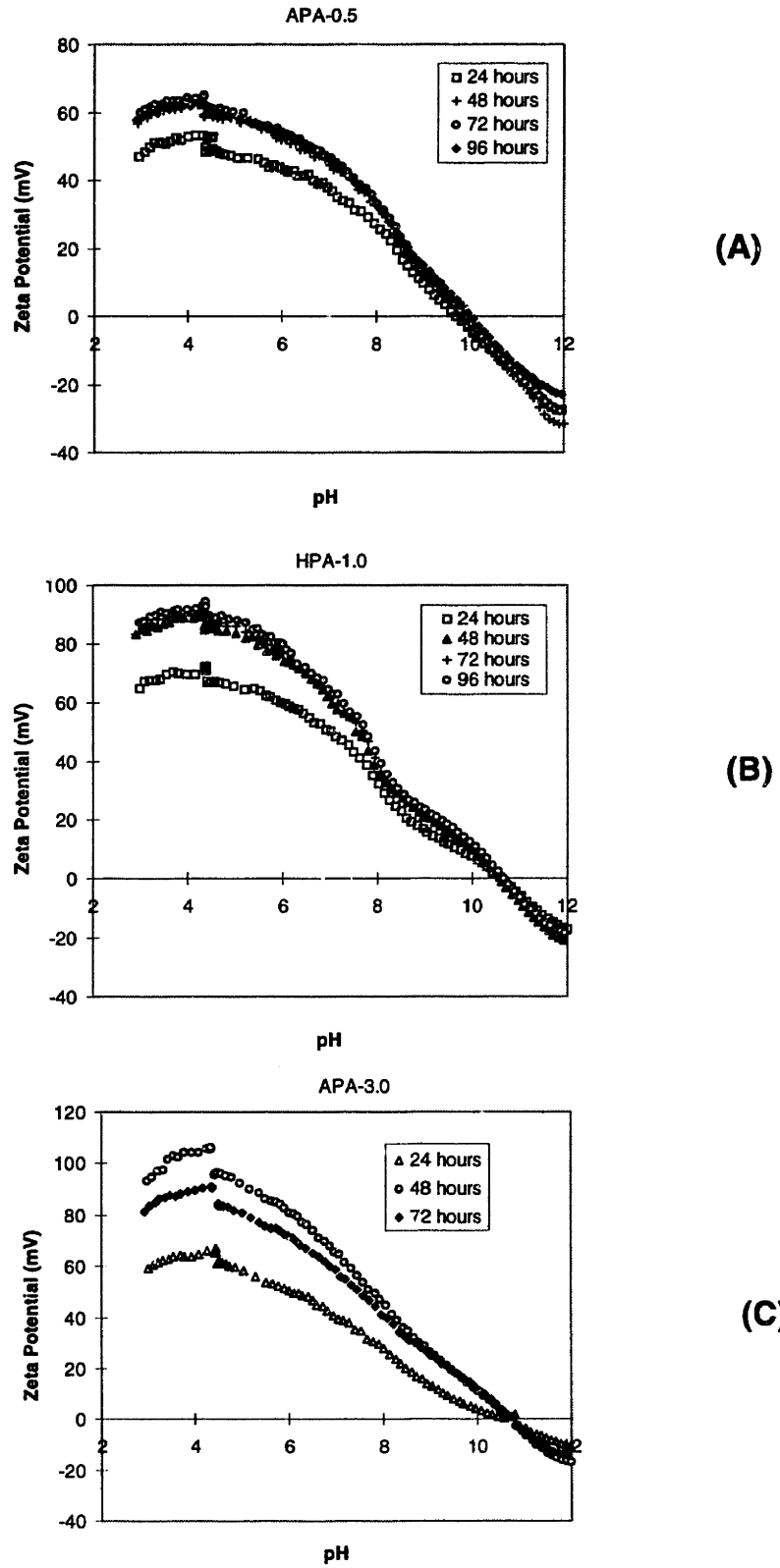

Figure 2.7. Time-dependence of the zeta potential for three Ceralox powders: **A)** APA-0.5 **B)** HPA-1.0 **C)** APA-3.0.

magnitude of the zeta potential increased for each sample after milling for 48 hours. The magnitude of the zeta potential decreased after milling between 48 and 72 hours for APA-3.0. The magnitude of the zeta potential decreased between 72 and 96 hours for the APA-0.5. The zeta potential remained essentially constant for the HPA-1.0 powder between 72 and 96 hours of milling.

2.7.3. Green density of slip cast samples

Powder bed samples were prepared by slip casting each of the 35 v/o Ceralox slurries at 24 hour intervals. The green densities of the powder beds were determined using mercury porosimetry (Micromeritics, Norcross, GA). The green density of the slip cast samples and the corresponding zeta potentials of the slurries are listed in Table 2.4. The green densities vary slightly between samples. The green densities of APA-0.5 are slightly greater than those of HPA-1.0, while the densities of APA-3.0 are the lowest. The powder morphology and particle size distribution will play a large role in the green density. The correlation between the zeta potential and green density is shown in Figure 2.8. The green density increases with increasing zeta potential for each of the powders. This figure emphasizes the importance of maximizing zeta potential to achieve the optimum packing density.

Table 2.4. Zeta potential of the slurry and green density of slip cast samples.

Powder	Milling Time (hours)	Zeta Potential (mV)	Density (g/cm^3)
APA-0.5	24	52.8	2.463
APA-0.5	72	65.0	2.584
APA-0.5	96	62.9	2.563
HPA-1.0	24	72.3	2.406
HPA-1.0	72	91.9	2.474
HPA-1.0	96	94.2	2.536
APA-3.0	24	67.1	2.199
APA-3.0	72	90.9	2.337

2.7.4. Effect of Acid Concentration on Alumina Slurry Stability

Jooho Moon examined the behavior of a series of slurries prepared with nitric acid concentrations between 0.015 M and 0.18 M. The pH of each slurry was measured immediately after mixing and after milling for 24 hours. The viscosity was also

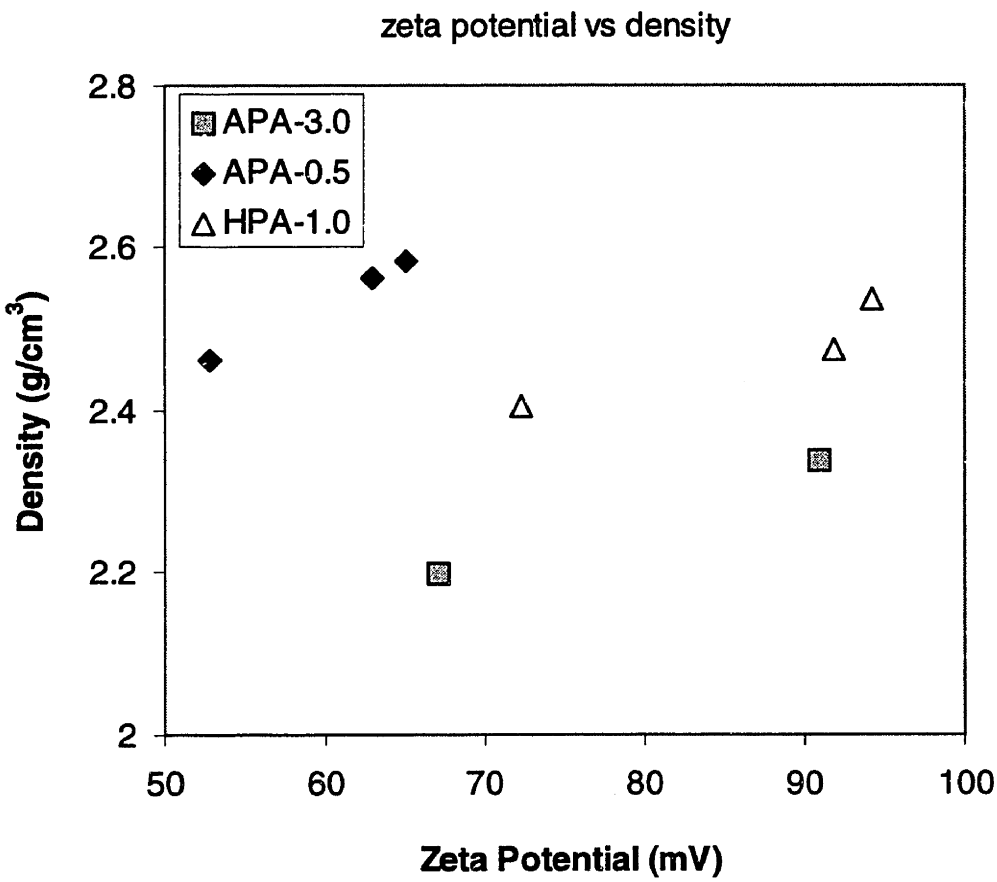

Figure 2.8. Zeta potential versus density for Ceralox powders

measured after milling for 24 hours. Samples were slip cast and mercury porosimetry was performed to determine the green density and mean pore size.

The results are summarized in Table 2.5. The pH increased during the milling process. Viscosity data for 40 volume percent HPA-1.0 slurries are shown in Figure 2.9. The viscosity is shear-thinning for all three slurries. The viscosities of slurries prepared with 0.015 M and 0.045 M nitric acid were very similar, despite the fact that the pH of the 0.015 M slurry was 6.71. The pH of the 0.045 slurry was near the pH of maximum zeta potential for the alumina powder. The viscosity increased substantially with increasing acid concentrations above 0.045 M.

Viscosity data for slurries prepared with 0.09 M and 0.18 M nitric acid indicated that the slurries were probably flocculated. The concentration of nitric acid in these slurries exceeded the CCC for alumina reported by Overbeek, 5.2×10^{-2} M. The viscosities were considerably higher than slurries prepared with lower concentrations of acid. The slurries also exhibited a yield stress. This is consistent with the formation of a floc structure. The ionic strength increases with increasing acid concentrations. The nitric acid itself contributes to the ionic strength. The solubility of alumina also increases at extreme pH, further increasing the ionic strength. The green density and average pore size data also indicate that the slurry with 0.18 M nitric acid is the least stable.

Table 2.5. Effect of nitric acid concentration on slurry properties.

Solids Loading	Acid Conc.	As-prep. pH	pH after 24 hours	Viscosity at 300 s^{-1} (cP)	Green Density (%)	Ave. Pore Size (μm)
40	0.015 M	6.50	6.71	16.2	63.3	0.069
40	0.045 M	3.60	4.52	16.0	66.4	0.067
40	0.09 M	1.48	3.86	27.6	66.7	0.068
40	0.18 M	0.65	1.01	105.2	61.4	0.087
30	0.045 M	3.30	4.25	6.5	66.1	0.065

2.7.5. *Stabilization with Darvan 821A*

Darvan 821A is an ammonium salt of PMAA. Its stabilization mechanism was discussed in detail in section *2.5.1*. Zeta potential measurements were performed on slurries prepared with 0.125, 0.25, and 0.5 weight percent of Darvan 821A and Ceralox APA-0.5 powder. The weight percent is calculated by the weight of Darvan 821A

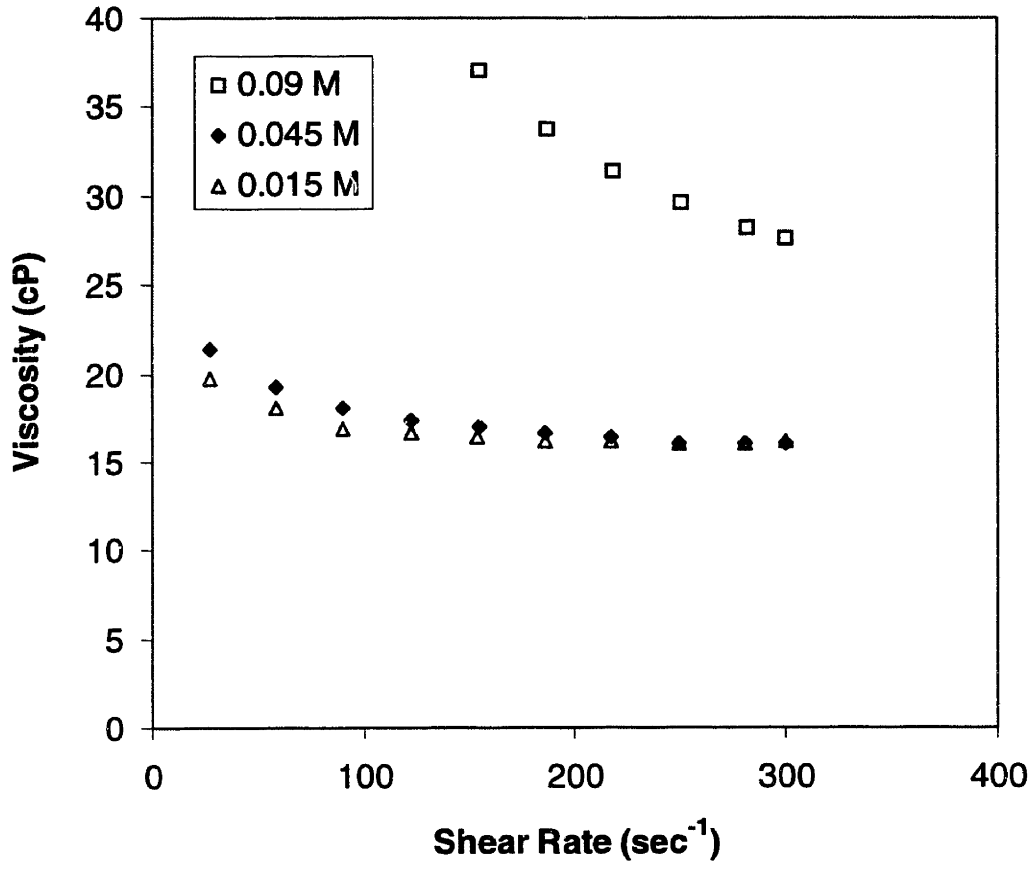

Figure 2.9. Viscosity data for 40 volume percent alumina slurries prepared with different concentrations of nitric acid

relative to the weight of alumina in the slurry. The results of the zeta potential measurements are shown in Figure 2.10. The IEP is strongly affected by the adsorption of Darvan 821A. PMAA imparts a negative surface charge due to dissociated carboxyl groups. The IEP shifts to lower pH as Darvan is added to the slurry because of the negative surface charge characteristics of PMAA. The IEP decreases from 10.0 with no Darvan 821A to 7.0, 5.9, and 4.0 for 0.125, 0.25, and 0.5 weight % Darvan 821A, respectively. Slurries prepared with PMAA are stable in regions where the pH is high. The magnitude of the zeta potential is also higher in slurries prepared with Darvan 821A. Slurries with solids loadings as high as 50 v/o and viscosities less than 15 cP were prepared with Darvan 821A.

2.8. Redispersion Behavior of Slip Cast Alumina Powder Beds

Powder beds prepared by the slurry-based 3DP process have considerable cohesive strength without binder. The part retrieval process is considerably more complicated than in the standard 3DP process in which the unprinted regions of the powder bed consist of loose powder. Part retrieval in the slurry-based 3DP process must be carried out by redispersing the unprinted regions of the powder bed(Figure 2.11). The slurry chemistry and processing must be optimized for both stability and redispersion behavior, and the two are not completely independent. The redispersion behavior was examined to determine the mechanisms which control it.

The redispersion behavior was measured using the set-up shown in Figure 2.12. A wire mesh basket was suspended into a beaker of liquid. The powder bed sample was placed into the mesh basket. The balance was interfaced with a computer, and the mass of the suspended sample was recorded continuously. The mass of the suspended sample decreased as the powder bed redispersed, and the loose powder fell through the wire mesh holder. Redispersion behavior was measured as a function of the powder type, slurry chemistry, and redispersion liquid. Six different types of alumina powder were tested, and the redispersion behavior was measured in deionized water, methanol, and a basic solution. The slurries used to prepare the samples were all 35 v/o alumina with 0.10 M nitric acid concentration, unless otherwise noted. The slurries were ball-milled for 48 hours. The samples tested for redispersion were prepared by slip casting discs

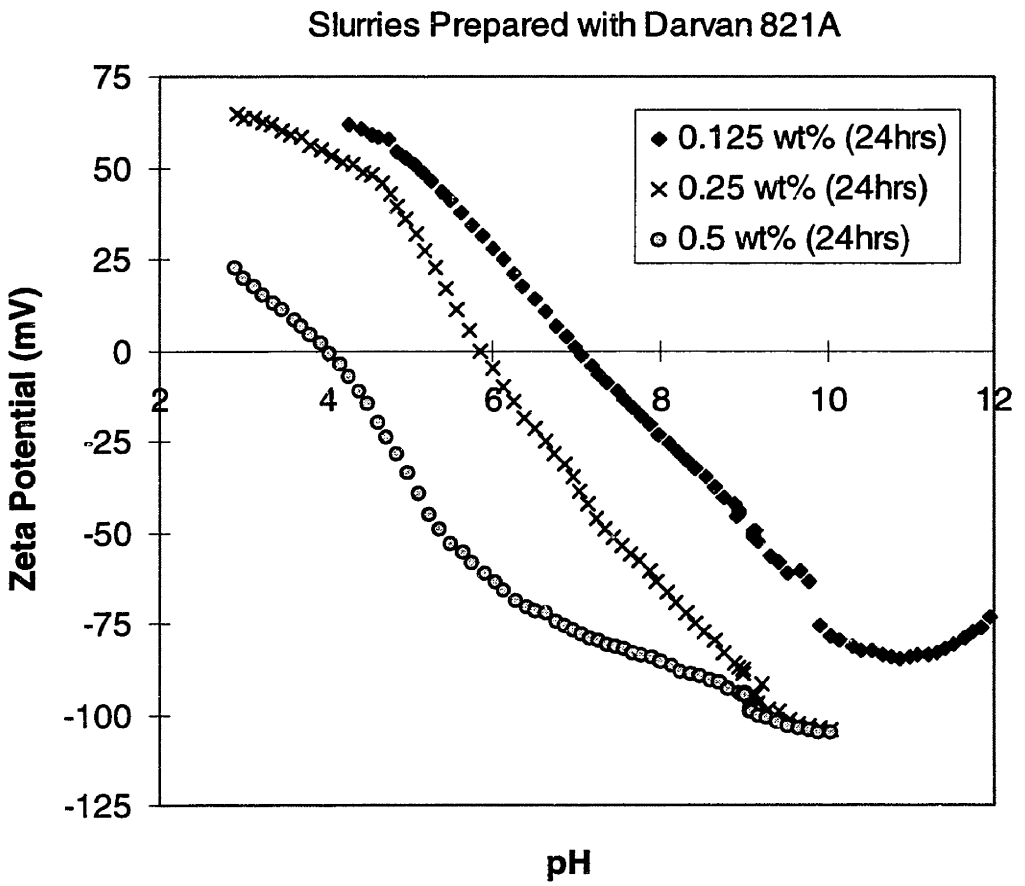

Figure 2.10. Zeta potential measurements for slurries prepared with Darvan 821A.

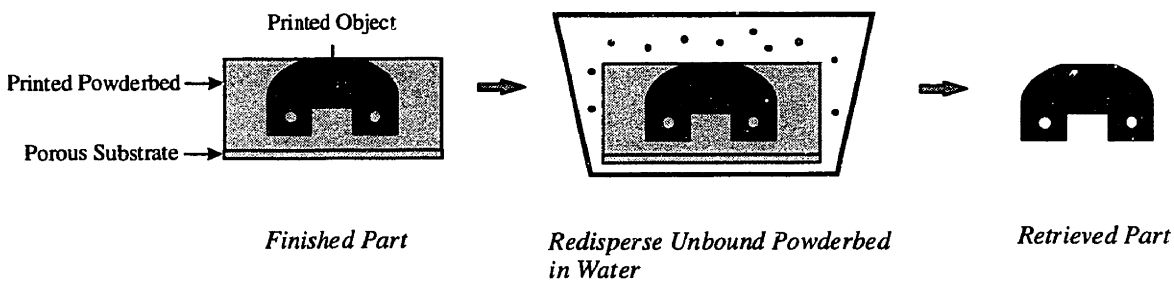

Figure 2.11. Schematic representation of part retrieval process.

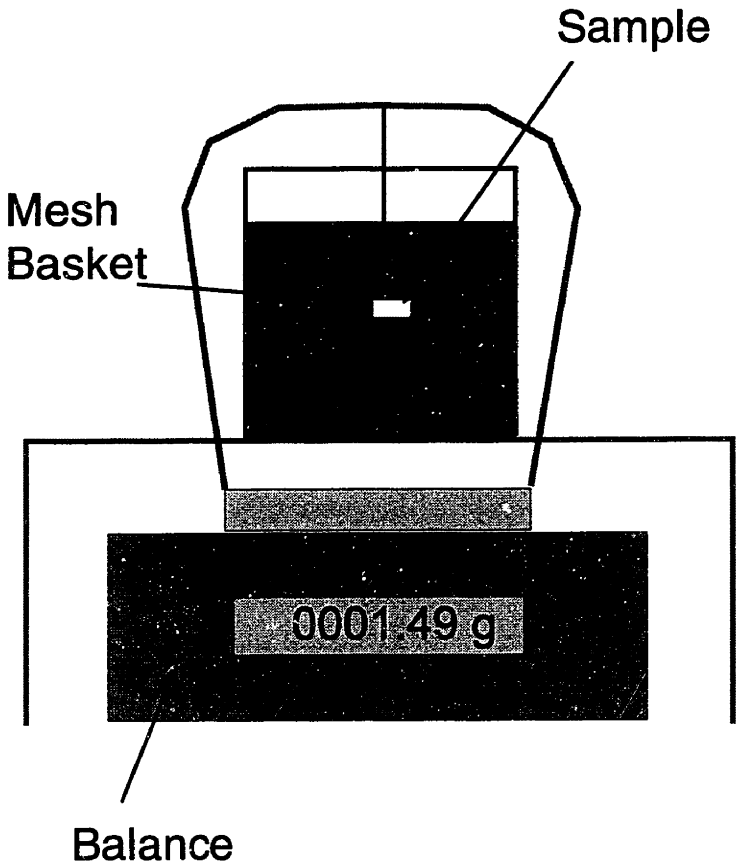

Figure 2.12. Schematic of the apparatus for measuring redispersion behavior of powder beds.

approximately 3 mm thick and 25 mm in diameter. The discs were allowed to air dry for at least two days. The slip cast discs were cut into rectangular blocks with a mass of about 0.5 grams.

Samples were quickly submerged into the wire mesh sample holder. Powder beds prepared with APA-0.5 powder exploded violently after being submersed for a few seconds in water and in the basic solution. An audible pop was observed and the sample would break into several pieces.

The results of several redispersion measurements with alumina powder are summarized below. The results are plotted in terms of normalized mass versus time. The mass was normalized by dividing the mass measured at any given time by the maximum mass of the suspended sample. The normalized mass can therefore vary from 1 (no redispersion) to 0 (complete redispersion). The percent redispersed can also be calculated:

$$\% \text{ Redispersed} = 100(1 - \text{normalized mass}) \tag{2.25}$$

2.8.1. Effect of Powder Type

The redispersion behavior in deionized water of samples prepared with four alumina powders is shown in Figure 2.13. The powders tested were Ceralox APA-0.5, Ceralox HPA-1.0, 3 μm Norton powder, and Baikalox GE-1. The GE-1 had a nominal particle size of 3 μm. The redispersion behavior differs substantially between the different powders. The APA-0.5 sample exploded into several pieces very quickly, but very little change in the sample was observed after the initial explosion. The HPA-1.0 sample gently broke into several pieces. Small amounts of powder slowly fell away from the surface of the sample. The samples prepared with 3μm Norton and GE-1 powders redispersed very well. The samples appeared to 'melt' when placed in water. The samples slumped into mounds of powder. The powder then fell freely through the wire mesh sample holder.

The redispersion behavior was clearly dependent upon the particle size of the powder. The APA-0.5 and HPA-1.0 have nearly identical surface chemistry and morphology. The densities of the samples were 2.58 and 2.48 g/cm^3 for the APA-0.5 and HPA-1.0, respectively. The HPA-1.0 clearly redispersed much better than the APA-0.5.

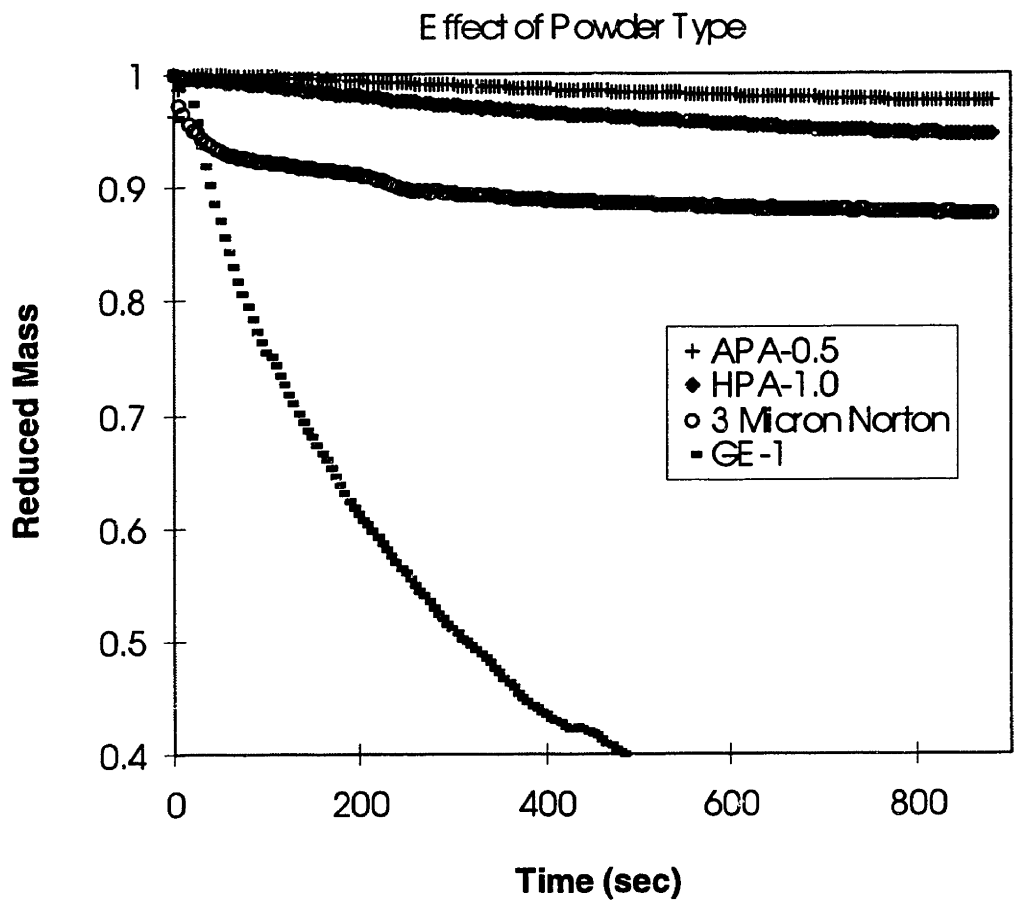

Figure 2.13. Effect of powder type on redispersion behavior of powder beds.

The HPA-1.0 sample was very soft and easily broke up with slight shaking. The APA-0.5 sample was hard and did not break up with slight shaking.

The 3 μm Norton and GE-1 powders spontaneously redispersed and also illustrated the effect of both packing density and particle size. The densities of the 3 μm Norton and GE-1 were 1.68 and 1.75 g/cm^3, respectively. Both samples redispersed to a fine powder when placed in water. These results indicated that the number of particle-particle contacts are critical to the redispersion behavior. The number of particle-particle contacts varies inversely with the cube of the particle size. The number of contacts will also decrease with decreasing packing density.

The sintering behavior of ceramics is also dependent upon particle size and packing density. Increasing the particle size and decreasing packing density will have a negative impact upon the sinterability of the powder bed. Three micron alumina powder will generally not sinter to full density even if the green density is greater than 60% theoretical. Therefore, the redispersion behavior of the powder bed and its sintering characteristics appear to be a fundamental trade-off.

2.8.2. *Effect of Adding Polyethylene Glycol to the Slurry*

Polyethylene glycol is a water-soluble polymer that is commonly used in ceramics processing. High molecular weight PEG (M_w>1000000) is often used as a binder for ceramics that are formed by injection molding.[65] Low molecular weight PEG is used as a plasticizer in many tape casting applications. PEG is a viscous liquid at room temperature when the molecular weight is less than ~1000. Higher molecular weights are waxy solids. PEG dissolves quickly in water at room temperature.

PEG was incorporated into the solvent prior to adding the alumina powder to the slurry. The amount of PEG added was calculated in weight percent relative to the mass of alumina in the slurry. The stability of slurries prepared with PEG showed no noticeable difference compared to slurries prepared without PEG. The magnitude of the zeta potential of slurries prepared with PEG was slightly greater than slurries prepared without PEG. The green densities of slip cast samples were also nearly identical.

The redispersion behavior of APA-0.5 powder beds prepared with PEG is shown in Figure 2.14. Figure 2.14a illustrates the impact of adding PEG with molecular weight

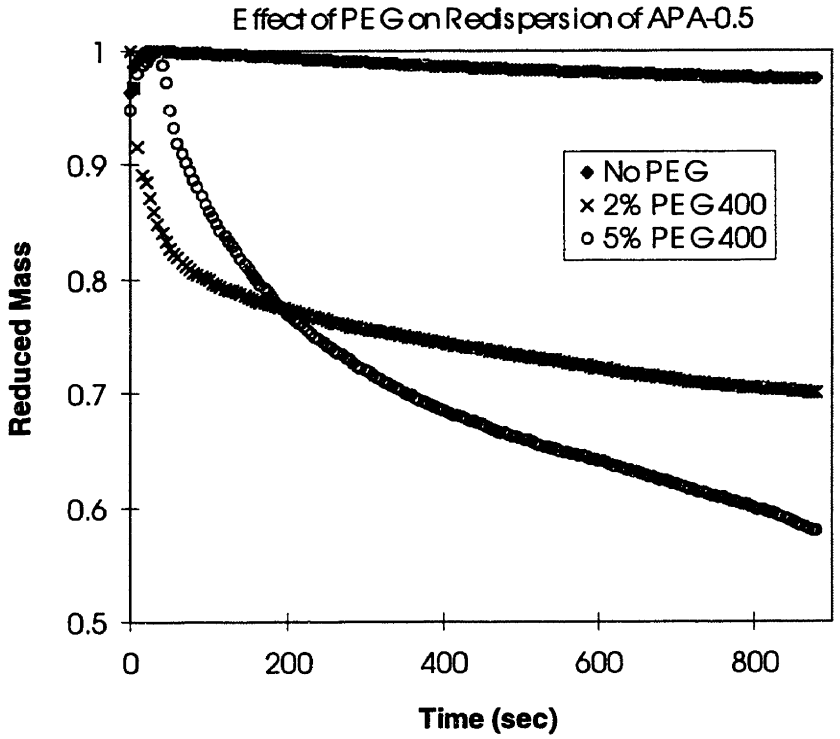

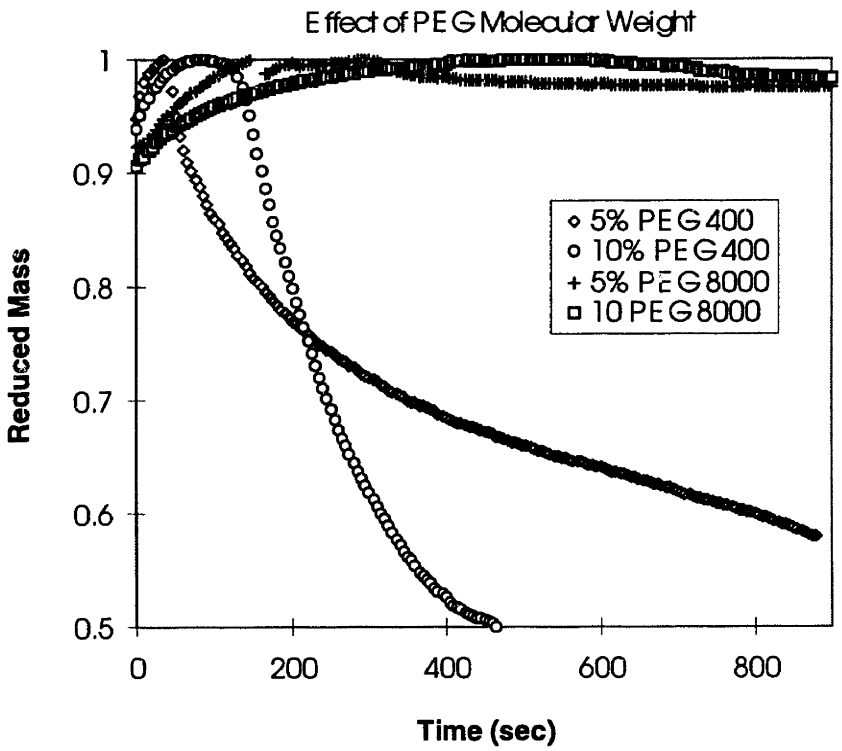

Figure 2.14. Effect of PEG additions on the redispersion behavior of powder beds prepared with APA-0.5 powder.

400 (PEG 400). The redispersion improves substantially with additions of PEG to the slurry. Samples with 2 weight percent or more PEG did not explode like samples with no PEG. The APA-0.5 samples containing PEG behaved similar to the 3 μm Norton and GE-1 samples; the powder bed slumped and dispersed to a fine powder. The extent of redispersion improved with increasing amounts of PEG 400.

Figure 2.14b illustrates the effect of PEG molecular weight on redispersion of APA-0.5 powder beds. Samples prepared with PEG 8000 did not redisperse well. The samples remained essentially intact and were sticky to the touch.

Low molecular weight polymers are subject to volatilization at moderate temperatures. The vapor pressure of the polymer increases with decreasing molecular weight. Volatilization of PEG may be a critical factor since some binder materials being studied for the slurry-based 3DP process are thermally cured. The effect of heating on the PEG content and redispersion behavior was examined.

Powder beds prepared with HPA-1.0 powder and 2 weight percent PEG 400 were heated for 6 hours at 110, 150, and 200°C. The PEG content was determined using thermogravimetric analysis (TGA). The samples were heated to 900°C in flowing nitrogen at a rate of 2°C/minute. The weight of the sample was monitored with time. The weight loss of the sample was equal to the amount of PEG present in the sample. The amount of PEG present in the samples is listed in Table 2.6. The effect of heating on redispersion is shown in Figure 2.15. The percent redispersed after 15 minutes decreased as the heating temperature increased, following the decrease in PEG content. The percent redispersed dropped to nearly zero for heating temperatures 150°C and higher.

Table 2.6. PEG 400 content in HPA-1.0 samples after heating for six hours (2 weight percent initially)

Heating Temperature (°C)	Weight % PEG	% Redispersed
Room Temp.	2.0	81.8
110	1.4	68.2
150	0.5	0.7
200	0.3	1.7

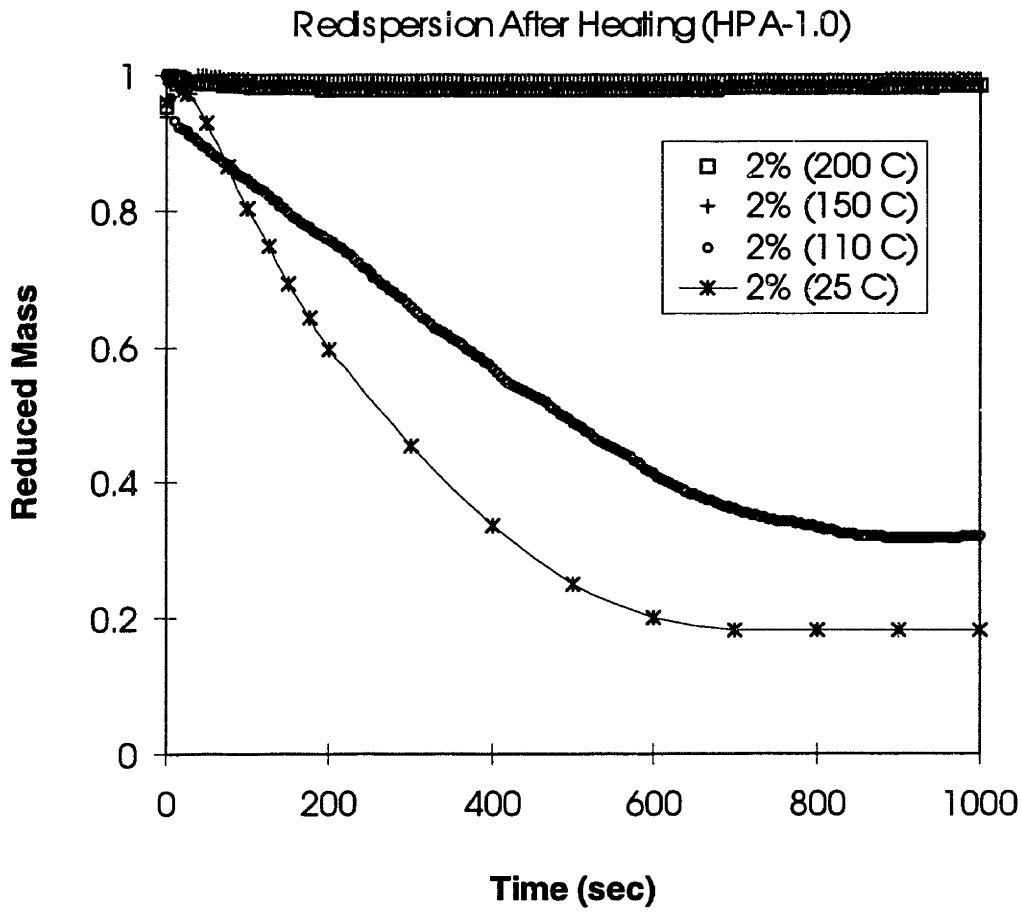

Figure 2.15. Effect of heating the samples for 6 hours at various temperatures on the redispersion behavior. Powder beds were prepared with HPA-1.0 powder.

The effect of using Darvan 821A as a dispersant on the redispersion was also investigated (Figure 2.16). Samples were prepared with 0.5 weight percent Darvan 821A and APA-0.5 powder. The percent redispersed after 15 minutes in water was 0.7% for a sample with no PEG and 2.1% for a sample with 2 weight percent PEG 400. The samples behaved similar to samples containing PEG 8000. The saturated powder beds remained cohesive and sticky to the touch.

2.8.3. Effect of the Redispersion Solvent

Selected samples were also redispersed in methanol and in a basic solution prepared by adding ammonium hydroxide to deionized water to adjust the pH to 10. The IEP of the alumina powders is near pH 10. The pH of deionized water was approximately 5. The role of electrostatic repulsion on the redispersion behavior was determined by comparing redispersion where the electrostatic repulsion is high (pH = 5) and redispersion where there is no electrostatic repulsion (pH=10). Redispersion in methanol indicated the effect of the surface tension of the liquid. The surface tensions of methanol and water are 24 and 72 dynes/cm, respectively. Figure 2.17 shows the redispersion behavior of several samples in water, methanol, and base. The percent redispersed is highest in deionized water for all of the samples and lowest in methanol. The percent redispersed in base is greater than zero despite the fact that the electrostatic repulsion is zero.

The redispersion behavior for all samples is summarized in Table 2.7. The percent redispersed after sitting in the redispersion medium for 15 minutes is listed. The data are consistent with the observations that redispersion improves with increasing particle size and increasing content of PEG 400. Redispersion is best in deionized water for all samples.

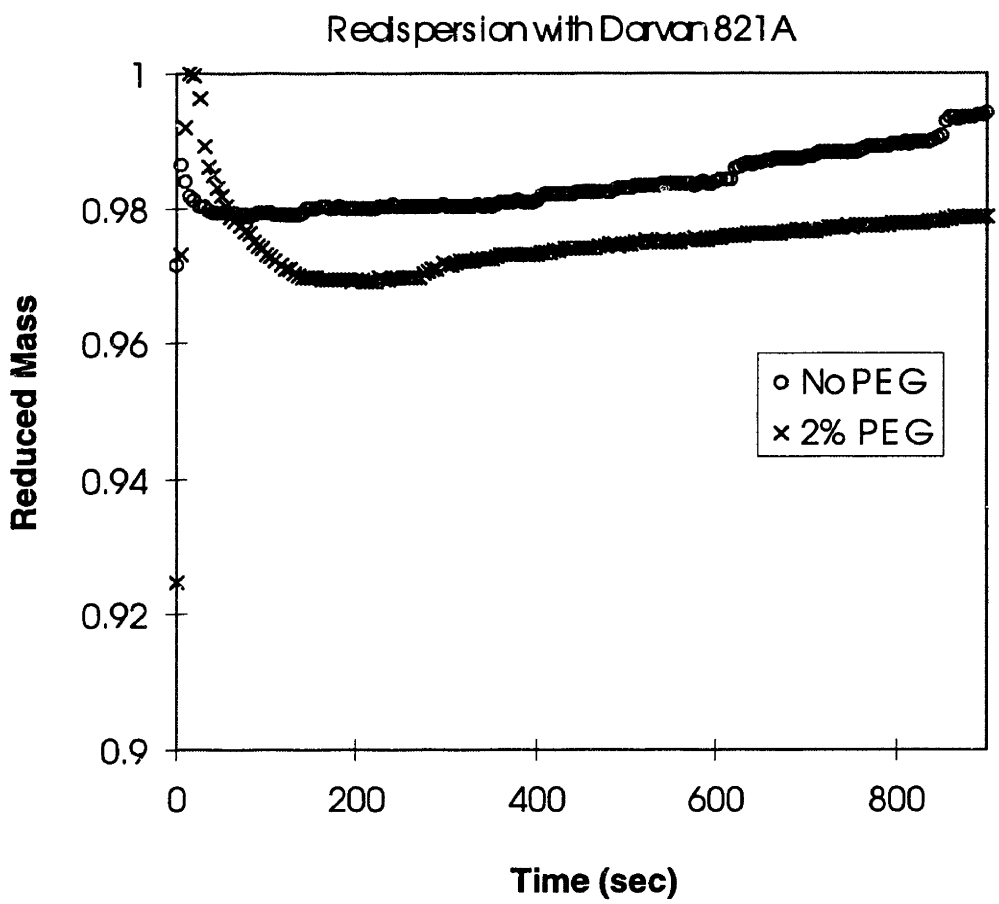

Figure 2.16. Redispersion behavior of powder beds prepared with Darvan 821A as the dispersant.

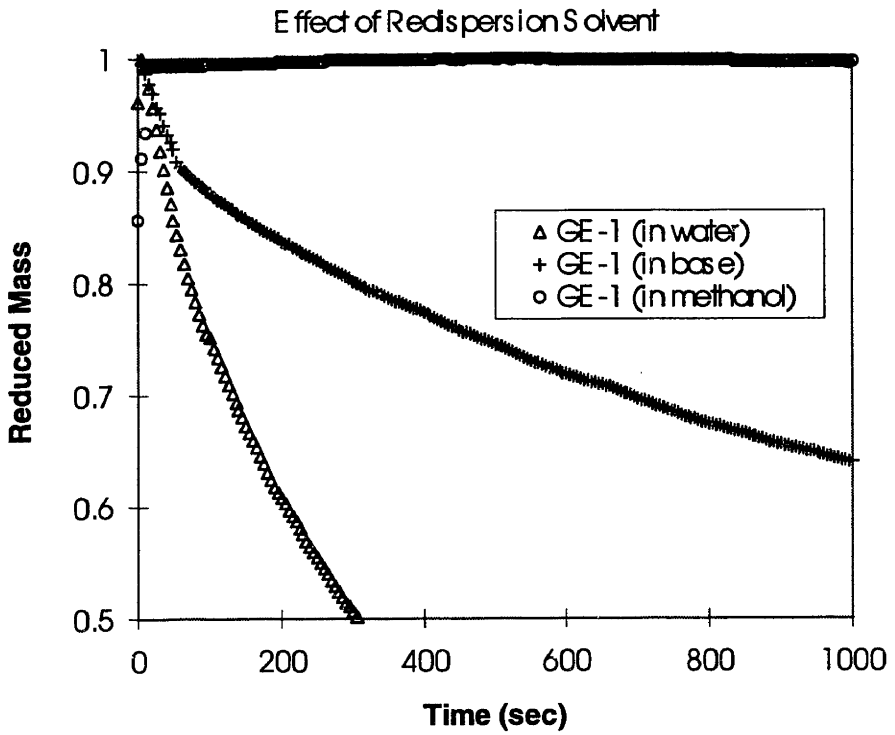

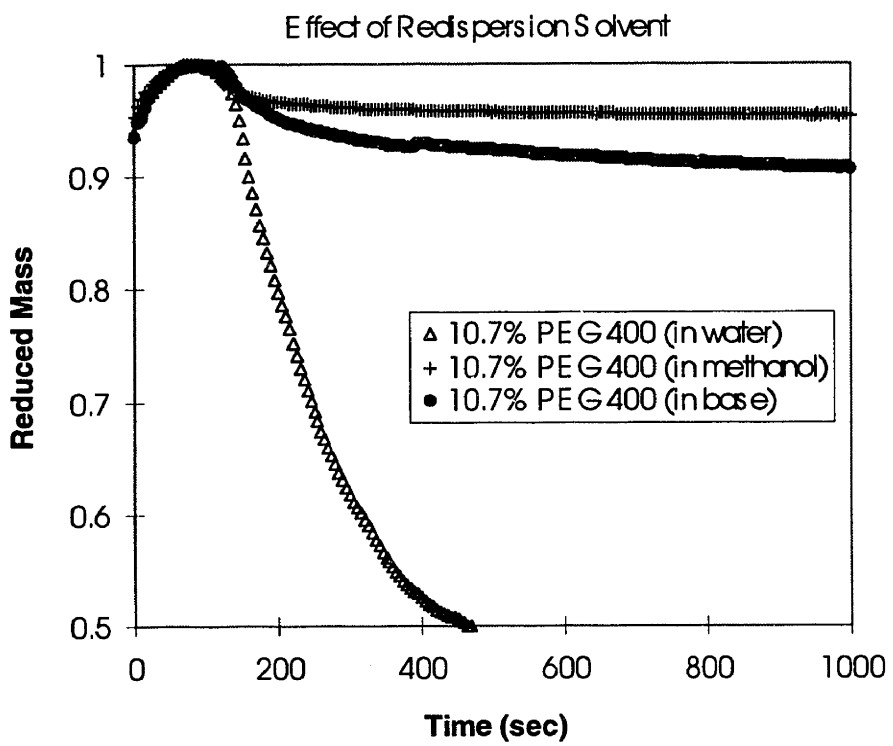

Figure 2.17. Effect of the solvent on the redispersion behavior.

Table 2.7. % Redispersed after 15 minutes

Powder Type	Dispersant	PEG Content	Heating	Redispersion Solvent	% Redispersed
GE-1	0.10M acid	none	none	Water	68.4
GE-1	0.10M acid	none	none	Base	34.4
GE-1	0.10M acid	none	none	MeOH	0.3
APA-0.5	0.10M acid	none	none	Water	2.5
APA-0.5	0.10M acid	none	none	Base	2.5
APA-0.5	0.10M acid	2% PEG 400	none	Water	30.0
APA-0.5	0.10M acid	5% PEG 400	none	Water	42.1
APA-0.5	0.10M acid	5% PEG 400	none	Base	8.7
APA-0.5	0.10M acid	5% PEG 400	none	MeOH	0.5
APA-0.5	0.10M acid	10% PEG 400	none	Water	57.3
APA-0.5	0.10M acid	10% PEG 400	none	Base	9.0
APA-0.5	0.10M acid	10% PEG 400	none	MeOH	4.5
APA-0.5	0.10M acid	5% PEG 8000	none	Water	2.5
APA-0.5	0.10M acid	5% PEG 8000	none	Base	9.1
APA-0.5	0.10M acid	5% PEG 8000	none	MeOH	0.0
APA-0.5	0.10M acid	10% PEG 8000	none	Water	1.6
APA-0.5	0.10M acid	10% PEG 8000	none	MeOH	2.5
Norton 1μm	0.10M acid	none	none	Base	8.1
Norton 3μm	0.10M acid	none	none	MeOH	0.2
HPA-1.0	0.10M acid	none	none	Water	5.4
HPA-1.0	0.10M acid	2% PEG 400	none	Water	81.8
HPA-1.0	0.10M acid	2% PEG 400	110°C, 6 hours	Water	68.2
HPA-1.0	0.10M acid	2% PEG 400	150°C, 6 hours	Water	0.7
HPA-1.0	0.10M acid	2% PEG 400	200°C, 6 hours	Water	1.7
HPA-1.0	0.5% Darvan 821A	none	none	Water	0.7
HPA-1.0	0.5% Darvan 821A	2% PEG 400	none	Water	2.1

2.9. Discussion

The colloidal stability and redispersion behavior are two critical elements in the slurry-based 3DP process, each of which is dependent upon the slurry chemistry. The solubility of alumina in aqueous solutions is critical to both the stability and the redispersion behavior. The ionic strength of the solution increases with time as alumina is dissolved. Also, reprecipitation of aluminum trihydroxide, $Al(OH)_3$, is likely after the slurry dries. This will increase the strength of particle-particle contacts[66] and impede redispersion.

Aluminum hydroxides are amphoteric and are soluble in both strong acids and strong bases. Solubility of $Al(OH)_3$ as a function of pH is shown in Figure 2.18.[67] The solubility is low between pH 5 and 8 but increases rapidly below pH 4 and above pH 9. Takeda et.al.[68] reported similar results for the dissolution of alumina in aqueous

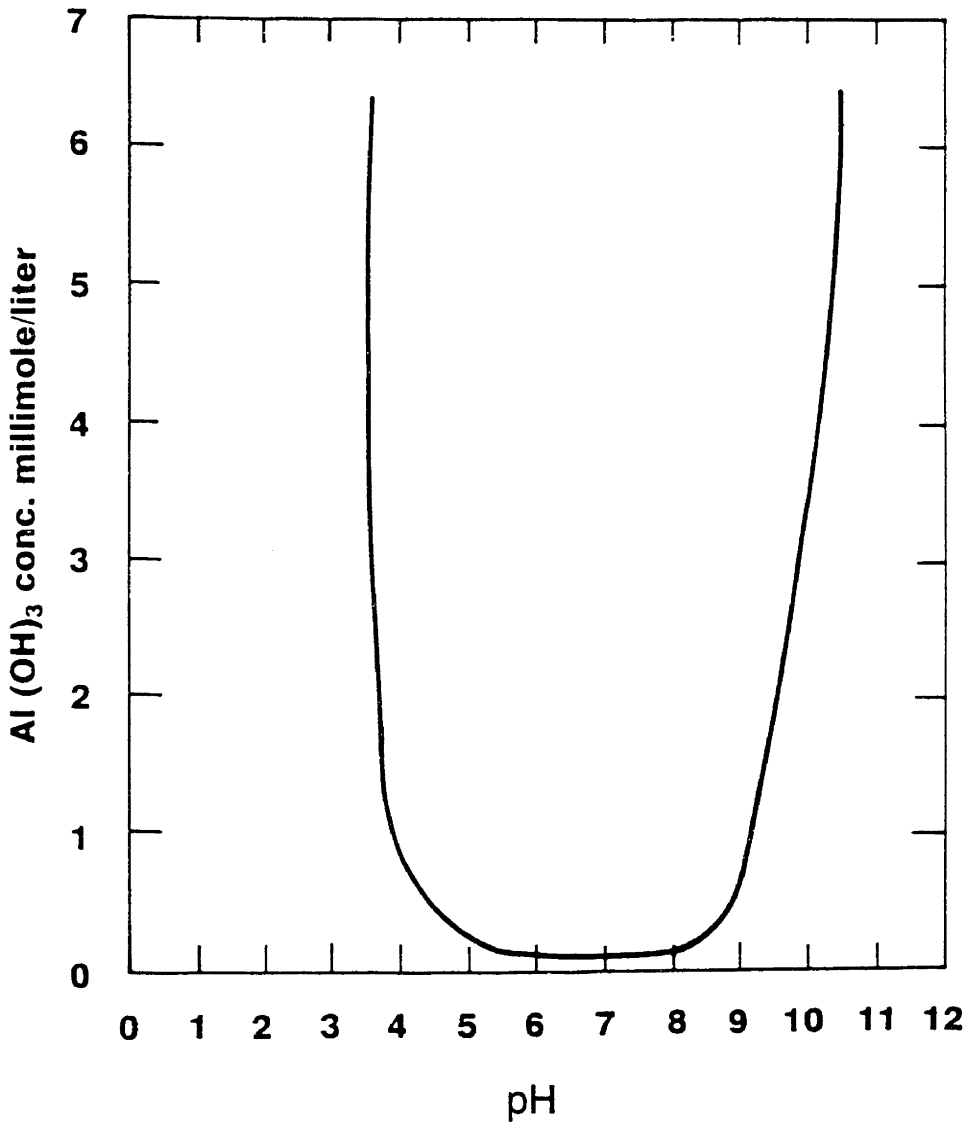

Figure 2.18. Solubility of $Al(OH)_3$ as a function of pH

solutions. The pH of alumina slurries with 0.05 M nitric acid typically stabilizes around pH 4.5 to 5.0. Adding acid to reduce the pH to the point of maximum zeta potential (~pH 4) is not recommended, since the increased solubility of alumina leads to a self-defeating condition. The ionic strength increases rapidly and the slurry soon becomes less stable.

The concentration of nitric acid should be minimized for these reasons. The slurry lifetime is increased for lower concentrations of nitric acid. Slurries prepared with 0.10 M nitric acid are stable for about 5 days before flocculation becomes noticeable. Slurries prepared with 0.05 M nitric acid may be stable for more than 7 days. However, there is still a critical window during which the slurry may be used. The minimum time that the slurry should be aged is dependent upon the mixing technique. Alumina slurries need to be agitated to expose the surface and break up agglomerates. The rate at which new surface is exposed is dependent upon the energy of mixing. The maximum in the zeta potential is observed after milling for roughly 48 hours for most slurries. However, most slurries are stable with low viscosity after milling for only 12 hours. High energy ultrasonication can also be used to rapidly break up the agglomerates and disperse the slurry.

The redispersion behavior is dependent upon the number and strength of particle-particle contacts. The number of particle-particle contacts is dependent upon the particle size and packing density. Sintering rates are strongly affected by the powder packing, so reducing the number of particle contacts is only feasible to a small extent. The strength of particle-particle contacts is the desired mechanism for improving the redispersion behavior of the powder bed.

Low molecular weight PEG appears to reduce the strength of the particle-particle contacts. The PEG will be left at the necks of the particles as the slurry dries. This may prevent the reprecipitation of $Al(OH)_3$ at the necks. The PEG is also very soluble in water. The polymer chains will extend as liquid enters the powder bed during the redispersion process, acting as an additional force pushing the particles apart.

Excess pressure due to entrapped air may also contribute to the redispersion. Khanuja discussed cracking during the redispersion process using a theory proposed by Heertjes.[69] Excess pressure builds up as liquid infiltrates into a porous body and entraps air. The excess pressure is equal to the capillary pressure of the powder bed:

$$\Delta P = \frac{2\gamma_{LV}\cos\theta}{r_{pore}}, \tag{2.26}$$

where γ_{LV} is the surface tension of the liquid, θ is the contact angle, and r_{pore} is the pore radius. This excess pressure leads to the explosion observed when APA-0.5 samples are submerged in water. APA-0.5 samples that were submerged while under vacuum or that were submerged in low surface tension solvents did not explode.

Excess pressure that is capable of causing explosion must be avoided to prevent possible propagation of cracks into the printed parts. However, it appears that some degree of excess pressure is beneficial to the redispersion process. The redispersion behavior of samples in basic solution and in methanol presents two cases in which the electrostatic repulsive forces are low. The percent redispersed in basic solutions was higher than in methanol for all samples except APA-0.5 with 10 weight percent PEG. (In that particular case, the variation in percent redispersed in base and in methanol was within the error of the measurement.) The capillary pressure is much higher for the basic solution than for the methanol, and the excess pressure may help separate particles in the bed.

2.10 Conclusions

Slurry chemistry and processing is critical for both the slurry stability and redispersion of powder beds. Classic DLVO theory provides the basic framework for understanding the optimization of slurry stability. Repulsive forces must be established between particles to overcome the van der Waals attractive forces. Electrostatic repulsive forces are established by the surface charge of alumina controlled by the solution pH. The zeta potential is maximized around pH 4.3 for slurries prepared with Ceralox powders. The packing density of samples correlates with the magnitude of the zeta potential of the slurry.

Redispersion behavior is improved substantially with the addition of PEG to the slurry. The PEG is highly soluble in water and weakens the strength of particle-particle contacts. Loss of PEG due to volatilization during heating should be minimized. The time and temperature for thermal curing affect the PEG content that remains in the powder bed. The effects of volatilization can be reduced somewhat by thermally curing

samples in a closed container with excess PEG. This is done by placing the sample and an open dish of PEG into a dessicator. The lid is placed on the dessicator and it is placed in the oven to heat. This will act to saturate the environment within the dessicator with PEG vapor and reduce the amount of PEG lost from the samples. Redispersion can also be improved by increasing particle size and decreasing packing density, but these approaches will be at the expense of the sintering behavior.

Polymeric components in the slurry have the greatest impact on the redispersion behavior. Low molecular weight PEG improves redispersion while higher molecular weight PEG (PEG 8000) inhibits redispersion. High molecular weight PEG is used as a binder. It's likely that the strength of powder beds is considerably higher with PEG 8000, and the solubility of the PEG is lower. Polymeric dispersants must also be used with caution. Samples dispersed with Darvan 821A did not redisperse well. Entanglement of adsorbed polymer chains and reaction of the carboxyl groups is likely. The redispersion behavior of slurries prepared with dispersants will have to be tested on an individual basis.

There is no "optimum" slurry composition since trade-offs must be made between sinterability and redispersability. The Ceralox APA-0.5 and HPA-1.0 have proven to sinter extremely well. The other powders studied display poor sintering characteristics due to their size and poor particle packing. Slurries stabilized with 0.05 M nitric acid possess a good combination of high stability and relatively long life.

CHAPTER 3
POWDER BED FORMATION AND MICROSTRUCTURE

3.1. Introduction

The reliability and effectiveness of engineered ceramic components depend largely on the microstructure. Trapped pores act as strength-limiting flaws in structural ceramics and act as scattering points in electro-ceramics. The microstructure of the green powder bed, namely the packing density and distribution of porosity, determines the ultimate microstructure of the sintered component. Slurry stability is the first step towards achieving uniform microstructures with high packing density. The manner in which the slurry is deposited to form the powder bed is the next key element.

The formation of the powder bed in the slurry-based 3DP process is analogous to slip casting. Slurry is deposited onto a porous substrate in a controlled manner. The capillary pressure of the substrate withdraws the solvent from the slurry. The slurry layer *casts* to form the powder bed layer. The powder bed is a saturated solid body after casting is complete, and the powder bed is dried to control saturation.

Several approaches have been investigated to deposit the slurry to form the powder bed. The effectiveness of each of these processes will be discussed with respect to the microstructure of the powder bed. Cracking of the powder bed is a problem that may occur during the formation of the powder bed. The criteria for forming crack-free powder beds will be discussed in the next chapter.

3.2. Spray Deposition

Spray deposition was the first approach investigated for depositing the slurry. The slurry was deposited by atomizing the slurry with a spray nozzle and rastering the sprayer across the substrate (Figure 3.1). Several different types of spray nozzles were investigated. Each of the nozzles created a fine mist of slurry droplets. The advantages and drawbacks of each of these nozzles are discussed in Caradonna's thesis[70].

Slurries were deposited onto a porous substrate by rastering a spray nozzle across the substrate. The amount of slurry deposited onto the substrate was controlled by varying the slurry flow rate, line spacing of the raster pattern, and raster velocity (print

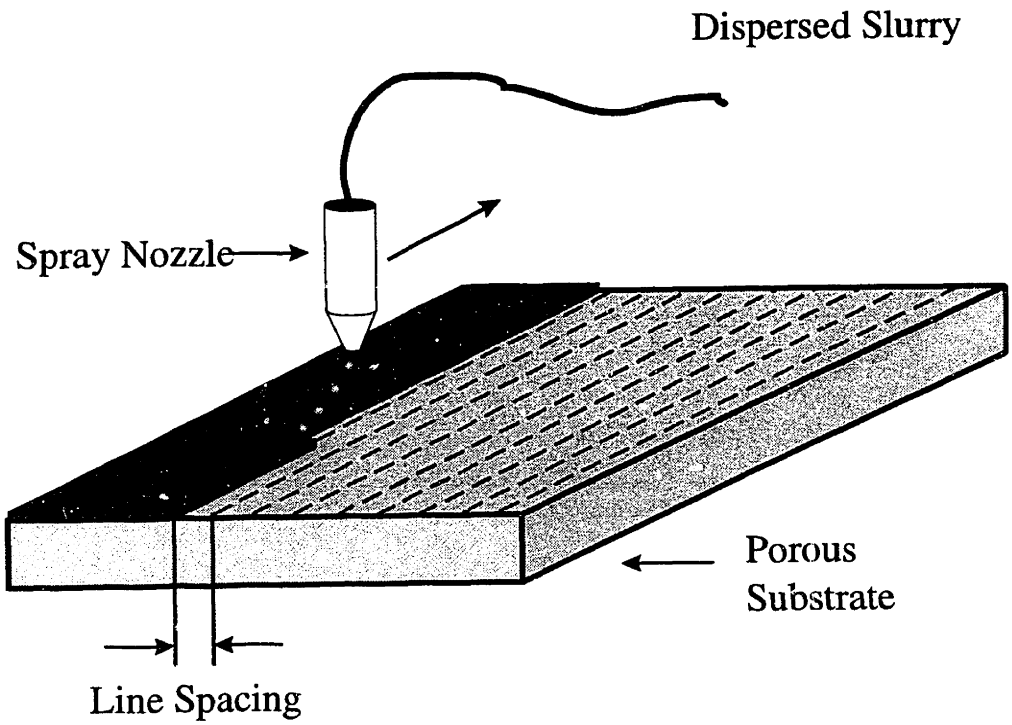

Figure 3.1. Schematic of the raster pattern used to deposit the slurry

speed). The powder bed was dried by heating with a 500 W lamp for 45 seconds. This deposition process was repeated several times to build up the ceramic body.

Several different types of substrates were used. Porous substrates work the best since the slurry is able to slip cast when it is deposited. Plaster substrates work very well since slurries cast very quickly when deposited on them. Plaster is not very durable, and the substrates degrade with use. Borosilicate glass filter discs (Ace Glass Co.) are very durable and also cast well. The casting properties of the substrate are only significant for the first few layers. The surface finish of the powder beds and the casting behavior of the slurry depend on the type of powder used in the slurry after about 5 layers have been deposited.

The microstructure of the powder beds was studied using mercury porosimetry. Mercury porosimetry gives information about both bulk density and the size distribution of porosity. The measurements are carried out by placing a porous sample into a glass penetrometer. The penetrometer and sample are evacuated and then back-filled with mercury. Mercury is non-wetting and will not penetrate the pores of the sample without applied pressure. The pressure of the system is increased to force the mercury into the sample. The infiltration of the mercury into the sample follows the Young and Laplace equation:

$$\Delta P = \frac{2\gamma_{LV}\cos\theta}{r_{pore}}. \tag{3.1}$$

Large pores will be filled first, followed by smaller pores as the pressure is increased. The amount of mercury that is forced into the sample is measured continuously. Mercury porosimetry data is often plotted as cumulative intrusion volume of mercury versus pore size. Jumps in the cumulative intrusion volume indicate the relative volume of pores present in the sample at a given pore size.

Mercury porosimetry data for two powder beds prepared using a piezo-atomizing nozzle are shown in Figure 3.2. The powder bed prepared with 30 volume percent slurry had a green density of only 1.89 g/cm^3 (47.7% theoretical) and had a bimodal distribution of pores sizes. The powder bed prepared with 15 volume percent slurry had a green density of 2.07 g/cm^3 (52.3% theoretical). The number of large pores was significantly lower for the powder bed prepared with 15 volume percent slurry.

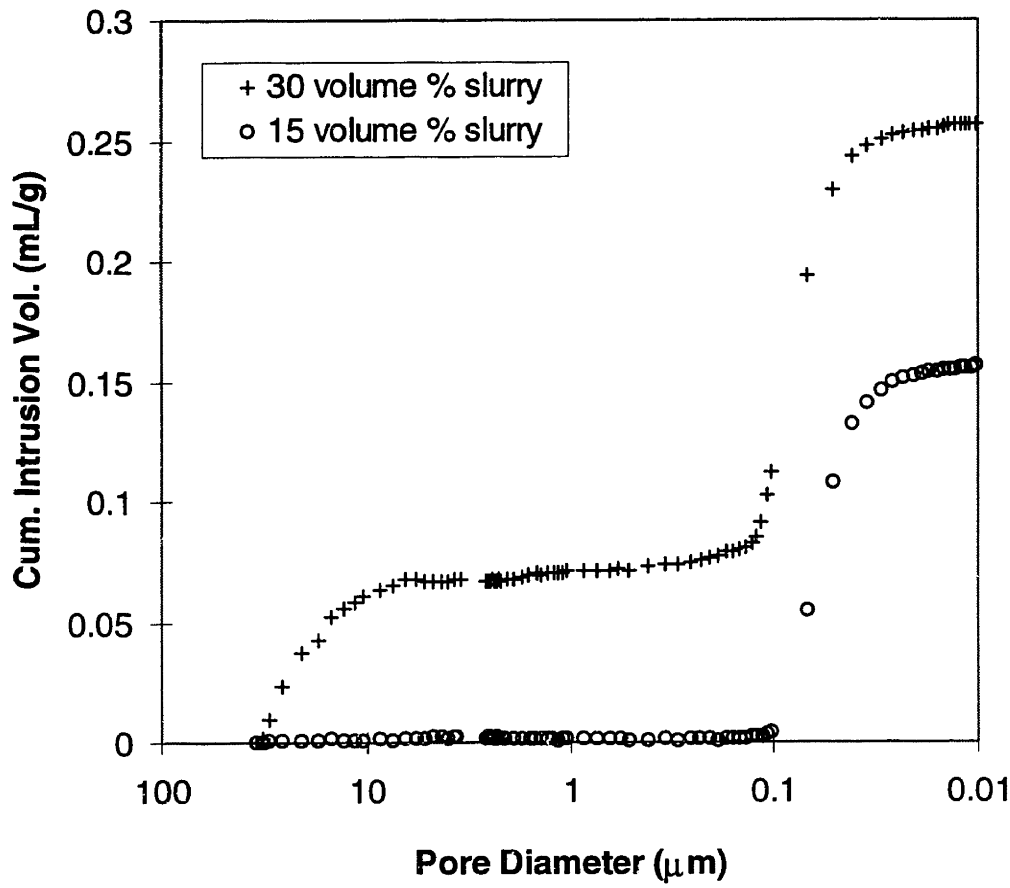

Figure 3.2. Mercury porosimetry data of powder beds formed with piezo-atomizing spray nozzle.

Powder beds prepared with the spray deposition technique were rough when the solids loading of the slurry was greater than ~20 volume percent. This was a major problem since the solids loading affects the build rate of the powder bed. Cracking of the powder bed is also more severe when the solids loading is low.

The spray deposition technique introduced a number of problems. The spray pattern of the nozzles was not uniform and made it impossible to precisely control the layer thickness. Slurry build up on the tip of the nozzles affected the flow rate and the spray pattern. The poor microstructure of the powder beds was the greatest limitation and necessitated a different slurry deposition technique.

3.3. Slurry Jetting

The slurry jetting technique was the next process examined for depositing the slurry. Khanuja first investigated jetting ceramic slurries through ink-jet printing nozzles. Khanuja examined the possibility of increasing the packing density of spray dried powder beds by depositing slurry. The slurry jetting process deposits slurry through an ink-jet printing nozzle onto the powder bed. The nozzle is rastered across the powder bed to deposit the slurry precisely. The slurry jetting process offers much greater control than the spray deposition process. The flow rate of the slurry is easily controlled and monitored. The slurry placement is very precise, since the slurry jet is less than 150 μm in diameter. The slurry nozzle was also easily incorporated with the hardware of the 3DP machine and did not require major machine modifications.

The slurry is fed to the nozzle using a pressure vessel system shown schematically in Figure 3.3. Slurry is placed inside the pressure vessel. The slurry is then filtered with an in-line nylon filter before being fed to the nozzle. Removing agglomerates from the slurry is essential to prevent clogging. The flow rate is dependent upon the viscosity of the slurry, the pressure of the system, and the nozzle diameter. Flow rate is measured continuously by measuring changes in the mass of the slurry. The pressure vessel is placed on top of a balance. The balance is interfaced to the computer, and the flow rate is measured continually.

A variety of nozzle sizes and nozzle types has been examined. The differences between various types of nozzles were discussed by Caradonna. This thesis will only

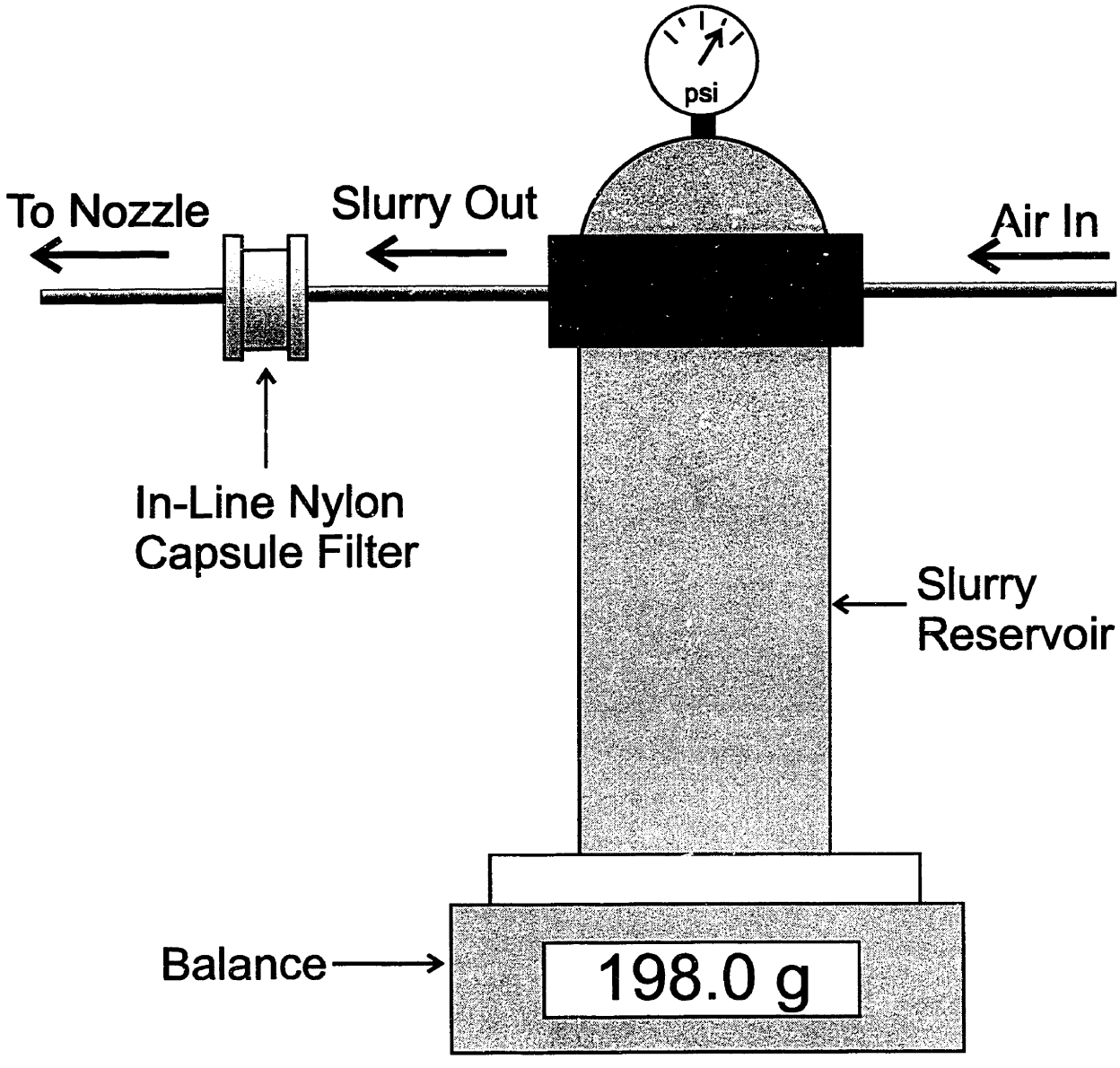

Figure 3.3. Schematic of the slurry feed system

discuss results of powder beds prepared with 127μm alumina nozzles (Gaiser Tool Co., Ventura, CA). The nozzle is rastered across the powder bed hundreds of times for each layer, so nozzle stability and flow rate need to be closely monitored. Instability of the slurry jet may be exhibited in three ways: total clogging of the nozzle, partial clogging, and jet deflection. It is important to detect instabilities quickly to keep the process tightly controlled. Total clogging of the nozzle is observed immediately. Partial clogging is more difficult to detect since it affects slurry flow rate. Jet deflection occurs when particles or debris collect at the tip and affect the direction of the slurry jet.

Slurry jets spontaneously break up into droplets. Droplet break off occurs at some distance from the tip of the nozzle, called the break off distance. The break off distance is dependent upon the nozzle geometry as well as the properties of the liquid including viscosity, surface tension, and flow rate. The distance between the nozzle and the substrate, the working distance, should be less than the break off distance. The slurry jet drifts due to air flow when the working distance is too large. Powder beds formed at working distances greater than the break off length were very rough and contained large pores.

3.3.1. Effect of Slurry Jetting Conditions on Powder Bed Microstructure

A series of experiments was performed to analyze the effect of slurry jetting variables on the microstructure. The properties of slurry-jetted powder beds were compared to samples prepared by slip casting the slurry. The slip cast samples represent the upper limit in the quality of the microstructure and packing density of the powder beds. Large deviations between the microstructures of jetted powder beds and slip cast powder beds were used to indicate conditions in which jetted powder beds were subpar. The microstructure of powder beds were characterized using mercury porosimetry and scanning electron microscopy (SEM).

Powder beds were prepared with Ceralox APA-0.5 (0.5 μm) and Ceralox HPA-1.0 (1.0 μm) alumina powder. The slurries were 35 volume percent alumina, 0.05 M nitric acid, and 2 weight percent PEG 400. The slurries were ball-milled for five days before use. The flow rate of the slurry was kept constant at 2 cm^3/min for all powder beds prepared in this series of experiments. The line spacing was varied between 200 and

600 μm, and the print speed was varied from 150 to 250 cm/sec. Each layer of the powder bed was dried for 45 seconds using a 500 W drying lamp. The powder beds were completely dry after this time. The powder beds were allowed to cool for approximately 30 seconds before the next layer was deposited. The slurry jetting conditions are listed in Table 3.1.

Table 3.1. Slurry jetting conditions used to generate powder beds

Powder	Print Speed (cm/sec)	Line Spacing (μm)
APA-0.5	200	300
APA-0.5	250	300
APA-0.5	200	400
APA-0.5	250	400
APA-0.5	200	500
APA-0.5	250	500
HPA-1.0	150	200
HPA-1.0	250	200
HPA-1.0	150	400
HPA-1.0	250	400
HPA-1.0	150	600
HPA-1.0	250	600

Mercury porosimetry was performed on each of the powder beds. The cumulative intrusion volume of mercury versus pore size is plotted in Figure 3.4 for series of powder beds prepared with 0.5 μm and 1.0 μm alumina powder. The 0.5 μm powder beds shown were jetted at 250 cm/sec, and line spacings were 300, 400, and 500 μm. The 1.0 μm powder beds were jetted at 150 cm/sec with line spacings of 200, 400, and 600 μm.

The properties of the samples are summarized in Table 3.2. The slip cast samples had higher densities and smaller average pore diameters than the jetted powder beds. The differences in pore size and packing density were more dramatic for the 1.0 μm powder beds. The density of the 1.0 μm slip cast sample was 63.1% of the theoretical density and the average pore diameter was 0.073 μm. The densities of the 1.0 μm jetted powder beds were between 51.6% and 55.1%, and the average pore diameters were about 0.12 μm. The density of the 0.5 μm slip cast powder bed was 65.5% with average pore diameter of 0.049 μm. The densities of the 0.5 μm jetted powder beds were between 60.1% and 63.4% with average pore diameter of 0.061 μm.

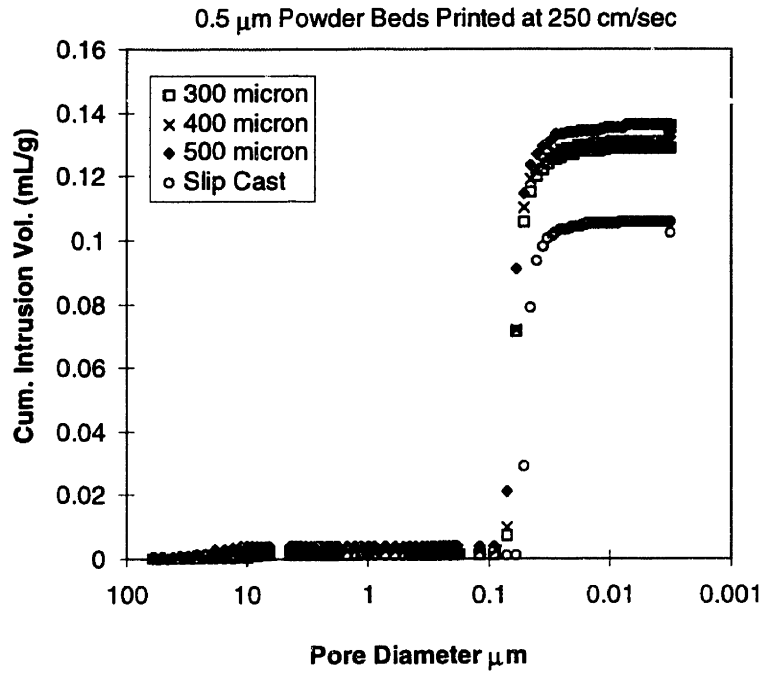

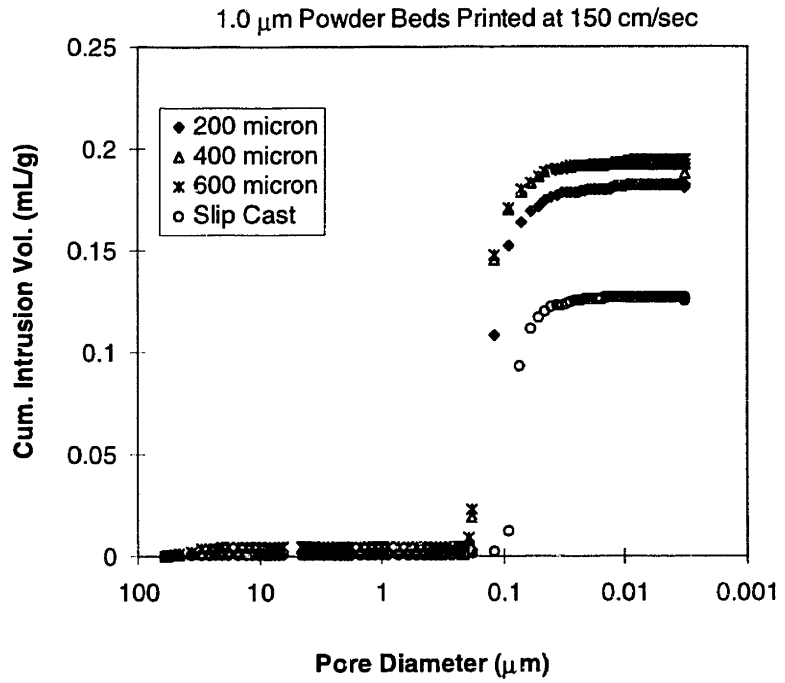

Figure 3.4. Mercury porosimetry data of powder beds prepared by jetting APA-0.5 and HPA-1.0.

Table 3.2. Summary of mercury porosimetry data for powder beds shown in Figure 3.4.

Powder	Speed (cm/sec)	Line Spacing (μm)	Green Density (% Theo.)	Pore Diam. (μm)	Intr. Vol. at 1 μm (mL/g)
APA-0.5	slip cast	slip cast	65.5	0.049	0.0011
APA-0.5	250	300	63.4	0.061	0.0013
APA-0.5	250	400	62.8	0.061	0.0027
APA-0.5	250	500	60.1	0.061	0.0039
HPA-1.0	slip cast	slip cast	63.1	0.073	0.0008
HPA-1.0	150	200	55.1	0.121	0.0009
HPA-1.0	150	400	54.2	0.120	0.0029
HPA-1.0	150	600	51.6	0.119	0.0046

The microstructures of the powder beds were dependent upon the jetting variables. The density of jetted powder beds decreased as the line spacing increased. More importantly, the number of large pores also increased with increasing line spacing. Pores larger than 1 μm are especially detrimental since they are unlikely to be removed during sintering. Large pores get trapped within the body and act as performance-limiting flaws.

The number of large pores present within the green body were quantified by looking at the cumulative intrusion volume from mercury porosimetry measurements. The cumulative intrusion volume at 1 μm will indicate the volume of pores 1 μm and larger. The effect of jetting variables on the number of large pores is shown in Figure 3.5. The number of large pores increased with increasing line spacing at a given print speed. The number of large pores also increased with increasing print speed for a given line spacing.

3.3.2. Defects in Slurry-Jetted Powder Beds

The large pores observed in mercury porosimetry measurements are indicative of defects that form during the jetting process. Observations from SEM cross-sections correlated very well with the mercury porosimetry data. Large pores and defects were observed in SEM cross-sections of powder beds that contained a high concentration of large pores determined by porosimetry. Figure 3.6A shows a 0.5 μm powder bed that was jetted with a line spacing of 500 μm. A triangular-shaped pore about 10 μm in size

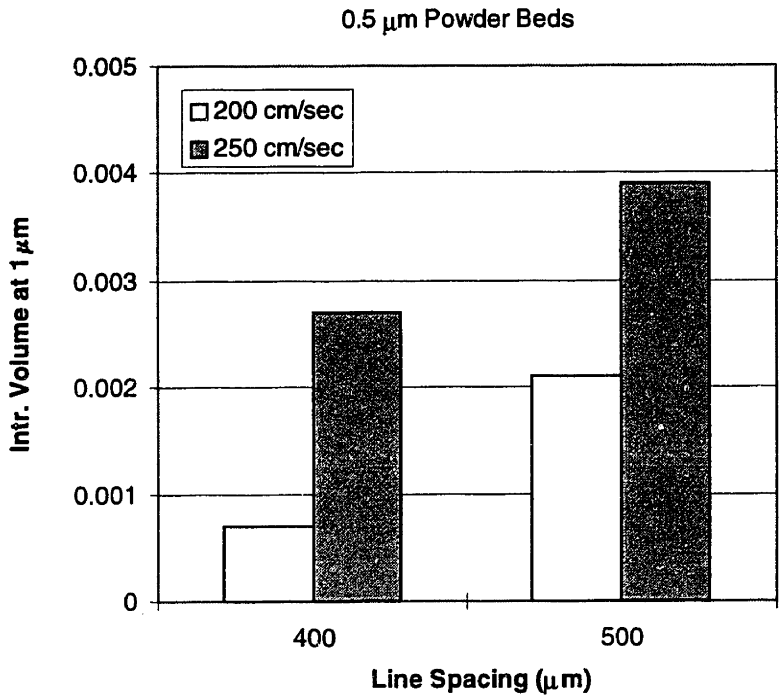

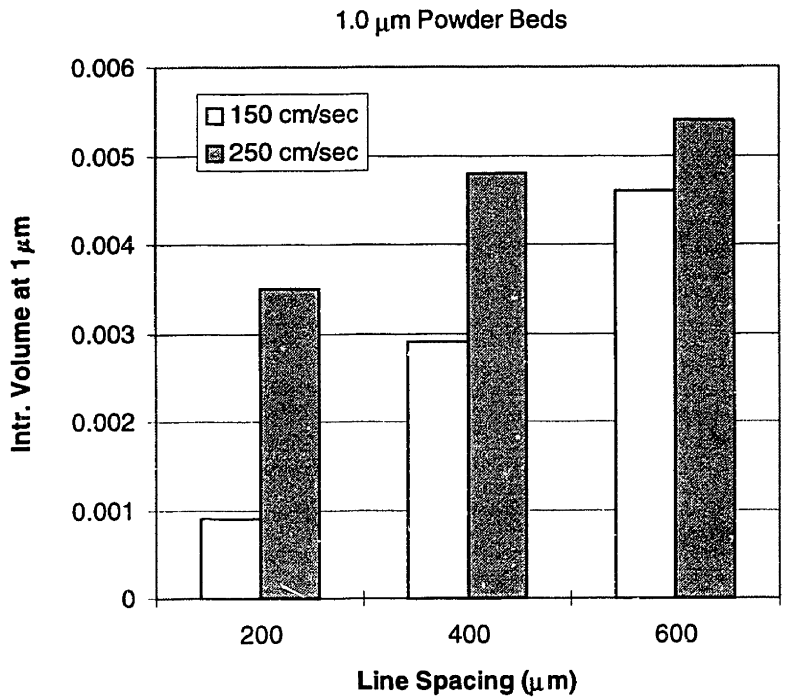

Figure 3.5. Effect of print speed and line spacing on the number of large pores in the powder bed.

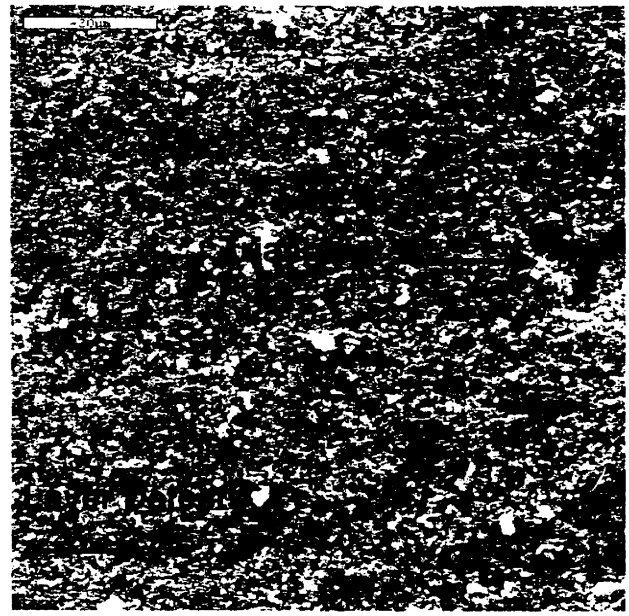

(A)

(B)

Figure 3.6. SEM X-section of slurry-jetted powder beds showing effect of line spacing (A) Triangular pores and defects observed at 500 μm line spacing (B) Uniform microstructure observed at 200 μm line spacing (APA-0.5 powder, 250 cm/sec print speed)

is shown. Defects along the layers are also evident. Figure 3.6B shows a 0.5 μm powder bed prepared with a line spacing of 200 μm. The microstructure is uniform and does not show any large, distinctive pores. Individual layers within the powder bed can not be distinguished.

Defects are introduced due to the manner in which lines of slurry merge with adjacent lines in the powder bed. Single lines of slurry form primitives with a crown-shaped cross-section due to differences in the rate of slip casting at the edges. The shape of a single line as it casts is shown schematically in Figure 3.7. Figure 3.7A shows the cross-section of the slurry line immediately after jetting. Liquid is drawn into the powder bed due to capillary pressure. The liquid flux is higher at the edges of the line, and the slip casting rate is higher at the edge. The higher liquid flux at the edges leads to increased casting and the crown shape of the solid cast line (Figure 3.7C). The relative dimensions of the line depend on slurry flow rate and solids loading, nozzle geometry, and print speed.

Jooho Moon performed a series of experiments to study how slurry-jetted lines merge together. Surface profilometry was used to examine adjacent line pairs deposited by slurry jetting. Line pairs were formed by rastering the slurry nozzle up and down the fast axis a single time. Figure 3.8 shows profilometry data for three sets of line pairs with varying line spacing. The line pair formed at a line spacing of 200 μm has a peak in the center of the profile. Slip casting of slurry-jetted lines is complete in approximately 50 milliseconds. Jetted lines slip cast before the adjacent line of slurry in the raster pattern is deposited. The width of single lines prepared under these conditions is greater than the 200 μm line spacing. The second line of slurry overlaps with the first line, and the peak in the center of the line pair is formed. The second graph shows a line pair formed at a line spacing of 250 μm. The profile shows a small valley between the first and second lines. There is also a smaller peak (relative to 200 μm line spacing) adjacent to the valley. The final graph shows the profile of a line pair formed with a line spacing of 300 μm. The profile shows two uniform lines with a large valley in between. There is little interaction between the lines since the line spacing is about the same width as the slurry line.

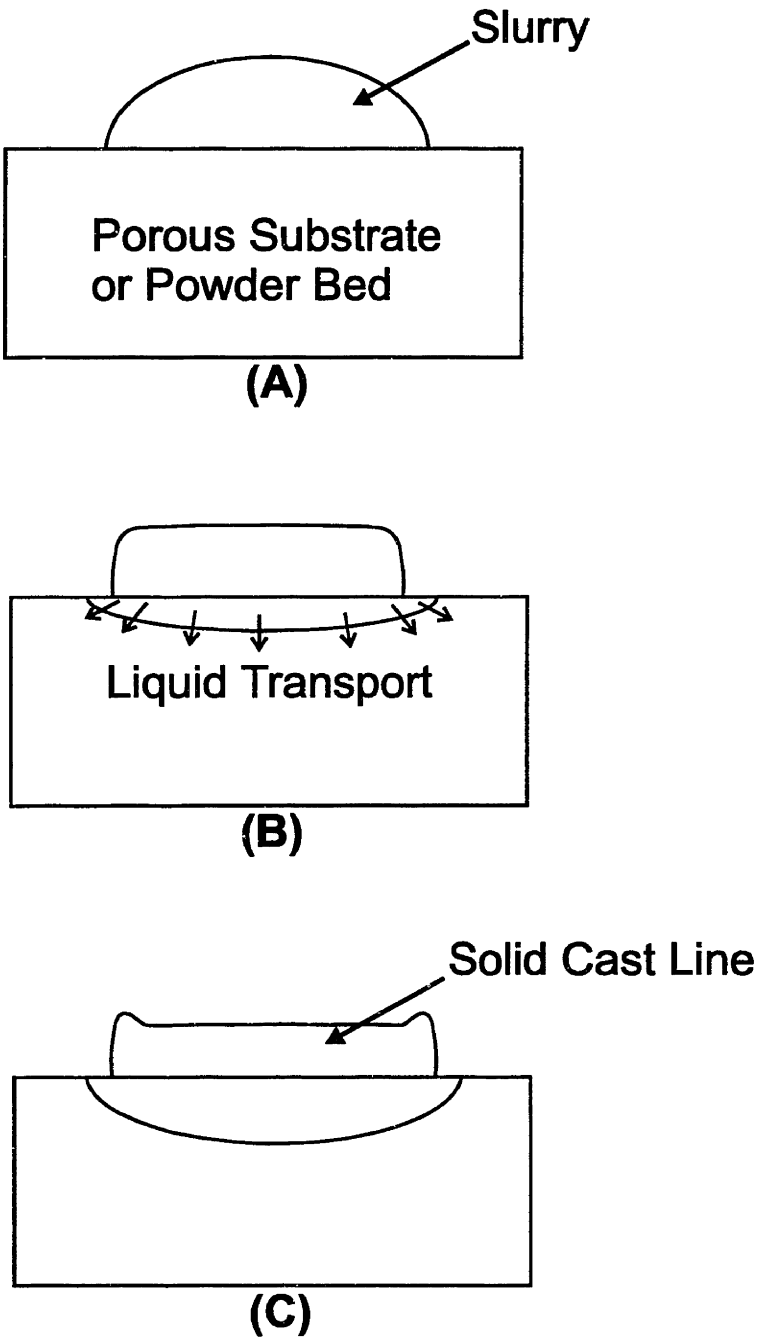

Figure 3.7. Cross-section of a line of slurry as it slip casts. (A) Slurry line immediately after jetting (B) Liquid migrates to the porous body from the slurry (C) Solid cast line after slip casting is complete

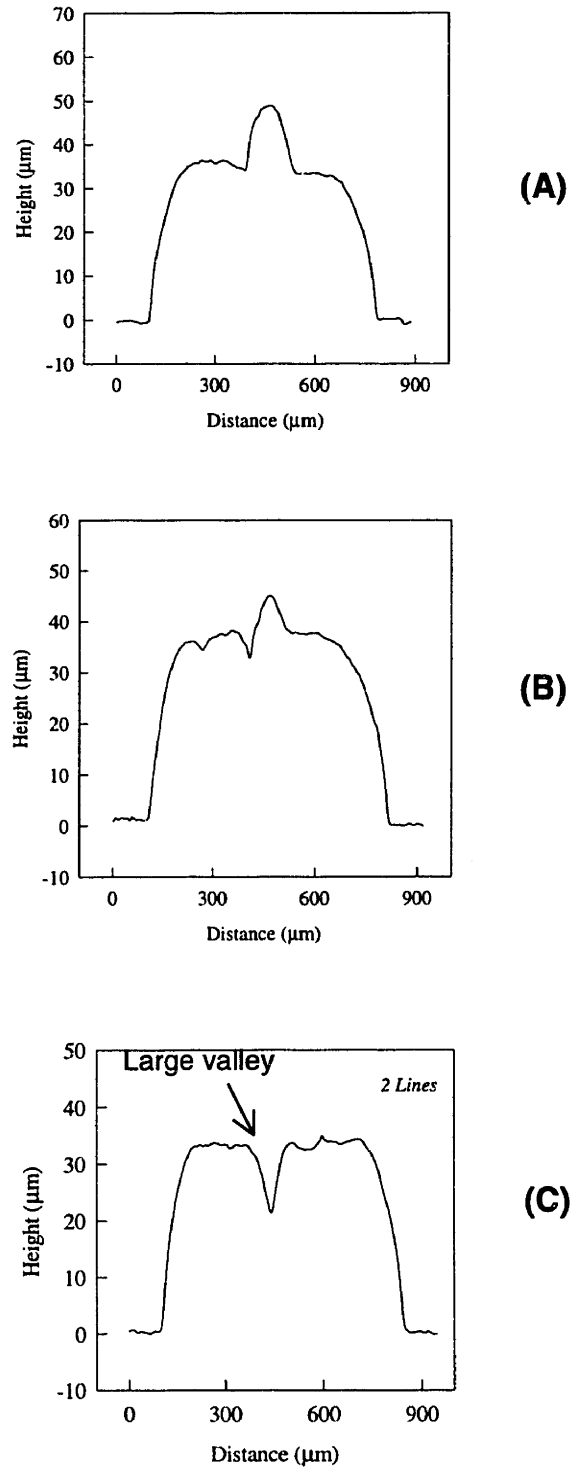

Figure 3.8. Surface profilometry of slurry-jetted line pairs at varying line spacings. A) 200 µm B) 250 µm C) 300µm

The distinctive triangular pores are the result of the raster pattern of the slurry nozzle and the manner in which lines of slurry merge. The raster pattern of jetted powder bed layers is shifted by one half of the line spacing for successive layers. The raster pattern is shown schematically in Figure 3.9. Each line of slurry is drawn as a cylinder for simplicity to illustrate how successive layers are deposited. The profilometry data indicate that large valleys are present between slurry lines deposited at large line spacings. The next layer of slurry will deposit a line directly over this valley. A void will be produced if the slurry does not perfectly fill the valley between slurry lines. The casting rate of the slurry is very high and allows very little time for the slurry to fill the valley. The slip casting essentially seals off the pore and prevents it from being filled by the slurry.

3.3.3. Sintered Powder Beds

Powder beds were fired in air at various temperatures to observe the densification and evolution of microstructure. The temperature of the furnace was increased at a rate of 10°C/minute up to the sintering temperature. The temperature was held for one hour at the sintering temperature and cooled to room temperature at a rate of 20°C/minute. The sintering temperatures that were examined were 1100, 1400, 1600, and 1650°C.

Densities of the samples were measured using Archimedes' method. SEM cross-sections were prepared by polishing the samples with 0.25 μm polishing abrasive. The samples were then thermally etched by firing the samples at a temperature 200°C below the sintering temperature for one hour.

Complete density data are listed in Table 3.3. The change in density versus sintering temperature for two jetted beds is shown graphically in Figure 3.10. The 0.5 μm powder bed was jetted at a speed of 250 cm/sec and a line spacing of 400 μm. The initial green density of the 0.5 μm jetted powder bed is slightly less than that of the slip cast bed. The sintered densities of the jetted bed and the slip cast bed converge at higher sintering temperatures. The densities of the beds after sintering at 1650°C are both very high, 99.0% (slip cast) and 98.7% (jetted).

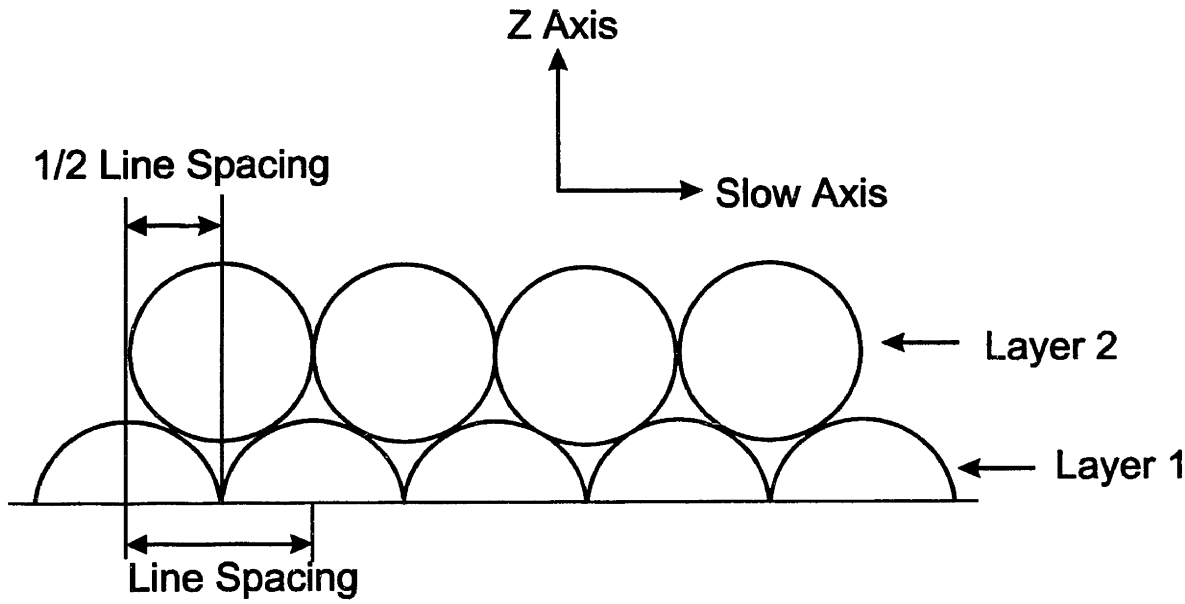

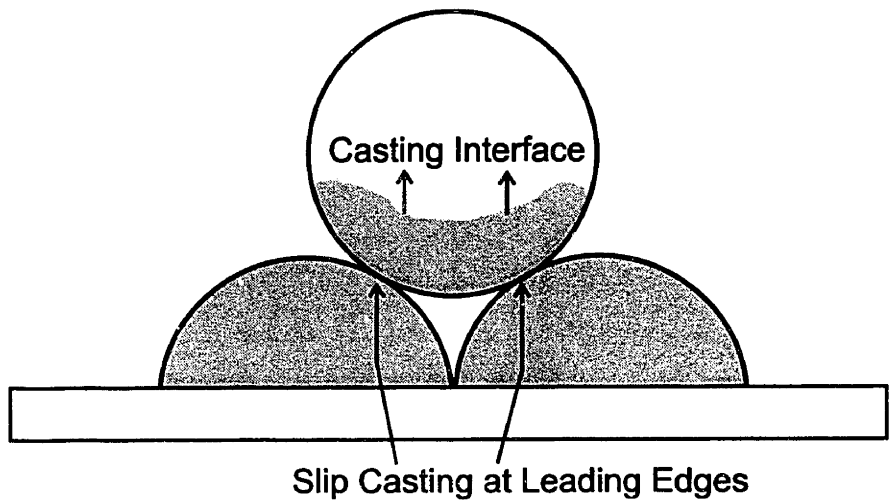

Figure 3.9. Staggered raster pattern used for creating slurry-jetted powder beds and schematic showing the formation of triangular pores.

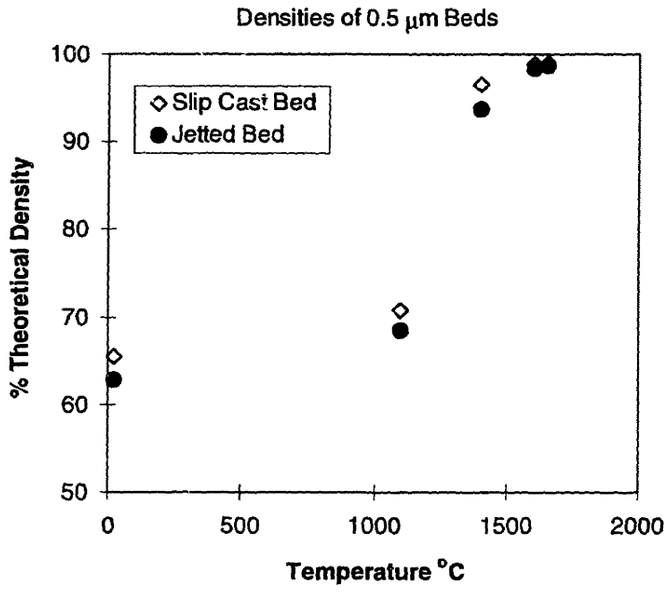

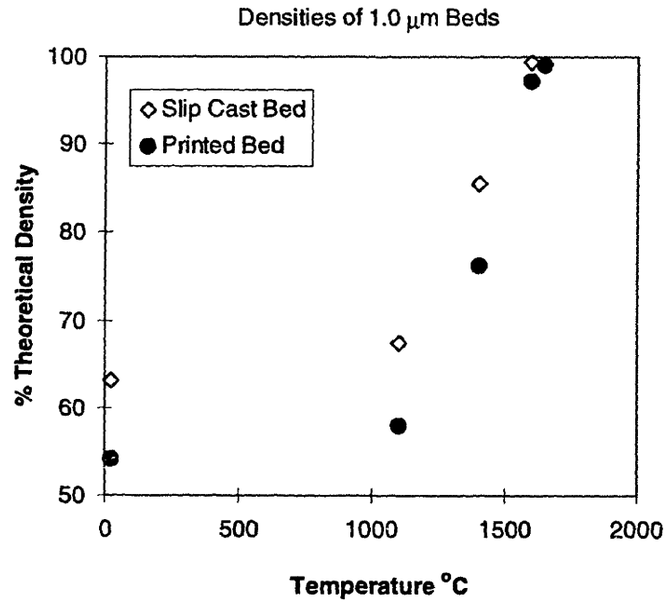

Figure 3.10. Effect of sintering temperature on density for powder beds prepared with 0.5 μm and 1.0 μm powder.

Table 3.3. Densities of sintered powder beds

Powder	Print Speed (cm/sec)	Line Spacing (μm)	Sintering Temp. (°C)	Density (% Theo.)
APA-0.5	250	300	1100	68.6
APA-0.5	250	400	1100	68.5
APA-0.5	250	500	1100	69.4
APA-0.5	200	300	1100	68.6
APA-0.5	250	400	1100	68.4
APA-0.5	Slip Cast	Slip Cast	1100	70.8
APA-0.5	250	400	1400	93.7
APA-0.5	Slip Cast	Slip Cast	1400	96.5
APA-0.5	250	400	1600	98.3
APA-0.5	Slip Cast	Slip Cast	1600	98.8
APA-0.5	250	300	1650	98.6
APA-0.5	250	400	1650	98.7
APA-0.5	250	500	1650	98.1
APA-0.5	Slip Cast	Slip Cast	1650	99.0
HPA-1.0	150	200	1100	59.1
HPA-1.0	150	400	1100	58.0
HPA-1.0	150	600	1100	57.5
HPA-1.0	Slip Cast	Slip Cast	1100	67.4
HPA-1.0	150	400	1400	76.2
HPA-1.0	Slip Cast	Slip Cast	1400	85.5
HPA-1.0	150	400	1600	97.2
HPA-1.0	Slip Cast	Slip Cast	1600	99.3
HPA-1.0	150	200	1650	98.9
HPA-1.0	150	400	1650	99.0
HPA-1.0	150	600	1650	98.9
HPA-1.0	Slip Cast	Slip Cast	1650	99.2

The green densities of jetted and slip cast powder beds prepared with 1.0 μm powder differed substantially. However, the sintered densities converged and reached very high values despite the discrepancy in green densities. The sintered densities of powder beds prepared with 1.0 μm powder were actually higher than 0.5 μm powder beds. The densities of slurry-jetted powder beds sintered at 1650°C are listed in Table 3.4. The densities of all powder beds approached 99% theoretical, even under conditions in which the population of large pores was high.

Table 3.4. Densities of powder beds sintered at 1650°C

Powder	Jetting Conditions	Density (% Theo.)
APA-0.5	250 cm/sec, 300 μm	98.6
APA-0.5	250 cm/sec, 400 μm	98.7
APA-0.5	250 cm/sec, 500 μm	98.1
APA-0.5	Slip Cast	99.0
HPA-1.0	150 cm/sec, 200 μm	98.9
HPA-1.0	150 cm/sec, 400 μm	99.0
HPA-1.0	150 cm/sec, 600 μm	98.9
HPA-1.0	Slip Cast	99.2

3.3.4. Sintered microstructures

Large pores were observed in SEM cross-sections of the sintered beds prepared by jetting. There was a strong correlation between the number of large pores observed in the sintered microstructures and the porosimetry data for the green parts. Figure 3.11 shows cross sections of 1.0 μm powder beds jetted at 150 cm/sec and sintered at 1650°C. The microstructures are fairly uniform with approximately 2 to 4 μm grain sizes. Some relatively large pores are observed in the cross sections. The number of large pores observed in the sintered microstructures increased as the line spacing of the raster pattern increased from 200 μm to 600 μm. Some of the large pores are aligned horizontally in the powder bed jetted at 600 μm. The large pores are probably the result of the defects that are generated by the jetting process.

Sintered cross sections of slip cast samples are shown in Figure 3.12. Some small porosity is observed. Abnormal grain growth is also evident, indicating the samples were over-fired. The sintering time or temperature was slightly too high for these samples.

(A)

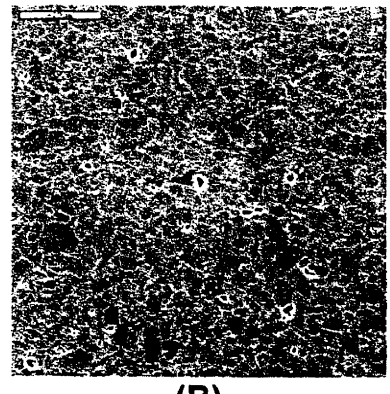

(B)

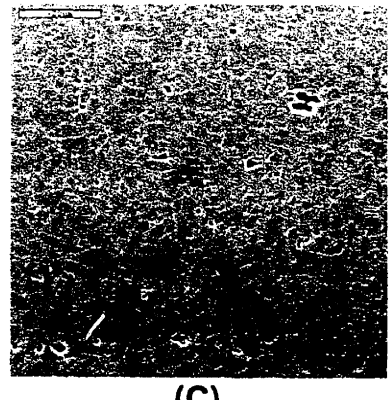

(C)

Figure 3.11. Microstructures of 1.0 μm jetted powder beds sintered at 1650°C. (A) 200 μm line spacing (B) 400 μm line spacing (C) 600 μm line spacing All powder beds were jetted at 150 cm/sec.

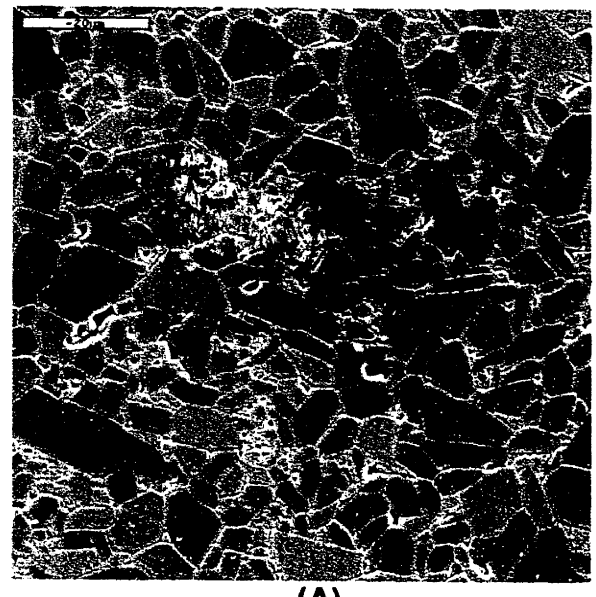

(A)

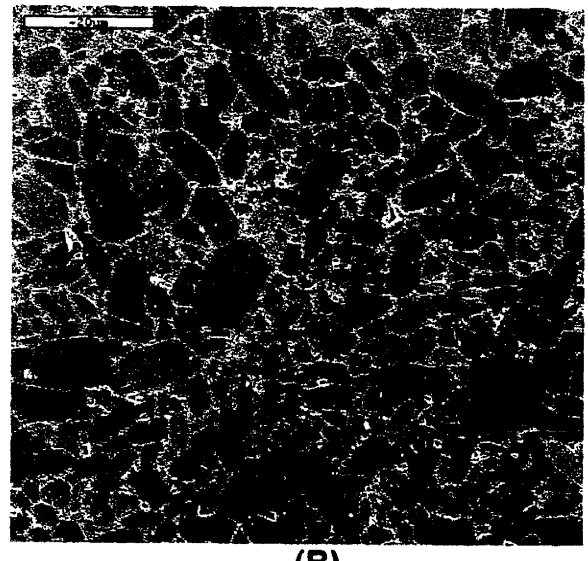

(B)

Figure 3.12. Slip cast samples sintered at 1650°C (A) 0.5 μm powder (B) 1.0 μm powder

Grains as large as 10 μm are present in both of these samples. There is very little difference in the sintered microstructures of the 0.5 μm and 1.0 μm samples.

3.4. Tape Casting

A modified tape casting process is another method that is currently being examined by Bjorn DeBear and Richard Holman for producing slurry-based powder beds. The tape casting set-up is shown schematically in Figure 3.13.[71] Slurry is deposited continuously between two blades that traverse across the powder bed. The front blade controls the size of the slurry pool in front of the second blade, the *doctor blade*. The height of the doctor blade controls the amount of slurry spread over the powder bed.

The tape casting method offers several advantages over the slurry jetting process. The speed of forming powder bed layers is increased substantially. The powder bed layers are formed with a single pass compared to rastering hundreds of times for the slurry jetting process. Propagation of bumps or defects in the powder bed is less likely since the doctor blade registers the height of the powder bed with each layer. The surface finish is also optically smooth.

Richard Holman[72] compared the microstructures of powder beds prepared by slurry jetting and tape casting. 30 volume percent 1.0 μm slurry was used for the study. The solvent of the slurry was a 3:2 ratio (by volume) water to methanol. The layer height was 100 μm for both powder beds. The green densities were 63.5% for the tape cast bed and 59.7% for the slurry-jetted bed. The powder beds were sintered for one hour at 1600°C. Sintered densities were 99.6% for the tape cast bed and 97.8% for the slurry-jetted bed. Figure 3.14 shows optical micrographs of the sintered beds using a Nemarski slide on the microscope. The Nemarski slide greatly enhances the contrast of surface features. The powder bed prepared by slurry jetting shows porosity aligned along distinct layers. The spacing between the layers of pores correlates with the spacing between layers. The powder bed prepared by tape casting does not indicate preferential alignment of the pores.

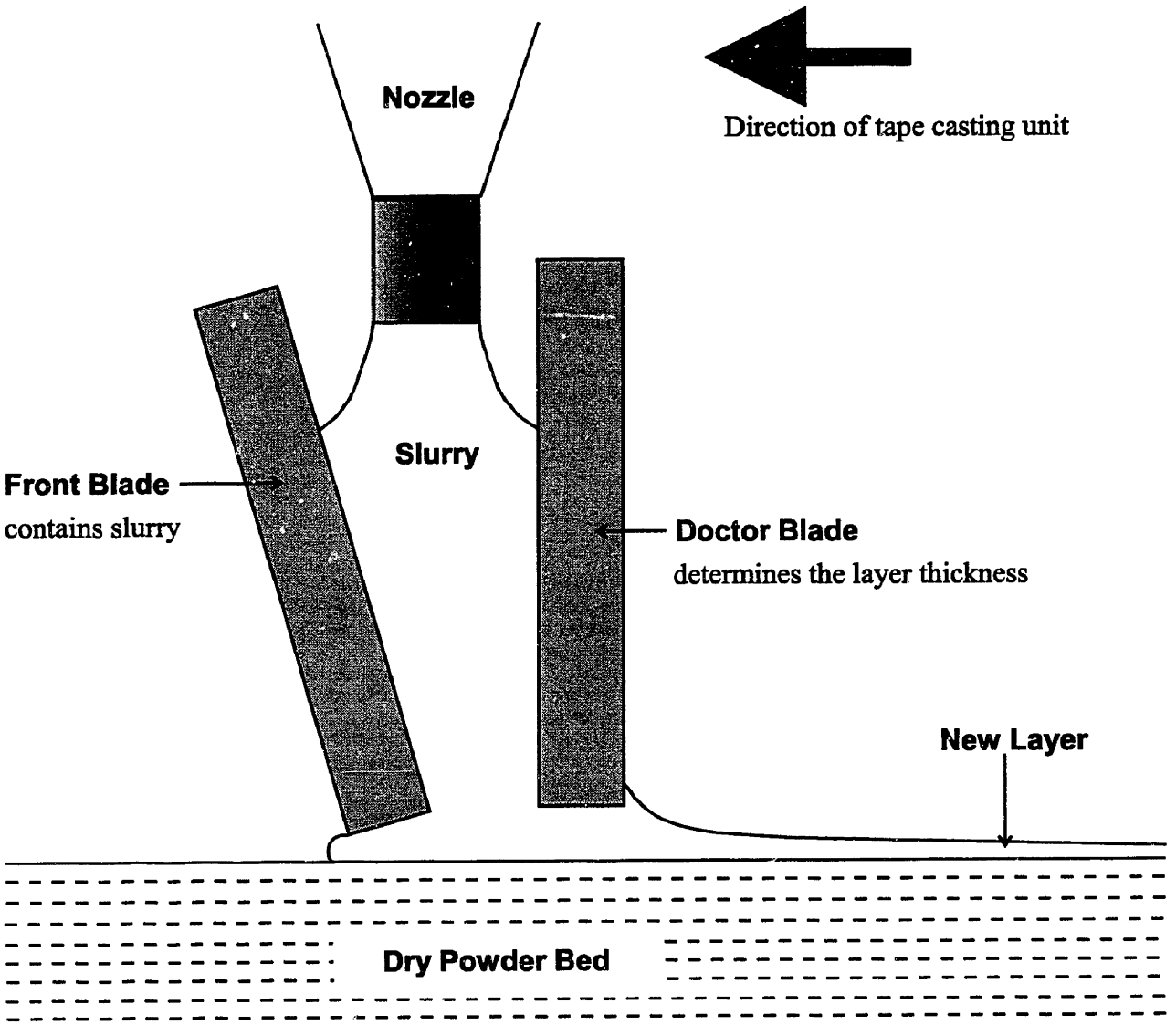

Figure 3.13. Schematic representation of the tape casting process for producing powder beds. (from DeBear)

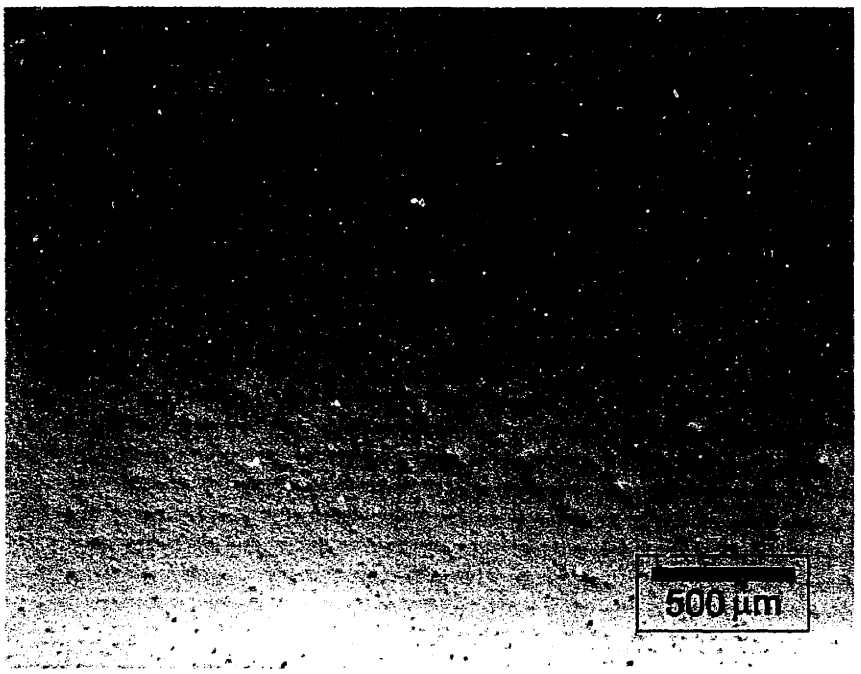

(A)

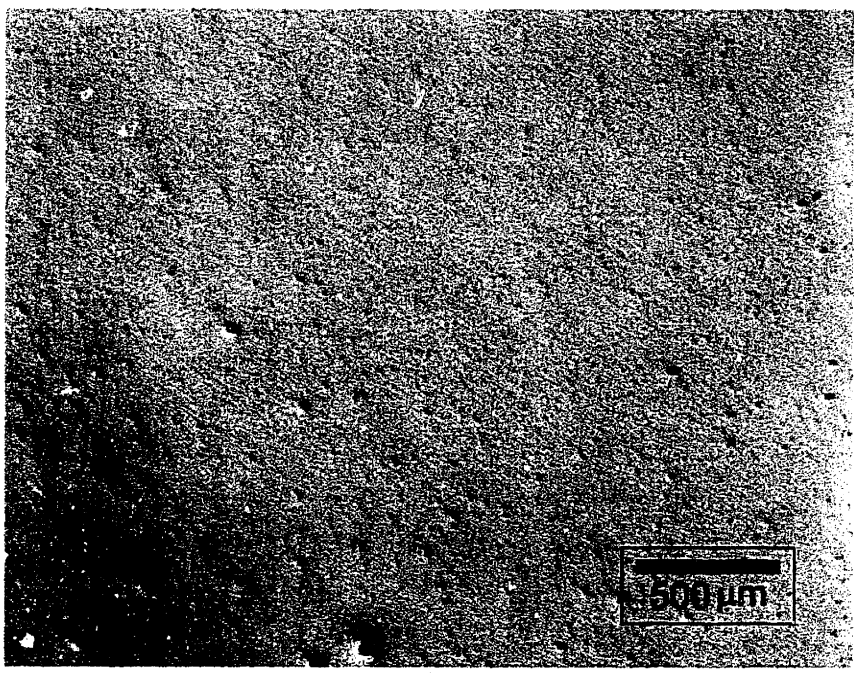

(B)

Figure 3.14. Optical micrographs of sinterered powder beds using Nemarski slide (A) Slurry-jetted powder bed (B) Tape cast powder bed

3.5. Conclusions

The slurry-based 3DP method is capable of forming uniform microstructures with high green density. By forming powder beds with a dispersed slurry, it is possible to form powder beds with very few intra-layer defects and no inter-layer defects.

Defects are generated when slurry interacts with the underlying powder bed in isolated areas. Defects were especially high in powder beds prepared by spray deposition. Individual droplets of slurry are deposited over a wide area using spray deposition. The individual droplets are able to cast before they merge with other slurry droplets. The powder bed is formed as the result of millions of small droplets of slurry casting on the powder bed. Every time a droplet impacts the powder bed, there is some probability that the droplet will not perfectly fill underlying surface roughness. Decreasing the solids loading of the slurry helped reduce the number of large pores since the slurry has lower viscosity. The slurry droplet also remains fluid for a longer time and there is a greater probability that droplets will merge before they cast.

Defects were reduced substantially with the slurry jetting process since the number of interactions between the slurry and underlying powder bed is reduced by orders of magnitude. Each layer of the powder bed is formed by aligning hundreds of slurry lines. There is also some probability of a defect each time a line of slurry impacts the adjacent lines of slurry. The number of defects produced by the slurry jetting process is dependent upon the line spacing. At small line spacings, slurry lines overlap and merge together. At large line spacings, the slurry lines are separated and leave a valley between adjacent lines. These valleys are not likely to be completely filled when the next layer of slurry is deposited.

The profile of slurry-jetted lines depends on numerous variables. The flow rate, print speed, slurry viscosity, slurry stability, solids loading, powder type, and the solvent in the slurry will all effect the geometry of jetted lines. It is impossible to give precise experimental parameters for *the* optimum powder bed microstructure. The parameters that optimize powder bed microstructure may also conflict with other aspects of the process such as controlling cracking or controlling slurry/binder interactions. (These aspects will be discussed in the next chapters.)

Defects in tape cast powder beds are the lowest since the slurry is deposited in a single pass. The surface of the powder bed is very smooth and reduces the chances of trapping voids and interlayer defects. Intra-layer defects are avoided since the slurry forms a continuous layer. Trapped bubbles within the slurry will lead to defects, but the microstructure of powder beds produced from preliminary experiments is very promising.

Propagation of errors is one final area of concern for the powder bed formation mechanism. Spray deposition and slurry jetting both propagate surface defects from one layer to the next. Height differences across the powder bed grow with successive layers as the powder bed is formed. Tape casting will substantially reduce, if not eliminate, the propagation of errors since the doctor blade defines a layer height.

CHAPTER 4
CONTROLLING CRACKING IN MULTI-LAYER CERAMIC BODIES

4.1. Introduction

The slurry-based 3DP process is one of a number of ceramic processes that utilize thin layers. Generating thin ceramic layers has been studied extensively for various ceramic applications. The tape casting process has been used for nearly 50 years for manufacturing ceramic sheets.[73,74] Multi-layer ceramic capacitors (MLC) and multi-layer ceramic packages (MLCP) are two devices in which ceramic tapes are stacked and laminated to form the component.[75] Laminated ceramics formed from tape cast sheets have also been studied for structural ceramic applications.[76,77] Hyatt[78] has reviewed the processes for making thin ceramics.

New processes for making multiple layer ceramics have also been reported recently. Mistler[79] has proposed a method for making high strength alumina substrates using a multiple-layer casting process. Willoughby and Evans[80] have also described a process very similar to the spray deposition process described in Chapter 3. They produced alumina and alumina-zirconia layers 20-30 μm thick using a conventional spray gun. Laminates as thick as 1 mm were produced with no evidence of inter-layer defects. However, they reported problems with cracking under certain conditions.

Cracks in the powder bed pose a major threat to the effectiveness of the slurry-based 3DP process. A single crack within the powder bed will destroy the printed component. The mechanisms responsible for cracking must be understood to increase the reliability of the process. The theory of cracking in ceramic bodies will be reviewed briefly. The source of cracking in slurry-based 3DP powder beds will be discussed, and approaches to avoid cracking will be presented.

4.2. Literature Review

Wet processing techniques enable fabrication of high green density ceramics with low defect concentrations. However, drying the cast body may lead to cracking and

warping. Cracks caused by drying stresses are often encountered in wet processing methods such as tape casting.[81,82] Scherer has presented a thorough review of drying with particular reference to the drying of gels.[83] Chiu and Cima studied the drying behavior of granular ceramic films on a rigid substrate.[84,85] They analyzed the fracture behavior of films assuming a biaxial stress develops due to the capillary tension in the pore liquid. In their study, the ceramic film was constrained by the rigid substrate, and the drying stress must be as high as the capillary pressure of the liquid.

Chiu and Cima argued that the tensile stress due to the capillary pressure acts on the entire film. The mechanics of cracking of thin films on rigid substrates was studied by Hu et al.[86] They suggest that a critical cracking thickness (CCT) exists where biaxially stressed films thicker than the CCT will crack. The CCT depends on the biaxial stress, σ, and the fracture resistance, K_c, of the film:

$$\mathrm{CCT} = \left(\frac{K_c}{1.4\sigma}\right)^2. \tag{4.1}$$

K_c for ceramic films is dependent upon the film composition and microstructure and may be increased by using organic binders. The magnitude of the biaxial stress, σ, is dependent on the capillary pressure, P_c, of the liquid. Capillary pressure for a cylindrical pore is:

$$P_c = \frac{2\gamma_{LV}\cos\theta}{r_{pore}}, \tag{4.2}$$

where γ_{LV} is the surface tension of the liquid, θ is the contact angle, and r_{pore} is the pore radius.

Chiu and Cima measured the drying stress directly. Observations of the measured drying stress were consistent with stress caused by capillary pressure. The stress decreased as γ_{LV} was lowered and r_{pore} was increased. Figure 4.1 shows measured values of the stress versus saturation, where saturation is defined as the percentage of porosity in the body that is filled with liquid. Maximum stress was observed when the saturation of the film was slightly less than 100%, and the liquid had just receded into the film.

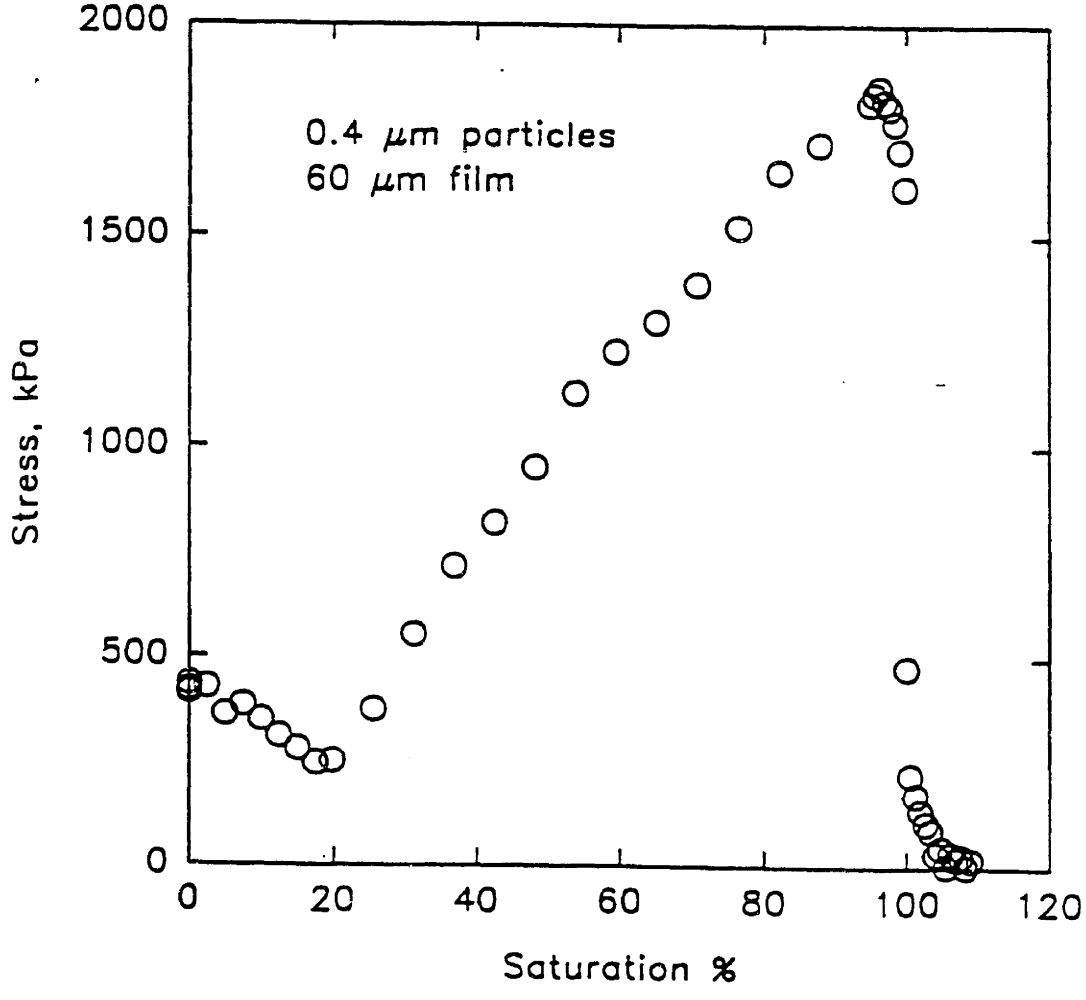

Figure 4.1. Stress versus saturation (Chiu)

Cracking was observed in films that were thicker than the CCT, and was observed near the time of the maximum drying stress when the drying rate was greater than 1×10^{-4} kg/(m^2·sec). They observed that the CCT for alumina films varied nearly linearly with the average particle size.

The cracking theory proposed by Chiu and Cima suggests two routes for increasing the critical cracking thickness of ceramic films: increasing the toughness of the ceramic layer or reducing the capillary stress. Lowering the surface tension of the solvent or increasing the pore size can reduce the capillary stress. The toughness can be increased substantially by using organic binders. Relatively thick tape cast layers can be formed because of large volume fractions of binder in the tape.

Increasing the strength of the powder bed by adding an organic binder is not feasible for the slurry-based 3DP process since 3DP relies on placing the binder selectively to define the geometry of the part. The redispersion behavior also depends on weak particle-particle contacts.

4.3. Experimental Procedure

Powder beds were prepared using the slurry-jetting process described in Chapter 3. A 127 μm alumina nozzle was used for all experiments. All slurries were electrostatically-stabilized with nitric acid. Ceralox HPA-1.0 and APA-0.5 alumina powders were used for the powder beds. Triton X-100 nonionic surfactant and methanol were also used in selected slurries. The solids fraction of alumina in the slurry was varied from 0.15 to 0.42. 2 weight percent PEG was used in all of the slurries. PEG is a viscous liquid at this molecular weight. Preliminary experiments indicated that PEG did not affect the strength of the powder bed. The slurry was ball-milled for a minimum of 48 hours with alumina milling media.

The experimental variables that were examined were slurry composition, powder type, slurry solvent, and the amount of slurry deposited per layer. The amount of slurry deposited onto the substrate was controlled by varying the slurry flow rate, line spacing of the raster pattern, and print speed. The powder bed was dried by heating with a 500 W

lamp for 45 seconds. The surface temperature of the powder bed was ~115°C after this time. The layer deposition process was repeated several times to build up the ceramic body.

The thickness of the deposited slurry (t_{slurry}) and the thickness of the dried powder bed layer (t_{layer}) can be calculated using mass balance relationships:

$$t_{slurry} = \frac{\text{Slurry flow rate}}{\text{raster line spacing} * \text{raster velocity}} \tag{4.3}$$

$$t_{layer} = t_{slurry}\left(\frac{\text{solids fraction of the slurry}}{\text{packing fraction of the powder bed}}\right) \tag{4.4}$$

The calculated total thickness of the powder bed is simply a summation of t_{layer} for each of the layers. The packing fraction of the powder bed varied from ~0.55 to 0.65 depending on the deposition conditions and powder type. The average packing fractions were 0.62 ± 0.02 and 0.57 ± 0.03 for APA-0.5 and HPA-1.0 powder beds, respectively. These packing fractions will be used for all necessary calculations in this chapter.

4.4. Experimental Observations

Powder beds were formed with varying slurry-jetting conditions and solids fractions in the slurry. The slurry lines jetted onto the porous powder bed quickly slip cast during the slurry-jetting process. The freshly jetted surface was specularly reflective due to the reflected light from the liquid in the slurry. The liquid was quickly drawn into the dry, porous medium below the layer due to capillarity. The powder bed surface was then opaque.

Cracking was observed in several powder beds formed from 0.5 μm alumina. Cracks were often very small and difficult to detect in poor lighting. In powder beds that cracked, the initial cracks were noticed just after the liquid disappeared from the surface. This should be the point of maximum capillary stress as the liquid interface is drawn into the body. The liquid from the jetted slurry infiltrated into the powder bed in less than 5 seconds in all cases, typically much less than 1 second.

Table 4.1 lists some representative deposition conditions. Cracking did not strictly correlate with t_{layer} to define a CCT for the powder bed. Rather, the cracking behavior was strictly dependent upon the amount of liquid that was deposited and the type of powder that was used. A new variable, saturation thickness, was defined to capture the effect of the amount of liquid present. The saturation thickness, t_{sat}, is the thickness of the region that would be 100% saturated by a given volume of liquid. (Figure 4.2)

$$t_{sat} = t_{slurry}\left(\frac{\text{Liquid fraction of the slurry}}{\text{Pore fraction of the powder bed}}\right) \tag{4.5}$$

Table 4.1. Selected jetting conditions and observations for depositing powder beds

Powder Size (μm)	Slurry Solids Fraction	Slurry Flow Rate (mL/min)	Raster Speed (m/sec)	t_{layer}	t_{sat}	Observation
0.5	0.40	1.3	1.5	48	108	Cracked after 7 layers
0.5	0.40	1.3	0.8	45	102	Cracked after 5 layers
0.5	0.20	2.5	1.5	31	185	Cracked after 2layers
0.5	0.35	2.0	2.0	19	54	No cracks after >50 layers
1.0	0.35	2.0	2.5	52	144	No cracks after >150 layers

Graphs of the total thickness of the powder bed versus saturation thickness were compiled from powder beds formed with varied solids loading, raster line spacing, print speed, and slurry flow rate. Figure 4.3 shows the data for beds made with 0.5 μm alumina powder. The open circles represent layers in the powder bed that did not crack during the deposition process. Crosses represent layers of the powder bed that cracked. Powder beds formed at high saturation thicknesses inevitably cracked before the total thickness exceeded 400 μm. Crack-free powder beds were formed when the deposition conditions yielded low saturation thickness. A critical saturation thickness (CST) exists which is analogous to the CCT observed by Chiu and Cima for ceramic films. The

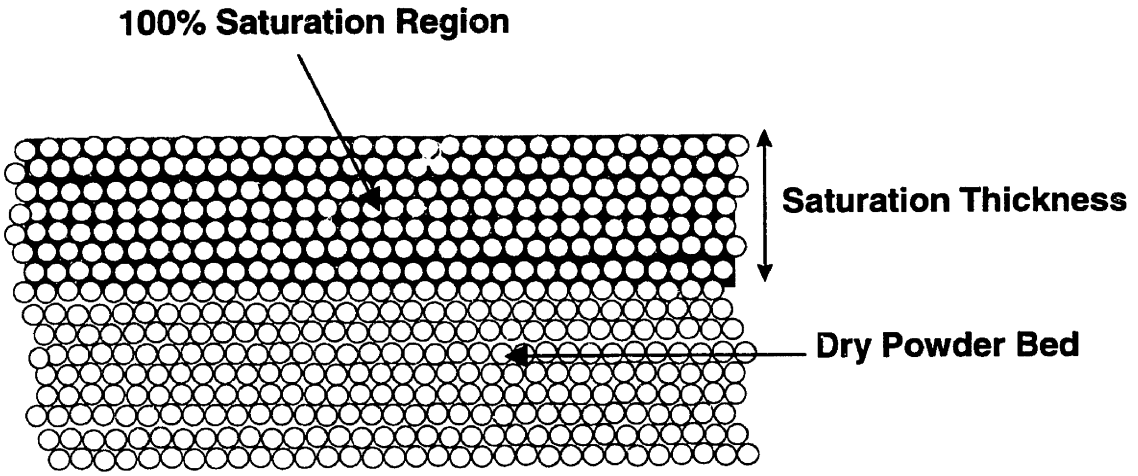

Figure 4.2. Schematic representation of the saturation thickness, t_{sat}, in a porous powder bed

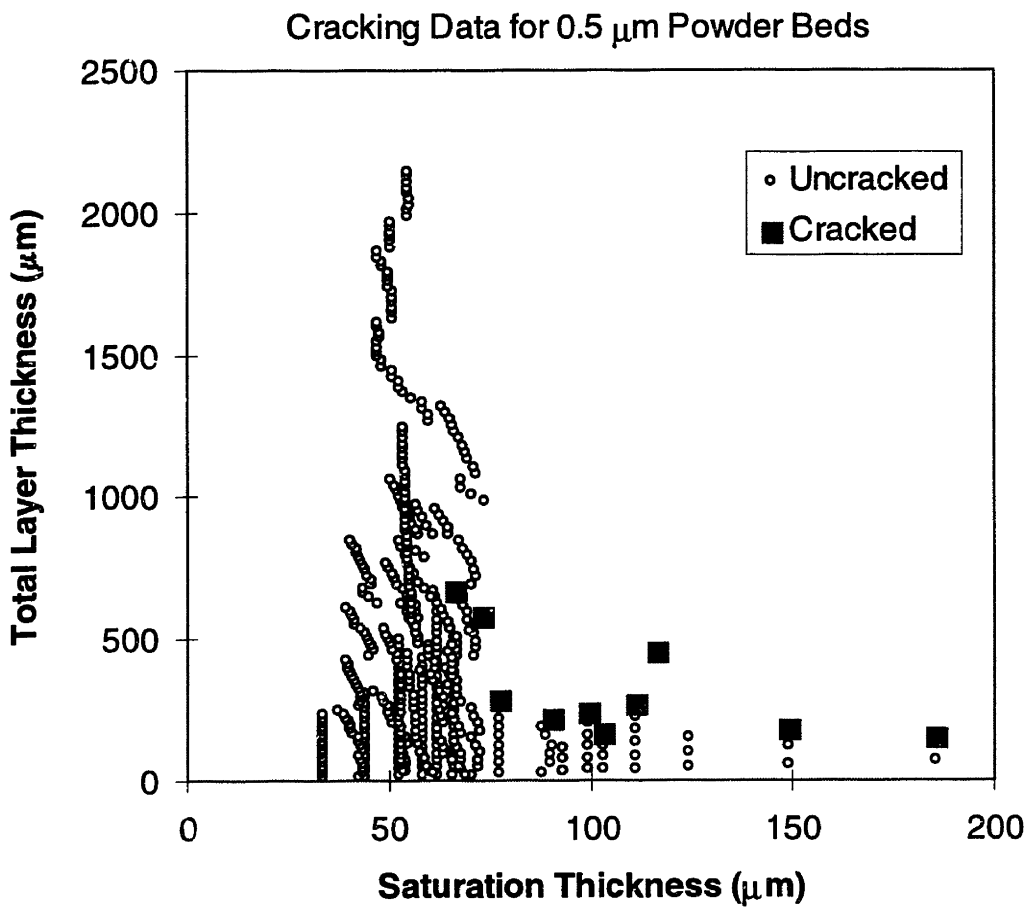

Figure 4.3. Effect of saturation thickness on the cracking behavior of 0.5 μm powder beds. Critical saturation thickness is about 65 μm.

critical saturation thickness for 0.5 μm powder was ~65 μm. This value is close to the CCT's reported by Chiu and Cima.

4.4.1. Impact of Powder Size

Figure 4.4 is a graph of total thickness of the powder bed versus saturation thickness for powder beds formed from 1.0 μm powder. Powder beds formed from 1.0 μm powder only cracked at very high saturation thickness. The critical saturation thickness was about 350 μm. This is inconsistent with Chiu and Cima's observation of a linear relationship between CCT and particle size. The capillary pressure may vary by more than a factor of 2. The fracture resistance of the powder beds also may not follow the relationship $K_c \propto d^{-1/2}$ as proposed by Kendall[87] for the fracture resistance of powder agglomerates.

4.4.2. Impact of Liquid Surface Tension

Surface tension of the liquid was reduced by using a water/methanol mixture for the slurry. Figure 4.5 indicates that powder beds prepared from slurries containing a four to one ratio of water to methanol in the solvent displayed a critical saturation thickness of ~95 μm. The surface tension of methanol/water solutions at 20°C is shown in Figure 4.6. Pure water has a surface tension of 72 dynes/cm while the surface tension of a 20 volume % solution of methanol is ~50 dynes/cm. Substituting these values into equations (4.1) and (4.2) suggests that the CCT should increase by about a factor of 2 with 20 volume % methanol, all else equal.

Surface tension of the liquid was also reduced using a surfactant. Triton X-100 (Aldrich Chemical Company, Milwaukee, WI) was added to the slurry to form an 0.1 weight % solution based on the amount of liquid. The surface tension of water was reduced from 72 to 32 dynes/cm with the addition of the surfactant. Figure 4.7 demonstrates the effect of adding surfactant to 0.5 μm slurry to reduce surface tension of the liquid. The CST of powder beds prepared with the surfactant increased to ~95 μm.

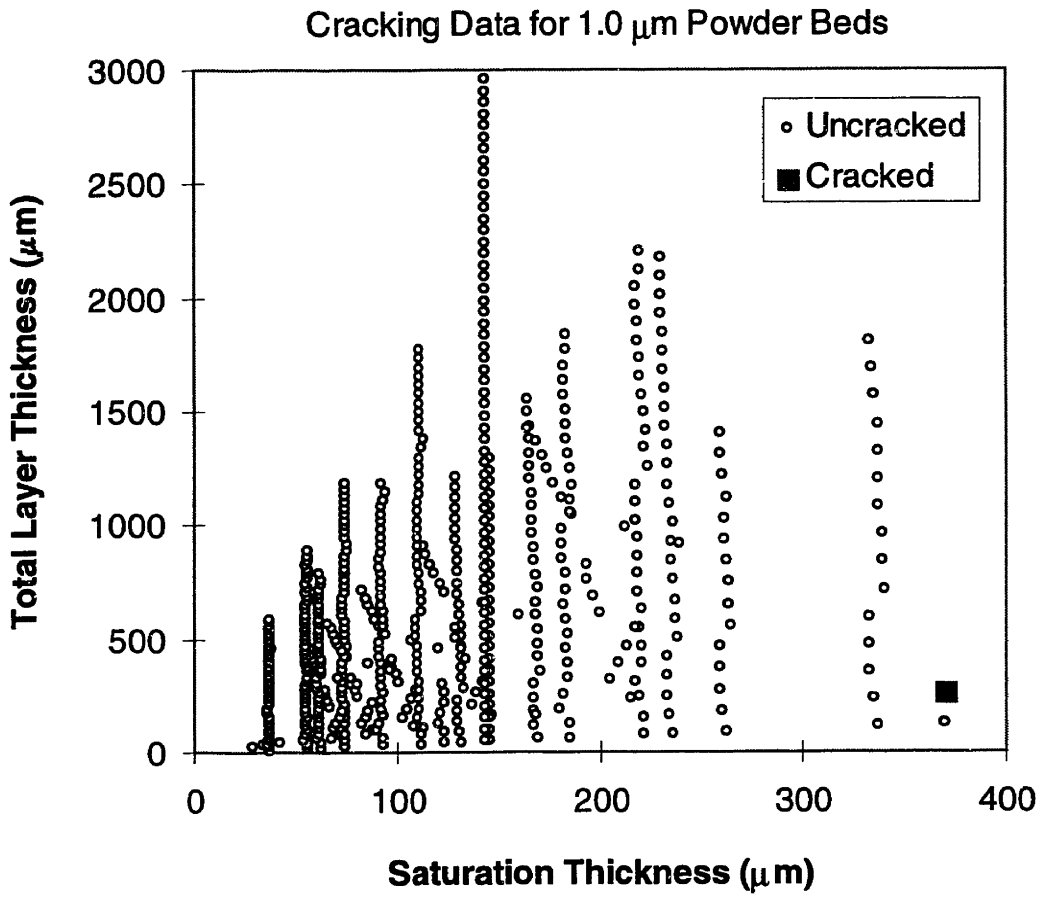

Figure 4.4. Total layer thickness versus saturation thickness for 1.0 μm powder.

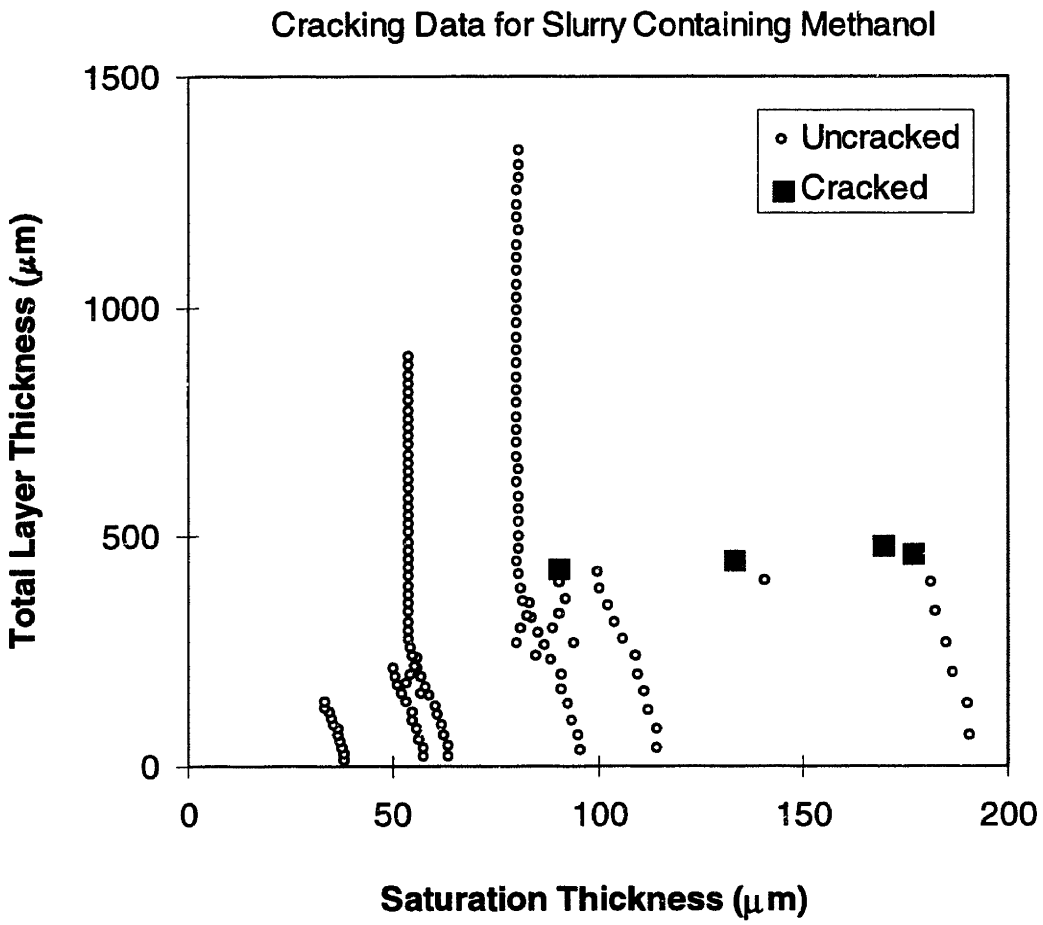

Figure 4.5. Effect of saturation thickness on cracking behavior of 0.5 μm powder beds with 4:1 water to methanol. Critical saturation thickness is ~95.

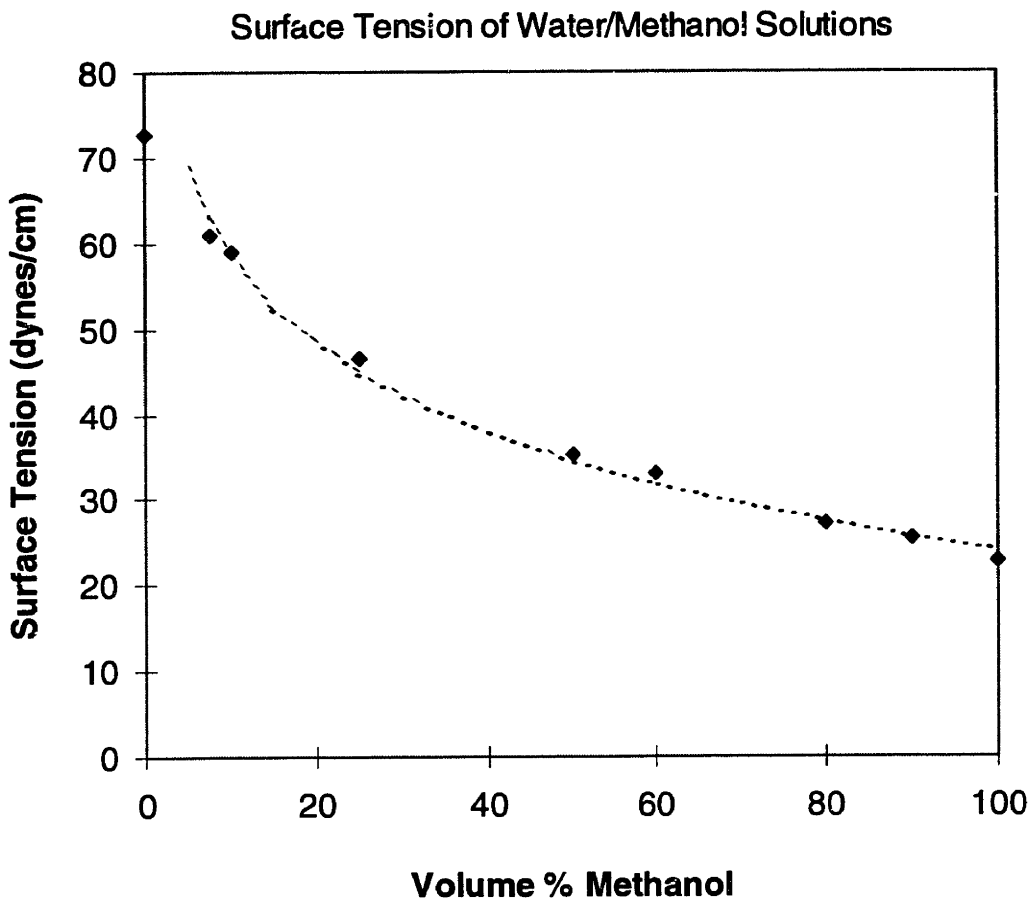

Figure 4.6. Surface tension of methanol/water solutions at 20°C

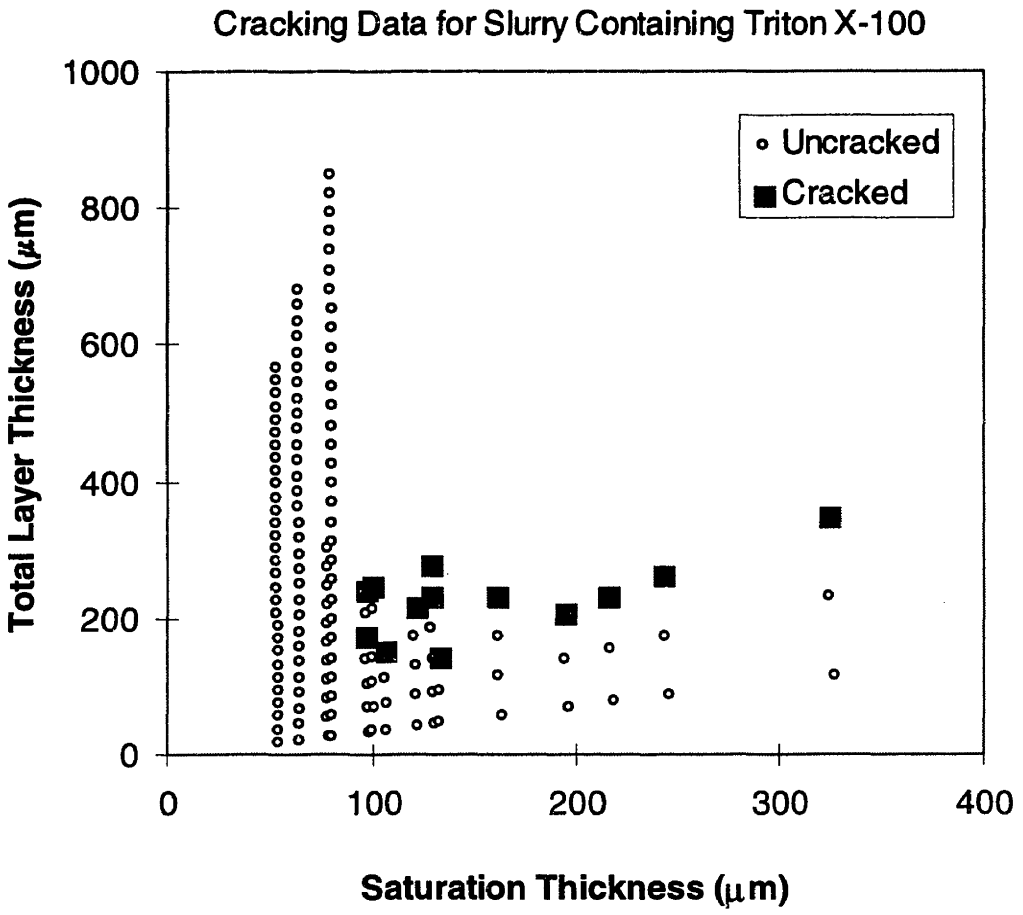

Figure 4.7. Cracking behavior of 0.5μm powder beds with 0.1% Triton X-100 added to the slurry.

This is about a 50% improvement compared to powder beds formed with no surfactant. The magnitude of the improvement is lower than the improvement that would be expected by a 56% reduction of the surface tension. However, interactions between the surfactant and the alumina may reduce the fracture resistance of the powder bed as reported by Chiu and Cima. Also, microscopic bubbles were observed occasionally in the powder bed due to the foaming nature of the surfactant. These voids could further weaken the powder bed.

4.4.3. Impact of Liquid Distribution

The effect of liquid distribution in the powder bed was also studied by jetting one layer, waiting for 30 seconds and then jetting a second layer without drying the previous layer. The saturation thickness for this two stage jetting process was calculated by adding the saturation thickness for each of the two layers. Figure 4.8 indicates that the critical saturation thickness is about 110 μm, nearly double the CST for jetting powder beds with a single pass. The top region of the powder will be nearly 100% saturated shortly after depositing the first slurry layer. As the liquid continues to infiltrate into the dry regions of the powder bed, the saturation near the surface will decrease. The liquid from the first pass is distributed within the powder bed prior to jetting the second layer of slurry.

4.4.4. Effect of Saturation Thickness on Microstructure

High density, crack-free powder beds were repeatedly formed with 0.5 μm powder by controlling the slurry deposition parameters and maintaining the saturation thickness below 65 μm. Figure 4.9 shows SEM micrographs of cross sections of powder beds prepared with low and high saturation thicknesses. The powder bed prepared by maintaining a low saturation thickness displays a uniform microstructure with no apparent cracks or lamination defects. However, the powder bed prepared with high saturation thickness displays large cracks.

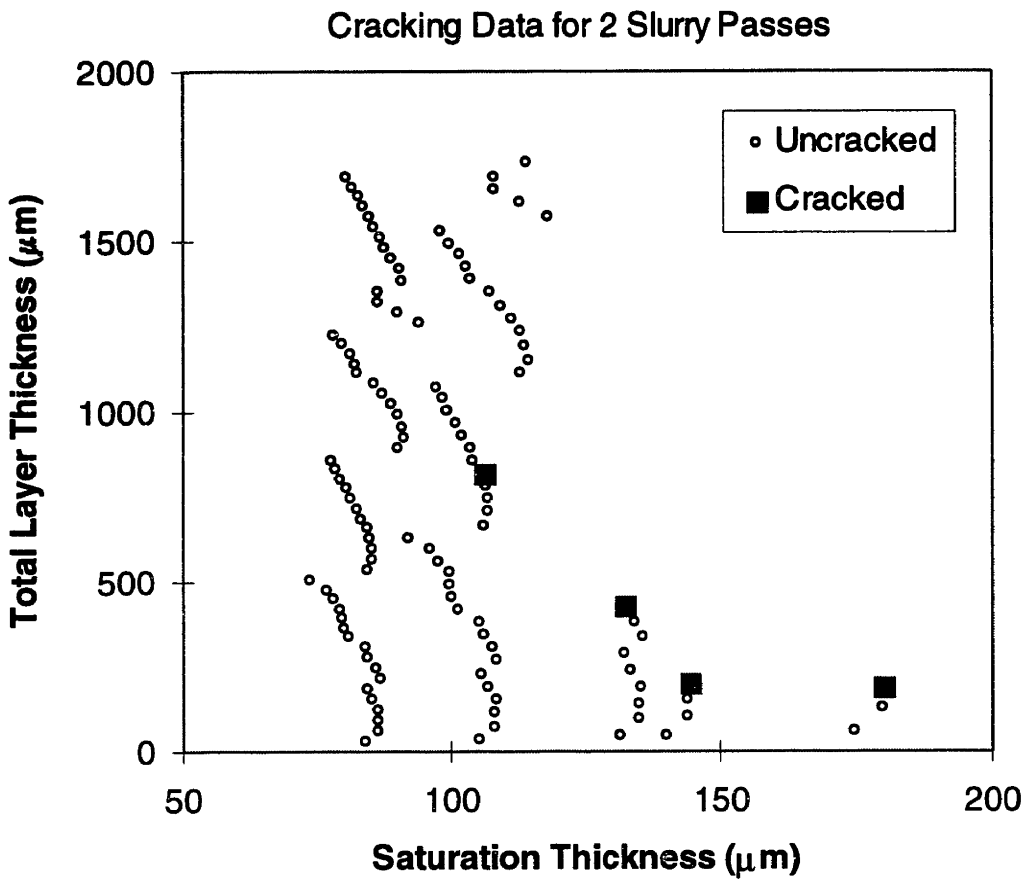

Figure 4.8. Cracking behavior of 0.5 μm powder beds formed with two slurry jetting sequences.

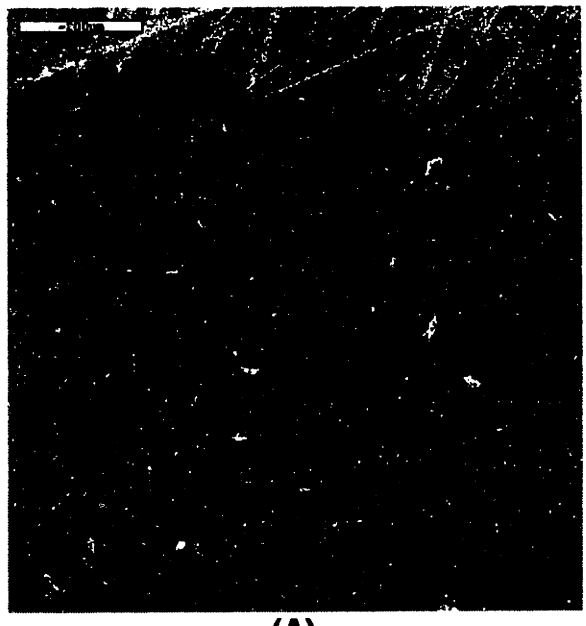

(A)

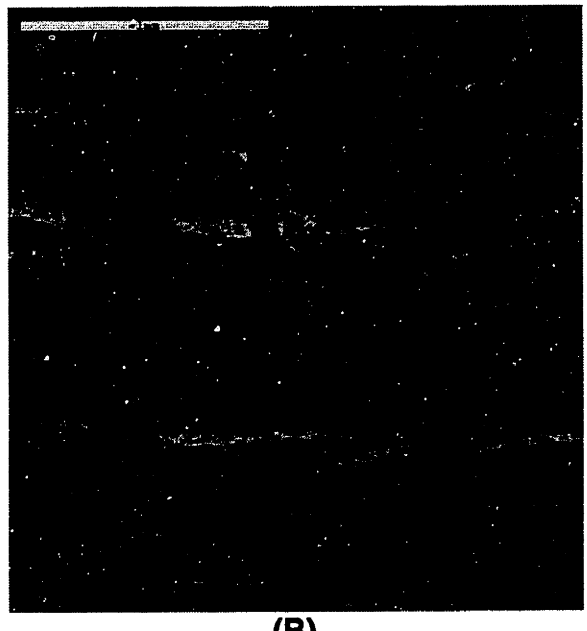

(B)

Figure 4.9. SEM micrographs of 0.5 μm powder bed cross-sections

A. Deposition conditions with low saturation thickness result in uniform, crack-free powder beds (t_{layer} = 19 μm, t_{sat} = 54 μm)

B. Deposition conditions with high saturation thickness result in cracked powder beds (t_{layer} = 63 μm, t_{sat} = 175 μm)

4.5. Determining Slurry Jetting Conditions

The cracking behavior of the powder bed constrains the range of the jetting variables. The layer height of 3DP powder beds needs to correlate with the height of the layer slice from the CAD model. The layer height is generally chosen to meet the constraints of build rate and surface finish. The slurry solids loading is variable over a relatively narrow range. The upper limit of solids loading is determined by the slurry viscosity. Viscosity increases rapidly as the solids loading increases above 40 volume percent. The lower limit of the slurry solids loading is fixed by the build rate. The build rate goes to zero as solids loading approaches zero. The flow rate through a specific nozzle may vary by about a factor of two or three. The slurry jet will not be a continuous stream at low flow rate. As a result, each nozzle diameter has a practical range for the flow rate of a specific slurry. The line spacing and print speed are variable over wide ranges.

Equations (4.4) and (4.5) can be used to calculate the layer height and saturation thickness produced under different jetting conditions. The layer thickness and saturation thickness are plotted as a function of line spacing in Figure 4.10. (The flow rate is 2.0 cm^3/min, and the print speed is 150 cm/sec.) The line spacing must exceed about 500 μm for the saturation thickness to fall below 65 μm for 40 volume percent slurry. The line spacing would have to greater than about 680 μm for 20 volume percent slurry. The saturation thickness increases with decreasing solids loading in the slurry while the layer height decreases with decreasing solids loading.

The maximum layer thickness that can be formed without intermediate drying is fixed by the critical saturation thickness. The maximum layer thickness can be calculated by setting equation (4.4) equal to the CST. Solving for t_{slurry} and substituting into equation (4.5) yields the maximum layer thickness:

$$t_{layer}(\max) = CST\left(\frac{\text{solids fraction of the slurry}}{1-\text{solids fraction of the slurry}}\right)\left(\frac{1-\text{packing fraction of the powder bed}}{\text{packing fraction of the powder bed}}\right). \qquad (4.6)$$

Figure 4.11 shows the maximum layer thickness that can be formed as a function of the solids loading of the slurry for different CST's.

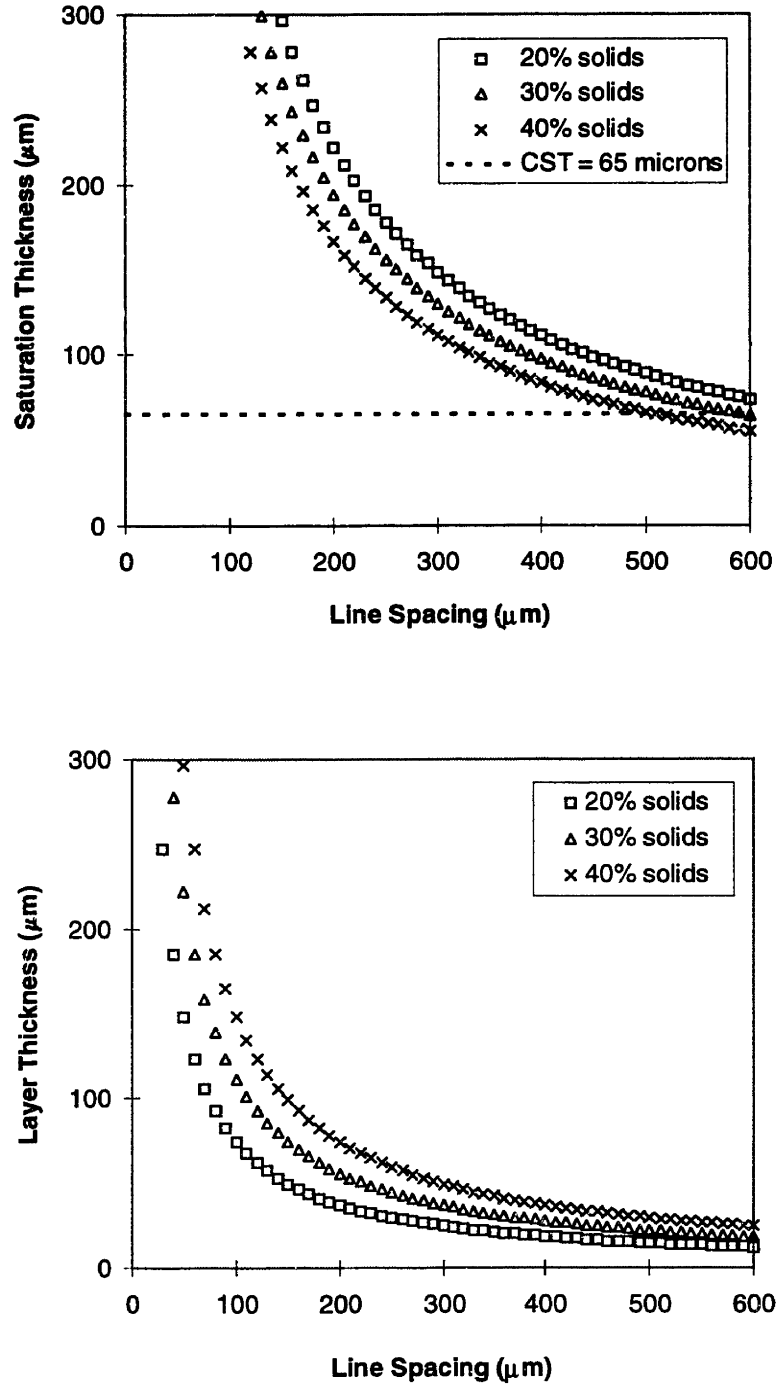

Figure 4.10. Layer thickness and saturation thickness calculations for jetted powder beds (Flow rate: 2cm^3/min, Print speed: 150 cm/sec)

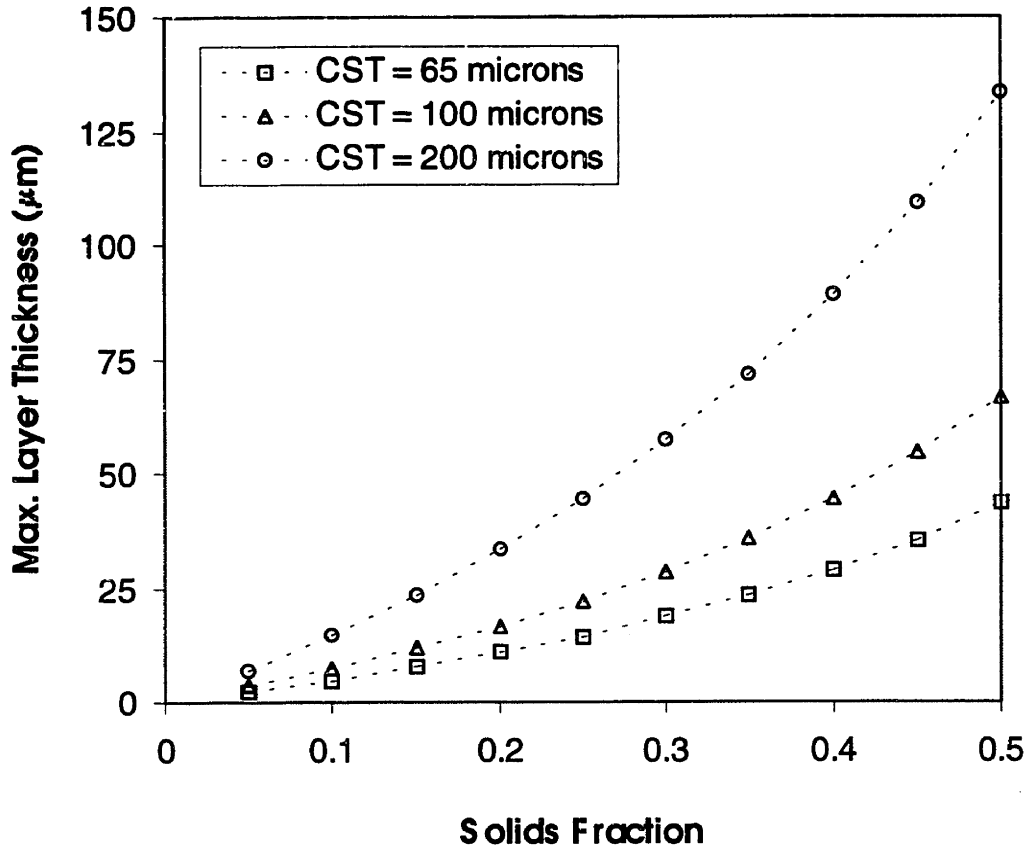

Figure 4.11. Maximum layer thickness that can be formed without intermediate drying.

4.6. Discussion

The migration of liquid and capillary stress in porous bodies has been reviewed by several authors.[88,89,90] Most of these liquid transport models use a continuum approach for liquid migration which is insufficient for the small scale we are observing here. The packing fraction and pore size of the powder bed vary with the jetting conditions. Powder bed microstructure is also very sensitive to any additives, such as surfactants. Despite these complexities, controlling the magnitude of the capillary stress appears to be the key to forming crack-free powder beds using the slurry-based process.

A qualitative model will be used to visualize the saturation and capillary stress within the powder bed. The capillary stress in this process results from the infiltration of the liquid from the freshly-jetted slurry into the previously dry powder bed. (Figure 4.12) At very short times the liquid will be concentrated in a narrow band near the surface of the powder bed. The saturation will be near 100% in this region, and the thickness of the saturated region, h, will be very close to t_{sat}. Therefore, t_{sat} is approximately the thickness over which the capillary stress acts just after jetting the slurry. The capillary stress is at a maximum near this point of 100% saturation. This correlates well with the observation that cracking occurred just as the liquid in the slurry receded into the powder bed. This system can now be treated as a stressed film of thickness t_{sat} on top of a dry powder bed that behaves like a rigid substrate. These assumptions make it possible to use Chiu and Cima's analysis by replacing the critical cracking thickness with the critical saturation thickness.

The saturation profile within the powder bed is time-dependent. At very short times, the liquid is concentrated near the surface of the powder bed. However, the saturation near the surface will decrease as the liquid migrates into the powder bed. This fact may explain the observed increase in the CST when the slurry was jetted a second time thirty seconds after the first layer of slurry was jetted. The liquid from the first layer of slurry is able to redistribute itself throughout the powder bed before the next dose of liquid arrives. The thickness of the region near 100% saturation will be much smaller than in the case where the same amount of liquid is deposited in a single dose.

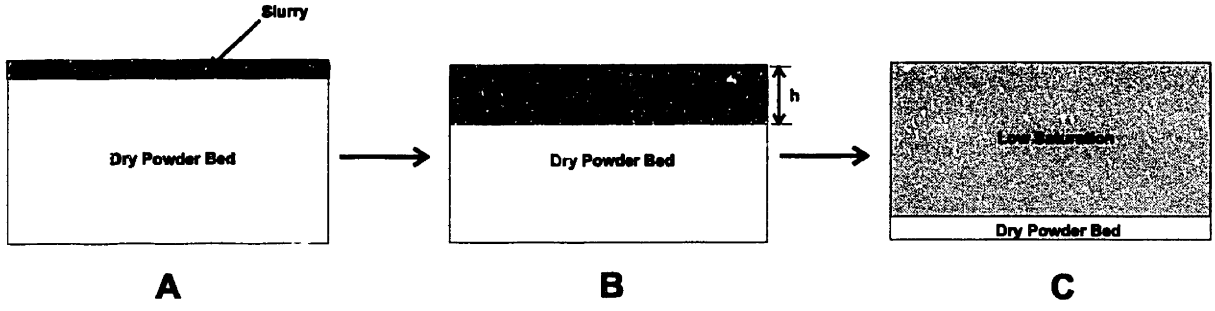

Figure 4.12. Schematic representation of liquid infiltration into the powder bed. A. Slurry is sprayed onto the initially dry powder bed. B. A region of thickness h is near 100% saturation at very short time. C. The liquid redistributes itself at long time to form a low saturation region.

Larger pore size will reduce the capillary stress, but it may also have a significant impact on the saturation profile within the powder bed. Washburn's equation implies that the liquid transport rate in a capillary is proportional to pore size:

$$\frac{dl}{dt} = \frac{r_c \gamma_{LV} \cos\theta}{4\eta l}, \tag{4.7}$$

where l is the length of the capillary, r_c is the capillary radius, γ_{LV} is the surface tension of the liquid, θ is the contact angle, and η is the viscosity of the liquid. This may account for the differences in cracking behavior between 0.5 μm and 1.0 μm powder beds. The permeability of 1.0 μm powder beds is higher and may be able to redistribute the liquid more quickly within the powder bed.

The observed critical saturation thickness for 1.0 μm powder beds is probably artificially high as determined by these experiments. Hundreds of lines of slurry are jetted to form the powder bed. The liquid from the first line may have sufficient time to be distributed throughout the powder bed before the final line is jetted. This will reduce the effective saturation thickness. Powder beds prepared by tape casting may have a lower saturation thickness than 350 μm since the slurry is quickly spread over the powder bed. The liquid will not have as much time to redistribute compared to slurry jetting.

4.7. Conclusions

Cracking phenomena in a multi-layer ceramic forming process are analogous to the theory developed by Chiu and Cima for cracking phenomena in ceramic films. Cracking in the slurry-based 3DP process can be controlled by maintaining the saturation thickness determined by the jetting conditions below a critical value. The critical saturation thickness (CST) observed for slurry-based 3DP powder beds is a function of the powder type, surface tension of the solvent, and fracture resistance of the powder bed. Variables that reduced the capillary pressure increased the CST. The CST was increased by increasing the pore size of the powder bed or reducing the surface tension of the

solvent. The amount of slurry that can be deposited without cracking is a function of the CST, the solids fraction of the slurry, and the packing fraction of the powder bed.

Crack-free, multi-layer powder beds can be formed using the slurry jetting process by maintaining the saturation in the powder bed below a critical saturation thickness. The results are consistent with cracking due to capillary stress within the powder bed. Methods to reduce capillary pressure were successful at increasing the CST.

The cracking behavior of any new powder/solvent system should be characterized prior to attempting to make parts. Graphs of saturation thickness versus total thickness provide an easy tool for characterizing the cracking behavior of slurry-based 3DP powder beds.

CHAPTER 5
IMPACT OF THE BINDER ON THE PROCESS

5.1. Introduction

The binder impacts several areas of the process physics. Binder/powder bed interactions determine the geometry of primitives and stitching between adjacent primitives and layers. The binder also effects the interaction of the slurry during powder bed formation. The binder must meet several strict criteria. The binder must infiltrate into submicron powder size beds. The binder must be insoluble in the redispersion solvent to make part retrieval possible. The binder must also have sufficient strength and rigidity. The intrinsic properties of the binder are also critical to its performance in ink-jet printing and binder-powder interactions. Important intrinsic properties include surface tension, viscosity, conductivity, pH and chemical stability.

Several binder materials have been examined for use in the slurry-based 3DP process. Resolution of the printed part in the 3DP process mainly depends on binder-jet performance and binder-powder bed interactions. This chapter will examine the effect of the binder on the process physics. Candidate binder materials will be discussed. The interactions between the binder and the powder bed will be discussed briefly. The interaction between the slurry and the binder-printed region will be examined in greater depth.

5.2. Evaluation of Binder Systems

Several binder systems have been evaluated for the slurry-based 3DP process. The binders can be characterized as two general classes: solution phase binders and emulsion binders. Emulsion (or latex) binder systems are commonly used in industry in slurries prepared for tape casting or spray drying. Emulsion binders are available from numerous suppliers (such as Rohm and Haas) and can be tailored for aqueous or organic systems. Solution phase binders that are common in ceramics processing include polyacrylic acid (PAA) and polyvinyl alcohol (PVA).

5.2.1. *Emulsion Binders*

Jooho Moon examined several acrylic latex and wax emulsion phase binder systems. The particle size of emulsion binders measured using dynamic light scattering is shown in Figure 5.1. Emulsion phase binders did not penetrate into the powder bed regardless of the binder particle size. Emulsion phase binders coalesced and formed a surface film on the powder bed. The smallest particle size of polymeric binders studied was 14 nm in the Estek 1200 polyester latex. No penetration of the binder was observed despite the pore size of 120 nm for the 1.0 μm powder bed.

Wax emulsion binder systems also formed a surface film when printed onto the powder bed. However, waxes with low melting points could be melted and infiltrated into the powder bed. Low melting point waxes such as carnauba wax and paraffin infiltrated the powder bed easily with moderate heating. Wax binder systems were unattractive for two reasons. Waxes are hydrophobic, and the slurry did not wet the printed region well. This lead to inter-layer defects. Parts printed with wax were also relatively soft and flexible.

5.2.2. *Polyacrylic Acid (PAA)*

Polyacrylic acid (Figure 5.2) was studied as a binder material by Khanuja, Arthur[91], and Knezevic[92]. PAA is a water-soluble solution phase binder that is easily incorporated into the standard printhead. Carboxyl groups on the PAA chemisorb to the surface of alumina to form carboxylates. The chemisorption makes the PAA insoluble in water after printing onto alumina. Parts printed with PAA had relatively low strength and were easily damaged during retrieval. The parts were also relatively soft and flexible. PAA serves as a good system to investigate the binder-powder bed interactions, but it was eliminated as a viable binder candidate because of its low strength.

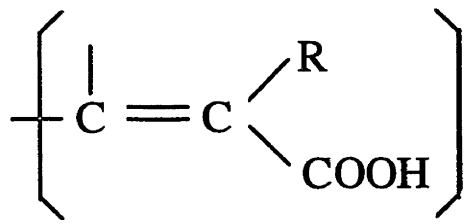

Figure 5.2. Molecular structure of PAA

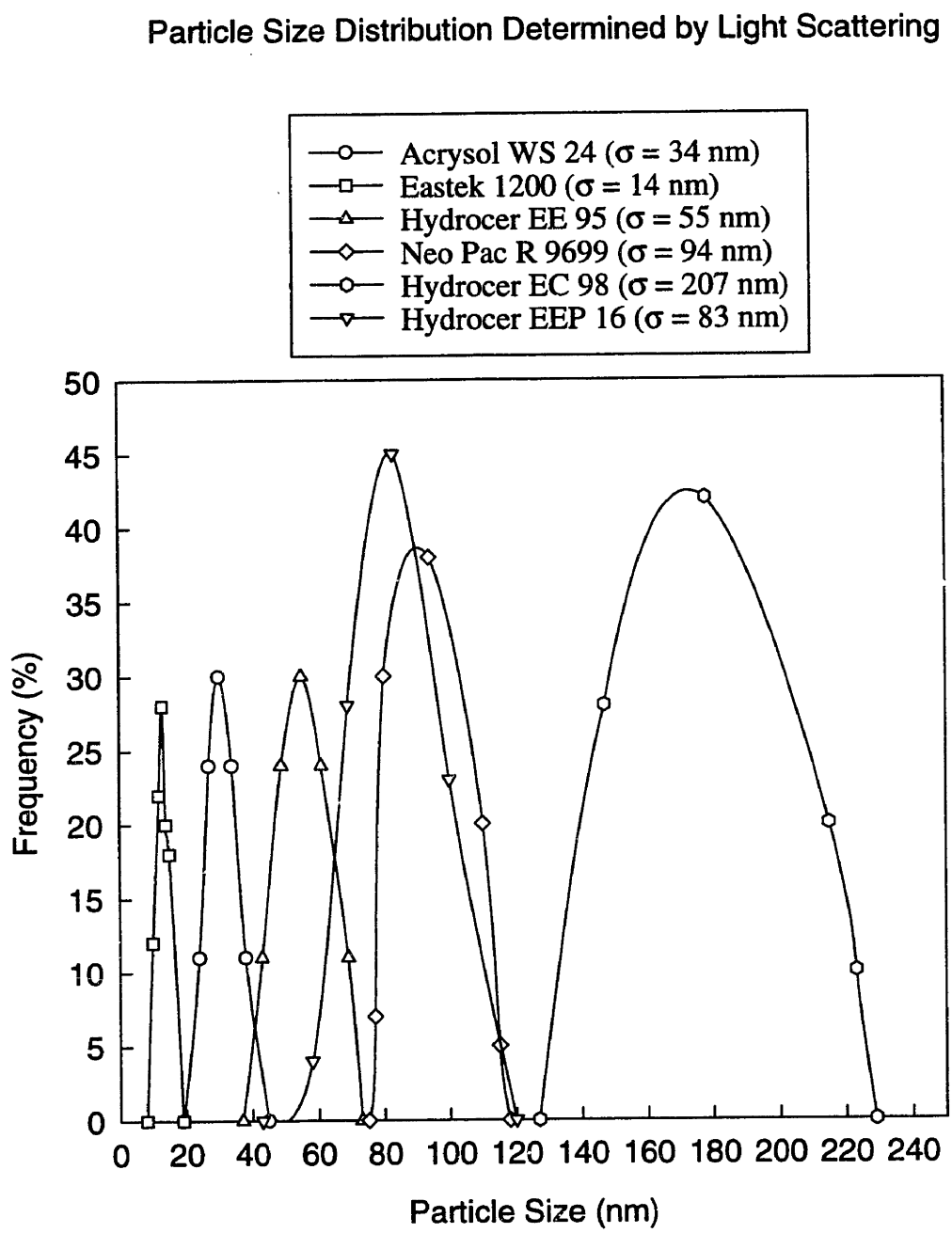

Figure 5.1. Particle size of emulsion phase binders (from J. Moon)

5.2.3. *Furfuryl Resin*

Furfuryl resin (Figure 5.3) is used as a precursor for forming glassy carbon[93,94,95]. The resin thermally polymerizes to form a rigid solid and pyrolizes in inert atmosphere to form microporous carbon. The resin was a 50:50 mixture of furfuryl alcohol monomer and furfuryl alcohol homopolymer (Quacorr Furfuryl Alcohol and 1300 Resin, QO Chemicals, West Lafayette, IN). The binder solution was formed by diluting the resin mixture in acetone with a ratio of 5:1 acetone to resin mixture. Surface tension and viscosity of the furfuryl resin binder solution were difficult to measure due to the high evaporation rate of acetone. The viscosity of the solution was less than 1 cP, and the surface tension was close to that for pure acetone, 23 dynes/cm.

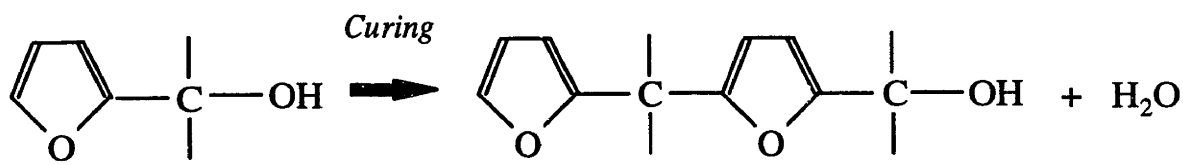

Figure 5.3. Molecular structure of furfuryl resin

Several parts were printed using furfuryl resin binder. Special precaution was required for safety. All experiments were performed in a fume hood to minimize exposure to acetone vapor. Furfuryl alcohol also poses health risks. All binder fluid lines were teflon to be compatible with acetone. The powder bed was formed using the slurry-jetting process with a 127 μm alumina nozzle.

Test parts were printed using a 45 μm continuous jet nozzle. The geometry of the parts was controlled by using masks. The binder saturation was varied to yield between 6 and 10 volume percent *furfuryl resin* on the basis of alumina. The regions printed with binder were dark brown, however the topology of the powder bed was unaffected by the binder. After printing, the parts and powder bed were heated for one hour at 110°C to thermally polymerize the binder. The parts were retrieved by redispersing the powder bed in water. The parts were very strong and could easily be handled without causing damage.

Parts printed with furfuryl resin binder displayed excellent surface finish. Figure 5.4 shows the top, bottom, and side surface finish of a printed part using HPA-1.0 powder. The bottom surface is planar with no evidence of scalloped surfaces. The surface finish at the top is controlled by the surface finish of the powder bed in general. The surface finish of the angled side is the most remarkable feature. The side is smooth and shows no stair-stepping. Inter-layer defects, or lamination defects, were not observed in any parts printed with furfuryl resin.

Mercury porosimetry of the unprinted powder bed and the region printed with binder indicated that the furfuryl resin has no impact on the microstructure of the printed part (Figure 5.5). The microstructure and packing density of the parts were controlled by the slurry jetting conditions. Sintered densities of printed parts were very high (>98%). The sintered density of the printed part deviated very little from the sintered density of the unprinted powder bed.

Bleeding was a major problem with furfuryl resin binder. The binder has very low surface tension and viscosity and spreads very easily within the powder bed. Figure 5.6 shows the cross section of a bar with a channel in the center. The part was printed with a 250 μm line spacing, 200 cm/sec print speed, and 100 μm layer height. The concentration of furfuryl resin was 8 volume percent on the basis of alumina. The edges of the part are rounded and indicate that the binder *bled* during printing. (The discoloration and cracks are the result of mounting and grinding the sample.)

The extensive bleeding made dimensional control impossible and furfuryl resin was eliminated as a viable binder system. However, several characteristics about it were attractive. The binder did not affect the infiltration of subsequent layers of slurry that were deposited, and microstructure was controlled by the slurry jetting process. The surface finish of angled sides was also very promising. These results indicated that *selective* bleeding may be a potential approach to improve the surface finish of angled sides.

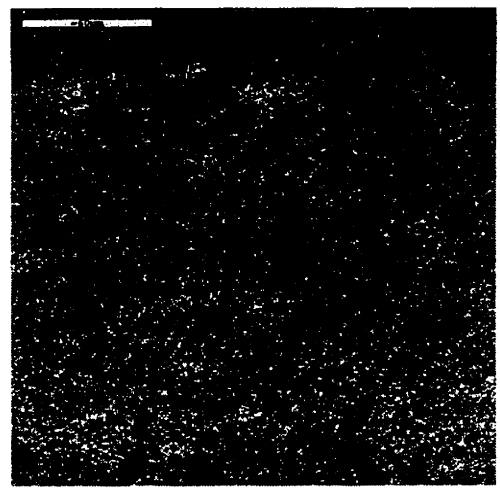

(A)

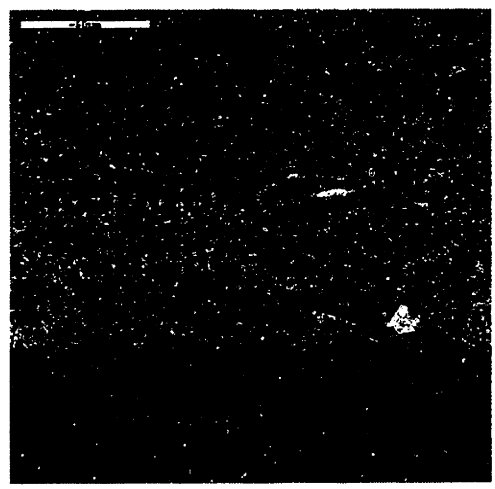

(B)

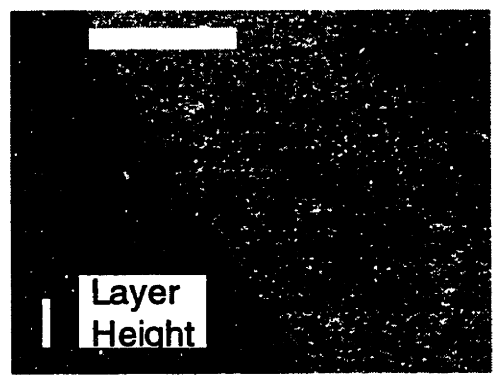

(C)

Figure 5.4. Surface finish of parts printed with furfuryl resin binder. A) Top surface B) Bottom surface C) Side surface

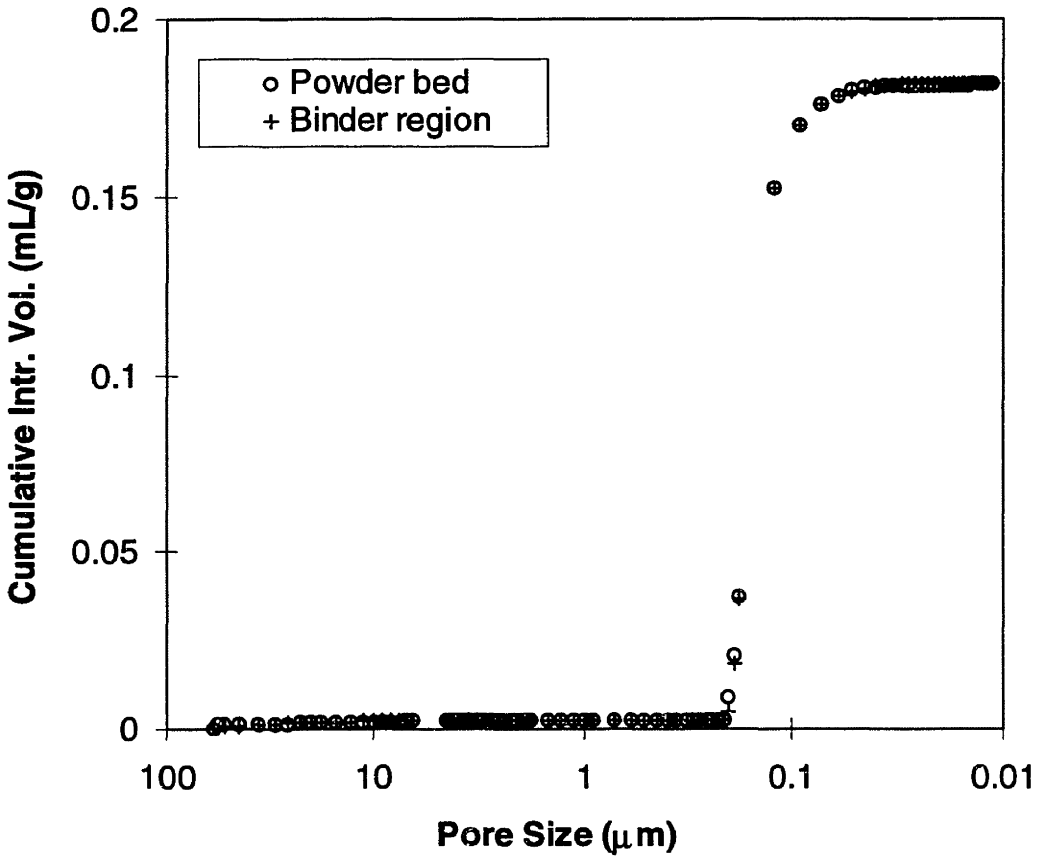

Figure 5.5. Mercury porosimetry of the unprinted powder bed and the part printed with furfuryl resin binder

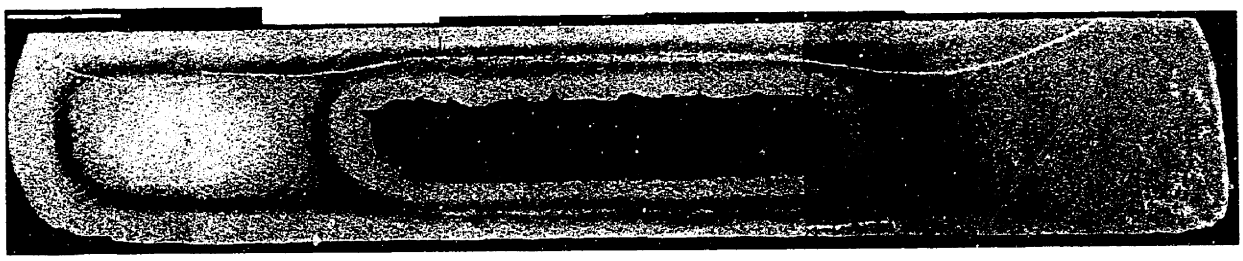

Figure 5.6. Cross section of bar printed with furfuryl resin binder. (8 volume percent furfuryl resin on the basis of alumina, scale bar = 1 mm)

5.2.4. *Joncryl™ Binder*

Joncryl™ (S.C. Johnson Polymer) is a water-based solution phase binder that was used effectively as a binder. It is a styrene-acrylic copolymer (Figure 5.7) that thermally crosslinks. Acrylics form strong, stiff solids. Binder burn-out from the part is easily achieved during the firing cycle, and binder residue is not significant in the sintered component. Joncryl, like most acrylics, is hydrophobic after drying. Water-soluble acrylics are commonly used as floor waxes because of this.

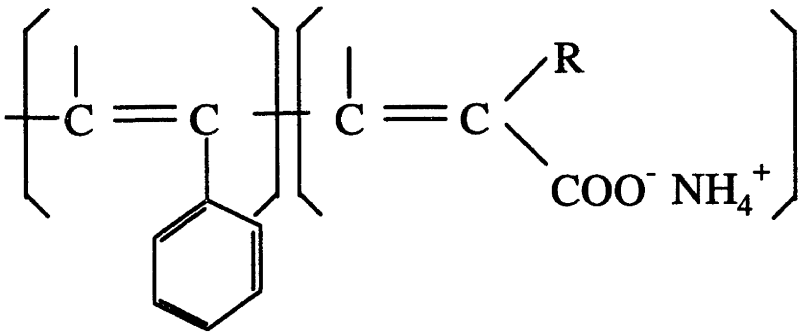

Figure 5.7. Molecular structure of Joncryl binder

Solution phase binders easily infiltrate into slurry-based 3DP powder beds. Surface tension and viscosity of solution phase binders can also be varied to some extent to optimize binder-powder bed interactions. Joncryl binders have been used as the primary binder for the slurry-based 3DP process because of their relatively high strength and easy incorporation into the current printhead design. Interactions between the slurry and Joncryl binder will be discussed in the following sections. The properties of parts printed with Joncryl binder will be discussed in detail in the next chapter.

5.3. Binder-Powder Bed Interactions

Arthur and Knezevic studied the interactions between the binder and the powder bed in the slurry-based 3DP process. The physics of the interactions between the binder and the powder bed during printing are examined in great detail in these theses. This section will briefly examine the infiltration kinetics and line widths of various binder

systems with respect to the physical properties of the binder (surface tension, viscosity) and the powder bed (pore size, surface roughness, etc.).

Binder-powder bed interactions in the slurry-based 3DP system differ substantially from the interactions in the standard 3DP process described by Bredt and Fan[96]. There are two major distinctions between the powder beds prepared by the slurry-based process compared to the standard process. The slurry-based powder bed is cohesive and is not affected by the ballistic impact of the binder droplets. The pore size is also more than an order of magnitude smaller in slurry-based powder beds. The permeability and infiltration kinetics are, therefore, much lower for the slurry-based powder beds. Approaches to calculate permeability and infiltration kinetics will be covered in following sections. Infiltration kinetics vary linearly with pore size, while the permeabilities are inversely proportional to the square of the pore size. The calculated permeabilities for powder beds with 60% packing density are 2.5×10^{-16} m^2 and 8.9×10^{-13} m^2 for 0.5 μm and 30 μm powders, respectively.

Binder droplets remain on the surface of the slurry-based powder bed after impact. The binder infiltrates into the powder bed due to capillary pressure. Interactions between binder droplets on the surface affect the resolution of binder primitives. The infiltration kinetics and frequency at which droplets impact the surface control the interactions between droplets.

5.3.1. Width of Binder Primitives

The width of binder primitives was characterized for each of the binders on different powder beds. Primitive dimensions were used to determine the maximum line spacing and layer height for printed parts. Single lines of binder were printed into slurry-based powder beds using a continuous jet print head with a 45 μm orifice. The width of the line in the powder bed was measured using an optical microscope with a calibrated scale. Amaranth was added to PAA and Joncryl binders to give the binders a dark red color. Furfuryl resin lines were dark brown.

The width of the line is dependent upon the amount of binder deposited per unit length of the line. This quantity is defined as the binder dose and is calculated by dividing the flow rate by the print speed:

$$\text{Binder dose} = \left(\frac{\text{flow rate (cm}^3\text{/sec)}}{\text{print speed (cm/sec)}} \right). \tag{5.1}$$

The units of binder dose are cm^2.

Arthur calculated the theoretical width of binder lines assuming that the binder line comes to equilibrium with the powder bed surface. The cross-section of the binder line is assumed to form a circular cap. The cross-sectional area of the binder line is equal to the binder dose. In equilibrium, the width of the binder line is determined by the contact angle of the binder on the powder bed:

$$\text{line width} = 2\left(\frac{\text{binder dose } (\sin^2\theta)}{\theta - \sin\theta\cos\theta} \right)^{1/2}. \tag{5.2}$$

This model implies that the line width should vary as the square root of the binder dose.

Figure 5.8A shows the line width as a function of binder dose for three solution phase binders printed into a HPA-1.0 powder bed prepared by slip casting. The line widths of furfuryl resin binder were the largest. Furfuryl resin binders possess both low viscosity and low surface tension. The solution perfectly wets alumina and spreads spontaneously. The volume fraction of polymer in the binder solution also had an impact on the line width. Lines formed from 10 volume percent PAA were about 30% wider at a given binder dose than lines formed from 20% PAA. Viscosity of solution phase binders increases with increasing polymer content while the surface tension is relatively unaffected. The data imply that line width increases with decreasing viscosity and surface tension. The line widths of 10 volume percent Joncryl 52 are slightly larger than 10 volume percent PAA.

Knezevic has measured the width of binder lines prepared using a drop-on-demand (D.O.D.) print head. D.O.D. print heads are capable of printing very low binder doses. Line widths measured by Knezevic for 20 volume percent PAA in a HPA-1.0 powder bed are plotted in Figure 5.8B. The data are plotted along with data for lines printed with a continuous jet print head and the line width calculated by equation (5.2).

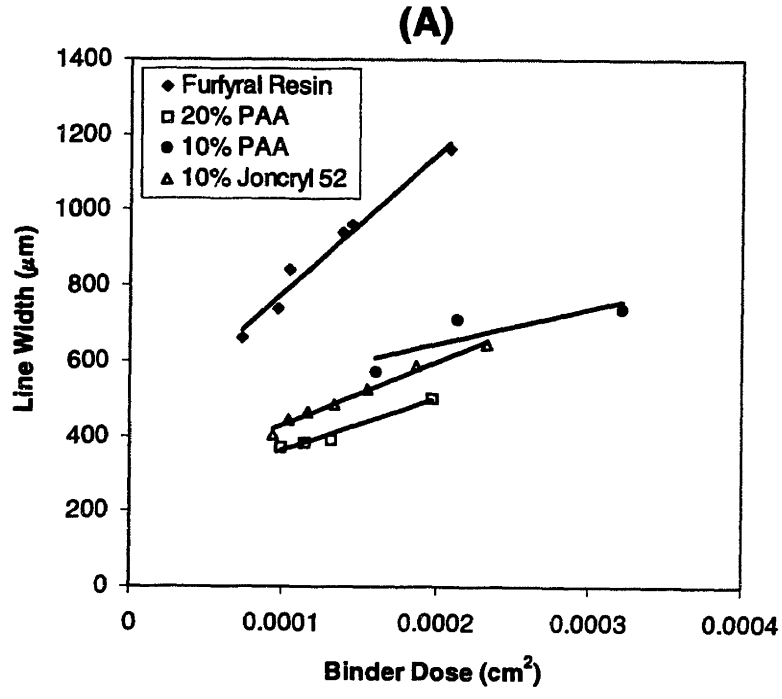

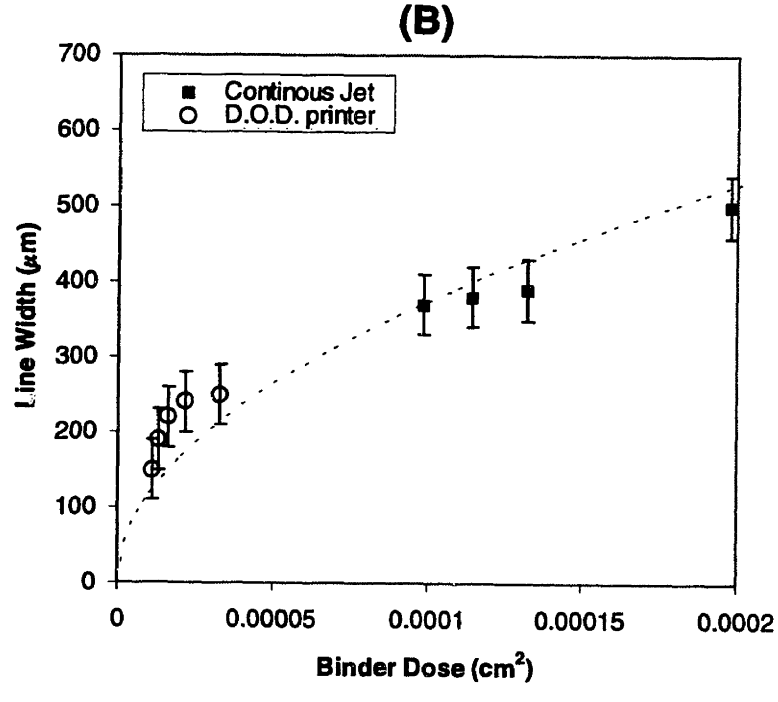

Figure 5.8. Line widths of solution phase binders into 1.0 μm powder beds
(A) Solution phase binders printed with 45 μm continuous jet print head
(B) 20% PAA solution printed with D.O.D. and continuous jet print head

The experimental data appear to follow the theoretical calculations within the error of the measurements.

The line widths of binder primitives were also measured on different types of powder beds. 10 weight percent PAA (M_w=5000) was printed into four powder beds. The binder dose was 0.00015 cm^2. Three powder beds were prepared using APA-0.5 powder. The top surface of a powder bed formed by tape casting was used for one powder bed. The top surface of the tape cast powder bed was very smooth and had a mirror finish. Two powder beds were slurry-jetted. One of the slurry-jetted beds was buffed smooth using fine grit polishing paper. The fourth powder bed was formed by slip casting 9 μm Norton powder. The bottom surface was buffed smooth before printing. The line widths are listed in Table 5.1.

The powder beds prepared from APA-0.5 powder indicated that the line width decreases with increasing surface roughness. The line width was 650 μm for the tape cast powder bed and decreased to 420 μm for the slurry-jetted (un-buffed) powder bed. The powder size also had a significant effect on the measured line width. The line width was only 270 μm for the 9 μm Norton powder bed.

The experimentally-determined line width is expected to deviate from the theoretical line width as the surface roughness increases and as the infiltration kinetics of the binder increases. Surface roughness will impede the spreading of the binder on the powder bed. The infiltration kinetics may also prevent the binder from having sufficient time to spread on the surface of the powder bed prior to infiltrating. The pores in the 9 μm Norton powder bed are more than an order of magnitude larger than the HPA-1.0 powder bed. The infiltration kinetics increase linearly with pore size. This may explain the narrower lines observed in the 9 μm Norton powder bed.

Table 5.1. Line widths of 10 weight percent PAA in different powder beds (Binder dose = 0.00015 cm^2)

Powder Bed	Line Width (μm)
APA-0.5 (Tape Cast)	650
APA-0.5 (Slurry-Jetted, Buffed)	580
APA-0.5 (Slurry-Jetted, Un-Buffed)	420
9 μm Norton (Slip cast)	270

5.3.2. Binder Infiltration Kinetics

The binder infiltration kinetics were measured directly using a high-speed video camera (Kodak Model 1210). The video camera was capable of recording video at 1000 frames per second. The camera was set up with a low angle of incidence to the powder bed. The lighting set-up was critical for high contrast images. The powder bed was backlit using monochromatic light. The light was reflected onto the powder bed at a low angle using a mirror. The mirror helped polarize the light and allowed for more precise control of the lighting compared to direct lighting.

Single lines of binder were video taped as they infiltrated into the powder bed. The binder line was clearly visible on the surface of the powder bed. Figure 5.9 shows a binder line 2 milliseconds after it was deposited onto the powder bed. The infiltration process is shown schematically in Figure 5.10. The width of the binder line on the surface decreases as the binder infiltrates into the powder bed. The binder-saturated region grows as the liquid infiltrates. The time at which the binder disappears from the surface of the powder bed was observed directly using the video.

The infiltration times of several Joncryl binders into HPA-1.0 and APA-3.0 powder beds were measured. The powder beds were prepared by slurry jetting and then buffed smooth. Two different molecular weights of Joncryl were examined. The molecular weights of the Joncryl binders are 1700 and 4900 for Joncryl 52 and Joncryl 58, respectively. The binders were diluted with water or with water/isopropanol solutions to produce 10 volume percent and 15 volume percent polymer solutions. The surface tension and viscosity of several binder solutions are listed in Table 5.2. The viscosity of Joncryl 58 solutions was slightly higher than Joncryl 52 solutions. The viscosity increased with increasing concentrations of binder. The surface tension was about 40 dynes/cm for aqueous binder solutions. The surface tension was between 25 and 27 dynes/cm for binder solutions that contained a one-to-one ratio of water and isopropanol (IPA). Isopropanol also increased the viscosity of the solutions.

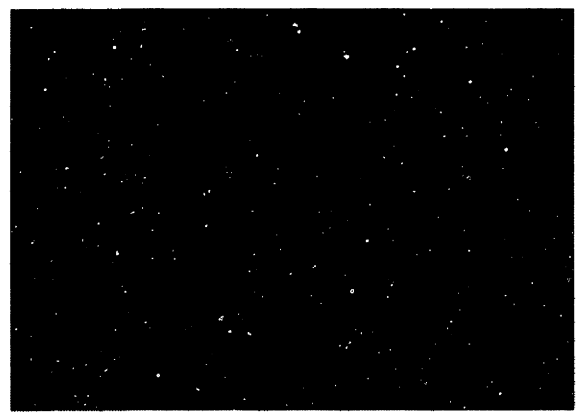

Figure 5.9. Joncryl binder line on the surface of the powder bed 2 msec after printing.

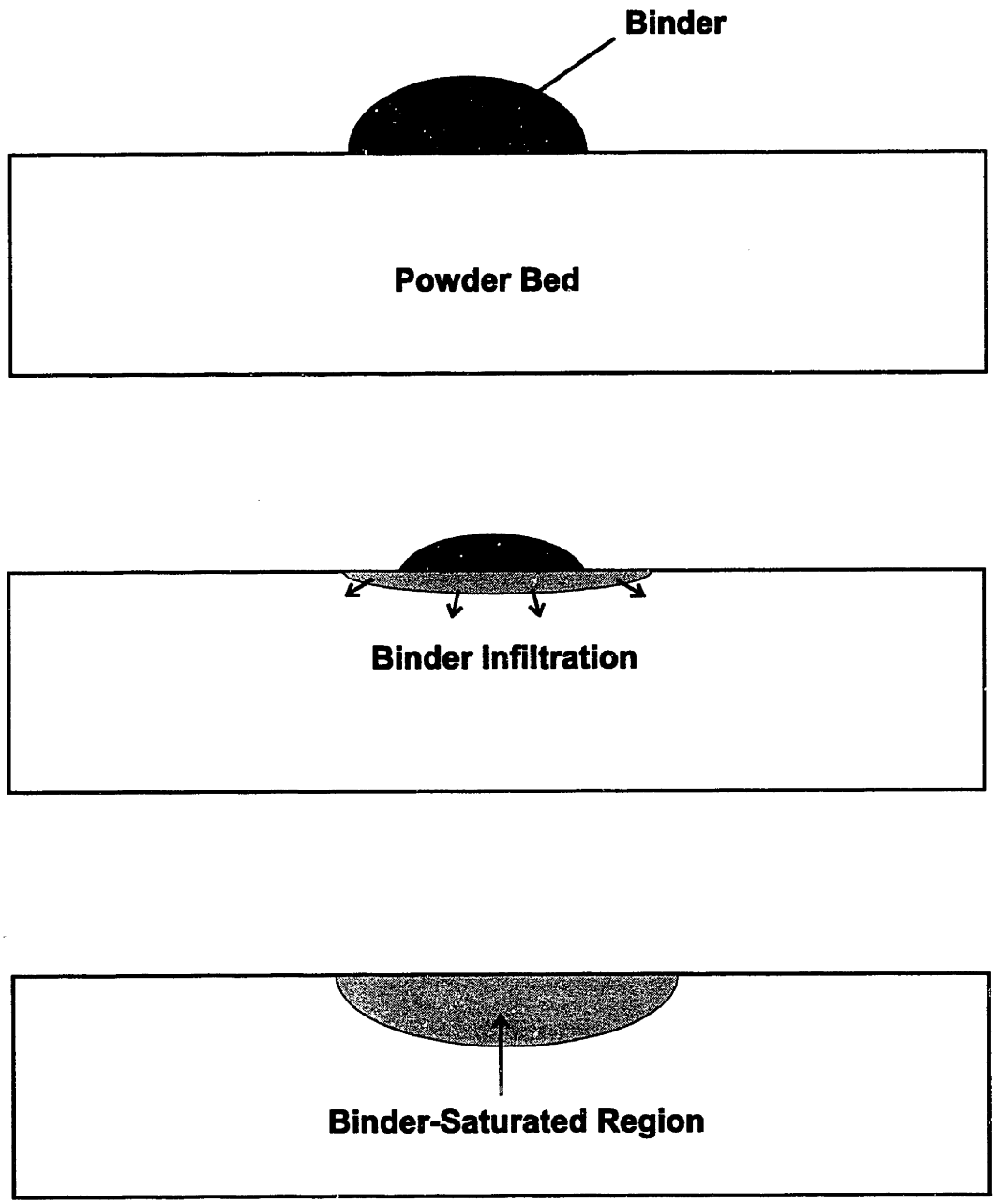

Figure 5.10. Schematic representation of binder infiltration

Table 5.2. Surface tension and viscosity of binder solutions

Binder Solution	γ (dynes/cm)	η (cP)	θ on Al_2O_3	$\frac{\gamma\cos\theta}{\eta}$
10% J52	40.4	3.3	20.8	11.6
15% J52	40.3	5.6	20.9	6.7
15% J58	40.3	5.6	41.7	5.4
15% J52 (water/IPA=1)	27.1	11.6	34.8	1.9
10% J52 (water/IPA = 1)	25.7	4.6	---	---
10% J58	39.7	3.7	---	---
15% J58 (water/IPA = 1)	27.0	11.7	---	---

Figure 5.11 is a plot of infiltration time versus binder dose for several binder solutions in a 1.0 μm powder bed. The infiltration times are roughly linear with the binder dose. The infiltration times increased with increased weight percent of binder, following the increased viscosity. The infiltration times were also higher for higher molecular weight binders. Figure 5.12 shows the infiltration times of 15 volume percent Joncryl 52 into 1.0 μm and 3.0 μm powder beds. The infiltration times for 3.0 μm powder beds were less than half the times for 1.0 μm powder beds. In general, the infiltration kinetics follow Washburn's equation. The infiltration times increased with increasing viscosity and decreased with increasing pore size and surface tension.

Levine and Neale report Washburn's equation for flow in a powder bed as:

$$\frac{dl}{dt} = \frac{kP_c}{\varepsilon\eta l}, \tag{5.3}$$

where l is the infiltration length, k is the permeability of the powder bed, P_c is the capillary pressure, ε is the void fraction of the powder bed, and η is the liquid viscosity. P_c is proportional to $\gamma\cos\theta$. The infiltration rate is, therefore, proportional to $\frac{\gamma\cos\theta}{\eta}$. The infiltration times plotted in Figure 5.11 indicate that the infiltration times for a given solution increased as $\frac{\gamma\cos\theta}{\eta}$ decreased.

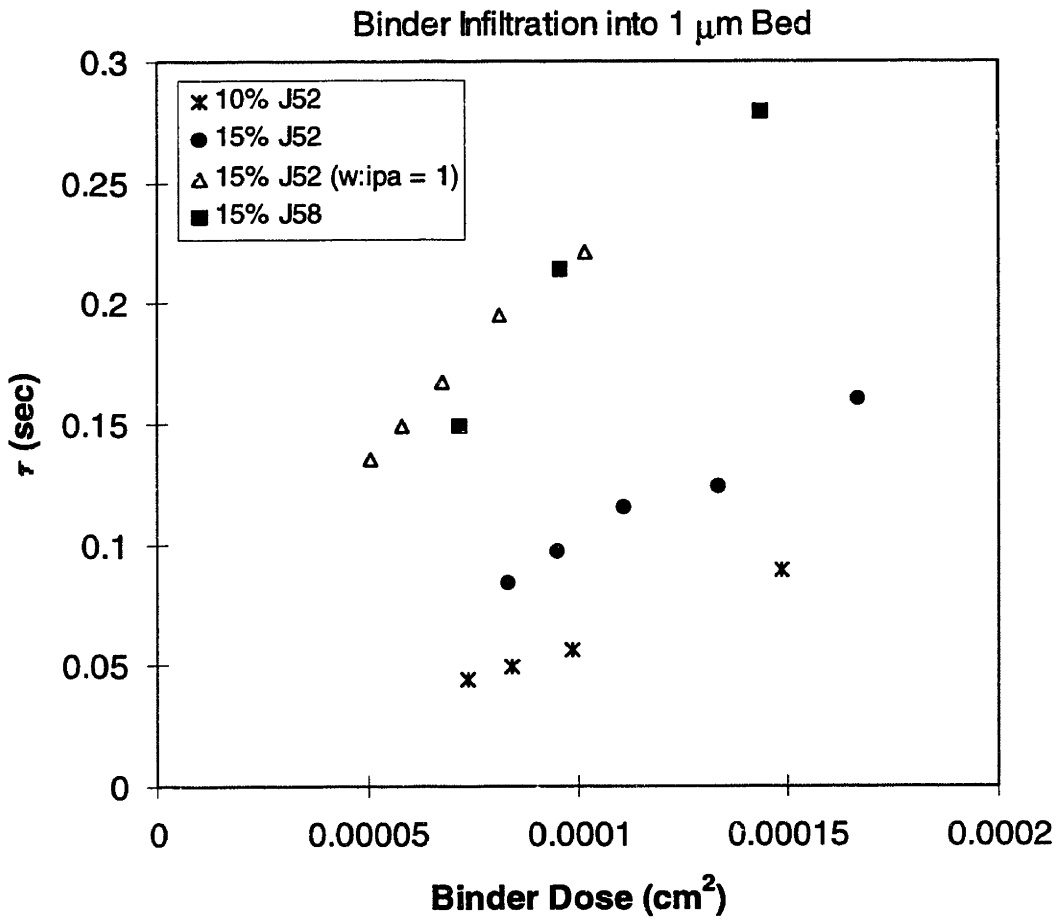

Figure 5.11. Binder infiltration times into 1.0 μm powder bed

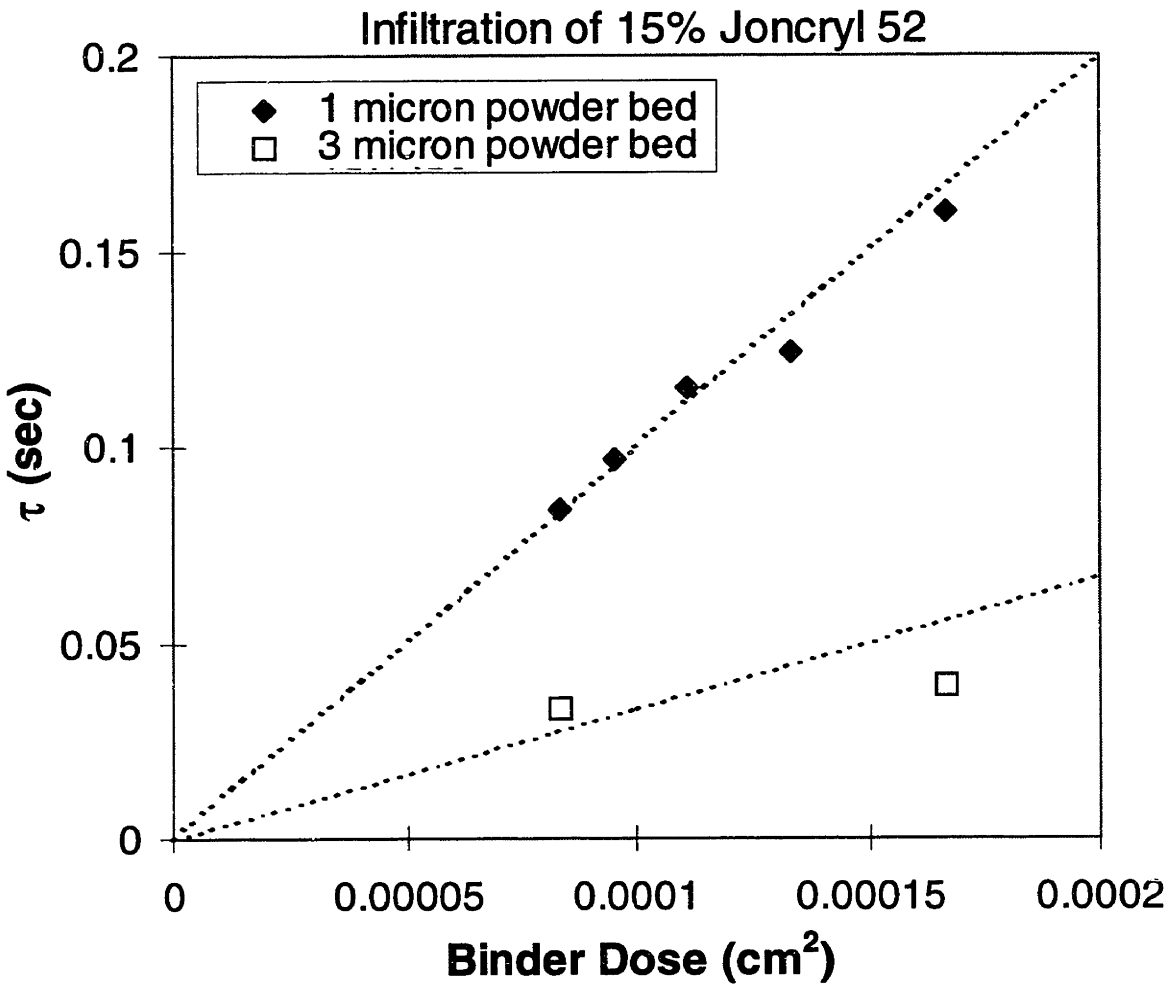

Figure 5.12. Effect of powder size on the infiltration time of 15% Joncryl 52 binder (Permeabilities are 7×10^{-18} m^2 and 6×10^{-17} m^2 for the 1 μm and 3 μm beds, respectively.)

Approaches to calculate the infiltration time of a liquid in a porous powder bed are outlined in Appendix A. The time, t_{inf}, for a liquid column of a height, h^o, to infiltrate into the powder bed can be calculated by using:

$$t_{inf} = \frac{(h^o)^2 \eta}{2\varepsilon k P_c}. \tag{5.4}$$

The width and the height of a binder line are both proportional to the square root of the binder dose. The infiltration time, t_{inf}, is proportional to the square of the height, so infiltration time should vary linearly with binder dose and have a zero intercept. The measured infiltration times shown in Figures 5.11 and 5.12 are linear with binder dose.

Infiltration times calculated using equation (5.4) are compared to the measured infiltration times in Table 5.3. The measured values are approximated at a binder dose of 0.0001 cm^2 using the linear regression value for each experimental data series. Infiltration times are calculated using two different permeabilities for the powder bed. The calculated permeability is 8.3×10^{-17} m^2 using 5.2 m^2/g for the specific surface area of the HPA-1.0 powder. The calculated infiltration times were much lower than the measured infiltration times using this permeability. The optimum permeability was determined by minimizing the difference between the calculated infiltration time and the measured infiltration time. This permeability was 7×10^{-18} m^2 for the HPA-1.0 powder bed.

The infiltration times were also calculated for the 3 micron powder bed. Figure 5.12 shows the measured infiltration times for 15% Joncryl 52 in HPA-1.0 and APA-3.0 powder beds. The calculated infiltration times for the two powder beds are also plotted assuming permeabilities of 7×10^{-18} m^2 and 6×10^{-17} m^2 for the HPA-1.0 and APA-3.0 powder beds, respectively.

Table 5.3. Binder infiltration times (Binder dose = 0.0001 cm^2)

Binder	Measured Infiltration Time (sec)	Calculated Infiltration Time (sec) ($k=8.3x10^{-17}$ m^2)	Calculated Infiltration Time (sec) ($k=7x10^{-18}$ m^2)
10% J52	0.06	0.017	0.058
15% J52	0.10	0.029	0.100
15% J58	0.21	0.036	0.125
15% J52(w/IPA=1)	0.22	0.103	0.349

5.4. Impact of Binder on Slurry Casting Kinetics

Producing uniform layers is a critical step in controlling the geometry of the 3DP part. Layers of the powder bed are formed by depositing a uniform layer of slurry onto the dried previous layers of the powder bed. Capillary forces from the dry powder bed quickly withdraw liquid from the freshly-deposited slurry. The powder bed is then dried with heating lamps prior to printing binder into the powder bed.

The slip casting of the powder bed layers is a colloidal filtration process in which the solvent in the slurry is rapidly removed from the thin layer of slurry. The casting rate is dependent upon the properties of both the slurry and the powder bed. The casting rate is expected to differ locally for slurry-based 3DP powder beds since selected regions are printed with a polymeric binder solution. The regions in the powder bed printed with binder will have different pore structures and wetting behavior than regions that have not been printed with binder. The differences in casting rates for the two regions lead to a bump at the interface between the printed and unprinted region (Figure 5.13).

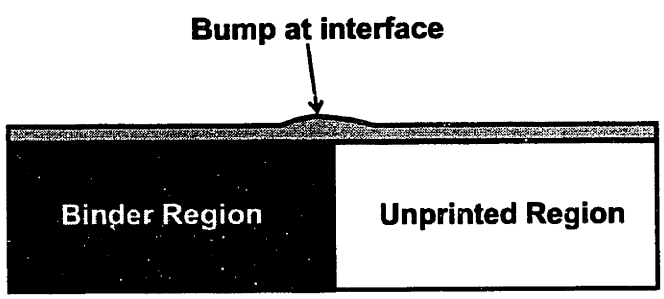

Figure 5.13. Schematic of the bump at the interface of the binder-printed region

This section will examine the influence of solid/liquid interactions on the colloidal filtration kinetics of slurry-based 3DP powder beds. The effect of slurry chemistry on the uniformity of layers will be discussed. A model of the differential casting kinetics will also be presented to identify key variables to control to optimize layer uniformity. The mechanism causing the bump at the interface of the binder-printed region and approaches to reduce its magnitude will be covered.

5.4.1. Observations of Single Lines of Slurry

Joncryl binder had a noticeable effect on the interaction of the slurry with the powder bed. The region of the powder bed printed with binder was clearly distinguished from the unprinted region after the slurry was jetted. The regions of the powder bed printed with binder were slightly depressed compared to regions that were not printed with binder. Figure 5.14 shows a bar printed with 10 volume percent Joncryl 52 binder. The interface of the binder-printed region displays a noticeable bump. The casting rate of the slurry was noticeably lower on the binder-printed region. The surface finish of the powder bed over the printed region also differed substantially from the unprinted region.

The interaction of the slurry with the powder bed was studied by jetting single lines of slurry across the interface of the binder-printed and unprinted regions. Photographs of single lines of slurry after casting are shown in Figure 5.15. Figure 5.15A shows a line of 30 $^{v}/o$ alumina slurry with only water as the solvent. The line shows a distinct bump at the interface between the binder-printed region and the unprinted region. Figure 5.15B shows a line of 30 $^{v}/o$ alumina slurry with a one-to-one ratio of water and methanol as the solvent. The line does not display any perturbations at the binder-printed interface.

The effect of the slurry solvent had similarly profound effects on the behavior of silicon nitride slurries. 30 volume percent silicon nitride slurries were prepared with three different solvents: water with 0.5% Triton X-100, water/IPA = 3, and water/methanol = 3. Figure 5.16 shows profilometry data for jetted lines on the binder-printed and unprinted regions. The shape of the slurry lines prepared with water(0.5% Triton X-100) differ substantially over the binder-printed and unprinted regions of the

Figure 5.14. Rectangular test bar showing the depression of the binder-printed region.

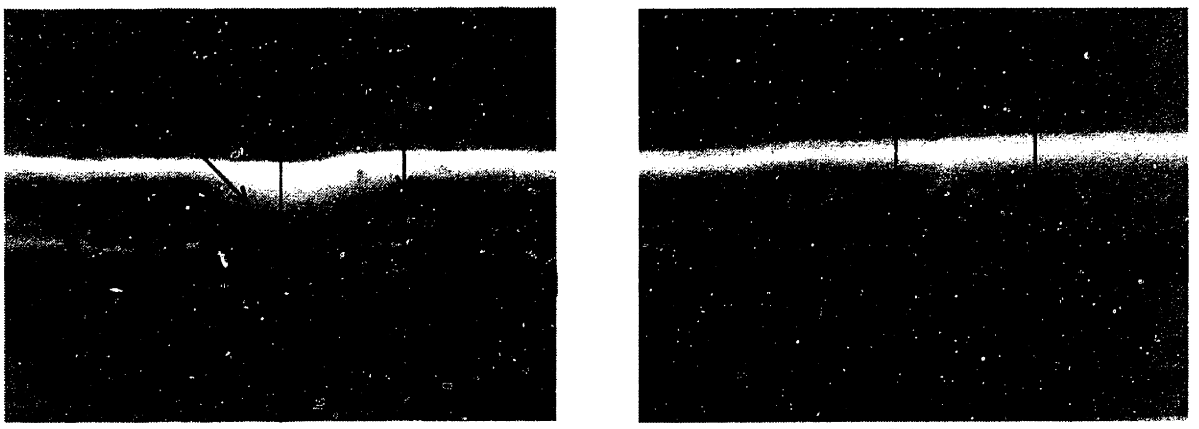

(A) (B)

Figure 5.15. Singles lines of slurry jetted across the interface of the binder-printed and unprinted regions. (A) Slurry solvent is water (B) Slurry solvent is Methanol/Water = 1

powder bed. The geometries of the lines are closer for the slurry that contained methanol. The lines were nearly identical over the binder-printed and unprinted regions when the slurry solvent was water/IPA = 3.

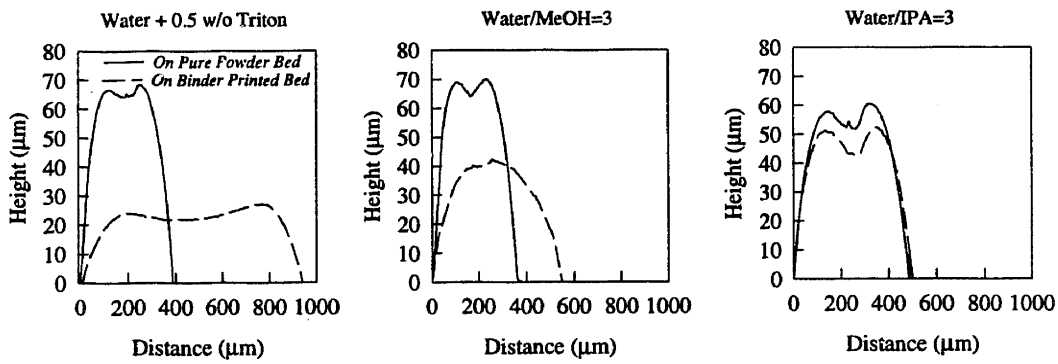

Figure 5.16. Profiles of single lines of silicon nitride slurry comparing the geometry on the binder-printed and unprinted regions (from J. Moon)

5.4.2. Direct Observation of Differential Casting Rates

Figure 5.17 shows a time series of photographs for a slurry line casting at the interface of the Joncryl binder-printed region. Slurry was deposited through a 127 µm nozzle across the powder bed and videotaped at 1000 frames per second. The fluid slurry formed a uniform line across the powder bed as it was deposited. Reflected light from the surface of the fluid slurry was observed to monitor the progression of the slip casting process. The surface of the slurry line darkened as the liquid in the slurry was drawn into the dry powder bed below it. The slurry was quickly converted from a fluid to a saturated solid as the solvent was withdrawn. The time at which the slurry surface was no longer highly reflective was clearly observed when lighted with monochromatic light with a low angle of incidence.

The slurry cast quickly over the region that was not printed with binder while the slurry remained fluid for a longer time over the region printed with binder. Migration of the slurry from the binder-printed region towards the interface was observed by tracking the motion of a particle floating in the slurry. Slurry was observed to migrate from the

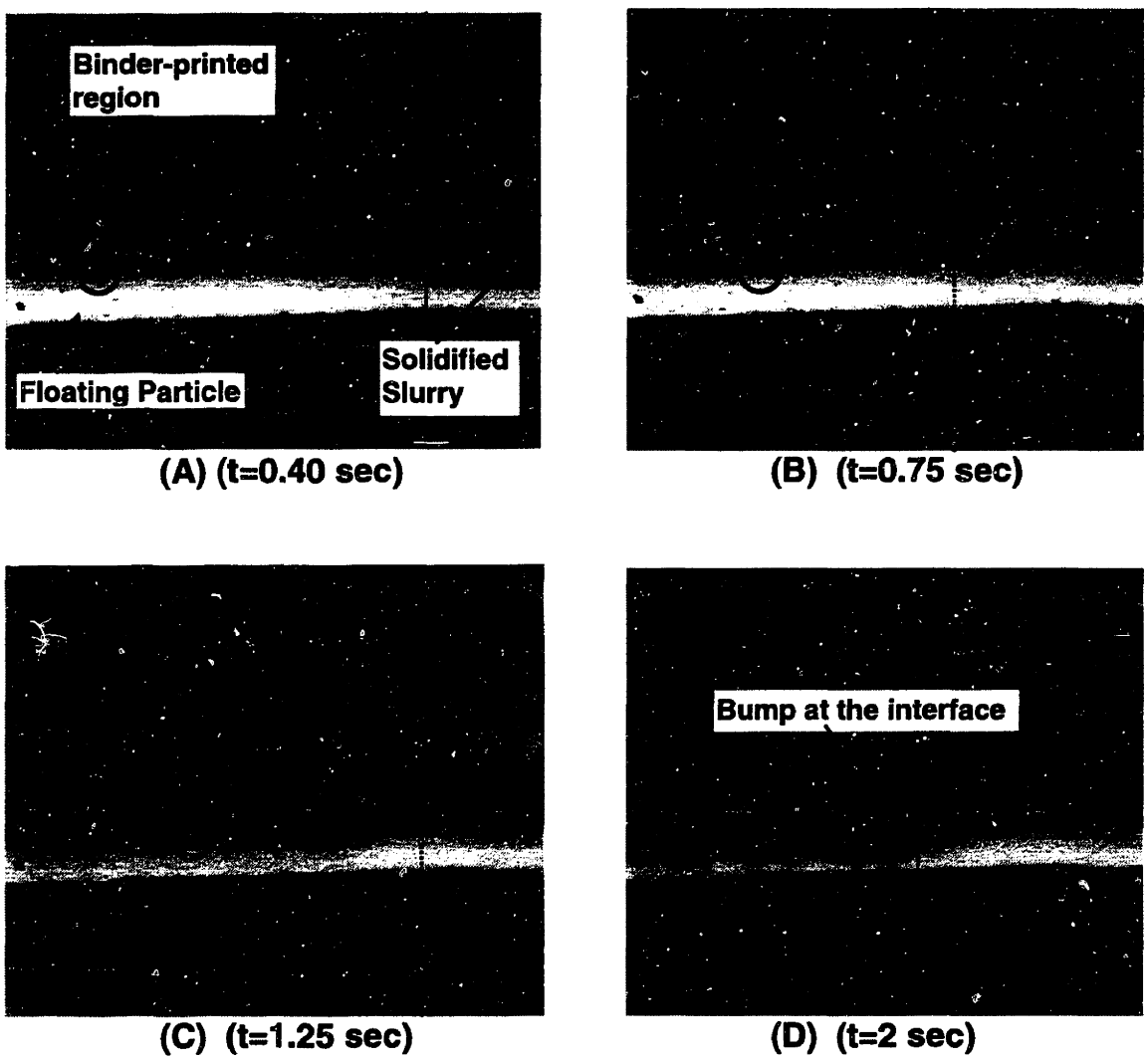

Figure 5.17. Photographs showing the slurry casting at the interface of the binder-printed region

region printed with binder to the unprinted region until the slurry became a saturated solid over both regions. The bump at the interface grew as the slurry migration progressed.

The preliminary video experiments indicated that the slip casting of the powder bed displayed three phases (shown in Figure 5.18). The slurry is fluid over the entire powder bed during Phase I. The slurry quickly slip casts over the region of the powder bed not printed with binder. The slurry remains fluid over the binder-printed region for a longer time. During Phase II, the slurry has cast over the unprinted region but remains fluid over the binder-printed region. The differential in the casting rates implies that liquid transport is higher on the unprinted region of the powder bed. This results in liquid migration from the slurry over the binder-printed region to the unprinted region. The slurry from the binder-printed region then begins to slip cast at the interface and forms a bump. The bump remains at Phase III when the slurry has cast over all regions of the powder bed.

5.4.3. Measuring the Slurry Casting Time

The observation of the differential casting behavior was the impetus for more rigorous high-speed video experiments to characterize the effect of slurry solvent and binder concentration on the casting rate of the slurry. A powder bed was prepared by jetting 35 volume percent HPA-1.0 slurry (0.05 M nitric acid, 2% PEG 400). The powder bed was buffed smooth. One centimeter wide regions of binder were then printed into the powder bed. Slurry lines were jetted across the powder bed perpendicular to the binder lines. The arrangement of the powder bed is shown in Figure 5.19. The video camera was positioned to examine the behavior over the binder-printed regions, the unprinted regions, and the interface of the binder-printed region. The time for jetted lines of slurry to slip cast was measured at each of these regions for five slurry compositions.

Six regions of binder were printed into the powder bed. Joncryl 52 and 58 were used. 10 and 15 volume percent binder solutions were printed. The binder was diluted in deionized water and also in water/IPA mixtures. The amount of binder deposited per binder region was carefully controlled and is measured by the *binder area density*. The

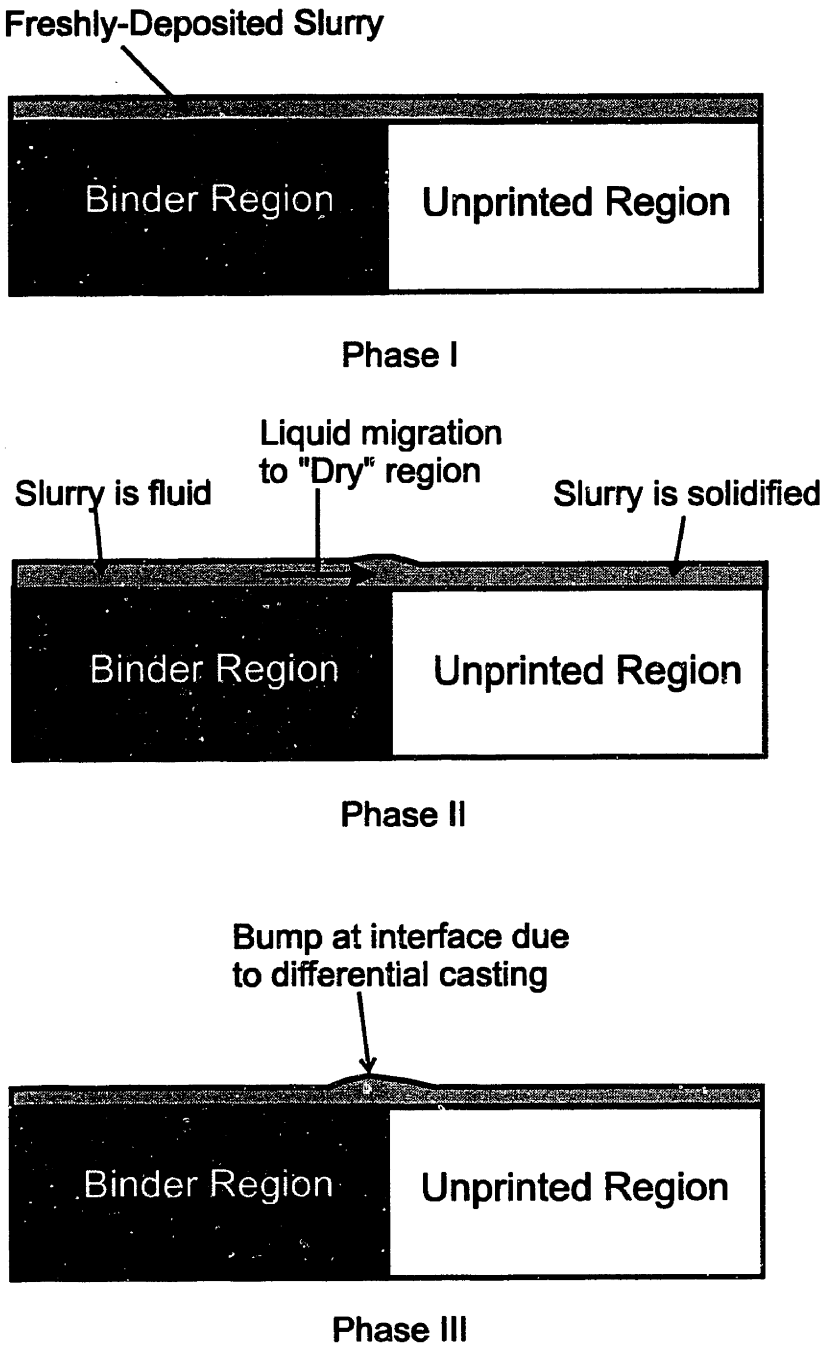

Figure 5.18. Schematic representation of the formation of the bump at the interface during the casting of the slurry layer

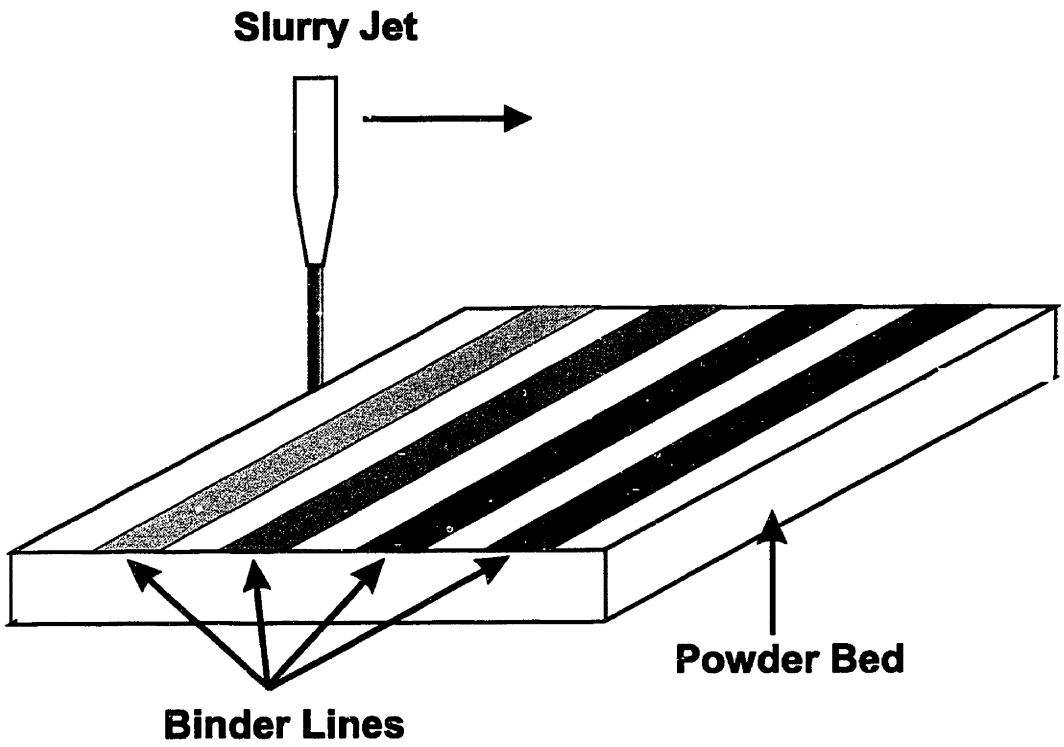

Figure 5.19. Powder bed configuration for measuring slurry casting times on binder-printed regions.

binder area density is the amount of *solid* binder material deposited per unit area of powder bed:

$$\text{binder area density} = \frac{\text{flow rate of binder solids}}{(\text{print speed})(\text{line spacing})}. \tag{5.5}$$

The binder composition and binder area densities for the six binder regions are listed in Table 5.4. The effect of binder area density, molecular weight of the binder, volume fraction of the binder, and IPA additions were determined by comparing the casting times over the six binder regions.

Table 5.4. Binder regions used for slurry casting experiments

Binder Region	Binder Composition	Binder Area Density (g binder/cm^2)
1	10% Joncryl 52 (Water/IPA=2)	5.8×10^{-4}
2	10% Joncryl 52 (Water/IPA=2)	2.9×10^{-4}
3	10% Joncryl 58 (Water/IPA=2)	5.8×10^{-4}
4	10% Joncryl 58 (Water only)	5.8×10^{-4}
5	15% Joncryl 58 (Water only)	8.7×10^{-4}
6	15% Joncryl 58 (Water only)	5.8×10^{-4}

The casting times were measured for five different slurries on the binder-printed regions and on the unprinted region. The slurry compositions are listed in Table 5.5. All slurries were prepared with HPA-1.0 powder, 2% PEG 400, and 0.05 M nitric acid. The complete list of slurry jetting conditions and casting times are listed in Table 5.6.

Table 5.5. Slurry Compositions

Solids Loading	Solvent Composition
40 volume %	deionized water
30 volume %	water with 0.1% Triton X-100
30 volume %	deionized water
30 volume %	water with 0.1% Triton X-100
30 volume %	water/methanol = 1

Table 5.6. Casting Times for Single Lines of Slurry

Slurry	Binder Region #	Slurry Flow Rate (g/min)	Casting Time (sec)
40%	1	6.4	0.556
40%	2	6.4	0.278
40%	3	6.4	1.838
40%	4	6.4	0.994
40%	6	6.4	1.328
40% (0.1% Triton)	1	6.3	0.650
40% (0.1% Triton)	2	6.3	0.320
40% (0.1% Triton)	unprinted	6.3	0.042
30%	1	7.1	1.611
30%	2	7.1	0.316
30%	unprinted	7.1	0.052
30% (0.1% Triton)	1	7.2	1.052
30% (0.1% Triton)	2	7.2	0.438
30% (0.1% Triton)	3	7.2	3.773
30% (0.1% Triton)	4	7.2	2.490
30% (0.1% Triton)	unprinted	7.2	0.052
30% (water/MeOH=1)	1	6.5	0.23
30% (water/MeOH=1)	2	6.5	0.146
30% (water/MeOH=1)	unprinted	6.5	0.094

Figure 5.20 shows the casting times for the five slurries on the unprinted powder bed and on binder regions 1 and 2. The casting times over the binder-printed regions were larger for all slurries. The casting times over binder-printed regions were more than an order of magnitude larger than over the unprinted regions for the slurries that did not contain methanol. The difference in casting times between the binder-printed regions and unprinted region was largest for the 30 volume percent slurry that contained only water in the slurry solvent. Casting times decreased for increased solids loading of the slurry. Triton X-100 surfactant had very little effect on the casting times of the slurries. The casting times actually increased slightly for the 40 volume percent slurry with the addition of 0.1% Triton X-100.

Adding methanol to the slurry solvent had the most dramatic impact on the casting times over the binder-printed regions. The relative differences between the casting times over the binder-printed and unprinted regions were within a factor of 2 for slurry with solvent consisting of water/methanol=1. The difference in casting times

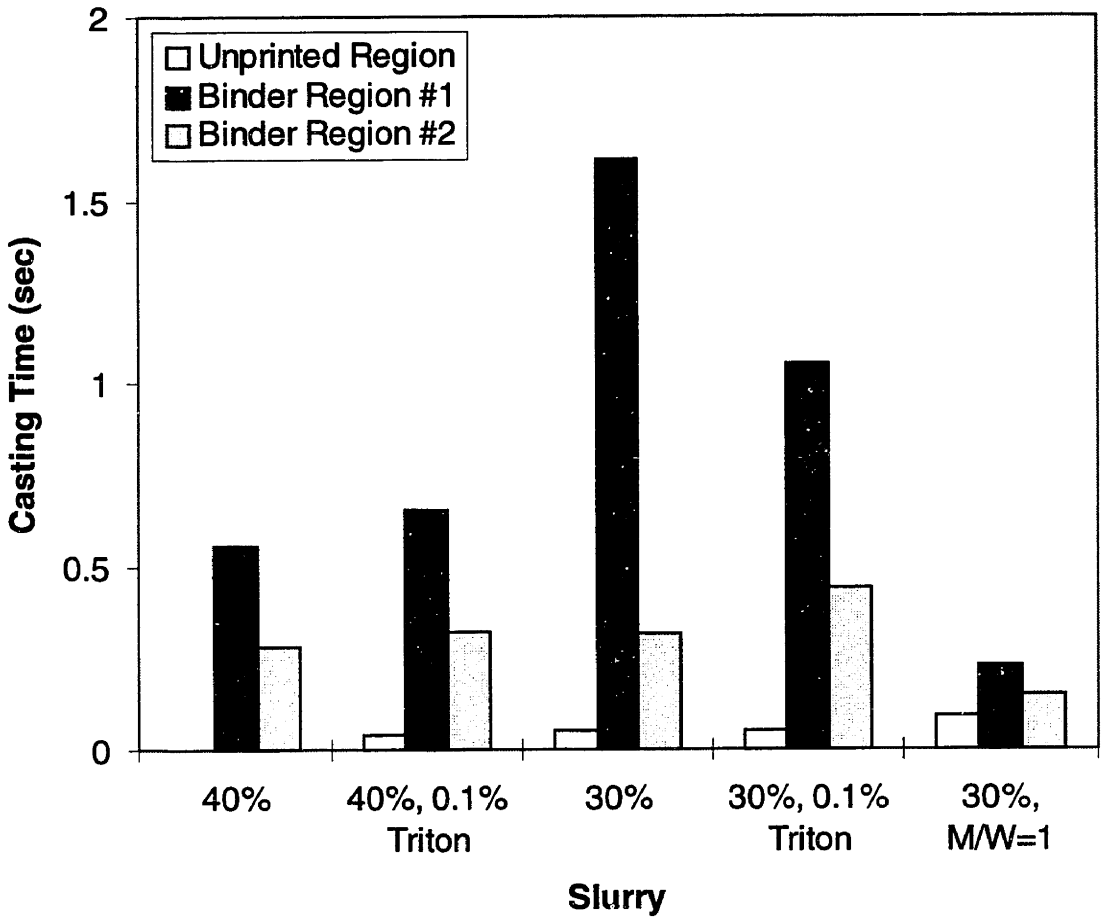

Figure 5.20. Casting times of slurries on the unprinted region and binder-printed regions 1 and 2

controls the amount of differential slip casting that occurs and controls the size of the bump at the interface of the binder-printed region. (See Figure 5.15 again.)

The data indicate that the casting time is a strong function of the quantity of binder present in the powder bed. The casting times increased with increasing binder area density for all slurries. This is intuitive since the binder will fill porosity in the powder bed and decrease both the total pore volume and average pore diameter. The printed powder bed also becomes more hydrophobic as the binder coats the surface of the alumina particles. The combination of reduced porosity and poor wetting characteristics decrease the driving force for liquid infiltration into the powder bed.

The effect of the molecular weight of the binder on the casting times was determined by comparing casting times over binder regions 1 and 3. Figure 5.21 shows that the casting times are larger over the region printed with Joncryl 58 compared to Joncryl 52. The intrinsic wetting behavior of the two binders should not differ. Therefore, the differences in the casting times are most likely due to the manner in which the binder is distributed in the powder bed. Joncryl 58 solutions have a slightly higher viscosity than Joncryl 52, and the Joncryl 58 probably does not infiltrate into the powder bed as much as Joncryl 52.

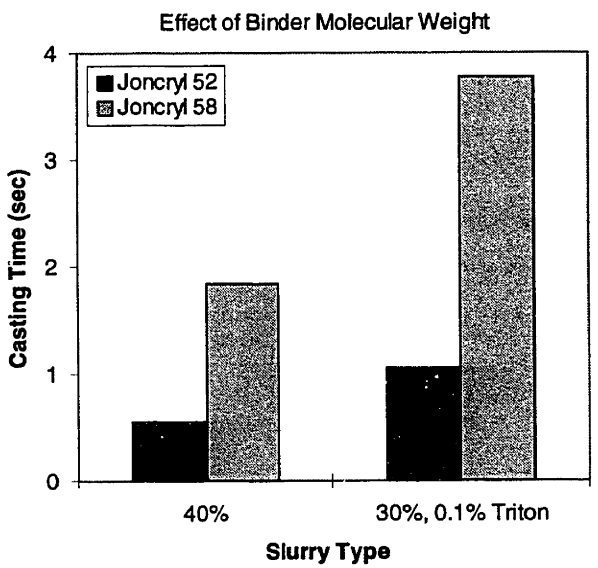

Figure 5.21. Effect of binder molecular weight on the slurry casting time (Joncryl 52 M_w=1700, Joncryl 58 M_w=4900)

The effect of the volume fraction of Joncryl in the binder solution can be understood by examining the casting times over binder regions 4 and 6. These two binder regions had the exact same binder area density and binder type. The only difference is that binder region 4 was deposited using 10 volume percent Joncryl 58 and binder region 6 was deposited using 15 volume percent Joncryl 58. Figure 5.22 shows the casting times of 40 volume percent slurry over these two regions. The casting time is larger over the binder area printed with 15% Joncryl. The only possible difference between the two areas is the distribution of the binder within the powder bed. The viscosity of the binder solution increases with volume fraction of binder. Lower viscosity solutions appear to spread over a larger area and are able to distribute the binder over a larger volume.

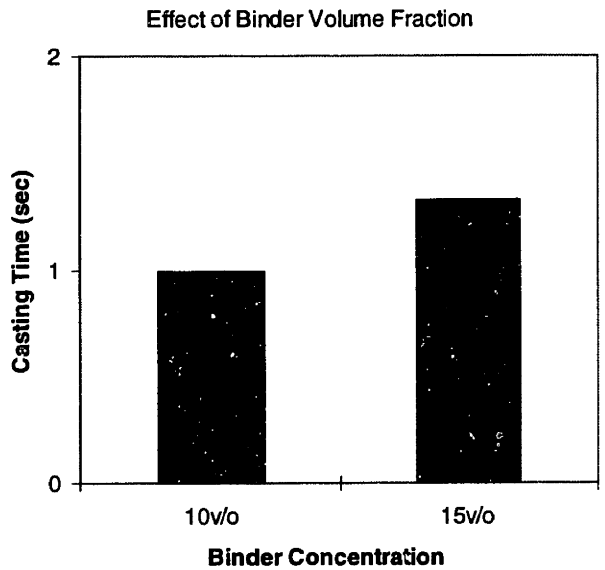

Figure 5.22. Effect of the volume fraction of binder in the solution on slurry casting time

Adding IPA to the binder solutions increases the viscosity and decreases the surface tension slightly. The casting times over regions 3 and 4 indicate that the casting times are larger over binder regions that contained IPA in the binder solution. This implies that the IPA inhibits the distribution of the binder throughout the powder bed.

The effect of molecular weight of the binder, volume fraction of the binder solution, and IPA all give indirect evidence about the distribution of the binder within the

powder bed. The factors that increased the viscosity of the binder solution also increased the slurry casting time. The binder area densities were identical, so any differences in slurry casting times must be accounted for by the distribution of the binder within the powder bed. The line width of binder primitives decreased with increasing viscosity of the binder solution. Low viscosity binder solutions are therefore able to distribute the binder over a larger volume. The concentration of the binder at the surface is lower, and the slurry casting time is also lower.

5.4.4. Profilometry of Test Bars

The bump caused by differential casting increases in magnitude with successive layers of the part. The magnitude of the bump at the interface was measured using profilometry for test bars printed with two different 35 volume percent slurries. One slurry contained only water as the solvent, and the other slurry had water/IPA = 1. Eight-layer test bars were printed using 4 volume percent Joncryl 58 binder solution. The powder bed layer height was 50 μm. The binder printing conditions were varied to adjust the volume fraction of binder in the printed parts. The binder printing conditions are summarized in Table 5.7.

Table 5.7. Binder printing conditions for 8-layer test bars

Binder Flow Rate	Print Speed	Line Spacing	Volume% Binder in Part
0.85 cm^3/min	200 cm/sec	500 μm	1.9%
0.85 cm^3/min	200 cm/sec	250 μm	3.8%
0.85 cm^3/min	100 cm/sec	125 μm	15.1%

The uniformity of rectangular test bars differed substantially depending on the binder concentration and slurry chemistry. The interface between the binder-printed and unprinted regions is barely observable for bars prepared with water/IPA=1 as the solvent in the slurry. The interface is very clear for parts prepared using slurry with only water as the solvent. Figure 5.23 shows two bars in the powder bed formed from the two slurries. The volume percent binder in each part is 15.1 volume percent. The printed region of the bar made using slurry with only water is very rough and irregular. The interface between

(A)

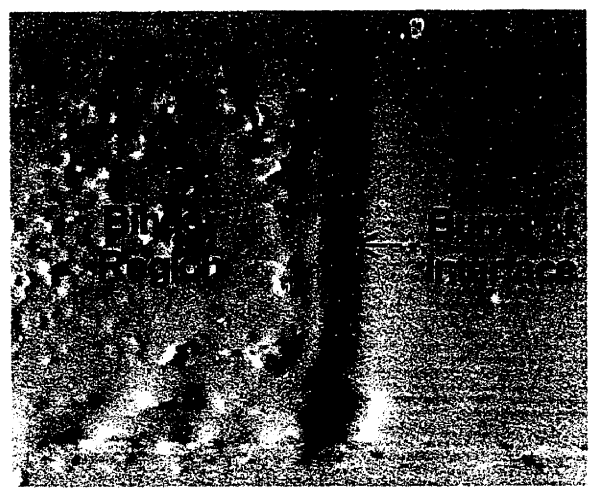

(B)

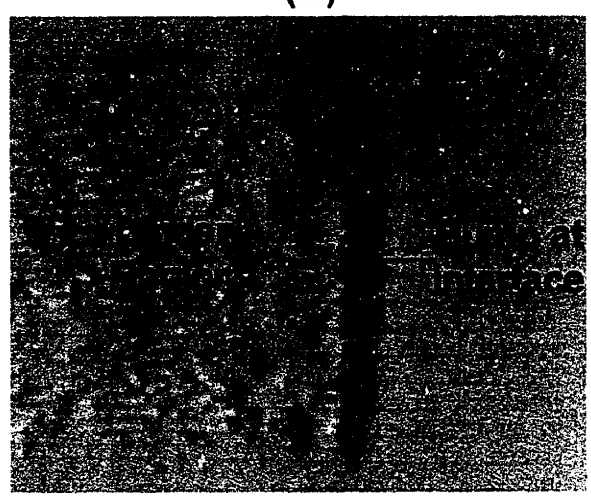

Figure 5.23. Photos showing the interface of the binder-printed region for bars with 15.1 volume percent binder A) Slurry solvent is water B) Slurry solvent is water/IPA=1

the binder-printed and unprinted regions is clearly visible. The bar prepared using slurry with water/IPA = 1 as the solvent is much more uniform.

The magnitude of the bump at the interface for the two sets of test bars is shown in Table 5.8. No interface is observed for water/IPA bars with 1.9 volume percent binder in the part. The interface is 100 μm for the water-based slurry with 1.9 volume percent binder and increases to 180 μm for bars printed with 15.1 volume percent binder. The bump at the interface was significantly smaller for water/IPA slurries at all binder contents.

Table 5.8. Profilometry Measurements

Slurry Solvent	Volume Percent Binder in the Part	Size of Bump at Interface
Water	1.9%	100 μm
Water	3.8%	150 μm
Water	15.1%	180 μm
Water/IPA=1	1.9%	0
Water/IPA=1	3.8%	10 μm
Water/IPA=1	15.1%	50 μm

5.4.5. Microstructure of the powder bed

Mercury porosimetry was used to characterize the pore structure of powder beds prepared with slurries with different solvents. All samples were fired at 600°C for 12 hours to burn out all organics prior to porosimetry measurements. Plots of cumulative and differential intrusion volume are shown in Figure 5.24 for the binder-printed and unprinted regions of the powder bed. The peak of the differential intrusion volume is ~0.12 μm for all samples. The peak of the differential intrusion plot is shifted slightly to lower pore sizes for the binder-printed region compared to the unprinted region. The plots of differential intrusion volume for slurry prepared with IPA/Water = 1 as the solvent is also shown in Figure 5.24. The plots for the unprinted region and the binder-printed region are nearly identical with no significant shift in the location of the peaks.

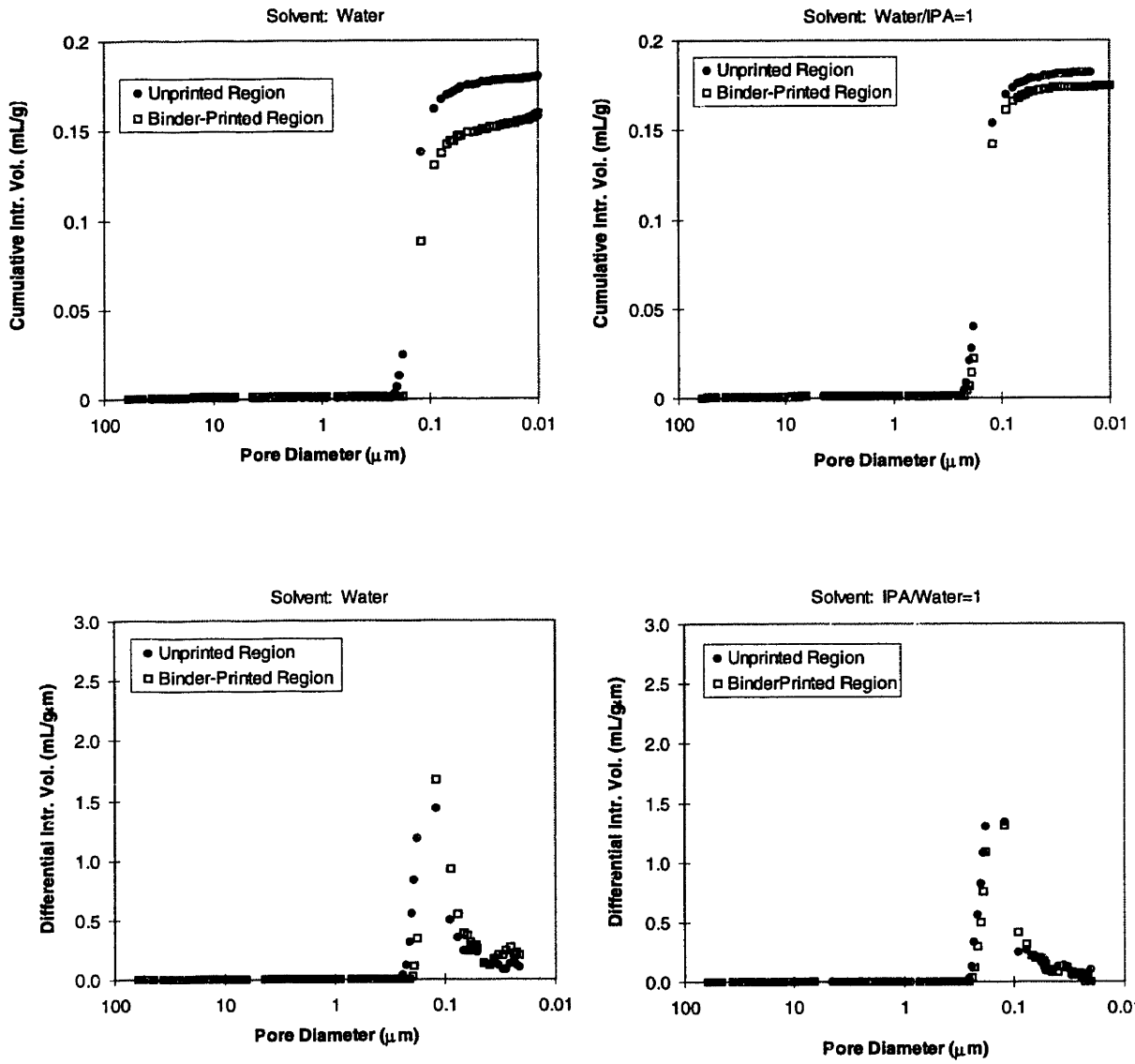

Figure 5.24. Cumulative and differential intrusion volume data for the unprinted region and the binder-printed region for slurries formulated with only water and Water/IPA mixtures in the solvent.

The bulk densities measured by mercury porosimetry are listed in Table 5.9. The density of the binder-printed region is larger than the unprinted region for both slurries. The relative difference in bulk density between the unprinted region and the binder-printed region is 5.4% for the water-based slurry while it is only 1.3% for the IPA/Water slurry. The pore structure and density data indicate that the microstructure of the powder bed differs for the two different regions and that the difference is more dramatic for slurries that contain only water in the solvent.

Table 5.9. Bulk densities of powder beds

Region of the Powder Bed	Slurry Solvent	Bulk Density (g/cm^3)	% Theoretical Density
Unprinted	Water	2.21	55.9
Binder-Printed	Water	2.33	58.7
Unprinted	IPA/Water = 1	2.24	56.6
Binder-Printed	IPA/Water = 1	2.27	57.3

5.4.6. Modeling the Slurry Casting - Colloidal Filtration

The data for casting times provide compelling evidence for the effect of differential casting rates on the formation of the powder bed. Matching the casting rates of the slurry over the binder-printed and unprinted regions reduces the magnitude of the bump at the interface. The effects of the chemistry of the slurry, the binder type, and the amount of binder on differential casting need to be understood to optimize the process.

Colloidal filtration proceeds as a filtrate is transported through a porous medium under an applied pressure. A solid cast layer builds up on the surface of the porous medium as the colloidal particles are filtered out of the slurry. Numerous models have been presented that examine the kinetics of colloidal filtration processes including slip casting, pressure slip casting, and filter pressing.[97,98,99,100] Aksay and Schilling presented a general kinetic model for colloidal filtration that can be used to evaluate the deposition of the powder bed in the slurry-based 3DP process.

The model developed by Aksay and Schilling considers the particle consolidation on the surface of a semi-infinite porous mold. (Figure 5.25) The location of the interfaces are denoted using ξ_s for the slurry/air interface, ξ_c for the cast/slurry interface,

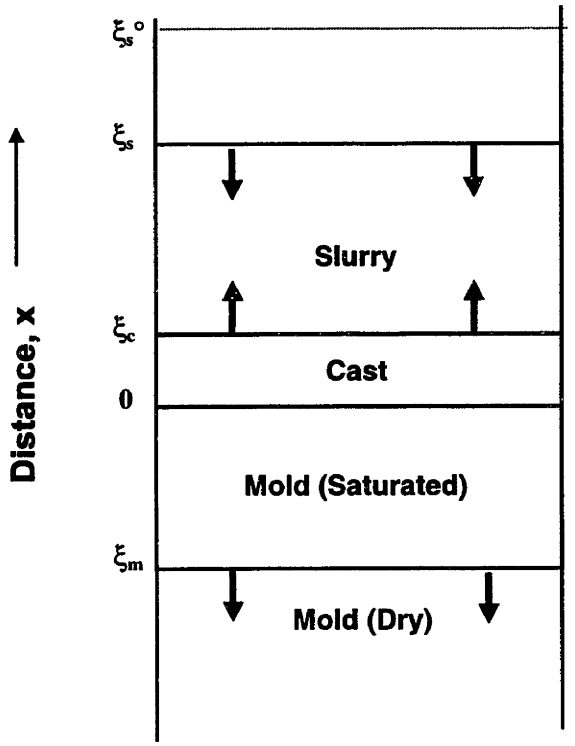

Figure 5.25. Schematic representation of the filtration system (after Aksay and Schilling)

and ξ_m for the liquid interface in the mold. The motion of the interface between the solvent and air in the mold, the interface between the cast layer and the slurry, and the interface between the slurry and air are related through mass balance relations.

$$\xi_s^\circ - \xi_s = n\xi_c = -\varepsilon_m\xi_m \tag{5.6}$$

The variable ε represents the volume fraction of voids, and n is defined as:

$$n = (1 - x_s - \varepsilon_c)/x_s, \tag{5.7}$$

where x_s is the volume fraction of solids in the slurry. Aksay and Schilling also expressed the fluid flux in terms of the locations of the interfaces:

$$J_f = \frac{d\xi_s}{dt} = -n\left(\frac{d\xi_c}{dt}\right) = \varepsilon_m\left(\frac{d\xi_m}{dt}\right). \tag{5.8}$$

An expression for the filtration rate was derived by Aksay and Schilling using Darcy's law and the conditions of continuity of the system established in (5.8). Darcy's law in a one-dimensional case is:

$$J_f = \left(\frac{k}{\eta}\right)\frac{dp}{dx}. \tag{5.9}$$

The pressure drops across the two materials will generally differ as shown in Figure 5.26. Aksay and Schilling expressed the total pressure drop ($p_t - p_o$) as:

$$p_t - p_o = \left(\frac{\xi_c^2}{t}\right)\left(\frac{\eta n}{2k_c} + \frac{\eta n^2}{2\varepsilon_m k_m}\right), \tag{5.10}$$

where k_c and k_m are the permeabilities of the cast layer and the mold, respectively. This equation implies that the casting process will follow a parabolic rate since a plot of ξ_c^2 versus t should be linear.

Equation (5.10) can be easily modified to study the casting rate in the slurry-based 3DP process. Slurry is deposited with a controlled height, ξ_s°, onto a dry powder bed. The dry powder bed acts as the *mold* in this case and withdraws liquid from the slurry to build up a cast layer. The slurry/air interface (ξ_s) and the slurry/cast interface (ξ_c) converge at a time defined as t*. The cast layer is fully saturated at this point, and the thickness of the new layer is ξ_c*. Substituting $\xi_c = \xi_s$ into (5.6) to solve for ξ_c*:

$$\xi_c^* = \frac{\xi_s^\circ}{n + 1}. \tag{5.11}$$

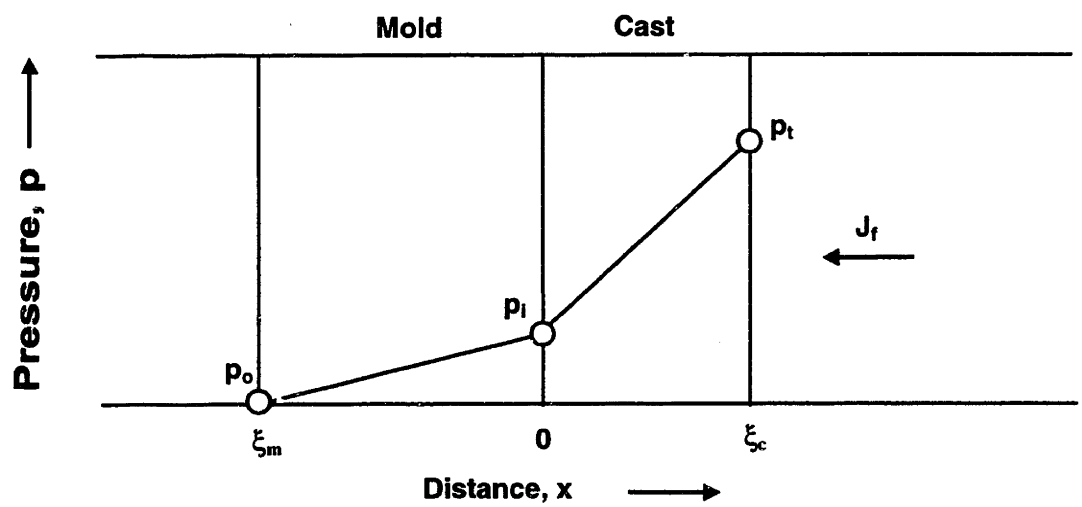

Figure 5.26. Hydraulic pressure profile across the mold and cast layer (after Aksay and Schilling)

The time at which casting ceases can be calculated by substituting (5.11) into (5.10) and solving for t*:

$$t^* = \frac{\left(\frac{\xi_s^o}{n+1}\right)^2}{p_t - p_o}\left(\frac{\eta n}{2k_c} + \frac{\eta n^2}{2\varepsilon_m k_m}\right). \tag{5.12}$$

The pressure drop across the filtration system, $p_t - p_o$, is the capillary pressure of the powder bed. Capillary pressure, Δp, can be calculated using the surface-to-volume ratio of the pore space[101]:

$$\Delta p = \frac{\gamma_{LV}\cos(\theta)S_p}{V_p}, \tag{5.13}$$

where γ_{LV} is the liquid/vapor interfacial energy, θ is the contact angle of the solvent on the solid, S_p is the surface area of the pore space, and V_P is the volume of the pore space.

The model of Aksay and Schilling implies that rapid consolidation rates are achieved by maintaining a high pressure gradient while maximizing the permeability of the powder bed. The Carman-Kozeny model is a simple formula to calculate permeability based on the specific surface area, S, and void pore fraction, ε, of the powder bed.

$$k = \frac{\varepsilon^3}{5S^2(1-\varepsilon)^2} \tag{5.14}$$

Figure 5.27 shows the dependence of permeability on pore fraction and particle size based on equation (5.14). The calculations assume the particles are spherical and monosize. The permeability increases by more than an order of magnitude when the pore fraction increases from 0.30 to 0.50. The pore fraction of most slurry-based powder beds is between 0.35 and 0.45, and the permeability based on (5.14) changes by about a factor of 3 over this range. The alumina powders studied have ranged in size from 0.5 μm to 3.0 μm. The permeability varies by a factor of 36 over this range according to (5.14). The permeability of powder beds prepared by the slurry-based process can therefore vary by more than two orders of magnitude depending on the particle size and pore fraction of the powder bed.

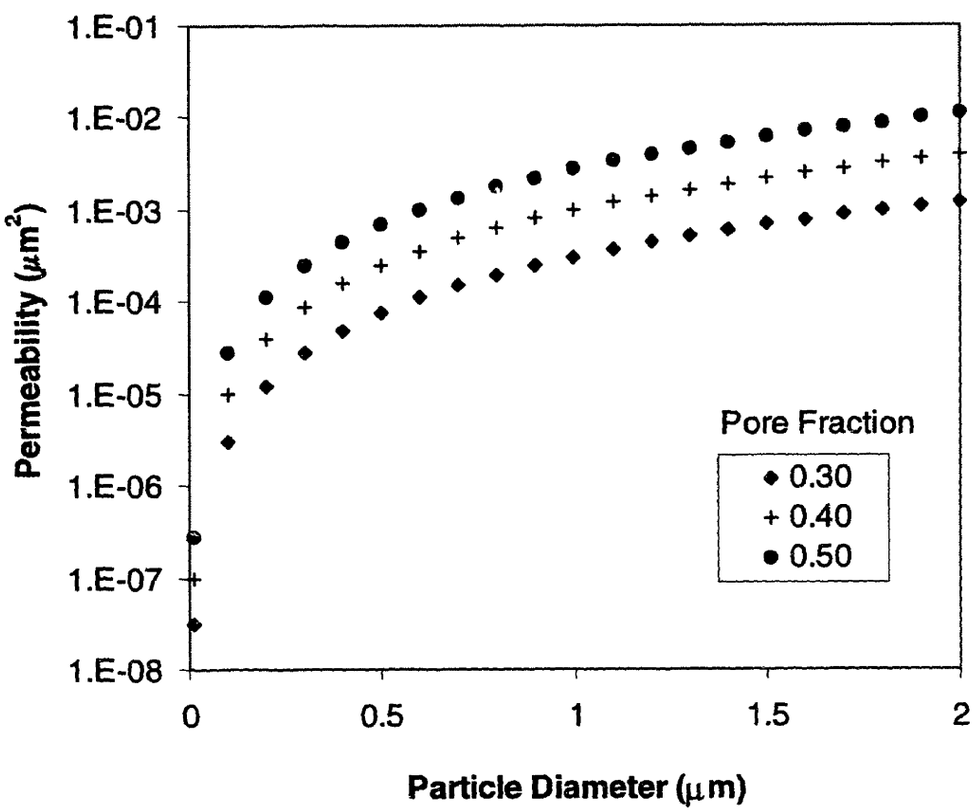

Figure 5.27. Permeabilities calculated from (5.14)

The nature of the powder bed is changed dramatically as binder is printed into the powder bed during the 3DP process. The binder fills some of the porosity and changes the contact angle of the solvent. The kinetics of the slip casting process will therefore differ over binder-printed regions versus unprinted regions.

Equation (5.12) can be used to calculate the time for the slip casting process to be completed over either region of the powder bed. Over the unprinted region, k_c and k_m, are identical since the "mold" and "cast" are the same material with identical bulk properties. The pore fractions, ε_c and ε_m, are also equal. Over the binder-printed region, the properties of the cast layer are the same as for the unprinted region. However, the void fraction (ε_m) and permeability (k_m) will differ in the binder-printed region. The void fraction in the binder-printed region will be:

$$\varepsilon_{binder} = \varepsilon_c - (1-\varepsilon_c)f_b, \qquad (5.15)$$

where f_b is the volume fraction of binder deposited on the basis of alumina. Note that f_b is not the volume fraction of the binder solution that is printed. Rather, it measures the amount of solid binder remaining in the powder bed after printing.

The contact angles of solvents were measured by observing a sessile drop with a goniometer. The contact angle on alumina was measured using a sintered, polished alumina sample. The contact angle on Joncryl 52 was measured by coating a microscope slide with 10 volume % Joncryl 52 and drying at 150°C for 1 hour. The Joncryl formed a clear, solid film with no cracks. Contact angle, viscosity, and surface tension data are shown in Table 5.10 for solvents used in the slurry. The contact angle of water on Joncryl was 70°, and the driving force for liquid infiltration is expected to be low on Joncryl-coated surfaces. Methanol and IPA reduced the contact angle on Joncryl significantly. Solutions of water/IPA =1 were perfectly wetting on Joncryl.

Table 5.10. Contact angle and viscosity of solvents used in the slurry

Liquid	γ (dynes/cm)	η (cP)	Solid	θ (°)
Water/IPA = 1	24.6	1.93	Polished alumina	13.7
Water/methanol = 1	37.0	0.80	Polished alumina	16.0
Water	70.1	1.00	Polished alumina	58.8
Water	70.1	1.00	Joncryl	70.0
Water/methanol = 1	37.0	0.80	Joncryl	28.3
Water/IPA = 1	24.6	1.93	Joncryl	0

The contact angle of the solvent in the binder-printed region will be approximated by the contact angle on pure binder. The slip casting times on the two regions, t^*_{binder} and $t^*_{unprinted}$, can be calculated for a given $\xi_s°$. The hydrophobic nature of the Joncryl binder and the difference in void space lead to larger values of t^*_{binder} compared to $t^*_{unprinted}$. The larger values of t^*_{binder} correlate with the larger casting times in Table 5.6 observed for slurry lines deposited on binder-printed regions.

Figure 5.28 shows the calculated casting times for 30 volume percent alumina slurries. (The volume fraction binder is 0.05 for the binder-printed region, and the surface area of the powder bed is 5.4 m^2/g.) Figure 5.28A shows the casting times over the binder-printed and unprinted regions of the powder bed when the slurry solvent is water. The casting times over the binder-printed region are 80% larger than the casting times over the unprinted region. Figure 5.28B shows the calculated casting times when the slurry solvent is Water/IPA=1. The casting times differ by only 15% due to the low contact angle of Water/IPA solutions on Joncryl.

Differential casting effects can be avoided by matching the casting rates over the two different regions. The binder affects the casting time calculated in equation (5.12) by changing the contact angle (and therefore Δp), ε_m, and k_m. The pore fraction (ε_m) and permeability (k_m) decrease as the volume fraction binder increases. The contact angle of the solvent on the binder-printed region must, therefore, be <u>lower</u> than on the unprinted region to equilibrate the casting rates of the two regions.

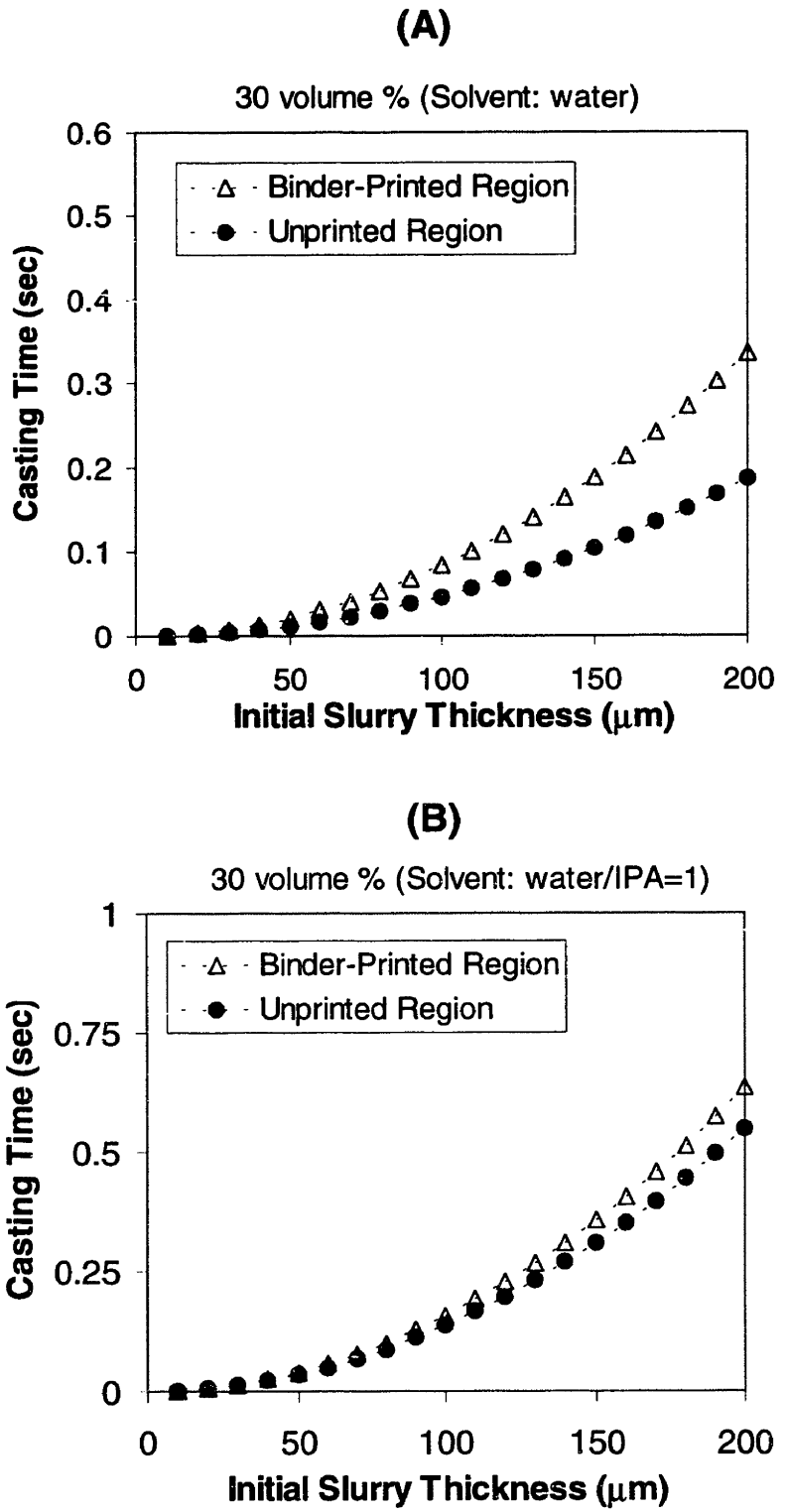

Figure 5.28. Calculated casting times for 30 volume percent slurry
(A) Slurry solvent: Water **(B)** Slurry solvent: Water/IPA=1

The ratio of $\frac{\cos(\theta_{unprinted})}{\cos(\theta_{binder})}$ necessary to match the casting rates can be calculated for different volume fractions of binder. Figure 5.29 shows the critical ratio of $\frac{\cos(\theta_{unprinted})}{\cos(\theta_{binder})}$ plotted as a function of volume fraction binder. When the ratio of the cos θ's is larger than the critical value, the casting rate is higher over the unprinted region. It is possible for the casting rate to be higher over the binder-printed region if the ratio of cos θ's is less than the critical value. The difference between the casting rates increases moving away from the critical value curve. The casting rate over the binder-printed region decreases as the volume fraction of binder increases for any given solvent.

The volume fraction of binder in slurry-based 3DP parts is typically between 0.04 and 0.08. The ratio of cos θ's must be between 0.87 and 0.74 to prevent differential slip casting for these binder contents. The contact angle ratios for the slurry solvents are shown in Table 5.11. The ratio for water is 1.51 and indicates the driving force for slip casting is significantly higher over the unprinted region. The ratio for water/methanol=1 is only 1.09. The relative driving forces for slip casting in the two regions are much closer for water/methanol solutions. However, the casting rate will still be slightly higher over the unprinted region for all volume fractions of binder. The ratio for water/IPA=1 is 0.97. At this ratio, the casting rates should be identical when the volume fraction of binder is 0.009. This agrees well with the profilometry data listed in Table 5.8. The profilometry results indicate that no bump was observed at the interface when the volume fraction of binder was 0.019.

Table 5.11. Ratio of cos θ's for slurry solvents

Solvent	$\frac{\cos(\theta_{alumina})}{\cos(\theta_{binder})}$
Water	1.51
Water/MeOH=1	1.09
Water/IPA=1	0.97

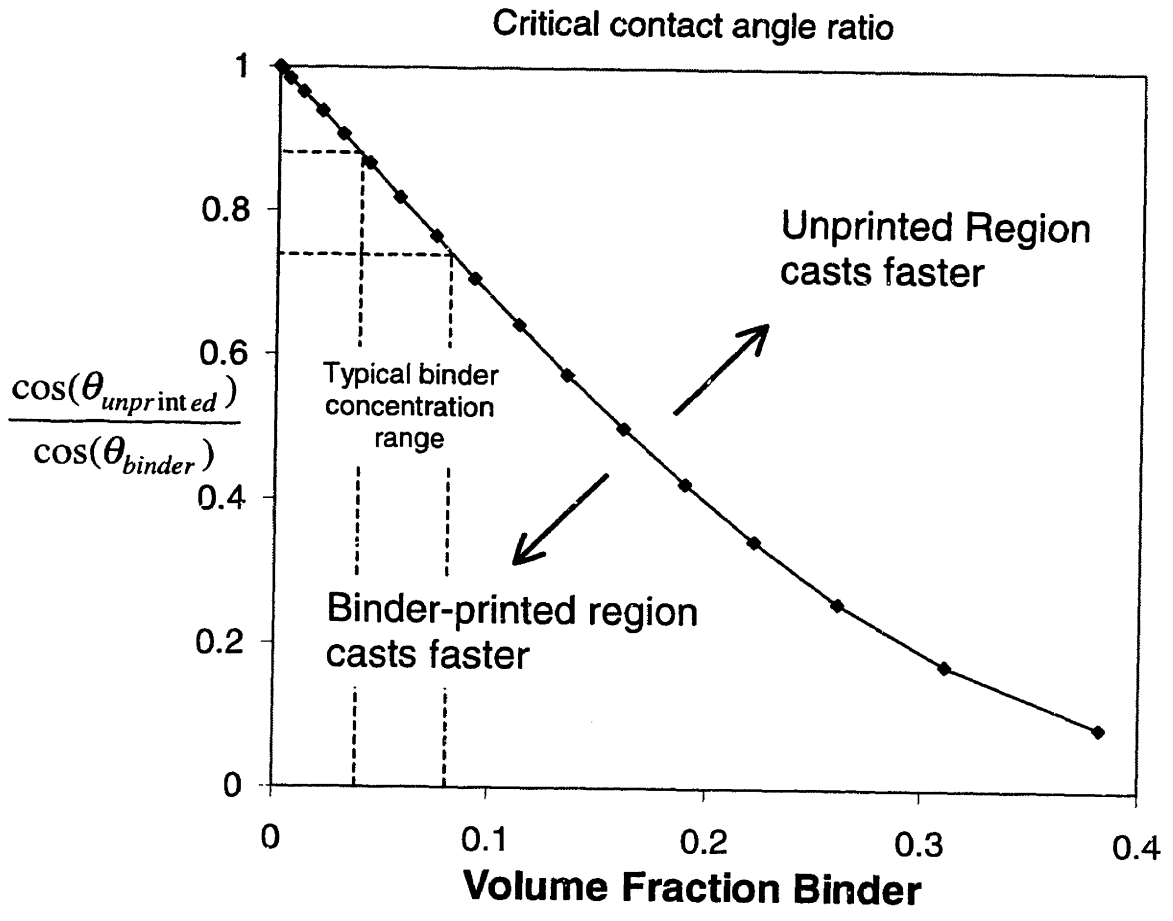

Figure 5.29. Critical cos θ ratio to match casting rates of binder-printed and unprinted regions. (Pore fraction = 0.60)

The magnitude of the bump at the interface due to slurry migration can also be estimated by examining the fluid fluxes in the powder bed. The bump at the interface results from the transport of slurry over the binder-printed region to the unprinted region. A schematic representation of the liquid transport is shown in Figure 5.30. The fluid flux is j_{binder} in the binder-printed region and $j_{unprinted}$ in the unprinted region. The length scale over which j_{binder} acts is L/2, one-half the length of the binder-printed region. The unprinted side is semi-infinite.

The differences in fluid transport in the two regions imply that liquid must be transported from the binder-printed region to the unprinted region to attempt to maintain a level fluid surface. This difference will lead to a disturbance in the fluid layer. (See Figure 5.30B) The volume of slurry, V, transported from the binder-printed side to the unprinted side is dependent upon the difference between j_{binder} and $j_{unprinted}$. The slurry migration will continue until the slurry has completely slip cast over the binder-printed region. The time at which slip casting is complete over the binder-printed region is t^*_{binder}. The total volume of slurry transported (per unit width) is calculated using:

$$V = \int_0^{t^*_{binder}} (j_{binder} - j_{unprinted}) \frac{L}{2} dt. \tag{5.16}$$

The liquid flux in each region is given by equation (5.8). The solution to equation (5.8) is:

$$j = \frac{d\xi_s}{dt} = -\frac{1}{2}\left(\frac{\Delta p n^2}{\frac{\eta n}{2k_c} + \frac{\eta n^2}{2\varepsilon_m k_m}} \right)^{1/2} t^{-1/2}. \tag{5.17}$$

The term in parentheses is constant with time for a given solvent and powder bed. The total volume of slurry transported, *V*, increases as the casting rates over the two regions diverge. Figure 5.31 shows the volume of slurry transported calculated from equation (5.16) for 30 volume percent slurry prepared with different solvents. *V* is smallest for water/IPA slurries and largest for slurries with only water as the solvent. *V* also increases for all slurries as the binder content increases from 0.05 to 0.10. The calculations indicate that *V* increases moving away from the critical cos θ curve shown in Figure 5.29.

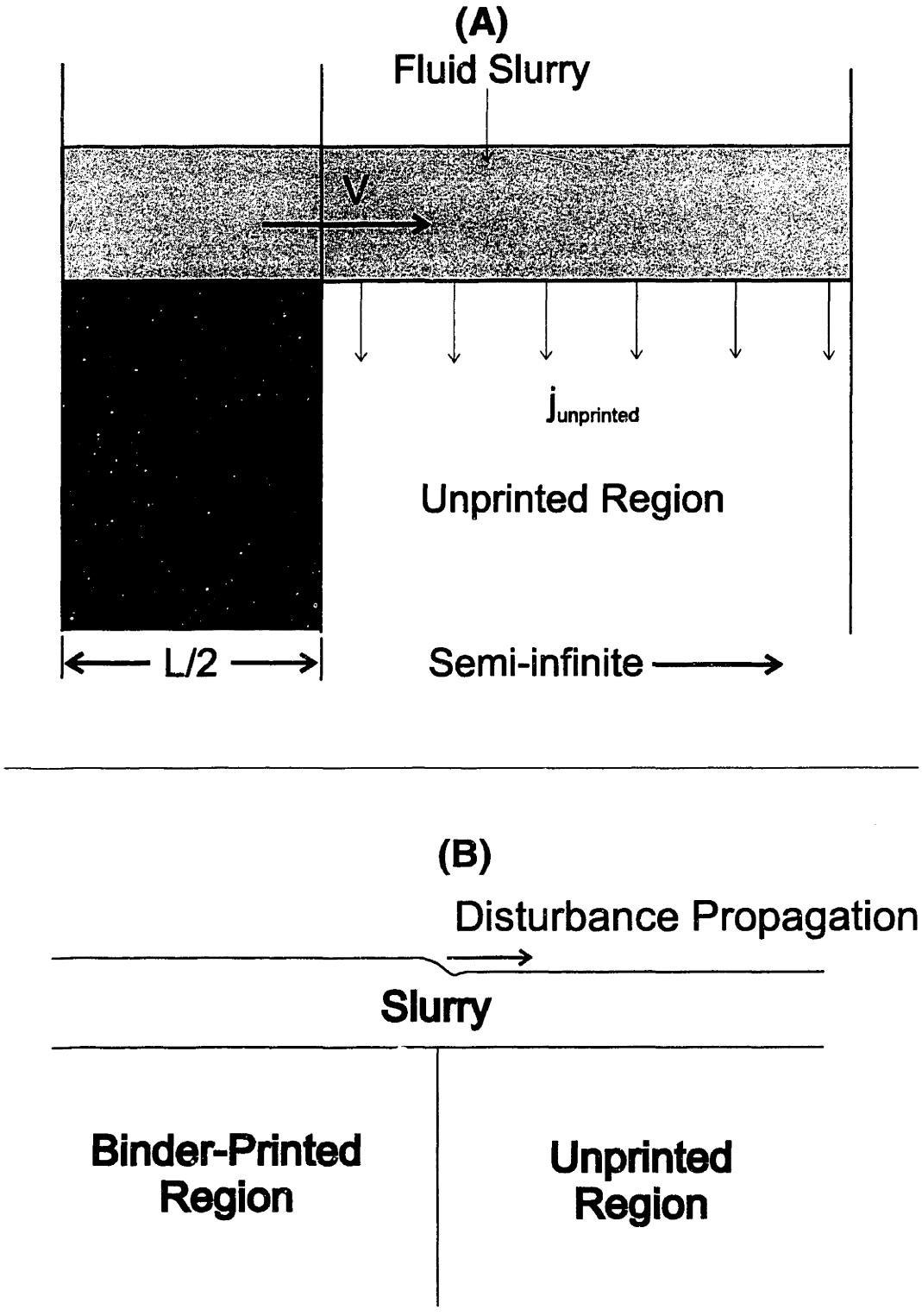

Figure 5.30. Model of fluid flow resulting from differential casting kinetics
(A) Schematic representation of fluid fluxes **(B)** Propagation of resulting disturbance in the slurry

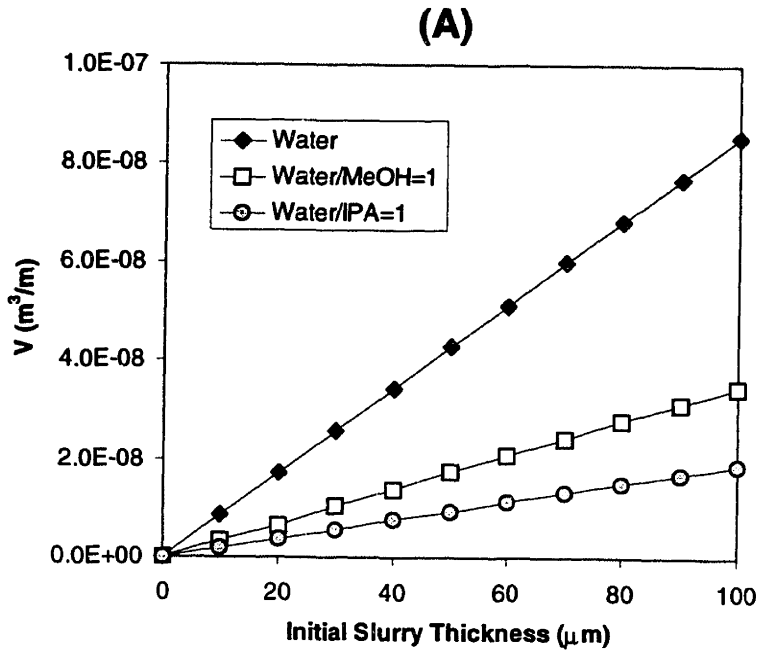

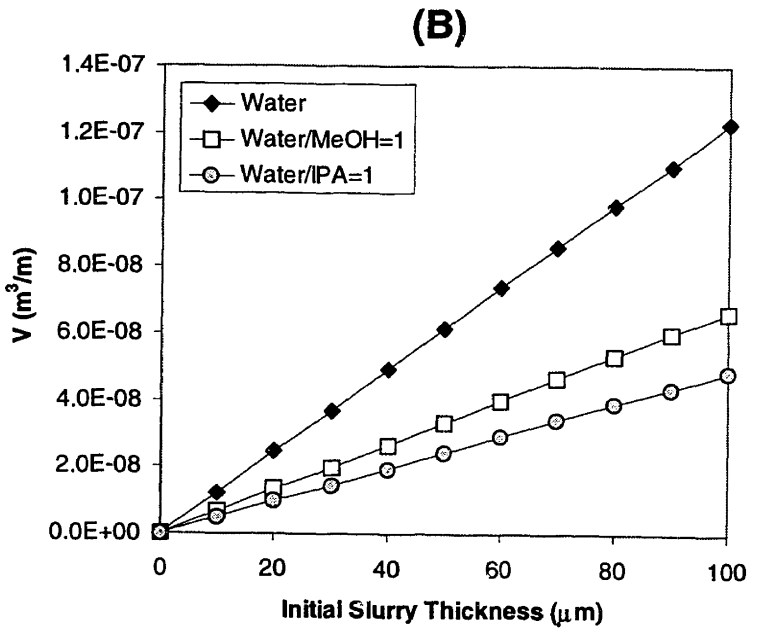

Figure 5.31. Volume of slurry transported, V, by differential casting for different slurry solvents (A) Volume fraction binder = 0.05 (B) Volume fraction binder = 0.10

The magnitude of the bump at the interface is dependent upon both the volume of slurry that migrates and the length scale over which the slurry is transported. Multiplying the velocity of slurry flow by the time it travels can approximate the length scale. The velocity, c, of a fluid disturbance in a thin layer of fluid is:[102]

$$c = \sqrt{gh}\,, \tag{5.18}$$

where g is the acceleration due to gravity and h is the depth of the liquid. The velocity of the disturbance differs from the actual flow of material. The velocity of slurry flow will be:

$$\text{velocity of slurry flow} = \frac{c\delta}{h}, \tag{5.19}$$

where δ is the height difference of the fluid surfaces. δ can be approximated as the slurry height minus the cast layer thickness:

$$\delta = \xi_s^o - \xi_c^*. \tag{5.20}$$

The length over which the disturbance moves will equal the velocity times the time for casting to occur on the unprinted side:

$$\textit{length scale of disturbance} = (\textit{velocity of slurry flow})(t^*_{unprinted}) \tag{5.21}$$

The length scale calculated for 30 volume percent slurries is shown in Figure 5.32. (The volume fraction binder is 0.05) The length scale is largest for Water/IPA=1 as the slurry solvent. The length scale calculated for water is very close to the observed width of the bump at the interface. The initial slurry layer thickness is typically 60 to 80 μm. The calculated length scales over this range are 0.7 to 0.1.5 mm. The observed widths of the bumps at the interface were typically ~0.5 to 1.0 mm.

The volume of slurry that migrates due to differential slip casting increases moving away from the critical cos θ's plotted in Figure 5.29. V is smallest for water/IPA solutions. The length scale of the disturbance is also largest for water/IPA solutions, implying the slurry is deposited over a larger distance. Conversely, V is largest for slurries containing only water as the solvent.

The height difference at the interface of the binder-printed region may also lead to slurry flow from the unprinted region to the binder-printed region. Scott Uhland[103] measured the height difference at the interface as the part thickness increased. The parts

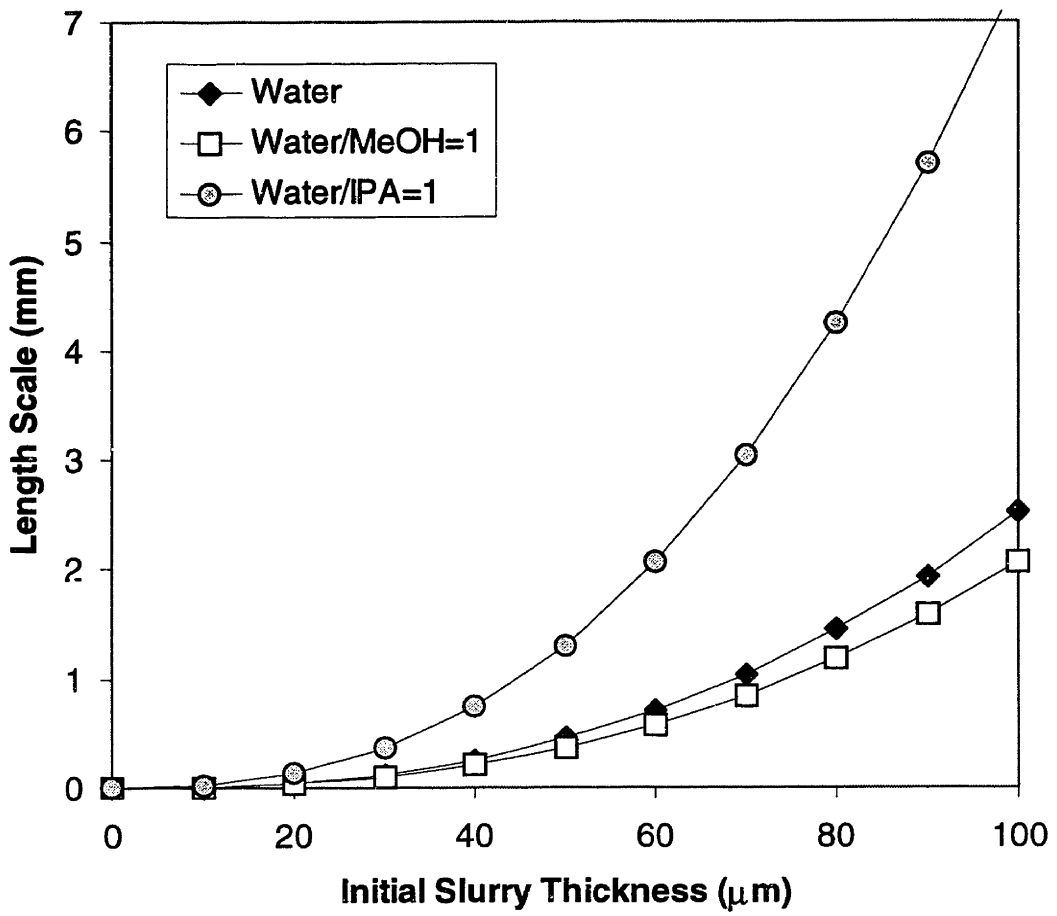

Figure 5.32. Disturbance length scale calculated from (5.21) (30 $^{v}/o$ slurries, volume fraction binder = 0.05)

were printed using 35 volume percent slurry with Water/IPA=1. The data measured by Uhland are shown in Table 5.12. The Δ Height appears to reach a steady-state value near 100 μm.

Table 5.12. ΔHeight at binder interface

Part Thickness (mm)	Δ Height (μm)
1.50	105 ± 19
5.00	85 ± 20
9.90	135 ± 33

The flow of slurry can be calculated using the approach followed to calculate the length scale of slurry migration. The height difference between the fluid surfaces will be equal to Δ Height of the powder bed regions. The velocity of slurry flow from the unprinted region to the binder-printed region is calculated using (5.19). The volume of slurry (per unit width) that backflows due to the powder bed height difference can be estimated by:

$$V_{back} = h \cdot \text{velocity of slurry flow} \cdot t^{*}_{unprinted} \cdot \qquad (5.22)$$

In order to reach a steady-state Δ Height, V_{back} must offset the slurry migration and density differences between the two regions. The steady-state value calculated using this approach is ~65 μm for 35 volume percent slurry with Water/IPA =1. (The calculation approach is given in Appendix B.)

The calculated magnitudes of the length scale and ΔHeight are close to observed values. However, the calculations assume inviscid flow. The assumption of inviscid flow is not rigorously valid and the fluid viscosity will affect the results of the calculations. This is discussed in further detail in Appendix B. The general approach that is followed, however, gives some insight into approaches to try to minimize the height difference. In order to reach a steady state ΔHeight, slurry must flow from the unprinted region to the binder-printed region. The volume of slurry that flows to the binder-printed region will depend on the velocity of slurry flow and the time that it flows. The velocity of flow will increase as viscosity decreases. The most obvious route to reduce viscosity is by reducing the solids loading. The time that the slurry flows is the

slip casting time over the unprinted region of the powder bed. The casting time calculated by (5.12) will increase as the solids loading of the slurry decreases. The casting time can also be increased by changing wetting properties and reducing the particle size. Modeling the slurry flow rigorously is extremely complicated, and additional experiments need to be performed to understand how or if the ΔHeight reaches a steady state value.

5.5. Discussion

The calculations of permeability and capillary pressure used in the model may differ from actual values. The effect of changes in the particle size, packing density, and volume fraction of binder in the part are able to be determined using the calculations. Reed[104] has questioned the validity of the Carmen-Kozeny model and suggests using an empirical technique. However, the permeability calculated by (5.14) is of the same order of magnitude of published values.[105] The calculated V_p/S_p is also within 20% of the pore radius at the peak of the differential intrusion plots. The model is not intended to explicitly predict the casting times. Rather, it is intended to give insight into the relative effect of the process variables on differential casting.

The colloidal filtration model is intended to point to routes to match the packing densities of the two regions and minimize the bump at the interface of the binder-printed region. The model proposes two routes to minimize the magnitude of the differential casting effect: reduce the amount of binder and control the contact angles of the solvent on the binder-printed and unprinted regions.

IPA and methanol in the slurry solvent reduce the contact angle of the solvent on Joncryl. The contact angle of water/IPA=1 on Joncryl was actually less than the contact angle on alumina. The effective contact angles that the solvents will have within actual powder beds will differ from the contact angles measured on the polished alumina and the Joncryl-coated slide. The contact angle on the binder-printed region will actually be a function of the amount of binder present and should approach the contact angle on pure alumina as the binder content approaches zero. Estimating the contact angle on the binder-printed region with the contact angle on the Joncryl-coated slide is reasonable

since the binder content in printed parts is sufficiently high to coat the particles. The concentration of binder will also be highest at the surface where the slurry solvent will contact the powder bed.

The *effective* volume fraction of binder in the powder bed can be reduced two ways: by controlling the *absolute* amount of binder that is deposited and by controlling how the binder is distributed within the powder bed. The absolute amount of binder that is deposited is simply the amount of binder per unit volume in the printed part. The binder distribution within the powder bed will control how much binder the slurry sees at the surface region of the printed part.

The concentration of binder in the surface region is inversely proportional to the penetration depth of the binder. For large penetration depths, the binder will be distributed over a larger volume. The amount of binder per unit volume is therefore lower for binders with large penetration depths. Methods to increase the penetration depth (or the line width) of the binder were effective at reducing the extent of the differential casting effect.

The measurements of line width indicate that both the powder bed and the binder are important variables. The surface roughness and pore size affect the spreading of a given binder. The viscosity of the binder also affects the extent of spreading. Line widths decreased as the viscosity of a given binder increased. Slurry casting times also indicated that the penetration of the binder decreased as the viscosity of the binder increased.

The pore structure and packing density are affected by the presence of the binder. The packing density is higher and the pore size is smaller in the binder-printed region compared to the unprinted region. Hong[106] and Ferreira et. al.[107] reported that the efficiency of particle packing in ceramic compacts is dependent upon the consolidation rate. Low consolidation rates allow the particles time to rearrange to an efficiently-packed structure. Consolidation rates are lower over the binder-printed region compared to the unprinted region. The differences in packing density were largest for slurries with only water in the solvent. The differences between the consolidation rates were also the largest for slurries prepared only with water. The differences between the packing

densities of the binder-printed and unprinted regions decreased as the difference between the casting times of the slurry over the two regions decreased. The difference in the packing density will further exacerbate the height difference at the interface of the printed region.

5.6. Conclusions

Differences in the slip casting rates over binder-printed and unprinted regions leads to differential slip casting at the interface. Differential slip casting affects the powder bed two ways: slurry migration and density differences. The differences in casting rates results from binder reducing the pore space in the binder-printed region and from differences in the wetting behavior. The differential slip casting leads to a bump at the interface and higher density in regions where the casting rate is lower.

The differential casting effect was measured directly using high-speed video. The casting rate of slurry over binder-printed regions decreased with increasing binder area density in the powder bed. The distribution of binder within the powder bed also affected the casting rate of the slurry. Binders with low viscosity spread over a larger volume. The casting time of slurry lines was lower over binder-printed regions in which the binder spread more.

The slurry solvent affects the wetting behavior of the slurry on the binder-printed and unprinted regions. Water/alcohol solutions reduce the contact angle on Joncryl-coated surfaces. The casting times for slurries over binder-printed regions were reduced substantially by using alcohol in the slurry solvent.

Several variables can be changed to minimize the differential casting. The slip casting model illuminates the effects of the process variables on the slip casting kinetics. The binder content in the part should be minimized to attempt to approach the critical cos θ ratio. The slurry chemistry should also be controlled to match the contact angle of the solvent on binder-printed and unprinted regions with the critical cos θ ratio. Both slurry migration and density differences are the result of the differential casting rates. These effects can be eliminated by matching the casting kinetics of the binder-printed and unprinted regions.

Water/IPA solutions work the best on Joncryl, and slurries with water/IPA=1 are stable with low viscosity. The binder distribution within the powder bed can also be changed to reduce the differential casting effect. Binders solutions that spread over a large volume will reduce differential casting. This suggests a trade-off between differential casting and the resolution of the printed part. Parts printed with 5 volume percent Joncryl binder solutions substantially improved the differential casting effects without any noticeable effects on the resolution of the parts.

CHAPTER 6
ALUMINA PARTS PRINTED WITH JONCRYL BINDER

6.1. Introduction

Joncryl binder was easily incorporated into the current print head design since it is a water-soluble solution phase binder. Several sets of experiments were performed to determine the effects of print conditions on microstructure and surface finish of printed parts. Parts were printed on two different 3DP machines. The laboratory hood machine was used for preliminary experiments to determine printing conditions. The hood machine does not have jet alignment or proportional deflection capabilities to optimize the binder printing. Larger, complex-shaped parts were printed on the Alpha machine based on the preliminary experiments on the hood machine. The binder droplet placement accuracy on the Alpha machine is ~10 μm. The Alpha machine also performs binder jet diagnostics each layer to maintain binder droplet accuracy.

6.2. Printing Procedure

The slurry-based printing process was shown schematically in Chapter 1. There are two distinct deposition processes. The powder bed is formed by jetting slurry, and the binder is deposited by ink-jet printing. The powder bed is dried after each deposition process with heating lamps. All alumina parts printed with Joncryl binder were prepared with HPA-1.0 powder. The powder beds were formed using the slurry-jetting process described in Chapter 3. Several foundation layers of powder bed were deposited before the first layer of binder was printed. The first one or two foundation layers of the powder bed formed on the substrate were usually somewhat rough. The powder bed structure usually evened out after the powder bed thickness exceeded 200 μm. The foundation layers were built up until the powder bed was at least 500 μm. The layer thickness for each jetted layer was usually between 20 and 50 μm. Layers thicker than 50 μm were formed by jetting and drying multiple times to avoid cracking.

After printing, the Joncryl binder was thermally cross-linked by heating the part within the powder bed for 1 hour at 150°C. PEG volatilization during heating degrades the redispersion behavior of the powder bed. An open container of PEG and the part

were heated together inside a dessicator to minimize the amount of PEG lost from the powder bed.

The powder bed redispersion process was performed very slowly and methodically. The porous substrate holding the powder bed and part was placed into a shallow pool of water. Water was allowed wick up through the substrate into the powder bed until the powder bed was fully saturated. The wicking process usually lasted more than 1 hour, depending on the thickness of the powder bed. Water was then gently rinsed over the powder bed to remove the part. The excess powder on the surface and within channels was removed by brushing it with a fine brush. The powder bed was also redispersed in an ultrasonic cleaner in some cases. Stronger parts were removed easily with this technique. However, the intensity of the cleaner was too high for weaker parts, and the surface of the parts eroded.

6.3. Binder Saturation Experiments

Several experiments were performed on the hood machine to determine the practical range of layer heights and binder saturations to print parts. Binder saturation is a measure of the amount of binder *solution* deposited into the powder bed. Binder saturation is the ratio of the volume of binder solution deposited to the pore volume in the powder bed for a given layer height.

$$\text{Binder Saturation (\%)} = 100\left(\frac{\text{Binder Solution Volume per Layer}}{\text{Pore Volume per Layer}}\right) \tag{6.1}$$

$$\text{Binder Solution Volume per Layer} = \frac{\text{Binder Flow Rate x Powder Bed Area}}{\text{Print Speed x Line Spacing}} \tag{6.2}$$

$$\text{Pore Volume per Layer} = \text{Pore Fraction x Powder Bed Area x Layer Height} \tag{6.3}$$

The binder saturation is a measure of the amount of total binder liquid deposited relative to the pore space of the powder bed layer. Binder saturation gives a sense of the degree of stitching between primitives and layers – high saturation implies there is a lot of liquid deposited into the powder bed that should spread over a larger volume compared to low saturation.

Another important variable to consider is the actual amount of solid binder material deposited. The amount of polymer binder that is deposited controls the strength

of the printed part. The volume percent of binder in the part is defined as the volume of binder solids deposited relative to volume of powder in the powder bed:

$$\text{Volume \% Binder in the Part} = 100\left(\frac{\text{Volume of Binder Solids per Layer}}{\text{Volume of Alumina Powder per Layer}}\right) \tag{6.4}$$

$$\text{Volume of Binder Solids/Layer} = \text{Volume of Binder Solution/Layer} \times {}^{v}/o\ \text{Binder} \tag{6.5}$$

$$\text{Volume of Alumina Powder/Layer} = \text{Packing Fraction} \times \text{Layer Height} \times \text{Powder Bed Area} \tag{6.6}$$

The volume % binder in the part is important to consider since the volume percent of Joncryl in the binder solution is a variable. It also gives a direct measure of the amount of binder that is present in the part after printing.

Test bars were printed with varying slurry composition, layer heights, binder line spacings, and volume fraction of Joncryl 52. The powder beds were jetted with 350 μm line spacing at 150 cm/sec. The binder line spacing was varied, and the binder print speed was 250 cm/sec. The compositions and printing conditions are listed in Table 6.1. The volume percent of binder in the part ranged from 2.4% to 21.7%. All bars were successfully removed from the powder bed. Parts with only 2.4% binder were noticeably weaker than parts with more than 5% binder.

The parts with the lowest binder concentration were printed with 400 μm line spacing. This line spacing is on the order of the line width of single line primitives. Stitching between primitives is expected to be poor, and the strength is low. Minimizing the amount of binder is key to minimizing the effects of differential casting, and part retrieval is possible with the volume percent of binder in the part as low as 2.4%.

Parts with more than 18 volume percent of binder delaminated. The infiltration of slurry into parts with that much binder was severely impeded. The slurry pooled on the surface of the printed region and did not completely slip cast for nearly one minute. Parts with less than 11 volume percent binder had uniform microstructures with no evidence of lamination defects. Figure 6.1 shows the effect of volume percent binder in the printed part. Figure 6.1A shows a delaminated part that contains 21.7 volume percent Joncryl. The microstructures of parts with less than 11 volume percent Joncryl were all very similar. Figure 6.1B shows a part with 10.9 volume percent Joncryl. The microstructure displays no evidence of lamination defects.

Table 6.1. Printing Conditions for Studying Binder Saturation

Part #	Slurry composition	Binder Composition	Binder line spacing	Layer Height (μm)	Volume % binder in part	Binder Saturation (%)
1	35% water/MeOH=1	15% J52 water/IPA=1	100	43	21.7*	216
2	"	"	200	43	10.9	108
3	"	"	300	43	7.2	72
4	"	"	400	43	5.4	54
5	"	"	100	86	10.9	108
6	"	"	200	86	5.4	54
7	"	"	300	86	3.6	36
8	"	"	400	86	2.7	27
9	35% water/MeOH=1	10% J52 water/IPA=1	100	43	21.0*	320
10	"	"	200	43	10.5	160
11	"	"	300	43	7.0	107
12	"	"	400	43	5.3	80
13	"	"	100	86	10.5	160
14	"	"	200	86	5.3	80
15	"	"	300	86	3.5	53
16	"	"	400	86	2.6	40
17	35% water (0.1% Triton)	10% J52 water/IPA=1	100	44	18.9*	285
18	"	"	200	44	9.5	143
19	"	"	300	44	6.3	95
20	"	"	400	44	4.7	71
21	"	"	100	88	9.5	143
22	"	"	200	88	4.7	71
23	"	"	300	88	3.2	48
24	"	"	400	88	2.4	36

* Part showed lamination defects

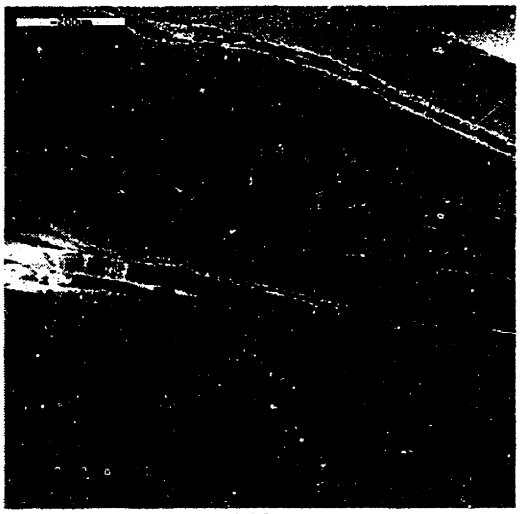

(A)

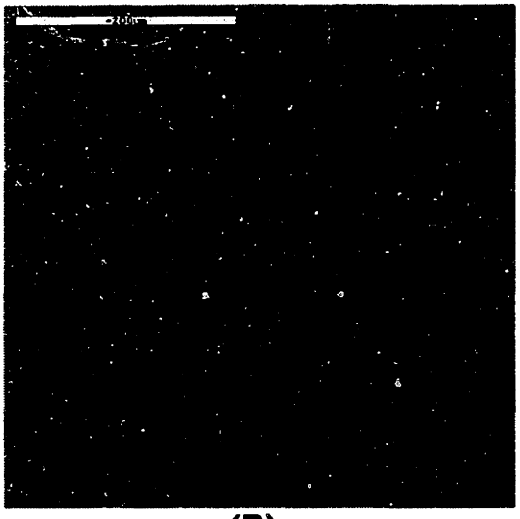

(B)

Figure 6.1. Effect of volume percent binder on the microstructure
A) Delaminated part, 21.7% volume percent binder
B) B) Uniform microstructure with no lamination defects, 10.9 volume percent binder

6.3.1. Surface Finish of Printed Parts

The surface finish of the top of the printed part was dependent on the slurry jetting conditions. Caradonna examined the surface finish of slurry-jetted beds in detail. Surface finish of jetted beds depends on the slurry composition, flow rate, print speed, and line spacing. Figure 6.2 show the top surface finish of a printed part. The surface profile is periodic and corresponds to the line spacing used to slurry-jet the powder bed.

The surface finish of the bottom and sides of the part is dependent upon the binder saturation and the extent of binder spreading. Figure 6.3 shows the bottom surface finish of three different parts. Figures 3A and 3B show parts printed with 10 volume percent Joncryl binder with line spacings of 200 μm and 400 μm, respectively. The surface finish is almost perfectly smooth for the part printed with 200 μm line spacing. The part printed with 400 μm line spacing indicates that the primitives are not completely merging, and voids are observed on the bottom surface. Poor stitching between primitives was observed at narrower line spacings for parts printed with 15 volume percent Joncryl 52. Figure 6.3C shows a part printed with 15 volume percent Joncryl at a line spacing of 300 μm. Voids are also observed on the bottom surface of the part due to poor stitching. Line widths of single line primitives decrease as the volume fraction of binder in the binder solution increases. This directly affects the stitching between primitives.

The surface finish along the sides is dependent upon both binder saturation and layer height of the powder bed. The effect of layer height is clearly observed when the binder saturation is low (<100%). Figure 6.4 shows the effect of layer height on the surface finish along the side of the part for two bars printed with 10% Joncryl 52 (water/IPA=1). The binder saturation was 80% for both bars. Figure 6.4A shows a part with 43 μm layer height. The edge is relatively smooth. The alignment of the binder jet during printing affected the surface finish. Figure 6.4B shows a part with the same binder saturation printed with 86 μm layer height. The individual layers are clearly distinguished. The shape of the primitive is also evident.

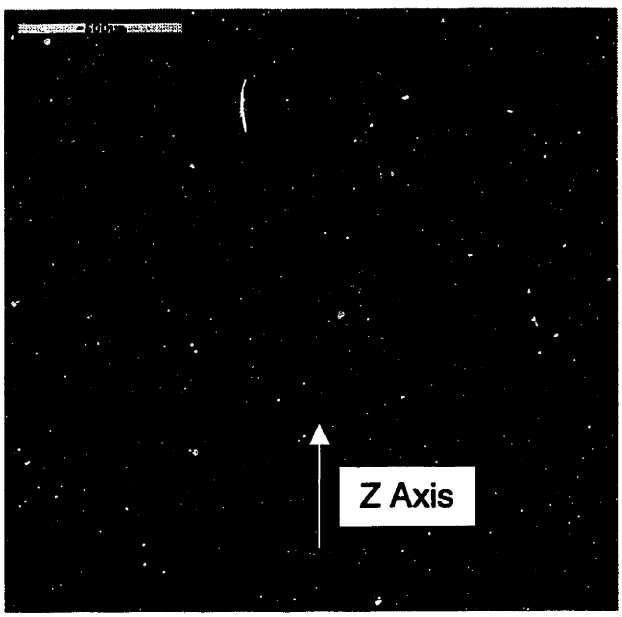

Figure 6.2. Top surface finish of part # 12

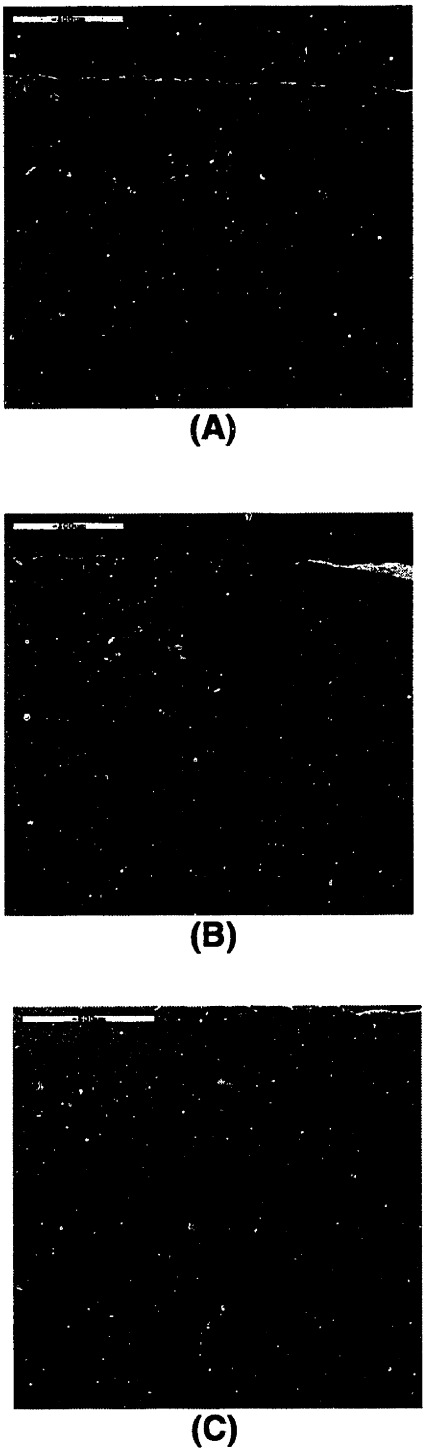

Figure 6.3. Bottom surface finish of parts A) 10% Joncryl, 200 μm line spacing B) 10% Joncryl, 400 μm line spacing C) 15% Joncryl, 300 μm line spacing

(A)

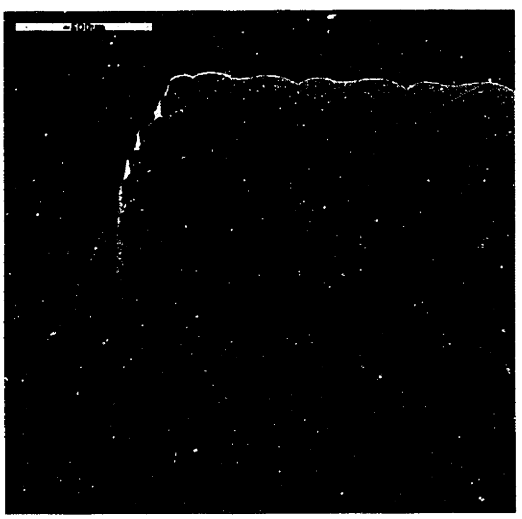

(B)

Figure 6.4. Effect of layer height on the surface finish of the sides A) 43 μm layer height, saturation = 80% B) 86 μm layer height, saturation = 80%

The surface finish was smoother for higher saturations. Figure 6.5 shows the side surface finish of a part printed on the Alpha machine. The part was printed with 10 volume percent Joncryl 52 (water/IPA =2). The layer height was 85 μm, and the saturation was 139%. The surface finish is very smooth and individual layers can not be clearly distinguished.

The surface finish of printed parts was measured by Uhland[103] using surface profilometry. The surface roughness (R_a) for bottom and vertical walls was 2.3 μm. The surface finish of the top surface was dependent upon both the slurry jetting conditions and the binder print style. Surface roughness was higher for parts with high concentrations of binder, since the slurry would pool on the surface prior to slip casting. However, the R_a for the top surface was only 1.9 μm for the part shown in Figure 6.5.

6.3.2. Mercury Porosimetry of Printed Parts

Mercury porosimetry measurements were performed on several bars printed with Joncryl. Each sample was fired for 6 hours at 600°C to burn out any organics prior to porosimetry measurements. Figure 6.6 shows the mercury porosimetry data for parts 10, 11, and 12 compared to the unprinted region of the powder bed. The density of the unprinted region is only 2.16 g/cm^3 (54.5%), while the average density of the printed parts is 2.33 g/cm^3 (58.8%). The average pore size is also smaller for the binder-printed regions.

There was no correlation between volume percent binder in the part and green density for parts containing 2% to 11% binder. Porosimetry data was erratic for the delaminated parts with greater than 11% binder. The green densities of the printed parts and unprinted regions are listed in Table 6.2.

The sintered densities of several parts fired at 1600°C for one hour are also listed in Table 6.2. The sintered densities of the printed parts were higher than the sintered powder bed and exceeded 98% theoretical. This indicated that carbon residue from the binder did not inhibit the sintered density. The microstructure of sintered, printed parts is shown in Figure 6.7. The sintered density of the part was 98.7%. The grain sizes were between 3 and 5 μm and exhibited normal grain growth. Some grain pull-out due to the

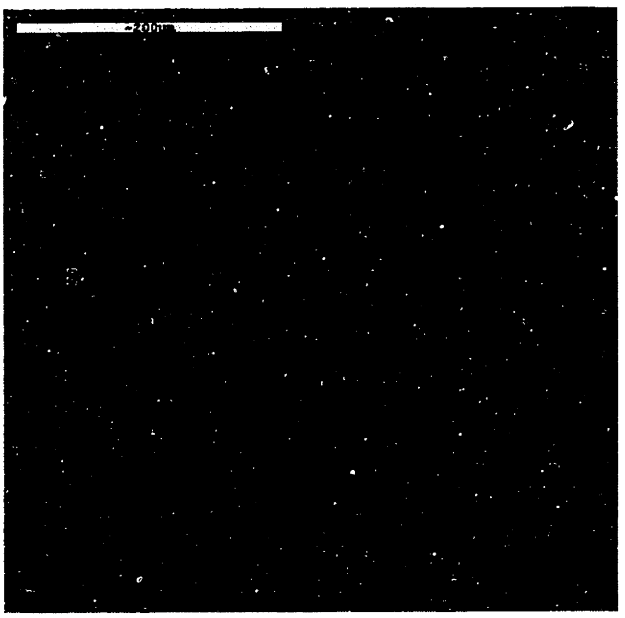

Figure 6.5. Surface finish of part printed on the Alpha machine (Layer height = 85 μm, saturation = 139%, 10% Joncryl 52 (water/IPA=2))

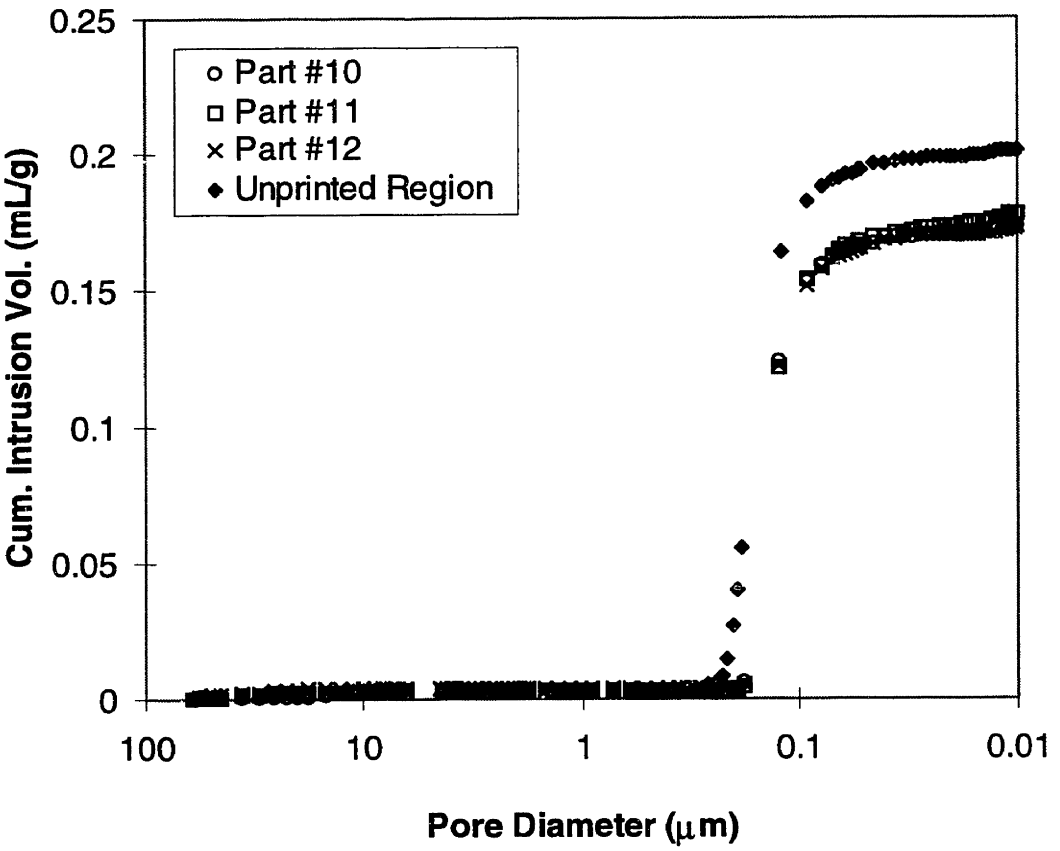

Figure 6.6. Mercury porosimetry of printed parts compared to the unprinted region of the powder bed.

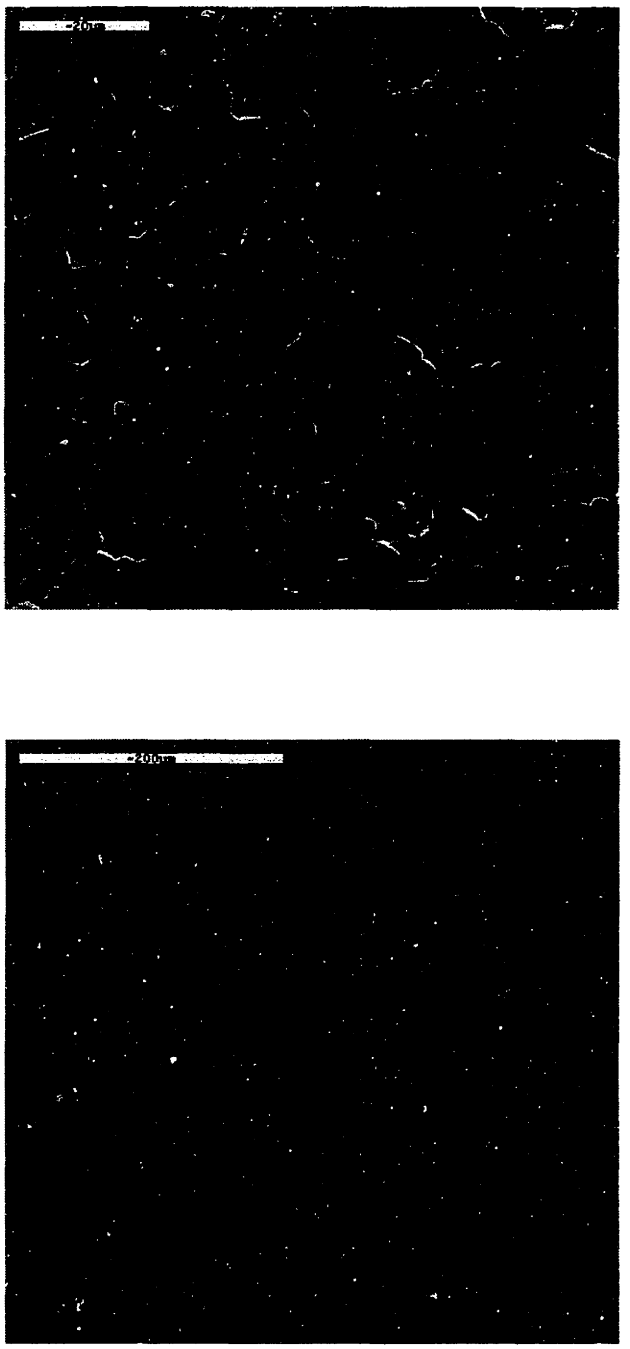

Figure 6.7. Sintered microstructure of printed part (Part printed 8-20-97, density = 98.7%)

grinding and polishing process is observed. Figure 6.7B indicates that the microstructure is uniform, and there is no evidence of defects incorporated due to the printing process.

Table 6.2. Densities of parts printed with Joncryl 52.

Part #	Green Density (%Theo.)	Sintered Density (%Theo.)
4	2.18 g/cm^3 (55.1%)	
6	2.27 g/cm^3 (57.3%)	
7	2.24 g/cm^3 (56.6%)	
Unprinted Region for Parts 9-16	2.16 g/cm^3 (54.5%)	3.86 g/cm^3 (97.4%)
10	2.25 g/cm^3 (56.8%)	3.90 g/cm^3 (98.4%)
11	2.22 g/cm^3 (56.1%)	3.91 g/cm^3 (98.7%)
12	2.45 g/cm^3 (61.9%)	3.91 g/cm^3 (98.7%)
13	2.33 g/cm^3 (58.8%)	3.90 g/cm^3 (98.5%)
14	2.24 g/cm^3 (56.6%)	3.89 g/cm^3 (98.3%)
15	2.29 g/cm^3 (57.8%)	3.88 g/cm^3 (97.9%)
16	2.31 g/cm^3 (58.3%)	3.89 g/cm^3 (98.2%)
Unprinted Region for Parts 17-24	2.21 g/cm^3 (55.8%)	
18	2.35 g/cm^3 (59.3%)	
19	2.32 g/cm^3 (58.6%)	
20	2.22 g/cm^3 (56.1%)	
21	2.34 g/cm^3 (59.1%)	
22	2.39 g/cm^3 (60.4%)	
23	2.43 g/cm^3 (61.4%)	
24	2.23 g/cm^3 (56.3%)	

6.4. Complex-Shaped Parts

Three additional criteria need to be considered to fabricate complex-shaped parts compared to printing test bars: the resolution of the primitives, powder removal from small channels, and scalability of the process. The resolution of the primitives was not a significant factor. The line width of Joncryl primitives is about 300 to 400 μm under the printing conditions used most frequently. Parts needed to be printed to examine the scalability and powder removal from small channels.

6.4.1. Rotors Printed on the Alpha Machine

"Large", complex-shaped parts were printed on the Alpha machine to determine the capabilities and limitations of the process. Most test bars were 30 layers or less with

a total thickness less than 3 mm. 8 mm high parts with simple geometries were first printed on the hood machine to determine suitable printing conditions. Figure 6.8 shows 100-layer parts printed on the hood machine. The slurry chemistry was 35 volume percent HPA-1.0, 0.05 M nitric acid, 2% PEG 400. The slurry solvent was water/methanol =1. The binder was 10 volume percent Joncryl 52 (water/IPA=2).

The powder bed was jetted with a line spacing of 300 μm and speed of 150 cm/sec. The slurry flow rate was ~1.7 cm^3/minute. This yielded layers 36 μm high. Two layers of slurry were jetted for each layer of binder making the effective layer height 72 μm. The binder was printed with 250 μm line spacing and 150 cm/sec print speed at a flow rate of 0.85 cm^3/min. The binder saturation was 130% with these conditions, and the volume percent of binder in the printed part was 8.7%.

The parts were very strong and could easily be handled without causing damage. The powder was also easily removed from the large channel by rubbing with a cotton swab during part retrieval. The green density of the part was 61.6% theoretical and sintered to 99.4% after firing at 1600°C for one hour.

Complex-shaped parts were printed on the Alpha machine using the general conditions used for the hood machine. The slurry and binder chemistries were not changed from the parts printed on the hood machine. The binder flow rate was slightly higher, 0.9 cm^3/minute, and the binder line spacing was 212 μm. The layer thickness was increased to try to offset the changes in binder printing conditions and maintain the binder saturation near 130%. Slurry flow rate was increased to 2 cm^3/min to increase the layer height to 85 μm. The binder saturation was 139%, and the volume percent binder in the parts was 9.4%.

Figure 6.9 shows as-printed and sintered parts printed on the Alpha machine. The total height of the parts was about 7 mm. The small holes in the rotors are less than 1 mm. The powder was removed from the holes without damaging the part by using thread to scrape out the unprinted powder. The sintered density of the parts was 99.1%.

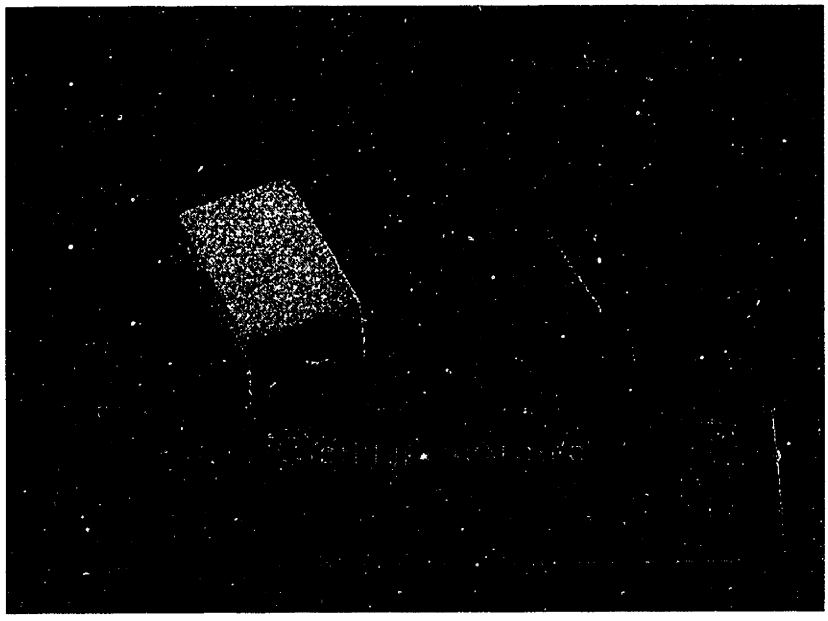

Figure 6.8. Parts printed on the hood machine

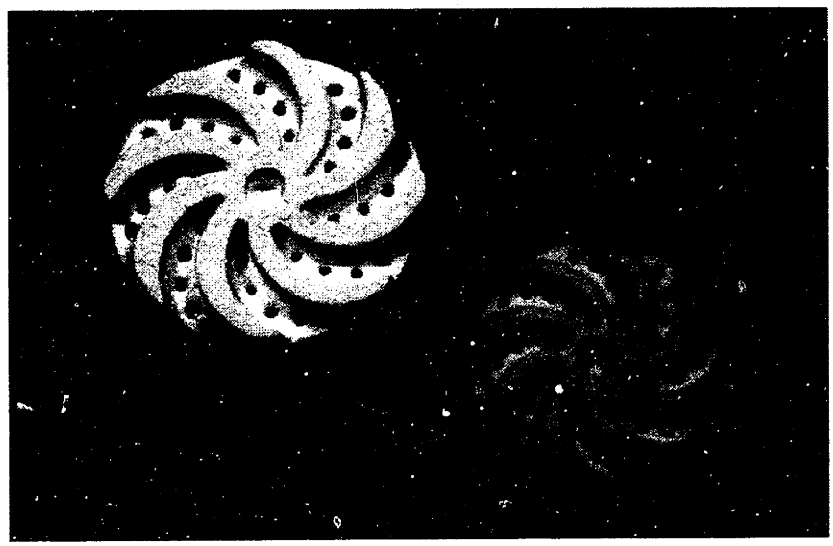

Figure 6.9. Alumina rotors printed on the Alpha machine

6.4.2. *Parts Printed while Shaving the Powder Bed*

The binder droplet placement accuracy is strongly dependent upon the working distance of the print head. The binder placement will vary if the working distance is not maintained at a fixed value. The bump at the interface of the binder-printed region that results from the differential casting effect will change the working distance of the print head over different regions of the powder bed. This problem is especially problematic for larger parts in which the bump at the interface grows with successive layers.

A method to register the height of the powder bed was tested to try to eliminate this problem. The printed region of the powder bed is depressed slightly into the powder bed. The powder bed was leveled with respect to the printed part periodically by shaving off the top of the powder bed. The process is shown schematically in Figure 6.10.

The shaving process was used while building a 1-inch high stator part. The printing conditions for the stator parts are listed in Table 6.3. The powder bed was shaved about every 10 to 15 layers for the 250-layer parts. The printed parts delaminated along three layers during the part retrieval process. The reconstructed parts are shown in Figure 6.11. The delaminated layers corresponded to layers that had been shaved. Scratches from the razor blade were clearly evident on the layers that delaminated. The sintered density, 97.7%, was the lowest of any printed part and may also indicate that defects were introduced by shaving.

Table 6.3. Printing conditions for stator part

Slurry Composition	32.5% HPA-1.0, 0.05 M nitric acid, 2% PEG 400, water/IPA=3/2
Slurry Flow Rate	2.1 cm^3/min
Slurry-Jetting Line Spacing	250 μm
Slurry-Jetting Print Speed	150 cm/sec
Layer Height	100 μm
Binder Composition	8% Joncryl 58
Binder Flow Rate	0.9 cm^3/min
Binder Line Spacing	202 μm
Binder Print Speed	150 cm/sec
Binder Saturation	124%
Volume % Binder in the Part	5.3%
Green Density	57.3%
Sintered Density (1600°C)	97.7%

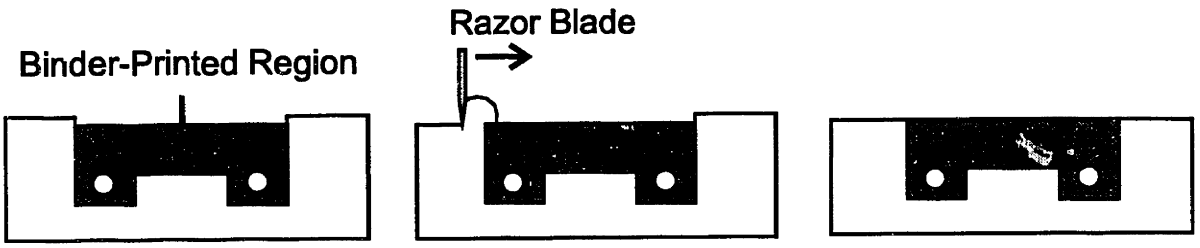

Figure 6.10. Schematic of the shaving process to level the powder bed

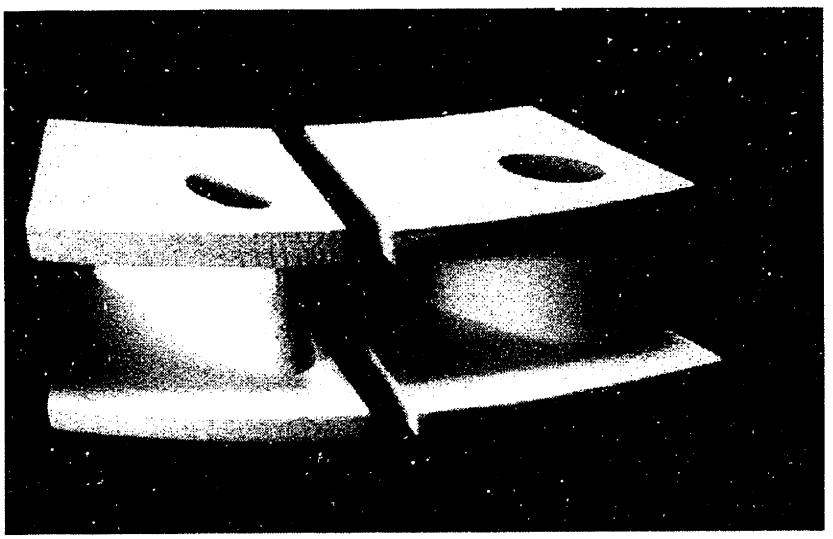

Figure 6.11. Reconstructed stator parts built using the shaving process to level the powder bed

6.5. Conclusions

Alumina parts were successfully fabricated with Joncryl binder using the slurry-based 3DP process. The amount of binder and how it is distributed throughout the part affect the microstructure and surface finish of printed parts. Very high concentrations of binder in the printed part lead to delamination. The polymer binder forms a film on the binder-printed region that prevents the slurry deposited in subsequent layers from forming an intimate bond by slip casting. These results indicate that the local concentration of binder in printed parts must be carefully controlled to prevent lamination defects. Regions in which excess binder is deposited will be vulnerable to delamination.

At lower binder concentrations, the slip casting process that forms the powder bed ensures that there is a uniform bond between layers. Depositing the material in a slurry form allows the particles to rearrange and pack efficiently. The Joncryl binder actually leads to higher packing density of the binder-printed region. Packing densities of the binder-printed region was typically around 60% theoretical. This value is sufficiently high to sinter the part to near theoretical density. Sintered densities of printed parts were greater than 98% theoretical. The sintered densities of the binder-printed parts were higher than the sintered density of the unprinted region. Therefore, the Joncryl binder does not inhibit sintering. Approaches that will improve the microstructure of the unprinted powder bed (tape casting or optimizing slurry chemistry for packing density) will improve the sintering.

Surface finish of printed parts is exceptional. Higher binder saturations improve stitching between primitives. At moderate saturations, individual layers are barely perceptible on vertical walls. The bottom surface finish is perfectly flat for parts printed with higher saturation. The surface finish of the top surface is controlled by the slurry-jetting process.

Increasing the scale of the process to build larger parts depends on reducing the magnitude of the bump at the interface of the binder-printed region. Three basic approaches can be followed to try to attack this problem:

1) Control the slurry deposition at each layer to form a level powder bed.
2) Remove the bump mechanically after it has formed.
3) Minimize the differential casting effect to prevent the bump from forming.

Method 1 may be accomplished to some extent with the tape casting technique of forming the powder bed. The doctor blade lays down a level layer of slurry and fills in the regions of the powder bed that were depressed. Method 2 was attempted with the shaving process. The failure of the shaving process illustrates the difficulties of trying to mechanically remove powder from the powder bed. The powder bed is relatively weak and mechanical forces can easily introduce defects into the powder bed. Also, any residual dust that may remain on the powder bed will act as a defect. Method 3 can be incorporated by utilizing the results of Chapter 5.

The extent of differential casting can be reduced by reducing the volume percent of binder in the part. Parts with as little as 2.5% binder had sufficient strength to survive part retrieval. Most printed parts had between 5% and 10% binder in the part. The results in Chapter 5 indicate that the volume fraction of Joncryl in the binder solution affects the distribution of binder in the part. Lower volume fraction binder solutions spread over a larger area and distribute the binder more uniformly. Parts printed with 5 volume percent Joncryl displayed almost no differential casting. Reducing the volume percent of binder in the printed part to the 2% to 5% range will reduce the differential casting significantly and large parts could be printed. There is clearly a trade-off between strength of the part and the magnitude of the bump at the interface when the wetting properties are non-ideal.

CHAPTER 7
CONCLUSIONS

The slurry-based 3DP process has been developed to meet the needs of fabricating engineered ceramic components: fine particle size, high green density, and uniform microstructure. The powder bed is formed from a dispersed slurry of ceramic particles. The fundamental interactions of the process differ substantially from the standard 3DP process, and a number of new issues were introduced. First of all, the powder bed is cohesive, and the powder bed needs to be redispersed to retrieve the part. The powder bed formation process controls the microstructure, and the process variables need to be controlled to form crack-free, uniform powder beds. Binder properties are also more restrictive in the slurry-based 3DP process. The binder must infiltrate into the powder bed and be insoluble during part retrieval.

The slurry-based 3DP process was successfully used to fabricate alumina components that sintered to >99% theoretical. The process is composed of a series of phenomena that depend on the interactions between solids and liquids in porous materials. The process has been developed to be applicable across numerous materials systems. The fundamental mechanisms involved in the process have been investigated to facilitate incorporating a variety of materials.

Capillary-driven transport affects all areas of the slurry-based 3DP process. Capillary-driven transport controls the casting of the slurry layer during the powder bed formation sequence. Liquid is withdrawn from the slurry by the porous layers of the underlying powder bed. The powder bed formation process and the rate at which liquid is withdrawn from the slurry affect the microstructure of the powder bed. Defects may be introduced into the powder bed any time slurry contacts the dry powder bed. The spray deposition process led to high concentrations of large pores in the powder bed since millions of slurry droplets impact the powder bed to form a single layer. The isolated slurry droplets cast very quickly on the surface of the powder bed. The concentration of large pores decreased as the solids loading of the slurry decreased. The slurry remained fluid on the surface of the powder bed longer and allowed droplets to merge before casting.

The slurry-jetting process reduced the concentration of defects in the powder bed substantially compared to the spray deposition process. The powder bed is formed by merging hundreds of slurry lines. Defects are controlled by the manner in which lines of slurry merge together. Preliminary experiments indicate that the tape casting process may further reduce the number of defects in the powder bed. The powder bed is formed with a single pass, and intra-layer defects are reduced.

Capillary pressure also controls cracking during powder bed formation. Capillary pressure was controlled by the surface tension of the solvent and the pore size of the powder bed. Cracking in multi-layer ceramic powder beds was avoided by controlling the amount of liquid deposited into the powder bed from the slurry. Powder beds displayed a critical saturation thickness that was dependent upon the powder size and surface tension of the solvent. The critical saturation thickness increased with increasing pore size and decreasing surface tension of the solvent. Crack-free powder beds were formed by maintaining the saturation thickness below the critical value.

The spreading behavior of binder in slurry-based 3DP powder beds is dependent upon the surface tension and viscosity of the binder solution. The spreading behavior affects the resolution of printed parts and also affects the distribution of binder within the part. Binder distribution affects the differential casting effect at the interface of the binder-printed region.

Differential casting occurs due to differences in the wetting behavior and the pore structure of the binder-printed region and unprinted region. Several different approaches can be taken to minimize the effects of differential casting. The volume fraction of binder in the printed part should be minimized to a point where the part has sufficient strength to survive part retrieval. Most parts were printed with 5 to 10 volume percent binder, but test bars with only 2 volume percent Joncryl binder were successfully retrieved. The binder distribution in the powder bed affected the differential casting effect. Differential casting was reduced on binder-printed regions that were printed with binder solutions that spread throughout a large volume. The chemistry of the slurry solvent is also critical for controlling differential casting. The contact angle on Joncryl binder was reduced by using water/alcohol mixtures. A critical ratio of the contact angles on the unprinted and binder-printed regions exists where the casting rate can be matched.

The casting rates over binder-printed and unprinted regions can be normalized by controlling the wetting characteristics and contact angle.

The microstructures of powder beds were dependent upon the casting rate. The green density of the part in the Joncryl-printed region was higher than the unprinted powder bed. The casting rate can be reduced by reducing the solids loading of the slurry, and green density may be improved with lower solids loading. The microstructure of printed parts displayed no evidence of lamination defects, except at very high binder concentrations. The slurry-based process allows the powder to pack efficiently and form a continuous powder bed.

Developing New Materials Systems

The slurry-based 3DP process was developed using alumina. New materials systems can be easily incorporated into the process by understanding the fundamental phenomena of the process. Silicon nitride and lead zirconate titanate (PZT) ceramic components have been fabricated using the general process developed with alumina. Figure 7.1 shows green and sintered silicon nitride components fabricated by the slurry-based 3DP process. The first step in developing a new materials system is optimizing the slurry chemistry to achieve high packing density and good redispersion. Redispersion behavior is dependent upon particle size and morphology. Several different powders should be screened initially to optimize slurry stability and redispersion behavior.

The slurry can be stabilized electrostatically or with polymeric dispersants. Polyelectrolyte dispersants have been successful for silicon nitride slurries used in the slurry-based 3DP process. The slurry stability can be measured directly using zeta potential measurements. The stability can also be observed indirectly by measuring the packing density of cast samples and measuring the viscosity of the slurry.

Slurry chemistry is critical to the redispersion behavior. Soluble species reprecipitate at the necks of the particles after the slurry is dried. The pH of the slurry should be controlled to minimize solubility. The solubility of silicon nitride is reduced using polyelectrolyte dispersants.[108] Alumina and silicon nitride solubilities increase dramatically at extreme pH. The pH of silicon nitride slurries stabilized with polyelectrolytes is more neutral than electrostatically-stabilized slurries.

Powder bed formation is the next step in adapting a new materials system. The cracking behavior of the powder bed should be studied. The critical saturation thickness of the powder bed needs to be identified to determine the slurry deposition conditions. The microstructure of the powder bed also needs to be fully characterized using mercury porosimetry. Large pores must be eliminated since they will be trapped as defects after sintering.

Binder printing conditions should be outlined by printing over a broad range of binder saturation, layer height, and binder solution chemistry. The spreading behavior of the binder is dependent upon the powder chemistry and microstructure. The minimum volume percent binder in the printed part will depend on the intrinsic strength of the powder bed itself. Silicon nitride powder beds prepared by the slurry-based process have had slightly lower packing density and strength than alumina powder beds. Binders with higher molecular weight have been used to increase the strength of printed silicon nitride parts. The effect of the binder on the microstructure of the printed parts needs to be characterized. Lamination defects caused by excess binder at the surface must be avoided.

Potential Applications

The slurry-based 3DP process can be used to fabricate a broad range of engineered ceramics components. Monolithic structural ceramic components made from alumina and silicon nitride have been fabricated with the process. Electro-ceramics are another area of interest. Multi-layer capacitors, inductors, and filters are three applications that may utilize the flexibility of the slurry-based process.

Functionally-graded materials (FGM's) may also be produced with 3DP. Dopants and second phase materials may be selectively printed within the component to change the properties of the material. Yoo has demonstrated the feasibility of fabricating zirconia-toughened alumina components with graded compositions. Uhland[103] has also changed the microstructure of silicon nitride locally by printing seeds that control grain growth. The slurry-based 3DP process is capable of controlling local composition and microstructure, as well as the macrostructure of the functional component.

APPENDIX A

USING WASHBURN'S EQUATION TO CALCULATE INFILTRATION TIMES

Levine and Neale report Washburn's equation for flow in a powder bed as:

$$\frac{dl}{dt} = \frac{kP_c}{\varepsilon \eta l}, \tag{A.1}$$

where l is the infiltration length, k is the permeability of the powder bed, P_c is the capillary pressure, ε is the void fraction of the powder bed, and η is the liquid viscosity. The solution to this equation is:

$$\frac{l^2}{t} = \frac{2kP_c}{\varepsilon \eta}. \tag{A.2}$$

The infiltration length, l^*, at which liquid disappears from the surface of the powder bed is directly proportional to the initial height, h^o, of a liquid column. A volume balance relationship can be used to relate l^* *and* h^o:

$$l^* = \frac{h^o}{\varepsilon}. \tag{A.3}$$

This equation assumes that the infiltration front is sharp and that the infiltrated region is 100% saturated. The time, t^*, for a liquid column of a height, h^o, to infiltrate into the powder bed can be calculated by substituting (A.3) into (A.2):

$$t^* = \frac{(h^o)^2 \eta}{2\varepsilon k P_c}. \tag{A.4}$$

Capillary pressure can be calculated using equation (5.11), and the permeability can be calculated from the Carman-Kozeny model (5.12).

The surface area, pore volume, capillary pressure, and permeability of a powder bed can be calculated by assuming the particles are uniform and spherical. The surface area , S, used in equation (5.12) is the surface area of the powder per unit volume of material:

$$S = \frac{\text{Surface Area}}{\text{cm}^3 \text{alu min a}} = 4\pi r^2 \cdot \frac{\#\text{particles}}{\text{cm}^3 \text{alu min a}}. \tag{A.5}$$

The number of particles per unit volume can also be calculated using:

$$V = \frac{4}{3}\pi r^3 \cdot \#\text{particles} = 1\text{cm}^3. \tag{A.6}$$

The value of S in terms of the particle diameter can be determined by rearranging (A.6) and substituting into (A.5):

$$S = \frac{\text{Surface Area}}{\text{cm}^3\text{alu min a}} = \frac{4\pi r^2}{\frac{4}{3}\pi r^3} = \frac{6}{D}. \tag{A.7}$$

The units for S will be m^{-1} and the units for k will be m^2 when S is substituted into (5.12).

The capillary pressure of the powder bed is calculated using the surface-to-volume ratio of the pore space. The surface area and volume of the pore space can be calculated on either a unit volume or unit mass basis. The surface area per unit mass, S_p, is:

$$S_p = \frac{6}{D\rho} \quad (m^2/g). \tag{A.8}$$

The volume of the pore space per unit mass, V_p, is:

$$V_p = \frac{\varepsilon}{(1-\varepsilon)\rho} \quad (m^3/g). \tag{A.9}$$

Equation (A.4) can be used to quickly calculate the infiltration kinetics of a liquid into a powder bed. It is also interesting to note that equation (5.10) and (A.4) converge as the solids loading in the slurry approaches 0. Equation (5.10) is a more general solution to a liquid infiltration problem in which the thickness of the infiltration front also grows due to slip casting of material in the slurry.

The height of the liquid column is dependent upon the binder dose. Tara Arthur's thesis outlines calculations to determine the geometry of the binder on the powder bed surface assuming the binder forms a circular cap. Assuming the binder line reaches an equilibrium shape, the width of the binder line depends on the binder dose and the contact angle of the binder:

$$\text{line width} = 2\left(\frac{\text{binder dose}(\sin^2\theta)}{\theta - \sin\theta\cos\theta}\right)^{1/2}. \tag{A.10}$$

The width and the height of the liquid column are both proportional to the square root of the binder dose. The infiltration time, t^*, is proportional to the square of the height, so

infiltration time should vary linearly with binder dose. The measured infiltration times shown in Figures 5.11 and 5.12 are linear with binder dose.

The infiltration times in section 5.3. are calculated using a binder dose of 10^{-4} cm^2. The line widths of Joncryl lines at this binder dose are about 500 μm. The height of the liquid column is assumed to be 20 μm under these conditions. The permeability of the powder bed was calculated using the Carman-Kozeny model. The specific surface areas of the APA-3.0 and HPA-1.0 powders are 1.4 m^2/g and 5.2 m^2/g, respectively. The permeabilities calculated for the 3 μm and 1 μm powder beds based on these values are 1.2×10^{-15} m^2 and 8.3×10^{-17} m^2, respectively.

The calculations assume uniform, spherical particles. The actual particles are irregularly-shaped with a distribution of particle sizes. The Ceralox powders are actually agglomerates of smaller primary particles. The particle size measured by sedimentation techniques is larger than the actual primary particle size. The particle sizes used in the calculations were varied to match the calculated specific surface area with the actual specific surface area of the powder. The measured surface areas were 1.4 m^2/g and 5.2 m^2/g for APA-3.0 and HPA-1.0, respectively. The equivalent spherical diameters used to match the surface areas to 1.4 m^2/g and 5.2 m^2/g were 1.1 μm and 0.29 μm, respectively.

APPENDIX B

The volume of slurry that is transported due to the height difference in the powder bed can be calculated using the approach outlined in Chapter 5. The volume of slurry that is transported (per unit width) can be estimated by the velocity of the slurry flow multiplied by the height of the slurry layer multiplied by the time of flow. The time of flow is the casting time over the unprinted region. The velocity of slurry flow is dependent upon the height difference between the fluid surfaces, δ.

The packing density of the binder-printed region is approximately 2% higher than the unprinted region. This implies that the layer thickness will be 2% smaller for the binder-printed region, even if no slurry migrates. The volume of slurry that backflows, V_{back}, must compensate for this 2% height difference in addition to the amount of slurry that migrates due to differential casting kinetics. For 100 μm slurry layers, the density difference will lead to ~1 μm differences in the powder bed height between the binder-printed and unprinted regions.

The height difference that results from slurry backflow can be calculated:

$$\Delta Height_{backflow} = \frac{V_{back}\left(\dfrac{slurry\ \text{solids loading}}{1\text{-pore fraction}}\right)}{\text{Length of Flow}}.$$

The length of flow is assumed to be the length of the binder-printed region, assuming the slurry flows freely over the binder-printed region. The magnitude of δ was varied to equate $\Delta Height_{backflow}$ to 1 μm. The value of δ that satisfied this criteria was ~49 μm.

The volume of slurry that backflows must also compensate for the slurry that migrates due to differential casting. This can be incorporated as follows:

$$\Delta Height_{net} = \frac{\left(V_{back} - V\right)\left(\dfrac{\text{slurry solids loading}}{1\text{-pore fraction}}\right)}{\text{Length of Flow}}.$$

The value of δ that satisfies this equation is ~65 μm.

The calculations of the velocity of slurry flow assume inviscid flow. The validity of this assumption can be checked a number of ways. One way is to calculate the thickness of the boundary layer and compare it to the thickness of the slurry layer.

Inviscid flow is a valid assumption if the boundary layer is only a small fraction of the fluid layer thickness. Assuming the boundary layer has a linear profile, the calculated boundary layer thickness was >90% of the slurry layer thickness for typical slurry-jetting conditions. This result indicates that inviscid flow is not a valid assumption for calculating the velocity of slurry flow.

REFERENCES

1. E. Sachs, M. Cima, J. Cornie, D. Brancazio, J. Bredt, A. Curodeau, T. Fan, S. Khanuja, A. Lauder, J. Lee, S. Michaels, "Three-Dimensional Printing: The Physics and Implications of Additive Manufacturing," *Annals of the CIRP*, **42**, pp. 257-60 (1993).

2. E. Sachs, M. Cima, P. Williams, D. Brancazio, J. Cornie, "Three Dimensional Printing: Rapid Tooling and Prototypes Directly from a CAD Model," *J. Eng. Ind.*, **114**, pp. 481-8 (1992).

3. E. Sachs, M. Cima, J. Bredt, A. Curodeau, T. Fan, D. Brancazio, "CAD-Casting: Direct Fabrication of Ceramic Shells and Cores by Three Dimensional Printing," *Man. Rev.*, **5**, pp. 117-26 (1992).

4. J. Yoo, K. Cho, W.S. Bae, S. Suresh, M. Cima, "Transformation -Toughened Ceramic Multilayers with Compositional Gradients", *J. Am. Ceram. Soc.*, **81** [1], pp.21-32 (1998).

5. B. Wu, "Microstructural Control During Three Dimensional Printing of Polymeric Medical Devices," Ph.D. Thesis, Massachusetts Institute of Technology (1998).

6. J.Bredt, "Binder Stability and Powder\Binder Interaction in Three Dimensional Printing," Ph.D. Thesis, Massachusetts Institute of Technology (1995).

7. T. Fan, Ph.D. Thesis, Massachusetts Institute of Technology (1995).

8. S. Khanuja, Ph.D. Thesis, Massachusetts Institute of Technology (1996).

9. J. Yoo, "Fabrication and Microstructural Control of Advanced Ceramic Components by Three Dimensional Printing," Ph.D. Thesis, Massachusetts Institute of Technology (1996).

10. B. Giritlioglu, "The Effect of Print Style on Mechanical and Microstructural Properties of Structural Ceramics Fabricated via Three-Dimensional Printing," M.S. Thesis, Massachusetts Institute of Technology (1996).

11. C. Herring, "Effect of Change of Scale on Sintering Phenomenon", *J. Appl. Phys.*, **21** [4], pp. 301-303 (1950).

12. C. Handwerker, J. Dynys, R. Cannon, R. Coble, "Dihedral Angles in Magnesia and Alumina. Distributions from Surface Thermal Grooves," *J. Am. Ceram. Soc.*, **73** [5], pp. 1371-1377 (1990).

13. S. Bennison, M.P. Harmer, "Effect of MgO Solute on the Kinetics of Grain Growth in Alumina," *J. Am. Ceram. Soc.*, **66**[5], pp. C90-C92 (1983).

14. J. Burke, "Role of Grain Boundaries in Sintering," *J. Am. Ceram. Soc.*, **40**[3], pp. 80-85 (1957).

15. C. Bruch, "Sintering Kinetics for the High Density Alumina Process" *Am. Ceram. Soc. Bull.*, 41[12], pp. 799-806 (1962).

16. Engineered Materials Handbook V. 4, Ceramics and Glasses, ASM International, Samuel J. Schneider, Jr., volume chairman (1991).

17. J. Reed, Introduction to the Principles of Ceramic Processing, John Wiley and Sons, New York (1988).

18. D. Richerson, Modern Ceramic Engineering, Marcel Dekker Inc., New York (1982).

19. B. McEntire, "Dry Pressing," Engineered Materials Handbook V. 4, Ceramics and Glasses, ASM International, Samuel J. Schneider, Jr., volume chairman, pp. 141-146 (1991).

20. M. Cima, J. Lewis, A. Devoe, "Binder Distribution in Ceramic Greenware During Thermolysis," *J. Am. Ceram. Soc.*, **72** [7], pp. 1192-1199 (1989).

21. G.N. Howatt, R.G. Breckenridge, J.M Brownlow, "Fabrication of Thin Ceramic Sheets for Capacitors," *J. Am. Ceram. Soc.*, **30**, pp. 237-242 (1947).

22. E.P. Hyatt, "Making Thin, Flat Ceramics - Review," *Am. Ceram. Soc. Bull.*, **65** [4], pp. 637-638 (1986).

23. R.E. Mistler, "Tape Casting: The Basic Process for Meeting the Needs of the Electronics Industry," *Am. Ceram. Soc. Bull.*, **69** [6], pp. 1022-1026 (1990).

24. K.P. Plucknett, C.H. Caceres, C. Hughes, D.S. Wilkinson, "Processing of Tape-Cast Laminates from Fine Alumina/Zirconia Powders," *J. Am. Ceram. Soc.*, **77** [8], pp. 2145-2153 (1994).

25. R. Ham-Su, D.S. Wilkinson, "Strength of Tape Cast and Laminated Ceramics," *J. Am. Ceram. Soc.*, **78** [6], pp. 1580-1584 (1995).

26. H. Chan, "Layered Ceramics: Processing and mechanical Behavior," *Annu. Rev. Mater. Sci.*, **27**, pp. 249-282 (1997).

27. J.D. Crawley, A.H. Heuer, W.S. Newman, B.B. Mathewson, "Computer-Aided Manufacturing of Laminated Engineering Materials," *Am. Ceram. Soc. Bull.*, **75** [5], pp. 75-79 (1996).

28. E. Griffin, D. Mumm, D. Marshall, "Rapid Prototyping of Functional Ceramic Composites," *Am. Ceram. Soc. Bull.*, **75** [7], pp. 65-68 (1996).

29. C. Griffin, D. Bautenbach, S. McMillin, "Desktop Manufacturing. LOM vs Pressing," *Am. Ceram. Soc. Bull.*, **73** [8], pp. 80-113 (1994).

30. F.F. Lange, "Approach to Reliable Powder Processing," *Ceramic Powder Science II*, pp. 1069-1083 (1987).

31. F.F. Lange, "Powder Processing Science and Technology for Increased Reliabilility," *J. Am. Ceram. Soc.*, **72**[1], pp. 3-15 (1989).

32. F.F. Lange, "New Interparticle Potential Paradigm for Advanced Powder Processing," *Ceramic Powder Science IV*, pp. 185-201 (1991).

33. I.A. Aksay, "Microstructure Control Through Colloidal Consolidation," Advances in Ceramics. Forming of Ceramics, Proceedings of a special conference of the 85th Annual Meeting of the American Ceramic Society, **9**, pp. 94-104 (1984).

34. I. Aksay, C. Schilling, "Colloidal Filtration Routes to Uniform Microstructures," Ultrastructure Processing of Ceramics, Glasses, and Composites, pp. 439-447, John Wiley & Sons, New York (1984).

35. A. Adamson, Physical Chemistry of Surfaces, 5th ed., Wiley, New York (1990).

36. J. Bear, Dynamics of Fluid in Porous Media, Elsevier (1972).

37. Levine, Neale, "A Theory of the Rate of Wetting of a Finely Dispersed Random Porous Network," pp. 241-260 in Wetting, Spreading, and Adhesion, J.F. Padday, ed., Academic Press (1978).

38. T. Arthur, M.S. Thesis, Massachusetts Institute of Technology (1996).

39. V. Knezevic," " M.S. Thesis, Massachusetts Institute of Technology (1998).

40. A. Bleier, "Stability of Ceramic Suspensions," Ch. 31 in Ultrastructure Processing of Ceramics, Glasses, and Composites, L.L. Hench and D.R. Ulrich, eds., John Wiley, New York (1984).

41. R.J. Hunter, Foundations of Colloid Science, Vol. I, Clarendon Press, Oxford (1987).

42. R.G. Horn, "Surface Forces and Their Action in Ceramic Materials," *J. Am. Ceram. Soc.*, **73**[5], pp. 1117-1135 (1990).

43. M.N. Rahaman, Ceramics Processing and Sintering, Marcel Dekker, New York (1995).

44. R.J. Hunter, Introduction to Modern Colloid Science, Oxford Press, Oxford (1993).

45. D.J. Shaw, Introduction to Colloid and Surface Chemistry, 4th ed., Butterworth-Heinemann, Oxford (1992).

46. J.N. Israelachvili, Intermolecular and Surface Forces, 2nd Ed., Academic Press, San Diego (1992).

47. B.V. Derjaguin, L.D. Landau, "Theory of the Stability of Strongly Charged Particles in Solutions of Electrolytes," *Acta Physiochem. URSS*, **14**, pp.633-662 (1941).

48. E.J.W. Verwey, J.Th.G. Overbeek, Theory of the Stability of Lyophobic Colloids, Elsevier, Amsterdam (1948).

49. T. Sato, R. Ruch, Stabilization of Colloidal Dispersions by Polymer Adsorption, Marcel Dekker, New York (1980).

50. D.H. Napper, Polymeric Stabilization of Colloidal Dispersions, Academic Press, London (1983).

51. H.C. Hamaker, "The London-van der Waals Attraction Between Spherical Particles," *Physics IV*, **10**, pp. 1058-1072 (1937).

52. E.M. Lifshitz, "The Theory of Molecular Attractive Forces Between Solids," *Sov. Phys. JETP*, **2**, pp.73-83 (1956).

53. G.A. Parks, P.L. deBruyn, "The Zero Point of Charge of Oxides," *J. Phys. Chem.*, **66**, pp. 967-973, (1962).

54. G.A. Parks, "The Isoelectric Points of Solid Oxides, Solid Hydroxides, and Aqueous Hydroxo Complex Systems," *Chem. Rev.*, **65**[2], pp. 177-198 (1965).

55. G.Y. Onoda, J.A. Casey, "Surface Chemistry of Oxides in Water," Ch. 30 in Ultrastructure Processing of Ceramics, Glasses, and Composites, L.L. Hench and D.R. Ulrich, eds., John Wiley, New York (1984).

56. J. Th. G. Overbeek, in Colloid Science, Vol. 1, Elsevier, Amsterdam (1952).

57. P. Hiemenz, Principles of Colloid and Surface Chemistry, Marcel Dekker, New York (1977).

58. J. Cesarano, I. Aksay, A. Bleier, "Stability of Aqueous α-Al2O3 Suspensions with Poly(methacrylic acid) Polyelectrolyte.

59. Y.K. Leong, "Exploitation of Interparticle Forces in the Processing of Colloidal Ceramic Materials," *Materials and Design*, **15**[3], pp. 141-147 (1994).

60. Y.K. Leong, P.J. Scales, T.W. Healy, D.V. Boger, "Interparticle Forces Arising from Adsorbed Polyelectrolytes in Colloidal Suspensions," *Colloids and Surfaces A*, pp. 43-52 (1995).

61. S. Biggs, T.W. Healy, "Electrosteric Stabilisation of Colloidal Zirconia with Low-Molecular-Weight Polyacrylid Acid," *J. Chem. Soc. Faraday Trans.*, **90**[22], pp. 3415-3421 (1994).

62. M.V. Parish, R.R. Garcia, H.K. Bowen, "Dispersions of Oxide Powders in Organic Liquids," *J. Mat. Sci.*, **20**, pp. 996-1008 (1985).

63. F.M. Fowkes, "Dispersions of Ceramic Powders in Organic Media," Advances in Ceramics, Vol. 21: Ceramic Powder Science, pp. 411-421 (1987).

64. G.D. Parfitt, J. Peacock, "Stability of Colloidal Dispersions in Nonaqueous Media," Surface and Colloid Science, v. 10, E. Matijevid, ed., Plenum Press, New York, pp. 163-226 (1978).

65. J. Zheng, J. Reed, S. Verma, "Ceramic Extrusion with PEG," *Am. Ceram. Soc. Bull.*, **73** [12], pp. 61-66 (1994).

66. R. Chiu, PhD Thesis, Massachusetts Institute of Technology (1991).

67. K. Wefers, C. Misra, "Oxides and Hydroxides of Aluminum," Alcoa Technical Paper No. 19, Alcoa Laboratories (1987).

68. S. Takeda, M. Kurose, I. Tari, "Surface Chemistry of Ceramic Powders in Aqueous Solutions," *Ceramic Powder Science IV*, pp. 203-208 (1991).

69. P. Heertjes, W. Witvoet, "Some Aspects of the Wetting of Powders," *Powder Technology*, **3**, pp. 339-343 (1970).

70. M. Caradonna, "The Fabrication of High Packing Density Ceramic Powder Beds for the Three Dimensional Printing Process," M.S. Thesis, Massachusetts Institute of Technology (1997).

71. B. DeBear, *personal communication.*

72. R. Holman, *personal communication.*

73. G.N. Howatt, R.G. Breckenridge, J.M Brownlow, "Fabrication of Thin Ceramic Sheets for Capacitors," *J. Am. Ceram. Soc.*, **30**, pp. 237-242 (1947).

74. E.P. Hyatt, "Making Thin, Flat Ceramics - Review," *Am. Ceram. Soc. Bull.*, **65** [4], pp. 637-638 (1986).

75. R.E. Mistler, "Tape Casting: The Basic Process for Meeting the Needs of the Electronics Industry," *Am. Ceram. Soc. Bull.*, **69** [6], pp. 1022-1026 (1990).

76. K.P. Plucknett, C.H. Caceres, C. Hughes, D.S. Wilkinson, "Processing of Tape-Cast Laminates from Fine Alumina/Zirconia Powders," *J. Am. Ceram. Soc.*, **77** [8], pp. 2145-2153 (1994).

77. R. Ham-Su, D.S. Wilkinson, "Strength of Tape Cast and Laminated Ceramics," *J. Am. Ceram. Soc.*, **78** [6], pp. 1580-1584 (1995).

78. E. Hyatt, "Making Thin, Flat Ceramics – A Review," *Am. Ceram. Soc. Bull.*, **65**[4], pp. 637-638 (1986).

79. R. Mistler, "High Strength Alumina Substrates Produced by a Multiple-Layer Casting Technique," *Am. Ceram. Soc. Bull.*, **52**[11], pp. 850-854 (1973).

80. C. Willoughby, J. Evans, "The Preparation of Laminated Ceramic Composites Using Paint Technology," *J. Mat. Sci.*, **31**, pp. 2333-2337 (1996).

81. M. Descamps, M. Mascart, B. Thierry, D. Leger, "How to Control Cracking of Tape-Cast Sheets," *Am. Ceram. Soc. Bull.*, **74** [3], pp. 89-92 (1995).

82. J. Lewis, K. Blackman, A. Ogden, "Rheological Property and Stress Development During Drying of Tape-Cast Ceramic Layers," *J. Am. Ceram. Soc.*, **79** [12], pp. 3225-3234 (1996).

83. G. Scherer, "Theory of Drying," *J. Am. Ceram. Soc.*, **74** [1], pp. 3-14 (1990).

84. R. Chiu, T. Garino, M. Cima, "Drying of Granular Ceramic Films: I, Effect of Processing Variables on Cracking Behavior," *J. Am. Ceram. Soc.*, **76** [9], pp. 2257-2264 (1993).

85. R. Chiu, M. Cima, "Drying of Granular Ceramic Films: II, Drying Stress and Saturation Uniformity," *J. Am. Ceram. Soc.*, **76** [11], pp. 2769-2777 (1993).

86. M. Hu, M. Thouless, A. Evans, "Decohesion of Thin Films from Brittle Substrates," *Acta Metall.*, **36** [5], pp. 1301-1307 (1988).

87. K. Kendall, "Agglomerate Strength," *Powder Metall.*, **31** [1], pp. 28-31 (1988).

88. J. Bear, Dynamics of Fluids in Porous Media, Dover, New York (1988).

89. F.A.L. Dullien, Porous Media: Fluid Transport and Pore Structure, 2nd ed., Academic Press, San Diego (1992).

90. A.E. Scheidegger, The Physics of Flow Through Porous Media, 3rd ed., University of Toronto Press, Toronto (1991).

91. T. Arthur, M.S. Thesis, Massachusetts Institute of Technology (1996).

92. V. Knezevic, M.S. Thesis, Massachusetts Institute of Technology (1998).

93. K. Percels Constant, J.R. Lee, Y.M. Chiang, "Microstructure Development in Furfuryl Resin-Derived Microporous Glassy Carbons," *J. Mater. Res.*, **11**[9], (1996).

94. E. Fitzer, W. Schafer, "The Effect of Crosslinking on the Formation of Glasslike Carbons from Thermosetting Resins," *Carbon*, **8**, pp. 353-364, (1970).

95. E. Fitzer, W. Schafer, S. Yamada, "The Formation of Glasslike Carbon by Pyrolysis of Polyfurfuryl Alcohol and Phenolic Resin," *Carbon*, **7**, pp. 643-648 (1969).

96. T. Fan, Ph.D. Thesis, Massachusetts Institute of Technology (1996).

97. D.S. Adcock, I.C. McDowall, "The Mechanism of Filter Pressing and Slip Casting," *J. Am. Ceram. Soc.*, **40**, pp. 355-362 (1957).

98. F. Tiller, C. Tsai, "Theory of Filtration of Ceramics: I, Slip Casting," *J. Am. Ceram. Soc.*, **69**, pp. 882-887 (1986).

99. B. Kostic, D. Kicevic, M. Gasic, "Mathematical Modelling of Ceramic Slip-Casting," *Ceramics International*, **16**, pp. 281-284 (1990).

100. I. Aksay, C. Schilling, "Mechanics of Colloidal Filtration," Advances in Ceramics. Forming of Ceramics, Proceedings of a special conference of the 85th Annual Meeting of the American Ceramic Society, **9**, pp. 85-93 (1984).

101. G. Scherer, "Theory of Drying," *J. Am. Ceram. Soc.*, **73**, pp. 3-14 (1990).

102. H. Lamb, Hydrodynamics, Dover Publications, New York (1932).

103. S. Uhland, personal communication.

104. J. Reed, "Liquid Permeability of Packed Particles: Why Perpetuate the Carmen-Kozeny Model?" *J. Am. Ceram. Soc.*, **76** [2], pp. 547-548 (1993).

105. A. Haerle, R. Haber, "Ultrasonic Real-Time Monitoring of Cake Structure During Slip Casting," *J. Am. Ceram. Soc.*, **78**, pp. 819-823 (1995).

106. C.W. Hong, "New Concept for Simulating Particle Packing in Colloidal Forming Processes," *J. Am. Ceram. Soc.*, **80**[10], pp. 2517-2524 (1997).

107. J.M.F. Ferreira, G. Tari, O. Lyckfeldt, "Influence of Magnesia on Drying Shrinkage Behaviour of Alumina," *Key Engineering Materials,* **132-136**, pp 358-361 (1997).

THESIS PROCESSING SLIP

FIXED FIELD: ill. _____ name _____

index _____ biblio _____

► COPIES: (Archives) Aero Dewey Eng Hum

Lindgren Music Rotch (Science)

TITLE VARIES: ► ☐ _____

NAME VARIES: ► ☒ Elliot

IMPRINT: (COPYRIGHT) _____

► COLLATION: 234 l.

► ADD: DEGREE: _____ ► DEPT.: _____

SUPERVISORS: _____

NOTES:

cat'r: date:

page:

► DEPT: MatSci + E ► J172

► YEAR: 1998 ► DEGREE: Ph.D.

► NAME: GRAU, Jason E.